REPORT ON RESEARCH ACTIVITIES FOR THE QUARTER APRIL 1 THROUGH JUNE 30, 1991

Prepared for

Nuclear Regulatory Commission
Contract NRC-02-88-005

Prepared by

Center for Nuclear Waste Regulatory Analyses
San Antonio, Texas

August 1991

REPORT ON RESEARCH ACTIVITIES FOR THE QUARTER APRIL 1 THROUGH JUNE 30, 1991

Prepared for

Nuclear Regulatory Commission
Contract NRC-02-88-005

Edited by

Wesley C. Patrick

Center for Nuclear Waste Regulatory Analyses
San Antonio, Texas

August 1991

TABLE OF CONTENTS

TABLE OF CONTENTS (Cont'd)

TABLE OF CONTENTS (Cont'd)

TABLE OF CONTENTS (Cont'd)

LIST OF FIGURES

LIST OF FIGURES (Cont'd)

LIST OF FIGURES (Cont'd)

LIST OF FIGURES (Cont'd)

LIST OF FIGURES (Cont'd)

LIST OF TABLES

LIST OF TABLES (Cont'd)

ACKNOWLEDGMENTS

This report was prepared to document work performed by the Center for Nuclear Waste Regulatory Analyses (CNWRA) for the U. S. Nuclear Regulatory Commission under Contract No. NRC-02-88-005. The research activities reported here were performed on behalf of the NRC Office of Nuclear Regulatory Research, Division of Engineering. The report is an independent product of the CNWRA and does not necessarily reflect the views or regulatory position of the NRC.

Each chapter of this report acknowledges those investigators who, although not specifically involved in writing the report, made significant contributions to the research projects. In addition, the authors gratefully acknowledge the technical support and technical reviews conducted by other members of the CNWRA and Institute staffs. Appreciation is particularly due Bonnie Garcia, Cathy Garcia, and Mary Ann Gruhlke, who prepared input to the individual chapters of the report, and to Pamela Smith, who prepared the final text of this document. We also acknowledge the able assistance of Curtis Gray, who provided graphical assistance, and Dr. Shirley Heller, who provided a full range of expert editorial services in the preparation of the final document.

1. EXECUTIVE SUMMARY

1.1. INTRODUCTION

This is one in a series of research quarterly reports that document and make available to the technical community work undertaken by the Center for Nuclear Waste Regulatory Analyses (CNWRA) as part of its contract with the U.S. Nuclear Regulatory Commission (NRC). Reports are prepared each calendar quarter and published as CNWRA documents. The fourth such report each year constitutes the annual progress report and is published as a NUREG/CR.

Each of the research projects discussed here is conducted in accordance with approved Research Project Plans, which were developed in response to research needs identified by the NRC and the CNWRA. These Plans are the vehicle for establishing the objectives, technical approach, justification, and funding for each of the studies. They also describe the interrelationships among the various projects which provide a sound basis for integrating research results. Because the Plans address primarily planning and management matters, they are not discussed in this project (with the exception of stating project objectives).

Eight individual research projects are discussed herein. Because several of the projects have only recently been initiated, they have relatively little work to report at this time. In such cases, this report provides basic information on the objectives of the new projects as well as early activities such as literature assessments. Other projects begun earlier have significant technical progress in laboratory, calculational, or field studies, or a combination of such investigations, to report.

This document provides, first, an Executive Summary that covers in capsule form the progress of each research project over the past quarter. The Executive Summary is followed by Chapters 2 through 9 representing each of the eight currently active research projects, respectively. Project objectives and a report of research activities and results (as appropriate) to date are given in each chapter.

1.2. UNSATURATED MASS TRANSPORT (GEOCHEMISTRY)

A major geologic feature potentially affecting the suitability of Yucca Mountain, Nevada, as a repository site for high-level nuclear wastes is the presence of thick, laterally-extensive zones of zeolitic tuff. Because of their sorptive properties, zeolites could provide important geologic barriers to migration of radionuclides from the repository to the accessible environment. To support the NRC's high-level waste program, the CNWRA is conducting experimental studies on the thermodynamic and ion exchange properties of zeolites under Task 3 of the Geochemistry Research Project. The objective of these studies is to generate data needed to evaluate the effectiveness of zeolitic tuffs as barriers to radionuclide migration.

Experiments have been proposed previously to evaluate phase equilibria between the zeolite minerals clinoptilolite and analcime and the aqueous solutions. Because of the absence

of dissolution/precipitation rate data for the zeolites, accurate prediction of the required duration to achieve equilibrium in the experiments is precluded. The first phase of the proposed experiments, therefore, involves determination of the rate of dissolution of the zeolite mineral analcime. This phase was initiated during the previous quarter, during which a set of scoping experiments was completed. Interpretation of the results for those experiments are given in the modeling section of Chapter 2. In addition, a new and more extensive set of experiments on analcime dissolution was initiated during this period based on the results of the scoping studies. Details of these new experiments and initial results are reported in the experimental section of Chapter 2.

In the modeling task of the Geochemistry Research Project, principles of thermodynamics, kinetics, and mass balance are applied to the interpretation of natural and experimental systems pertinent to Yucca Mountain. One specific objective is the interpretation of data generated in the experimentation task of the project. Theoretical interpretation permits extraction of meaningful and useful parameters from the experimental data, assists design of future experiments, and provides a methods to evaluate aspects of the models including theory and codes.

Kinetic and thermodynamic interpretations of experimental data for analcime dissolution indicate that equilibrium is approached in the experiments as shown by decreasing reaction rates and increasing saturation index. Dissolution is apparently stoichiometric with respect to Si and Al release, and congruent with absence of secondary phase growth. Based on interpertation of experimental data, a provisional rate constant for analcime dissolution under conditions far from equilibrium is deduced to be 1.4×10^{-15} moles cm^{-2} sec^{-1} . This rate constant value can be used in future data interpretation and in the design of a more complete set of experimental studies. Thermodynamic analyses indicate that data in the EQ3/6 data base (e.g., the equilibrium constant for analcime dissolution) will require some revision to correctly represent the experimental results.

1.3. THERMOHYDROLOGY

Technical issues and uncertainties for the Yucca Mountain HLW repository site indicate a need for research on thermohydrological phenomena, i.e., phenomena associated with heat and fluid flow, to provide information relevant to performance assessment and design criteria. The class of thermohydrological phenomena examined in this project includes phenomena driven by heat emanating from HLW emplaced in a geologic repository. Information derived principally from research is used to establish a knowledge base of thermohydrologic phenomena which will be utilized to assess models of processes used in performance assessments.

Data collected during the execution of separate-effects experiment Test 6 were evaluated in greater detail during the second quarter of 1991. The water saturation values calculated using information collected with the gamma-ray densitometer proved to be more quantitatively meaningful than was initially thought. These more meaningful results were achieved by

normalizing raw densitometer readings collected during Test 6 using standard baseline densitometer measurements of aluminum block standards located next to the test chamber.

Water saturation contours plotted using normalized densitometer results have provided valuable insight into the nature of liquid water flow in the test chamber during Test 6. Although the resulting plots, in general, concur with observations made using photographs of the dye tracer, other characteristics of the flow regime were not previously identified. Of particular interest is the elevated water saturation immediately ahead of the drying front along the lower boundary of the test chamber near the higher-temperature heat exchanger boundary. Although the increase in water saturation ahead of the drying front was indicated using the tensiometer results, not until the water saturation plots were made available was this phenomenon made apparent.

A post-processor program has been written to configure output data from the TOUGH code for direct input into TECPLOT, a graphics computer package. This post processor will permit more rapid assessment of results provided by TOUGH.

The revised Thermohydrology Research Project Plan was submitted to the NRC office of Nuclear Regulatory Research (RES). A meeting between RES and CNWRA staff was held on June 20, 1991, to discuss their comments with regard to the revised project plan. Progress on the project has continued pending resolution of these comments. Accordingly, material and instrumentation for the next series of laboratory experiments, designated Test 7, have been procured and are currently being assembled.

1.4. SEISMIC ROCK MECHANICS

A previously completed literature review of the state-of-the-art (NUREG/CR-5440) reveals that the seismic effects calculations performed to date on underground structures have not been supported by an adequate level of experimental and field investigations. The experimental support for most of the programs has focused on soils rather than on structurally complex rock formations. Computer programs are currently available to model dynamic events of underground structures in rock formations. However, these programs have not been validated with well-planned and rigorous experimental and field protocols. This Seismic Rock Mechanics Research Project is aimed at developing a better understanding of the key parameters affecting the repository under seismic loadings and consequently validation of computer programs for use in seismic assessment of underground structures in tuff media.

The activities performed for the Seismic Rock Mechanics Project during this reporting period included data analysis for the qualification studies of the Distinct Element Computer Code 3DEC against the benchmark analytical problem "Circular Excavation with an Adjacent Discontinuity in an Infinite Elastic Medium" and data collection from the instrumented field studies at the Lucky Friday Mine. Only the result for the qualifications studies is reported herein.

The benchmark analytical problem, "Circular Excavation with an Adjacent Discontinuity in an Infinite Elastic Medium," contains five cases. They are: (1) a plane of weakness intersecting an opening along the diameter perpendicular to the major principal stress, (2) a plane of weakness intersecting an opening along the diameter parallel to the major principal stress, (3) a plane of weakness intersecting an opening along a diameter with a 45-degree angle with respect to the major principal stress, (4) a plane of weakness perpendicular to the major principal stress and intersecting an opening nondiametrically, and (5) a plane of weakness transgressing the zone of influence of an opening.

The analytical solutions for the five cases were derived assuming plane stress condition by Kirsch. The 3DEC runs assumed plane strain conditions by restricting displacement in the Z-direction. However, induced shear stresses along the Z-direction on the planes of weakness are negligibly small compared with the shear stresses along the X- or Y- direction. The 3DEC results and the analytical solutions are therefore comparable. The 3DEC code appears not to be able to adequately simulate slip and separation on planes of weakness subject to the heterogeneous states of stress developed around excavations in stressed rock. Contrary to the prediction from the Kirsch solution, the 3DEC analyses give nonzero results for the shear stresses on the planes of weakness for both Cases 1 and 2. The nonzero shear stresses are very small compared with the associated normal stresses for Case 1; consequently, their impact is insignificant. For Case 2, the normal stresses on the plane of weakness near the excavation are generally small. In most conditions, they are close to zero. As a result, the ratios of the nonzero shear stresses to the associated normal stress may be greater than the assigned coefficient of joint friction and therefore may result in joint slip prior to joint separation. The numerical predictions of (1) slip instead of separation at the intersection of the plane of weakness and the excavation when $K = 1/3$ and (2) slip following separation when $K = 1/6$ confirm the previous statement. (Note: K is the ratio of applied minor principal stress to applied major principal stress.)

Similar errors on shear stress prediction introduced by the 3DEC code may be largely responsible for the prediction of slip prior to the excavation of the opening for Case 3 and for the inability of the 3DEC code to simulate the Case 3 problem. For Cases 4 and 5, the 3DEC code predicts slip at angles of joint friction substantially greater than the angles suggested by the Kirsch solution. The reason for the departure of the 3DEC predictions from the predictions of the Kirsch solution for Case 4 and 5 is not clear. However, when the assigned angle of joint friction (16.3 degrees) is considerably smaller than the critical angle (60 degrees), the 3DEC results for the normal and shear stress distribution on the plane of weakness for Case 4 are in a reasonable agreement with the independent solution from a boundary element code. This observation is true except in an area close to the boundary of the excavation.

1.5. INTEGRATED WASTE PACKAGE EXPERIMENTS

The NRC regulation 10 CFR 60.113 requires a waste package to provide substantially complete containment of radionuclides for a period of 300 to 1000 years. The NRC, in its role of licensor, must understand the important parameters that affect long-term performance of waste

package components and the applicability and limitations of the test techniques used to obtain these parameters. The goal of the Integrated Waste Package Experiments (IWPE) Project is to assist NRC in the licensing process and to provide information for timely prelicensing guidance to DOE. Because the current waste package concept, at least for spent fuel, relies essentially on a thin-walled container, most of the attention in the IWPE Project is focused on evaluation of degradation processes that affect the candidate container materials. The project consists of both confirmatory and exploratory activities and is divided into six tasks: Task 1, - Corrosion, Task 2 - Stress Corrosion Cracking, Task 3 - Materials Stability, Task 4 - Microbiologically Influenced Corrosion, Task 5 - Other degradation Modes, and Task 6 - General Reporting. The accomplishments in Tasks 1 and 5 are reported here.

Experimental investigation of the localized corrosion of type 316L stainless steel, using a screening type electrochemical test, was completed in this quarter. Initially, a two-level, full factorial test matrix was used that examined the effects of chloride, nitrate, sulfate, and fluoride as independent variables. Unlike the case of alloy 825 previously reported, a good correlation between electrochemical parameters and visual evidence of localized corrosion was observed. In order to compare the behavior of alloy 825 and type 316L stainless steel, the localized corrosion index (LCI) that was defined for alloy 825 was modified. Among the independent variables examined, chloride was found to be the only statistically significant factor, enhancing the localized corrosion susceptibility of 316L stainless steel. Alloy 825 showed superior localized corrosion resistance (lower modified LCI) compared to type 316L stainless steel. Further experiments found that nitrate becomes an important inhibitor of localized corrosion of 316L only at a concentration beyond that examined in the factorial matrix. Bicarbonate and sulfate inhibit localized corrosion effectively. Comparison to alloy 825 indicates that nitrate and sulfate are more effective inhibitors in alloy 825, presumably due to its higher alloyed chromium content.

Since bicarbonate is an important component of the groundwater and it plays a significant role in the corrosion of copper-base alloys, a systematic experimental determination of the bicarbonate concentration was conducted in various model solutions to assess the effect of other anions on the analysis. It was found that at low concentrations of bicarbonate (88 ppm), the presence of large concentrations of other anions, such as chloride, sulfate, and nitrate, resulted in an overestimate of the concentration of bicarbonate by about 15 percent. This may be attributed to ionic strength effects. At larger concentrations of bicarbonate (8800 ppm), the bicarbonate analysis was not affected by the presence of the other anions. However, it was found that fluoride interfered with the analysis at both bicarbonate levels, giving a positive error similar to that reported for other anions of weak acids (HNO_3 and H_2SO_3).

As part of Task 5 in the IWPE, hydrogen absorption and embrittlement kinetics in some of the candidate container materials were examined. The most important sources of hydrogen are believed to be the galvanic coupling of the container material to less noble borehole liner and corrosion in crevices generating acidic, reducing conditions. Techniques for measurement of hydrogen absorption kinetics have been established through a research program funded by CNWRA at Fontana Corrosion Center. Measurement of embrittlement susceptibility of alloys

825 and C-22 indicated that the former was not susceptible to embrittlement and that increasing the temperature from 25°C to 85°C decreased the tendency to embrittle. A major milestone report has been written assembling the data obtained by Fontana Corrosion Center and assessing the literature on the importance of hydrogen embrittlement under repository conditions.

1.6. STOCHASTIC ANALYSIS OF FLOW AND TRANSPORT

Quantitative characterization of large-scale flow and radionuclide transport through the heterogeneous unsaturated fractured rock of Yucca Mountain will be necessary to evaluate compliance with the siting criteria and performance objectives associated with the proposed Yucca Mountain HLW repository (10 CFR 60.122 and 60.113). Realistic modeling of the complex, heterogeneous flow and transport processes at Yucca Mountain will require incorporating the effects of relatively small-scale as well as large-scale space-time variability in modeling unsaturated flow and radionuclide transport. Examples of geologic features that can have significant effects on flow and transport are faults and fractures, finer fissures, and stratification leading to anisotropic behavior.

The specific objectives of the project are to: perform a review of the literature and assess available models and data relevant to the subject site, select a global approach to model large-scale flow and transport in unsaturated fractured rock, develop submodels for incorporation into the global model, perform large-scale simulations, and participate in the validation of flow/transport models for the Yucca Mountain repository.

Work accomplished during this quarter is described in Chapter 6. The main focus is on auxiliary hydrodynamic models for unsaturated heterogeneous geologic formations. As explained in earlier reports, auxiliary hydrodynamic models are needed in order to achieve realistic full-scale simulations of unsaturated flow and transport in complex three-dimensional environments like Yucca Mountain. In particular, there is a need for physically-based models of effective unsaturated conductivity in the following cases: (1) flow through a single rough-wall fracture imbedded in a porous medium (possibly with contact areas), (2) flow through a fracture network imbedded in a porous matrix (requires also realistic fracture network models), and (3) flow through a heterogeneous and stratified porous matrix (possibly with variable fracturing density). Work on items (1) and (2) is ongoing, and will be reported at later stages. Recent developments for case (3), based on a probabilistic formulation of unsaturated conductivity, are reported in some detail in Chapter 6. In particular, it was found that positive cross-correlation between saturated conductivity and the slope of the conductivity-suction curve yields a "critical" value of suction where most conductivity curves will interact, and anisotropic behavior is minimized. Furthermore, the analysis leads to the characterization of an upper envelope conductivity curve, which decays less rapidly with suction than locally measured curves.

1.7. GEOCHEMICAL ANALOGS

The Geochemical Natural Analog Research Project is designed to provide knowledge of the state of the art in natural analog studies applied to contaminant transport, to conduct

investigations of a specific site or sites, and to permit evaluation of the use of analog data to support modeling appropriate for performance assessment of a Yucca Mountain repository. The project began in February 1990; Task 1 of the project, "Literature Review," has been completed. The first activity within Task 2, "Identification of Site and Development of Workplan," has been completed with the submission of a workplan report for the Peña Blanca natural analog. Task 3, "Development of Methodology and Data Acquisition," and Task 4, "Interpretation of Data and Modeling," are in progress.

During this quarter, laboratory work including optical petrography, electron microscopy, X-ray diffractometry, and inductively coupled plasma emission spectrometry was conducted on samples from the Peña Blanca analog site to characterize the ore and host rock mineralogy and chemical composition. Based on these laboratory studies, on field research conducted at the site, and on information available in the literature, a workplan for natural analog research at the Peña Blanca site was developed (Pearcy and Murphy, 1991c).

Initial petrographic studies indicate that the Nopal Formation (the upper host rock at the Nopal I uranium deposit at Peña Blanca) is a rhyolitic tuff, densely welded and hematitic in unaltered zones, with a lithic vitrophyre at its base. Unaltered Nopal tuff consists of phenocrysts of quartz, feldspar, and biotite, and of minor volcanic fragments in a devitrified groundmass of cryptocrystalline quartz and feldspar. The Coloradas Formation (the lower host rock at the Nopal I deposit is a reddish, lithic-crystal, rhyolitic tuff with well-developed extaxitic textures. The tuff is densely welded and consists of volcanic fragments and phenocrysts in a devitrified groundmass of cryptocrystalline quartz and sanidine.

Though additional work is required to establish the physical conditions of uranium oxidation at Peña Blanca (e.g., temperature, hydrologic saturation, fluid compositions, and timing), initial work suggests that both solubility and rate limits for the proposed repository at Yucca Mountain, Nevada, can be assessed using information from the natural analog at Peña Blanca, Mexico. For example, UO_2 oxidation and transformation to secondary uranyl silicate minerals appear to be rapid relative to mass transport of uranium out of the Peña Blanca system. The rate-limiting process is likely to be transport in fluids with uranium contents controlled by interactions with uranyl silicate minerals such as uranophane, soddyite, and weeksite.

1.8. PERFORMANCE ASSESSMENT RESEARCH

During the previous quarter, work performed under Task 7 of the Performance Assessment Research Project has been expanded and slightly redirected to focus on the development of model validation strategies which are based on performance measures. This developmental work has been performed as part of CNWRA's contribution to Test Case 10, the Las Cruces Trench Experiment, of INTRAVAL. INTRAVAL is an international project which addresses the development of procedures to test the validity of mathematical models used to predict the fate and transport of radioactive substances in the geosphere.

The Las Cruces Trench is an extremely well instrumented, unsaturated zone flow and solute transport field experiment which is ideal for testing the validation methodologies developed in Task 7. Three conceptual models of the Las Cruces Trench field experiment have been developed and implemented using the PORFLO-3 computer code. These three models differ both in terms of the level of complexity with which the soil hydraulic properties are described and the detail with which the initial conditions are defined. The results of modeling the movement of bromide in each of the three conceptual models were analyzed using three measures: (1) Determination of the bromide plume moments, (2) travel-time statistics computed at specified compliance boundaries, and (3) integrated mass fluxes computed at specified compliance boundaries.

The first and third performance measures described above can be used to assess the degree to which the model has been calibrated. However, inasmuch as particle travel times were not obtained at the site, the second measure is used solely to assess the effect of model complexity. If a direct relationship among the three measures can be established, it is hoped that a corresponding relationship between the spatial resolution of the data used to characterize a site and the variability of each performance measure can be established as well.

Preliminary analysis of the second moments of the measured and computed bromide plumes suggests that the simplest model structure for the soil hydraulic properties coupled with the simplest description of the initial suction does the best job of replicating the shape and movement of the observed bromide plume. To date the second and third measures have been used simply to assess the degree of "containment" provided by the modeled geologic media. Comparison of the second and third performance measures yields apparently equivocal results when the results are interpreted from the standpoint of which conceptual model of the geologic media provides the most conservative assessment of the media's ability to prevent solute from reaching prescribed compliance boundaries. The ability to draw firm conclusions depends in large part on the vertical position of the plane or compliance boundary at which the two performance measures are evaluated. For compliance planes near the bromide source, the first-particle arrival times indicate that the most complex model provides the most conservative assessment of the geologic media's containment ability, while the time at which the centroid of the instantaneous mass flux passes a compliance plane indicates that the simplest model provides the most conservative assessment. The complex model appears to produce fast flow paths, although the bulk of the solute does not traverse these paths. For the compliance plane which is most distant from the source, the first-arrival time for the complex model actually exceeds that for the simplest model, while the time at which the centroid of the instantaneous mass flux passes this compliance boundary for the complex model is less than that for the simplest model. It is readily apparent that the position of the compliance surface greatly affects the degree of conservation of the conceptual model. The mechanics that account for this phenomenon will be explored and discussed in subsequent reports.

1.9. SORPTION MODELING FOR HIGH-LEVEL WASTE PERFORMANCE ASSESSMENT

An evaluation of the effectiveness of geologic systems as barriers to radionuclide migration requires an understanding of the chemical and physical process by which aqueous species are sorbed on geologic materials. These processes, which may include adsorption, ion exchange, or precipitation, are commonly represented collectively by empirical parameters, such as sorption coefficient (K_d) or retardation factor (R_f), in transport calculations supporting performance assessments of geologic repositories. However, there is active debate on the usefulness of these empirical parameters in quantitatively describing aqueous-solute/rock interactions for performance assessment calculations. It is recognized that transport models which use these parameters, particularly those that assume constant K_d's or R_f's, do not explicitly take into account many potentially important geochemical phenomena that occur during transport in natural systems, including aqueous complexation, precipitation/dissolution reactions, competitive sorption, changes in groundwater chemistry, and variability in substrate composition as well as effects of changes in temperature and pressure. Therefore, questions have been raised regarding the adequacy of transport calculations using K_d or R_f in performance assessment.

The objectives of this project are: (1) to obtain a mechanistic understanding of the important radionuclide sorption processes and the physical and chemical parameters that affect sorption behavior in the Yucca Mountain, Nevada, environment; (2) to investigate the applicability of coupled-hydrogeochemical models which use simple representations of sorption phenomena to Yucca Mountain performance assessment; and (3) to develop practical but scientifically defensible approaches to modeling sorption at Yucca Mountain and to developing the requisite databases to support such models. The project has been divided into three tasks, and only Task 1 and 3 are active at this time.

Activities conducted during this quarter in Task 1, which consisted of literature review and development of approach, focused on models that have been used to describe sorption of aqueous solutes on solid phases. Results of the literature review are discussed in Chapter 9. Task 3, which consists of experiments on uranium sorption on geologic media, was initiated during the middle part of this quarter. Activities under this task consisted of preparation of Na-clinoptilolite powder which will be used in the experiments, and evaluation of polarographic methods for the analysis of uranium in aqueous solutions. Results of these activities are also reported in Chapter 9.

2. UNSATURATED MASS TRANSPORT (GEOCHEMISTRY)

by Roberto T. Pabalan and William M. Murphy

Investigators: *William M. Murphy (CNWRA), Roberto T. Pabalan (CNWRA), James Prikryl (CNWRA), Timothy J. Griffin (CNWRA), and Christopher J. Goulet (CNWRA)*

2.1. EXPERIMENTAL STUDIES by Roberto T. Pabalan

2.1.1. Technical Objectives

A major geologic feature potentially affecting the suitability of Yucca Mountain, Nevada, as a repository site for high-level nuclear wastes is the presence underneath the proposed repository horizon of thick, laterally extensive zones of zeolitic tuff. Because of their sorptive properties, zeolites could provide important geologic barriers to migration of radionuclides from the repository to the accessible environment. To support the NRC's high-level waste program, the CNWRA is conducting experimental studies on the thermodynamic and ion exchange properties of zeolites under Task 3 of the Geochemistry Research Project. The objective of these studies is to generate data needed to evaluate the effectiveness of zeolitic tuffs as barriers to radionuclide migration.

Experiments have been proposed previously to evaluate phase equilibria between aqueous solutions and the zeolite minerals clinoptilolite and analcime (Murphy, 1991). The objective of the proposed experiments is to investigate techniques to resolve the problem of uncertainties in the standard-state thermodynamic properties of clinoptilolite. Because dissolution/precipitation rate data are absent for the zeolites, accurate prediction of the required duration to achieve equilibrium in the experiments is precluded. The first phase of the proposed experiments, therefore, involves determination of the rate of dissolution of the zeolite mineral analcime. This phase was initiated in the previous quarter, during which a set of scoping experiments on analcime dissolution was completed. Initial results of these experiments were reported previously (Pabalan, 1991). For convenience, the experimental conditions and a complete set of experimental results for the scoping studies are given in this report in Tables 2-1 to 2-4. Interpretation of these results are given in Section 2.2 of this chapter.

Based on the data from the scoping experiments, a more extensive set of experiments on analcime dissolution was initiated during this quarter. Details of these experiments and preliminary results are reported here.

2.1.2. Experimental Methods

Dissolution kinetic experiments were conducted by reacting weighed amounts of analcime powder with 1000 ml of 0.10 M NaCl - 0.010 M $NaHCO_3$ solutions. Characterization and preparation of the analcime material were described previously (Pabalan, 1991). Before adding analcime to the NaCl-$NaHCO_3$ solutions, the aqueous solutions were preequilibrated with

Table 2-1. EXPERIMENTAL MATRIX FOR ANALCIME DISSOLUTION SCOPING EXPERIMENTS.

Experimental Condition	ADTIIIA	ADTIIIB	ADTIIIC
Grain size based on nominal sieve opening	63-45 μm 230-325 mesh	63-45 μm 230-325 mesh	63-45 μm 230-325 mesh
Average grain length based on SEM photo	100 x 10^{-4} cm	100 x 10^{-4} cm	100 x 10^{-4} cm
Solution (400 ml)	0.10 M NaCl 0.010M $NaHCO_3$	0.10 M NaCl 0.010M $NaHCO_3$	0.10 M NaCl 0.010M $NaHCO_3$
Mass analcime	0.10 g	0.50 g	1.00 g
Temperature	25.0$\pm$0.1°C	25.0$\pm$0.1°C	25.0$\pm$0.1°C
Specific surface area	1800 cm^2g^{-1} BET measured	1800 cm^2g^{-1} BET measured	1800 cm^2g^{-1} BET measured
Initial pH	8.95$\pm$0.01°C	8.95$\pm$0.01°C	8.95$\pm$0.01°C
SA/SV	0.45 cm^{-1}	2.25 cm^{-1}	4.5 cm^{-1}

atmospheric CO_2(g) for several days until constant pH values were achieved. The measured pH of the solutions prior to addition of analcime was 8.99$\pm$0.01. The pH of the solutions was predicted to remain close to this value during the course of the experiment due to buffering by carbonate equilibria [Murphy (1991)].

Analcime powder in the following grain-size ranges were used: (1) 200-230 mesh (75-63 microns); (2) 230-325 mesh (63-45 microns); and (3) 325-450 mesh (45-32 microns). The scoping experiments reported previously indicated that reacting 1.0 g of the 230-325 mesh-size analcime powder with 400 ml of the NaCl-$NaHCO_3$ solution resulted in a dissolution rate which is sufficiently rapid and convenient for sampling and analysis. Based on the measured specific surface area of the 230-325 mesh-size powder equal to 1800 cm^2 g^{-1} (Pabalan, 1991), the initial total-solid-surface-area/solution-volume ratio (SA/SV) for that particular reaction was calculated to be 4.5 cm^{-1}.

It is convenient for the new set of experiments to have a rate of analcime dissolution approximately equal to that of the scoping experiment, so that proper sampling

Table 2-2. RESULTS OF ANALCIME DISSOLUTION SCOPING EXPERIMENTS: CONCENTRATIONS OF SiO_2 *vs.* TIME. EXPERIMENTAL CONDITIONS GIVEN IN TABLE 2-1. DETECTION LIMIT FOR SiO_2 IS 4.16 X 10^{-7} moles/kg.

Elapsed Time (hours)	Silica concentration (moles/kg SiO_2 X 10^6)		
	ADTIIIA	ADTIIIB	ADTIIIC
0.0	---	---	---
5.9	BDL	BDL	BDL
26.6	BDL	1.42	1.76
71.8	BDL	2.13	3.90
120.3	BDL	2.89	5.45
173.1	BDL	3.84	6.50
213.9	1.90	3.84	7.02
262.6	1.71	4.70	8.63
334.6	1.23	6.12	9.91
766.6	2.66	10.1	16.4
1174.6	5.98	17.8	25.4

intervals can be predetermined. Since dissolution rates are directly proportional to SA/SV, the mass of analcime grains to be reacted with 1000 ml of NaCl-$NaHCO_3$ solution in the new set of experiments can be adjusted to yield approximately the same SA/SV as in the scoping experiment.

In the absence of BET surface-area measurements on the 200-230 and 325-450 mesh-size analcime powder, their specific surface areas (S) were estimated from the equation (Murphy, 1989):

$$S = k/(\rho L) \qquad (2\text{-}1)$$

where k is a shape factor, ρ is the density of the solid (approximately 2.2 g cm^{-1} for analcime [Deer et al., 1966]), and L is an average length (cm) of the mineral grains. Values of L measured from scanning electron (SEM) photomicrographs of the 200-230, 230-325, and 325-450 mesh-size analcime are approximately 150×10^{-4}, 100×10^{-4}, and 90×10^{-4} cm, respectively.

Table 2-3. RESULTS OF ANALCIME DISSOLUTION EXPERIMENTS: CONCENTRATIONS OF Al *vs.* TIME. EXPERIMENTAL CONDITIONS GIVEN IN TABLE 2-1. DETECTION LIMIT FOR Al IS 20 ppb.

Elapsed Time (hours)	Al concentration (ppb)		
	ADTIIIA	ADTIIIB	ADTIIIC
0.0	---	---	---
5.9	BDL	BDL	BDL
26.6	BDL	BDL	BDL
71.8	BDL	BDL	BDL
120.3	BDL	BDL	71.5
173.1	BDL	BDL	71.0
213.9	BDL	BDL	90.8
262.6	BDL	BDL	68.8
334.6	BDL	BDL	101
766.6	BDL	125	220

The shape factor, k, was calculated from the measured surface area and L value for the 230-325 mesh-size analcime powder, and is approximately equal to 40. The shape factor for spheres is 6; therefore, the ratio 40/6 $\approx$ 7 gives the roughness factor for the analcime grains. Specific surface areas of the 200-230 and 325-450 mesh-size grains were then estimated to be 1200 and 2000 $cm^2\ g^{-1}$, respectively. To maintain approximately the same dissolution rate as in the scoping experiment (i.e., SA/SV equals 4.5 cm^{-1}), 3.75 g, 2.5 g, and 2.25 g of analcime powder corresponding to grain-sizes 200-230, 230-325, and 325-450 mesh, respectively, were each added to 1000 ml of 0.10 M NaCl-0.010 M $NaHCO_3$ solutions.

The analcime powder and aqueous solutions were reacted in 1000 ml polypropylene bottles, which were maintained at 25.0$\pm$0.1°C, and kept under agitation using a constant temperature water bath (Fisher Versabath 236). For each analcime grain size, duplicate solid+solution mixtures (labeled A and B) were reacted to check the reproducibility of the rate data. All together, six mixtures (labeled ACDTIA, ACDTIB, ACDTIIA, ACDTIIB, ACDTIIIA, and ACDTIIIB) were studied. To keep the experimental systems open to atmospheric $CO_2(g)$, the bottles were covered with a porous material. In addition to solution

Table 2-4. EXPERIMENTAL MATRIX FOR THE NEW SET OF ANALCIME DISSOLUTION EXPERIMENTS.

Experimental Condition	ACDTIA & ACDTIB	ACDTIIA & ACDTIIB	ACDTIIIA & ACDTIIIB
Grain size based on nominal sieve opening	75-63 μm 200-230 mesh	63-45 μm 230-325 mesh	45-32 μm 325-450 mesh
Average grain length based on SEM photo	150 x 10^{-4} cm	100 x 10^{-4} cm	90 x 10^{-4} cm
Solution (1000 ml)	0.10 M NaCl 0.010M $NaHCO_3$	0.10 M NaCl 0.010M $NaHCO_3$	0.10 M NaCl 0.010M $NaHCO_3$
Mass analcime	3.75 g	2.50 g	2.25 g
Temperature	25.0$\pm$0.1°C	25.0$\pm$0.1°C	25.0$\pm$0.1°C
Specific surface area	1200 cm^2g^{-1} calculated	1800 cm^2g^{-1} BET measured	2000 cm^2g^{-1} calculated
Initial pH	8.99$\pm$0.01°C	8.99$\pm$0.01°C	8.99$\pm$0.01°C
SA/SV	4.5 cm^{-1}	4.5 cm^{-1}	4.5 cm^{-1}

pH, initial concentrations of Na^+, Cl^-, and total carbonate were analyzed using Orion ion selective electrodes and are equal to 2460$\pm$20 ppm, 3680$\pm$40 ppm, and 494$\pm$12 ppm (as CO_2), respectively. The extent of reaction was followed by taking 50 ml samples, which were passed through 0.2 micron syringe filters, and analyzing SiO_2 and Al concentrations using a Milton Roy 1201 UV-Vis spectrophotometer. The pH and Na^+ concentrations were also analyzed. In addition, the weight of each bottle was carefully weighed before the start of the experiment as well as before and after a sample was taken, in order to account for evaporation losses and changes in the volume of the solutions. A summary of the experimental conditions for these experiments is given in Table 2-4.

The results for Al from the scoping experiments indicated some potential errors in the analytical technique used. Tests conducted to determine the source of the errors indicated that the pH of the samples and the Al standards must be relatively close to obtain accurate results using the eriochrome cyanine R method. Previous Al standards have been prepared by diluting commercially available 1000 ppm Al standards with deionized, high-resistivity (>17 megohm) water, which has a pH on the acidic side (<6). To ensure that pH between standards

and samples are identical, the new procedure uses the 0.10 M NaCl-0.010 M $NaHCO_3$ solution, which has been preequilibrated with atmospheric $CO_2(g)$ and which has the same pH as the experimental samples, to prepare the dilute Al standards.

2.1.3. Results

Results for the first 834 hours are given in Tables 2-5 to 2-8. Figure 2-1 is a plot of silica and aluminum concentrations vs. time for samples ACDTIA & B, ACDTIIA & B, and ACDTIIIA & B. These results indicate the same accelerated dissolution during the initial period as observed in the scoping experiments. This behavior is commonly attributed to dissolution of high-energy reaction sites or fine particles (cf., Schott et al., 1989). The concentrations of SiO_2 and Al in solution appear to be leveling off towards the later part of the experiment, and may indicate that the solutions are approaching equilibrium with analcime. Detailed calculations which take into account changes in the volume of the solutions will be reported in the next quarterly research report.

These experiments are continuing. Samples from the analcime+aqueous-solution system are planned to be taken up to about 1440 hours, at which time clinoptilolite powder will be added to the system to obtain data on clinoptilolite dissolution and on the approach to analcime+clinoptilolite+aqueous-solution equilibrium.

2.2. GEOCHEMICAL MODELING by William M. Murphy

2.2.1. Technical Objectives

The technical objective of the modeling task of the Geochemistry Research Project is to apply principles of thermodynamics, kinetics, and mass balance to the interpretation of natural and experimental systems pertinent to ambient and repository geochemical conditions at Yucca Mountain and to the prediction of the evolution of these systems. One specific objective is the interpretation of data generated in the experimentation task of the project. Theoretical interpretation permits extraction of meaningful and useful parameters from the experimental data, assists design of future experiments, and provides methods to evaluate aspects of the models including theory and codes.

2.2.2. Thermodynamic and Kinetic Analysis of Analcime Dissolution Data

Analcime-clinoptilolite equilibration experiments in the Geochemistry Research Project have been designed to commence with a study of the rate and mechanism of analcime dissolution and equilibration in a basic solution. The theoretical basis for these experiments and data from scoping tests have been reported (Murphy, 1991; Pabalan, 1991; Section 2.1 of this report). A kinetic and thermodynamic interpretation of the laboratory data is summarized in this report. In the scoping study, three separate dissolution experiments were conducted with different analcime mass to solution volume ratios. Results of the two experiments with the greater solid mass (and surface area) and larger variations in solution composition (ADTIIIB and

Table 2-5. DATA FROM ANALCIME DISSOLUTION EXPERIMENTS ACDTIA, IIA, AND IIIA

Measured SiO_2 Concentrations

Time (hours)	ACDT Sample IA 3.75g analcime (moles/kg) SiO_2	ACDT Sample IIA 2.50g analcime (moles/kg) SiO_2	ACDT Sample IIIA 2.25g analcime (moles/kg) SiO_2
0	0.00E+00	0.00E+00	0.00E+00
48	2.42E-06	1.85E-06	2.09E-06
95	4.46E-06	2.89E-06	2.66E-06
168	5.27E-06	4.60E-06	5.03E-06
261	7.02E-06	5.27E-06	6.12E-06
358	8.06E-06	6.59E-06	6.97E-06
497	9.34E-06	7.07E-06	7.64E-06
594	8.21E-06	6.17E-06	6.45E-06
713	1.06E-05	6.55E-06	7.02E-06
834	9.58E-06	6.83E-06	7.68E-06

Measured Al Concentrations

Time (hours)	ACDT Sample IA 3.75g analcime (moles/kg) Al	ACDT Sample IIA 2.50g analcime (moles/kg) Al	ACDT Sample IIIA 2.25g analcime (moles/kg) Al
0	0.00E+00	0.00E+00	0.00E+00
48	BDL	BDL	BDL
95	1.63E-06	1.14E-06	1.54E-06
168	3.01E-06	2.13E-06	2.23E-06
261	4.20E-06	2.82E-06	3.17E-06
358	4.82E-06	3.21E-06	3.85E-06
497	5.71E-06	4.82E-06	4.47E-06
594	5.81E-06	4.25E-06	4.73E-06
713	6.46E-06	4.66E-06	5.18E-06
834	6.07E-06	4.75E-06	5.20E-06

BDL - Below detection limit

Table 2-6. DATA FROM ANALCIME DISSOLUTION EXPERIMENTS ACDTIB, IIB, AND IIIB

Measured SiO_2 Concentrations

Time (hours)	ACDT Sample IB 3.75g analcime (moles/kg) SiO_2	ACDT Sample IIB 2.50g analcime (moles/kg) SiO_2	ACDT Sample IIIB 2.25g analcime (moles/kg) SiO_2
0	0.00E+00	0.00E+00	0.00E+00
168	5.08E-06	3.84E-06	4.98E-06
358	7.78E-06	5.69E-06	6.55E-06
664	7.40E-06	5.27E-06	5.93E-06

Measured Al Concentrations

Time (hours)	ACDT Sample IB 3.75g analcime (moles/kg) Al	ACDT Sample IIB 2.50g analcime (moles/kg) Al	ACDT Sample IIIB 2.25g analcime (moles/kg) Al
0	0.00E+00	0.00E+00	0.00E+00
168	3.09E-06	1.72E-06	2.17E-06
358	4.50E-06	3.23E-06	3.68E-06
664	5.41E-06	3.91E-06	4.44E-06

Table 2-7. DATA FROM ANALCIME DISSOLUTION EXPERIMENTS IA, IIA, AND IIIA

	ACDT Sample IA 3.75g analcime			ACDT Sample IIA 2.50g analcime			ACDT Sample IIIA 2.25g analcime		
Time (hours)	Total soln weight (g)	Na^+ (ppm)	Soln pH	Total soln weight (g)	Na^+ (ppm)	Soln pH	Total soln weight (g)	Na^+ (ppm)	Soln pH
0	1094.4	2420	8.99	1094.5	2470	8.99	1092.8	2460	8.99
48	1043.4	2550	8.98	1043.7	2540	8.99	1039.5	2540	8.98
95	992.7	2620	9.00	992.9	2580	9.00	988.7	2530	8.99
168	941.8	2550	8.99	941.9	2560	8.95	937.9	2500	8.97
261	890.9	2520	8.99	890.9	2520	8.99	886.9	2500	8.97
358	839.8	2480	8.97	840.0	2490	8.99	835.9	2480	9.01
497	788.6	2570	8.98	788.9	2520	8.97	784.8	2500	8.98
594	737.7	2500	8.99	737.9	2510	8.99	733.7	2500	8.98
713	686.7	2490	9.00	686.5	2510	9.00	682.5	2510	8.99
834	635.3	2500	8.98	635.5	2490	8.97	631.3	2500	8.97

Table 2-8. DATA FROM ANALCIME DISSOLUTION EXPERIMENTS ACDTIB, IIB, AND IIIB

	ACDT Sample IB 3.75g analcime			ACDT Sample IIB 2.50g analcime			ACDT Sample IIIB 2.25g analcime		
Time (hours)	Total soln weight (g)	Na^+ (ppm)	Soln pH	Total soln weight (g)	Na^+ (ppm)	Soln pH	Total soln weight (g)	Na^+ (ppm)	Soln pH
0	1094.8	2470	8.98	1094.3	2470	8.98	1093.2	2480	8.99
168	1043.0	2540	8.96	1042.9	2540	8.96	1041.9	2510	8.95
358	991.4	2490	8.98	991.6	2460	8.97	990.4	2500	9.00
664	939.0	2520	9.01	940.0	2510	8.99	938.7	2510	8.99

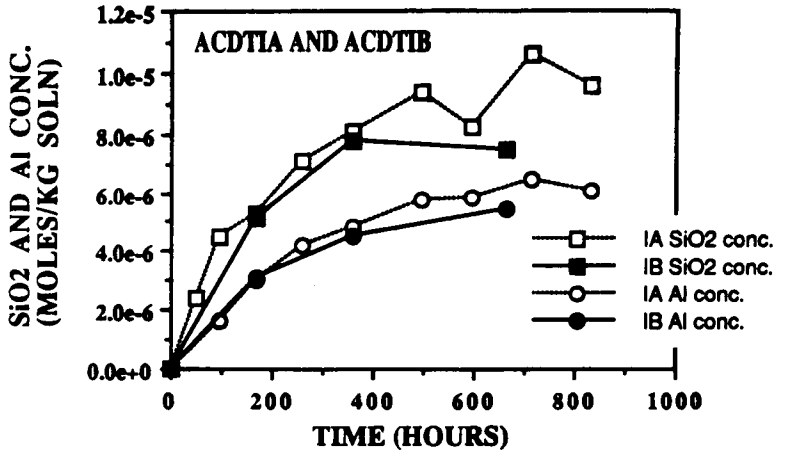

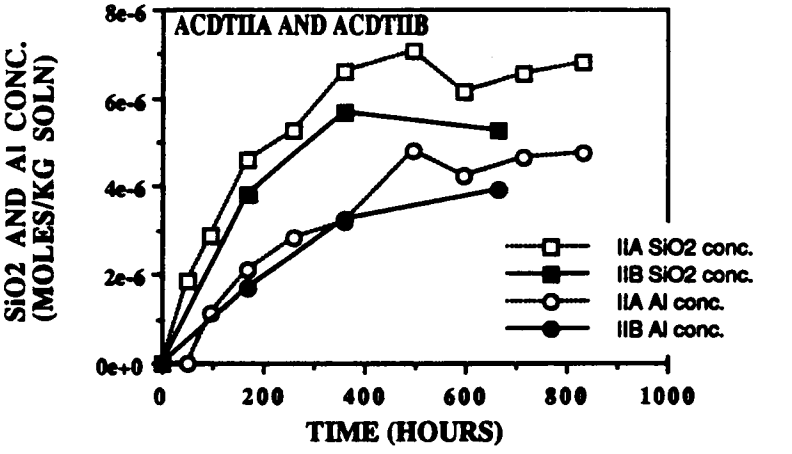

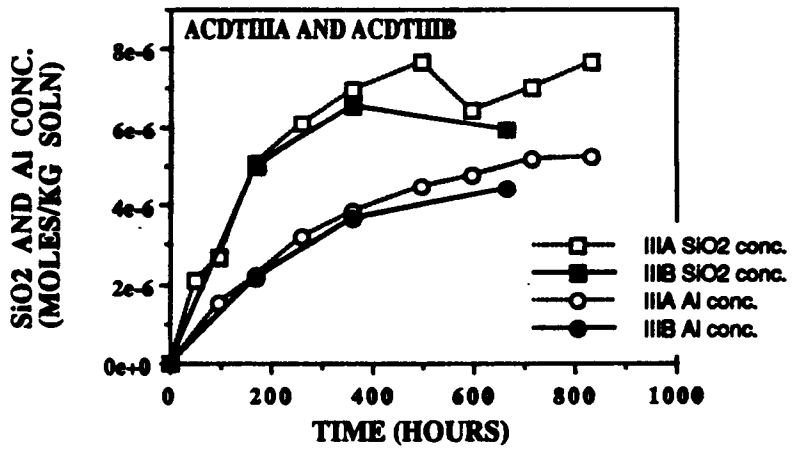

Figure 2-1. Concentrations of SiO_2 and Al in aqueous solutions reacting with analcime powder as a function of time

ADTIIIC) provide the most pertinent information, and are examined in detail in this report.

2.2.2.1. Mass and stoichiometry analyses

Tables 2-9 and 2-10 provide summaries of data for the two experiments. Column A in each table gives the time relative to the start of the experiment at which samples were extracted for chemical analysis. Columns B, C, and D give measured concentrations (molalities) of Si and Al, and pH in bold type. Values for Si and Al concentration given in plain type were estimated based on smooth interpolations or extrapolations of the concentration data. Estimated values are required where analytical data are missing to permit calculations of the mass of solute removed from the system during sampling. An estimate of removed solute is used in calculating the cumulative mass transfer to solution. Column E in Tables 2-9 and 2-10 gives the volume of water remaining in the reaction vessel following sampling at the specified time, for which both removal of solution by sampling and by evaporation were taken into account. Total evaporation was determined by the initial mass of water minus the mass of water removed in all samples minus the mass of water remaining at the termination of the experiment, amounting to approximately 3 percent of the initial solution. Evaporation was distributed linearly with time throughout the duration of experiment to obtain the solution volumes given in column E.

The cumulative number of moles released in each reaction vessel is given by

$$n_{I,R}(t_s) = m_I(t_s) W(t_s) + n_{I,E}(t_s) \qquad (2\text{-}2)$$

where $n_{I,R}(t_s)$ stands for the total number of moles of a particular component I (e.g., Si or Al) released to solution at the time of sampling t_s, $m_I(t_s)$ denotes the molality of component I at time t_s, $W(t_s)$ stands for the mass of the solvent in the reaction vessel prior to sampling at time t_s, and $n_{I,E}$ denotes the number of moles of component I removed from the experiment in all samples taken prior to time t_s, which is given by

$$n_{I,E} = \sum_{t_p < t_s} m_I(t_p) W_E(t_p) \qquad (2\text{-}3)$$

where $W_E(t_p)$ stands for the mass of solvent extracted at time t_p. [It is necessary to distinguish explicitly components (e.g., Si and Al) from aqueous species (e.g., SiO_2 and AlO_2^-) in the kinetic analysis presented below.]

Values for the cumulative release of Si calculated with Eqn. (2-2) are given in column F in Table 2-9 and 2-10, and moles of aluminum release are given in column

Table 2-9. DATA FROM ANALCIME DISSOLUTION SCOPING EXPERIMENT ADTIIIB

A	B	C	D	E	F
ADTIIIB Time (hours)	ADTIIIB Si conc. (molal)	ADTIIIB Al conc. (molal)	ADTIIIB pH	ADTIIIB Volume (ml)	ADTIIIB Si released (moles)
0	0.00E+00		**8.95**	400.5	0.00E+00
5.92	8.69E-06			360.4	3.48E-07
26.58	**1.42E-06**			320.2	**5.47E-07**
71.83	**2.13E-06**			279.6	**7.74E-07**
120.33	**2.89E-06**			239.0	**9.84E-07**
173.08	**3.84E-06**			198.4	**1.21E-06**
213.92	**3.84E-06**			157.9	**1.21E-06**
243.59	4.20E-06			156.5	1.26E-06
262.58	**4.70E-06**			116.3	**1.34E-06**
334.58	**6.12E-06**			75.4	**1.50E-06**
387.33	6.22E-06			73.7	1.50E-06
766.58	**1.01E-05**	**4.62E-06**		29.0	**1.74E-06**
772.83	1.16E-05		**8.99**	19.0	1.78E-06
1174.58	**1.78E-05**			4.0	**1.81E-06**

Table 2-10. DATA FROM ANALCIME DISSOLUTION SCOPING EXPERIMENT ADTIIIC

A	B	C	D	E	F	G
ADTIIIC Time (hours)	ADTIIIC Si conc. (molal)	ADTIIIC Al conc. (molal)	ADTIIIC pH	ADTIIIC Volume (ml)	ADTIIIC Si released (moles)	ADTIIIC Al released (moles)
0	0.00E+00	0.00E+00	**8.95**	400.7	0.00E+00	0.00E+00
5.92	1.38E-06	1.30E-07		360.6	5.54E-07	5.21E-08
26.58	**1.76E-06**	5.86E-07		320.4	**6.88E-07**	2.16E-07
71.83	**3.89E-06**	1.58E-06		279.9	**1.37E-06**	5.35E-07
120.33	**5.45E-06**	**2.65E-06**		239.3	**1.80E-06**	**8.32E-07**
173.08	**6.50E-06**	**2.63E-06**		198.7	**2.05E-06**	**8.26E-07**
213.92	**7.02E-06**	**3.36E-06**		158.2	**2.15E-06**	**9.70E-07**
243.59	8.13E-06	2.87E-06		156.9	2.32E-06	8.90E-07
262.58	**8.63E-06**	**2.55E-06**		116.6	**2.40E-06**	**8.40E-07**
334.58	**9.91E-06**	**3.75E-06**		75.8	**2.54E-06**	**9.77E-07**
387.33	1.09E-05	4.29E-06		74.2	2.61E-06	1.02E-06
766.58	**1.64E-05**	**8.16E-06**		29.8	**2.94E-06**	**1.27E-06**
772.83	1.64E-05	8.29E-06	**9.01**	19.7	2.94E-06	1.27E-06
1174.58	**2.54E-05**	1.23E-05		5.0	**3.00E-06**	1.29E-06

G of Table 2-10. A density of 0.001 kg solvent per milliliter of solution was used to convert volumes (column E) to masses (W). Bold entries in the tables identify data based on analytical measurements at the indicated time. Plain type entries in columns F and G are based on interpolated or extrapolated concentration data for the specified time. The cumulative release of Si in experiments ADTIIIB and ADTIIIC is shown in Figure 2-2 as a function of time. Systematic trends of the data are indicated by sketched curves. The slopes of the curves correspond generally to the rates of reaction, which are rapid at the outset and slow at the conclusion of the experiments. This is interpreted to be largely a consequence of the variation of reaction rate with approach to equilibrium.

The stoichiometry of Si and Al release in experiment ADTIIIC is illustrated in Figure 2-3, which is based on the data in Table 2-10. Corresponding analytical values for Si and Al are sparse, and the slope of the line regressed through the data in Figure 2-3 depends largely on extrapolated values. However, this slope equals 2.1, which corresponds closely to the ratio of Si to Al in analcime ($NaAlSi_2O_6 \cdot H_2O$). The data in Figure 2-3 give a strong indication that release of Si and Al from analcime was generally stoichiometric, and that incongruent precipitation of a secondary Al phase such as gibbsite did not occur. The positive intercept of this curve indicates a small initial rapid preferential release of silica. This release is likely to be an indication of a change (i.e. silica depletion) of the surface chemistry of the analcime in contact with the alkaline solution.

2.2.2.2. Empirical rate analysis

In silicate mineral dissolution experiments, an initial rapid rate of reaction is commonly observed, which is interpreted to be the consequence of dissolution of ultrafine particles and physically altered surface material (e.g., Holdren and Berner, 1979). This is generally followed by a period of constant reaction rate for conditions that are far from equilibrium. These features can be observed in the analcime data from the scoping studies. Figure 2-4 shows the specific moles of Si released as a function of time in the first four measurements of experiment ADTIIIB. The rate of reaction indicated by the slope of the line in Figure 2-4 was remarkably constant at 2.5×10^{-12} moles $gram^{-1}$ sec^{-1}. The surface area of the samples used in these experiments was determined by BET gas adsorption analysis to be 1800 cm^2 $gram^{-1}$. Using this value, the surface specific rate of reaction based on the curve in Figure 2-4 is 1.4×10^{-15} moles cm^{-2} sec^{-1}. Rates of analcime dissolution would be half these values assuming stoichiometric release of two moles of Si per mole of analcime. The positive intercept of this curve is an indication of the initial, transient, very rapid dissolution. Unlike ADTIIIB, the rate of dissolution in experiment ADTIIIC decreased with time during the initial 200 hours. This is probably the consequence of a longer period of initial transient rapid reaction and a more rapid approach to equilibrium. Both effects may be due to the greater analcime to solution mass ratio in ADTIIIC. The systematic decrease in the specific rate of Si release in experiment ADTIIIC is also illustrated in Figure 2-5. Points in this figure correspond to the average rates of release for each interval between sampling times, and are plotted at the times corresponding to the mid points of the intervals.

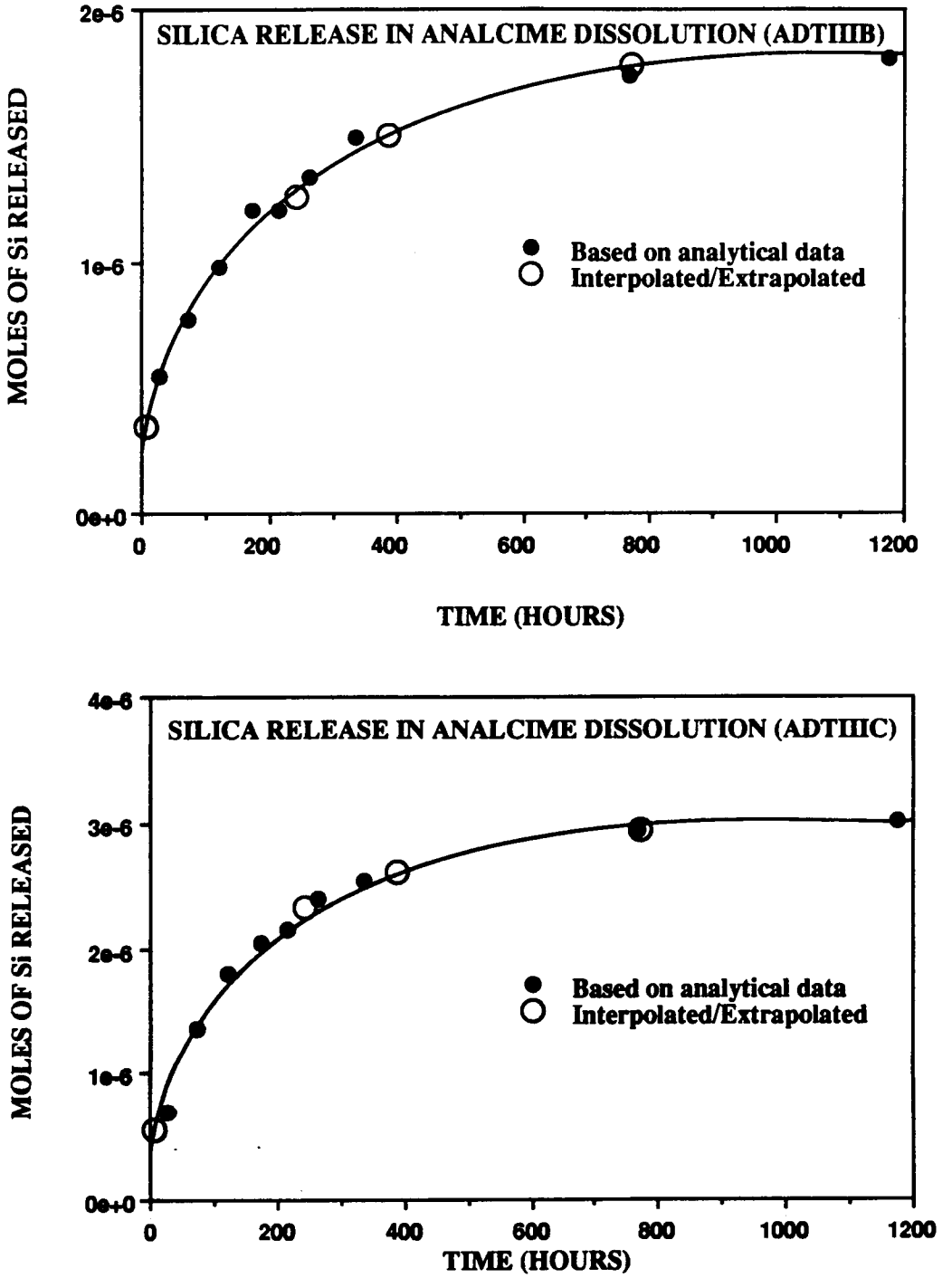

Figure 2-2. Total moles of Si released as a function of time in analcime dissolution experiments ADTIIIB (A) and ADTIIIC (B). Solid symbols represent data based on analytical measurements for the specified time. Open symbols are based on interpolated or extrapolated data.

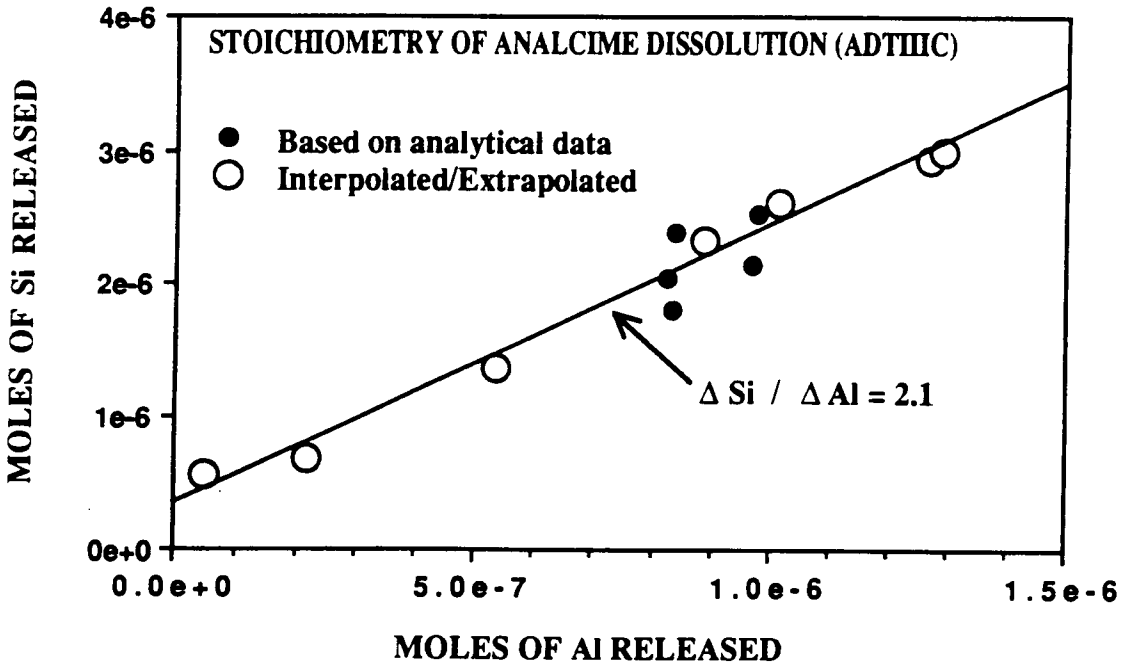

Figure 2-3. Moles of Si released versus moles of Al released representing the stoichiometry of analcime dissolution in experiment ADTIIIC. Solid symbols are based on analytical measurements for both Si and Al at the same time. Open symbols are based on interpolated or extrapolated data.

2.2.2.3. Theoretical rate analysis

A general rate equation for mineral dissolution can be written as

$$\frac{d\xi}{dt} = k^{*}s(1-Q/K) \qquad (2\text{-}4)$$

where ξ stands for the number of moles of dissolved reactant, t represents time, s denotes the surface area of the reactant, K stands for the equilibrium constant for the dissolution reaction, and Q denotes the reaction quotient for this reaction (e.g., Aagaard and Helgeson, 1982). The apparent rate constant, k^{*}, can depend in principle on solution composition (e.g. pH). However,

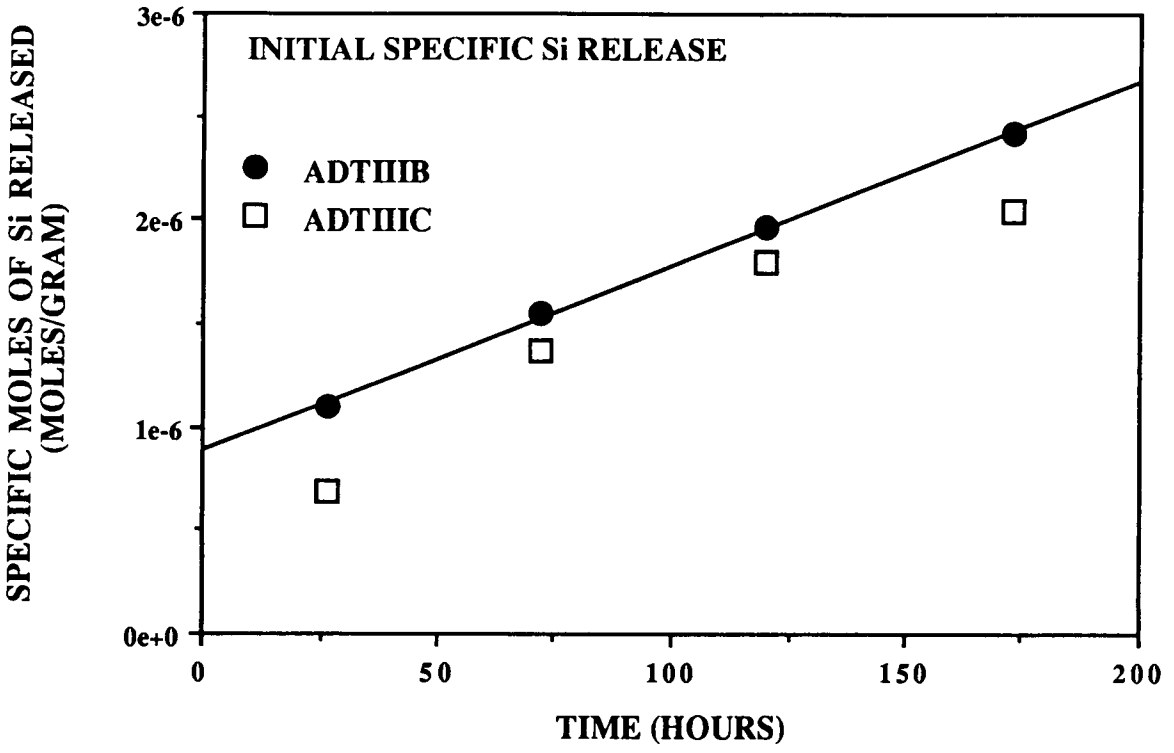

Figure 2-4. Initial specific release of Si as a function of time in analcime dissolution experiments ADTIIIB and ADTIIIC

conditions for the experiments reported here were designed such that compositional variations are minimal (Murphy, 1991), and k^* should be approximately constant.

Under the experimental conditions, the dominant dissolution reaction is

$$NaAlSi_2O_6 \cdot H_2O \leftrightharpoons Na^+ + 2SiO_2 + AlO_2^- + H_2O \ . \qquad (2\text{-}5)$$

Hence, the reaction quotient can be written as

$$Q = a_{Na^+} a^2_{SiO_2} a_{AlO_2^-} \qquad (2\text{-}6)$$

where a_{Na^+}, a_{SiO_2}, and $a_{AlO_2^-}$ stand for the thermodynamic activities of the subscripted aqueous species. At equilibrium K = Q.

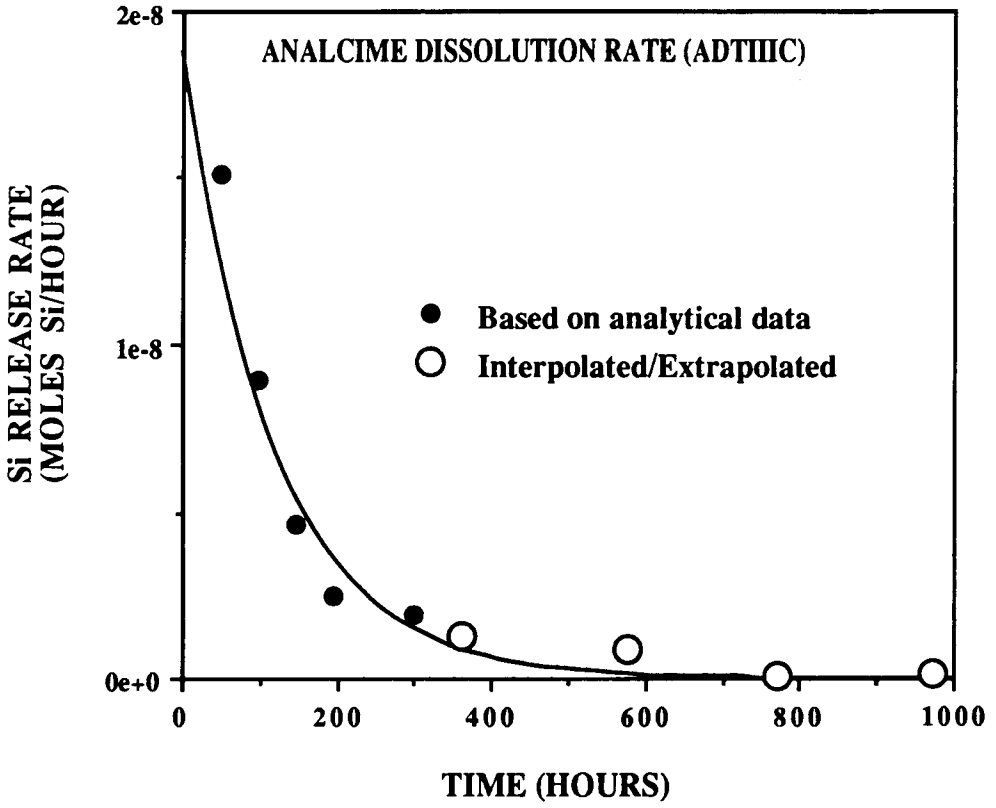

Figure 2-5. Rate of Si release as a function of time in experiment ADTIIIC. Average rates for intervals between sampling times are plotted at the mid point of the interval. Solid symbols are based on pairs of analytical measurements for successive sampling times. Open symbols are based on interpolated or extrapolated data.

Assuming that the number of moles of analcime dissolved is represented by stoichiometric release of Si, it follows that

$$\xi = n_{Si,R}/2 \tag{2-7}$$

and

$$\frac{d\xi}{dt} = \frac{1}{2}\frac{dn_{Si,R}}{dt} \tag{2-8}$$

By definition for each species i

$$a_i = m_i \gamma_i \tag{2-9}$$

where m_i and γ_i represent the molality and activity coefficient of species i. Species molalities (e.g., m_{SiO_2} and $m_{AlO_2^-}$) can be expressed in terms of the total molalities of the corresponding components (e.g., m_{Si} and m_{Al}) as

$$m_{SiO_2} = X_{SiO_2} m_{Si} \tag{2-10}$$

$$m_{AlO_2^-} = X_{AlO_2^-} m_{Al} \tag{2-11}$$

which define X_{SiO_2} and $X_{AlO_2^-}$ as mole fractions of the subscripted aqueous species among the total number of moles of the corresponding components in solution. A good approximation is that X_{SiO_2} and $X_{AlO_2^-}$ were constant during the experiments because the pH, carbonate concentration, and ionic strength of the solutions were closely buffered.

Assuming as well that release of Si and Al is stoichiometric as suggested by data in Figure 2-3, it is possible to write

$$n_{Si,R} = 2 n_{Al,R} \cdot \tag{2-12}$$

Substituting Eqns. (2-9) and (2-10) in Eqn. (2-2) and solving for a_{SiO_2} yields

$$a_{SiO_2} = \left(n_{Si,R} - n_{Si,E}\right) \gamma_{SiO_2} X_{SiO_2} / W \ . \tag{2-13}$$

Similarly, making use of Eqns. (2-11) and (2-12)

$$a_{AlO_2^-} = \left(n_{Si,R} - n_{Si,E}\right) \gamma_{AlO_2^-} X_{AlO_2^-} / (2W) \ . \tag{2-14}$$

Substituting Eqns. (2-13) and (2-14) in Eqn. (2-6) and substituting that result and Eqn. (2-8) in Eqn. (2-4) and rearranging yields

$$\frac{dn_{Si,R}}{dt} = 2k^*s - \frac{k^* s a_{Na^+} X_{SiO_2}^2 \gamma_{SiO_2}^2 X_{AlO_2^-} \gamma_{AlO_2^-} \left(n_{Si,R} - n_{Si,E}\right)^3}{KW^3} \ . \tag{2-15}$$

It is convenient to introduce a change of variables by writing

$$n_{Si,R} = n_{Si,R} - n_{Si,E} + n_{Si,E} \ . \tag{2-16}$$

Then

$$\frac{dn_{Si,R}}{dt} = \frac{d\left(n_{Si,R} - n_{Si,E}\right)}{dt} + \frac{dn_{Si,E}}{dt} \ . \tag{2-17}$$

For each interval between sampling $n_{Si,E}$ is constant, hence

$$\frac{dn_{Si,R}}{dt} = \frac{d\left(n_{Si,R} - n_{Si,E}\right)}{dt} \ . \tag{2-18}$$

Substituting Eqn. (2-18) in Eqn. (2-15) and letting

$$n_{Si,R} - n_{Si,E} = x \ , \tag{2-19}$$

the resulting equation can be written as

$$\frac{dx}{dt} = A + Bx^3 \tag{2-20}$$

where

$$A = 2k^*s \tag{2-21}$$

and

$$B = \frac{-k^*s\, a_{Na^+} X^2_{SiO_2} \gamma^2_{SiO_2} X_{AlO_2^-} \gamma_{AlO_2^-}}{KW^3} \,. \tag{2-22}$$

Assuming A and B are constant, Eqn. (2-20) can be integrated analytically to give

$$\begin{aligned} \int_{t_i}^{t_{i+1}} dt &= \int_{x(t_i)}^{x(t_{i+1})} \frac{dx}{A+Bx^3} \\ &= \frac{k}{3A}\left[\frac{1}{2}\log_e\left[\frac{(k+x)^3}{A+Bx^3}\right] + \sqrt{3}\tan^{-1}\left[\frac{2x-k}{k\sqrt{3}}\right]\right] \Bigg|_{x(t_i)}^{x(t_{i+1})} \end{aligned} \tag{2-23}$$

where $k = 3\sqrt{\frac{A}{B}}$.

Subject to the validity of the assumptions and approximations noted, the integrated rate equation can be used to regress the release rate data in each time interval. Among the limiting assumptions, the stoichiometry of Si and Al release appears to be most severe because of the apparent initial preferential release of silica. Brief treatment of analcime samples with the alkaline solution prior to their use in rate experiments could alleviate this complication as well as some ambiguities associated with rapid initial release of material from fine surface particles and damaged surfaces. Preliminary regressions using Eqn. (2-23) of the rate data from the scoping experiments have been performed using a value of k*s consistent with the slope of the line in Figure 2-4, and thermodynamic data used and derived in theoretical aqueous speciation studies discussed in section 2.2.2.4. A generally good correspondence was obtained between the experimental data and the form of the curve based on the theoretical rate equation. In the future, detailed data regressions will be applied to the more comprehensive data set described in section 2.1.

2.2.2.4. Thermodynamic analysis

Equilibrium aqueous speciation calculations for representative solutions in experiment ADTIIIC have been performed with the program EQ3 (version

EQ3NR.3245R124) with its composite thermodynamic data base (version DATA0.COM.R7) (Wolery, 1983). These calculations provide theoretical values for the saturation state of the solutions with regard to analcime and possible secondary phases. Selected results from the computed models are given in Table 2-11. For all calculations, the total Na content was fixed at $1.1x10^{-1}$ molal, which was the initial Na content. Evaporation and analcime dissolution would have increased this value only slightly. The pH was fixed at the analytical value or at 9.0 where analytical data were absent. The total carbonate content was obtained by adjusting its concentration to achieve charge balance in the speciated solutions. Resulting carbonate concentrations correspond to equilibrium CO_2 gas fugacities of approximately atmospheric CO_2 pressure, which was used to buffer the solutions. Analytical values of total Si and Al concentrations were used in the calculations, except for the Al value at 1174.58 hours which was based on extrapolation.

Results in Table 2-11 show that the solution evolved toward analcime equilibrium from undersaturation as represented by increasing values of log(Q/K) with time for the reaction $NaAlSi_2O_6 \cdot H_2O + 4H^+ \rightleftharpoons Na^+ + Al^{3+} + 2SiO_{2aq} + 3H_2O$.. The final positive value of log(Q/K) is an unrealistic indication that this final solution is supersaturated with respect to analcime. This result is most likely the consequence of uncertainty in the bulk aqueous solution composition (e.g., the extrapolated aluminum concentration), and uncertainty in the thermodynamic data in the EQ3 data base for aqueous speciation reactions and the analcime dissolution reaction. Nevertheless, the calculated saturation state index generally supports the conclusion that the solution closely approached analcime equilibrium in the experiment. The modeled solutions were also supersaturated with regard to the aluminum bearing minerals dawsonite, gibbsite, diaspore, kaolinite, paragonite, natrolite, and Na-beidellite at various stages of reaction. Although these results are subject to uncertainties similar to calculations of the analcime saturation state, some degree of supersaturation with respect to aluminum phases is expected because of their generally low solubilities. As noted above, the apparent stoichiometric release of Al and Si suggests that secondary precipitation of these phases did not occur. Solution metastability is indicated.

The equilibrium speciation calculations confirm the expectations noted above that the fraction of SiO_2 and AlO_2^- species among the total Si and Al contents remained approximately constant (Table 2-11). Approximate constancy of the calculated logarithm of the CO_2 fugacity at a value corresponding closely to the atmospheric pressure represents a partial validation of the speciation model. This value depends on theoretical charge neutrality given the analytical concentration data.

The saturation state of the solution with respect to Na-clinoptilolite can be calculated using clinoptilolite thermodynamic data from the data0.3245R4 version of the EQ3/6 data base, which are based on work by Kerrisk (1983). These calculations indicate that the solutions remained strongly undersaturated with respect to clinoptilolite at their termination. In future experiments, Na-clinoptilolite will be added to the analcime equilibrated solutions causing the system to evolve toward analcime-clinoptilolite equilibrium.

Table 2-11. THERMODYNAMIC PROPERTIES OF EXPERIMENTAL SOLUTIONS IN ANALCIME DISSOLUTION SCOPING EXPERIMENT ADTIIIC

Time (hours)	Analcime log Q/K	X_{SiO_2}	$X_{AlO_2^-}$	log (f_{CO_2} /bar)
120.33	-1.827	0.5164	0.999	-3.417
213.92	-1.476	0.5164	0.999	-3.417
334.58	-1.155	0.5164	0.999	-3.417
766.58	-0.395	0.5107	0.999	-3.429
1174.58	0.164	0.5107	0.999	-3.429

2.2.3. Conclusions

Kinetic and thermodynamic interpretations of experimental data for analcime dissolution indicate that equilibrium is approached in the experiments as shown by decreasing reaction rates and increasing saturation index. Dissolution is apparently stoichiometric with respect to Si and Al release, and congruent with the absence of secondary phase growth. A provisional rate constant for analcime dissolution under far from equilibrium conditions, 1.4×10^{-15} moles cm^{-2} sec^{-1}, can be used in data interpretation and in the design of a more complete set of experimental studies. Thermodynamic analyses indicate that data in the EQ3/6 data base (e.g. the equilibrium constant for analcime dissolution) will require some revision to correctly represent the experimental results.

2.3. References

Aagaard, P., and H. C. Helgeson. 1982. Thermodynamic and kinetic constraints on reaction rates among minerals and aqueous solutions. I. Theoretical considerations. *American Journal of Science 282*:237-285.

Deer, W. A., R. A. Howie, and J. Zussman. 1966. *An Introduction to the Rock-Forming Minerals*. London: Longman.

Holdren, G. R., Jr., and R. A. Berner. 1979. Mechanism of feldspar weathering - I. Experimental Studies. *Geochim. Cosmochim. Acta 43*:1161-1171.

Kerrisk, J. F. 1983. Reaction-path calculations of groundwater chemistry and mineral formation at Rainier Mesa, Nevada. LANL LA-9912-MS. Los Alamos, New Mexico: Los Alamos National Laboratory.

Murphy, W. M. 1989. Dislocations and feldspar dissolution. *Eur. J. Mineral.*, 1:315-326.

Murphy, W. M. 1991. Geochemical modeling. *Center for Nuclear Waste Regulatory Analyses Report (CNWRA) on Research Activities for Calendar Year 1990.* W. C. Patrick, ed. CNWRA 90-01A. San Antonio, Texas: CNWRA:2-25 to 2-55.

Pabalan, R. T. 1991. Experimental studies. *Report on Research Activities for the Quarter January 1 Through March 31, 1991.* W. C. Patrick, ed. CNWRA 91-01Q. San Antonio, Texas: CNWRA.

Schott, J., S. Brantley, D. Crerar, C. Guy, M. Borcsik, and C. Williame. 1989. Dissolution kinetics of strained calcite. *Geochim. Cosmochim. Acta* 53: 383-398.

Wolery, T. J. 1983. *EQ3NR A Computer Program for Geochemical Aqueous Speciation-Solubility Calculations: User's Guide and Documentation.* UCRL-53414. Livermore, California: Lawrence Livermore National Laboratory.

3. THERMOHYDROLOGY

by Ronald T. Green (CNWRA) and Steve Svedeman (SwRI)

Investigators: Franklin T. Dodge (SwRI), Ronald T. Green (CNWRA), Ronald H. Martin (CNWRA), Win Pe (CNWRA) and Steve J. Svedeman (SwRI)

3.1. INTRODUCTION

Technical issues and uncertainties for the proposed Yucca Mountain HLW repository site indicate a need for research on thermohydrological phenomena, i.e., phenomena associated with heat and fluid flow, to provide information relevant to performance assessment (PA) including definition of data requirements for site characterization and design criteria. The class of thermohydrological phenomena examined in this project includes phenomena driven by heat emanating from HLW emplaced in a geologic repository. Information derived principally from research is used to establish a knowledge base of thermohydrologic phenomena which will be utilized to assess models of processes used in PAs. This report summarizes the progress of the Thermohydrology Research Project performed during the second quarter of 1991.

3.2. TECHNICAL OBJECTIVES

The specific objectives of the Thermohydrology Research Project are summarized as follows:

- Perform a critical assessment of the state-of-knowledge of thermohydrology in unsaturated fractured media, in the context of present HLW-NRC program activities. This assessment will require an in-depth review of existing literature and on-going programs. It will focus on flow processes, heat transfer mechanisms, and the state-of-the-knowledge experimental methods in porous media.

- Perform a detailed dynamic similarity or similitude analysis on the complete set of governing equations relevant to unsaturated flow and determine the set of dimensionless parameters required to conduct appropriate laboratory simulations. In this analysis of modeling parameters, the range of parameter applicability and limitation on the magnitude of these parameters, as constrained by the principles of dynamic similarity, will be determined.

- Identify potential problems associated with the design and performance of laboratory simulations with scaled geometry, fluid, media, and other relevant properties subject to modeling distortion.

- Perform a series of separate effects experiments in order to identify and understand the role of each effect in the overall coupled processes involved in thermohydrologic phenomena.

- Design and perform comprehensive experiments whose results will continue to identify key dependent and independent parameters and their relationships to each other in the context of thermohydrologic issues.

- Develop the laboratory facilities, experimental methods, measurement techniques, and associated analytic skills to evaluate and validate other program results and to provide a high quality of technical assistance and research in support of NRC's licensing of a HLW repository.

- Examine and correlate laboratory results with field data to aid in the design of future field experiments.

The research project was originally delineated into five tasks for the purpose of accomplishing these objectives. Three of these tasks have been active: Task 1 - Assessment of the State-of-Knowledge of Thermohydrology in Unsaturated Media; Task 2 - Design and Execution of Preliminary Separate Effects Experiments; and Task 3 - Design of Unsaturated Zone Thermohydrological Experiments.

A draft revised Project Plan for the Thermohydrology Research Project was submitted to NRC/RES in May 1991 for comment. The revised Project Plan has not yet been approved by NRC/RES. The revised work plan was modified for the purpose of redefining the project tasks so that the objectives of the project could be pursued in a more direct fashion. These modifications were written to reflect in the project plan the greater understanding of thermohydrologic phenomena achieved through the course of the research project. Accordingly, selected portions of the revised plan have received greater attention than they were afforded in the original work plan. These include the investigation of matrix/fracture hydraulic properties; a higher involvement in numerical simulations of two-phase flow phenomena; and the execution of highly instrumented, two-dimensional experiments. The seven tasks of the draft revised Project Plan are as follows:

- Task 1 - Assessment of the State-of-Knowledge on Thermohydrology in Unsaturated Media.

- Task 2 - Design and Execution of Preliminary Separate Effects Experiments.

- Task 3 - Design and Execution of Thermohydrological Experiments in Unsaturated Media.

- Task 4 - Numerical Analysis of the Thermohydrological Phenomena Observed during Execution of the Laboratory Experiments. (Not funded at this time.)

- Task 5 - Investigation of Matrix and Fracture Hydraulic Properties. (Not funded at this time.)

- Task 6 - Collaboration with the University of Arizona Hydrology Department on the Field Heater Test at the Apache Leap Site. (Not funded at this time.)

- Task 7 - Quarterly and Annual Research Report Preparation.

The draft revised Thermohydrology Research Project Plan will be modified accordingly to incorporate the comments by NRC/RES.

3.3. SEPARATE-EFFECTS EXPERIMENTS

A total of six separate-effects experiments were conducted as part of Task 2 of the Thermohydrology Research Project. The sixth experiment was completed during the first quarter of 1991. Test 6 was designed to measure thermally induced fluid movement in a porous, partially-saturated, fractured medium. The test was intended to repeat Test 5 with several modifications to the test apparatus to provide a more controlled test. The test set up and protocol of Test 6 were described in the first quarterly report of 1991.

In essence, Test 6 consisted of a vertical, two-dimensionally configured test container filled with a uniform mix of glass beads. A vertically oriented artificial fracture was simulated in the medium by emplacing midway in the container a thin (approximately 300-500 micron) layer of glass beads that were coarser than the bead mix. The temperature of the right vertical boundary was held at 60°C, and the left vertical boundary was set at 20°C. The front and back vertical walls were constructed of clear plexiglass to permit visual inspection of the medium for the duration of the experiment. Tensiometers were installed at two locations in the container. Two ports permited the introduction of dye as a tracer of liquid water flow. Thermistors were attached to the two vertical-boundary heat exchangers and to the test container at three locations. The test medium was initially saturated at an average of 65 percent. The moisture was redistributed by gravity drainage prior to initiation of the heating portion of the tests. The duration of the test was 120 days of which 105 days were the heating phase and 15 days were a cool-down phase.

Variables measured during Test 6 were temperature, barometric pressure, suction pressure, and moisture content (indirectly measured using a gamma-ray densitometer). Barometric pressure was measured at ambient conditions. Temperature was measured for the ambient condition at the two heat exchangers and at three locations located equi-distantly along the lower back of the plexiglass side wall. Suction pressures were measured at two locations in the test container using tensiometers. Gamma-ray measurements were made at twenty-four locations (four rows of six measurements) in the test container to provide input to moisture content calculations and at two locations in aluminum blocks for baseline measurements. Additionally, dye was injected into the container at two points to indicate the direction of liquid water flow. A schematic of the test container dimensions and locations of the measurements is illustrated in Figure 3-1.

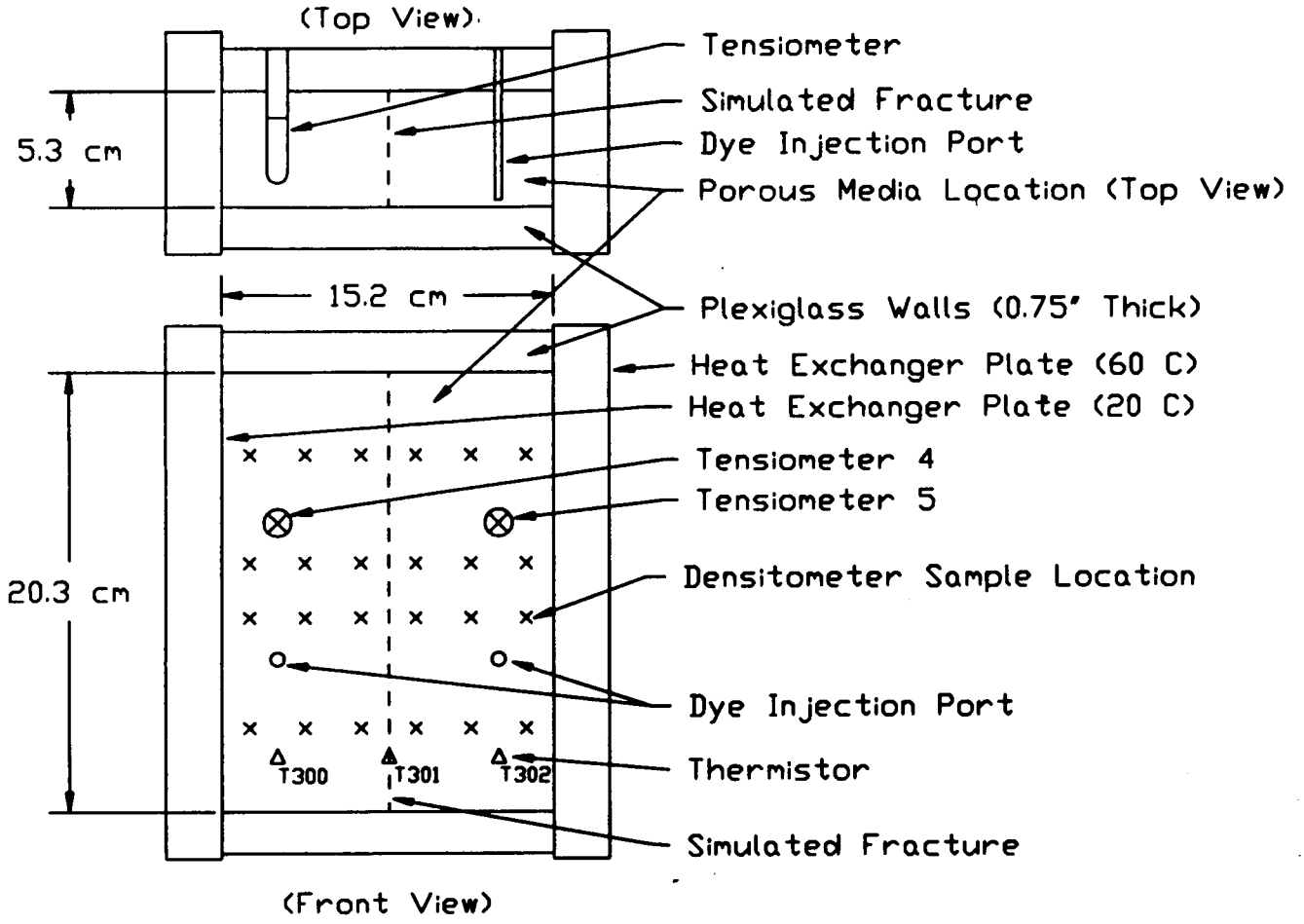

Figure 3-1. Schematic of test apparatus for Test 6

Plots of ambient barometric pressure and temperature, suction pressures, heat exchanger plate temperatures and temperatures recorded along the back outside surface of the plexiglass side wall are given in Figures 3-2 through 3-5. These data have been evaluated in greater detail during this reporting period.

As illustrated in Figure 3-2, the ambient temperature varied by almost 10°C, and the barometric pressure varied by approximately 0.5 psi. Variations in temperature and barometric pressure had an effect upon the detector portion of the gamma-ray densitometer. The effect of the variation in temperature was mitigated by encapsulating the detector first in insulation and later in a constant temperature thermal jacket. Difficulties resulting from temperature variations will be further minimized by conducting future experiments in a laboratory that has more strict environmental controls. The effect of variations in ambient pressure on the densitometer detector, however, cannot be as easily remedied.

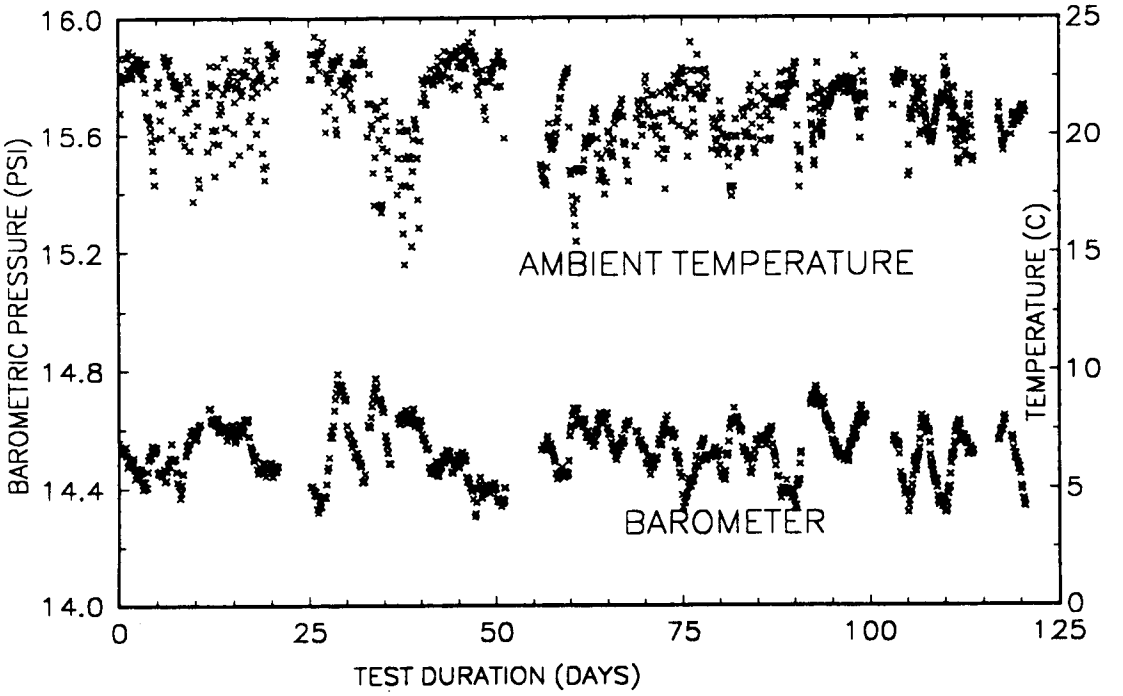

Figure 3-2. Ambient barometric pressure and temperature during Test 6

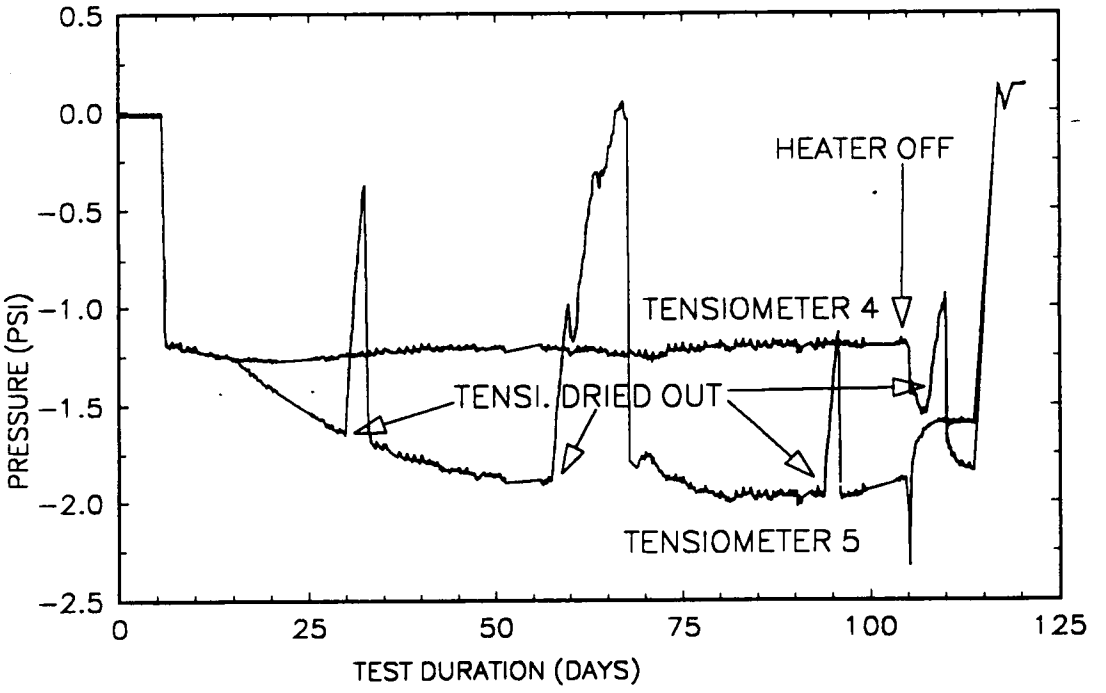

Figure 3-3. Tensiometer measurements during Test 6

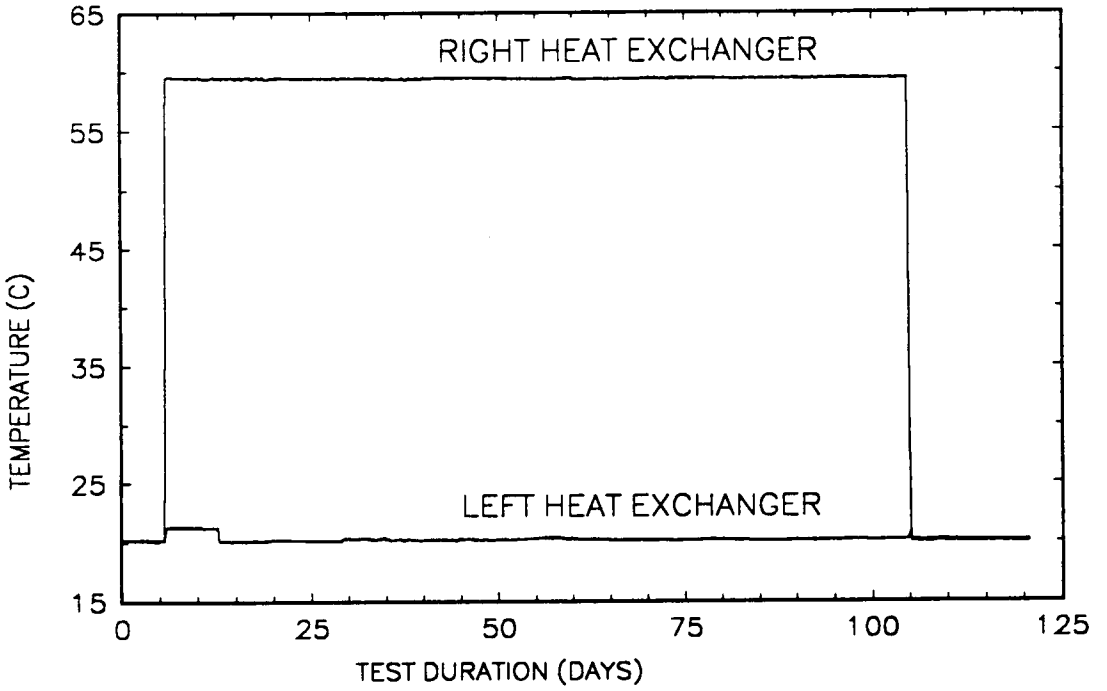

Figure 3-4. Heat exchanger plate temperatures

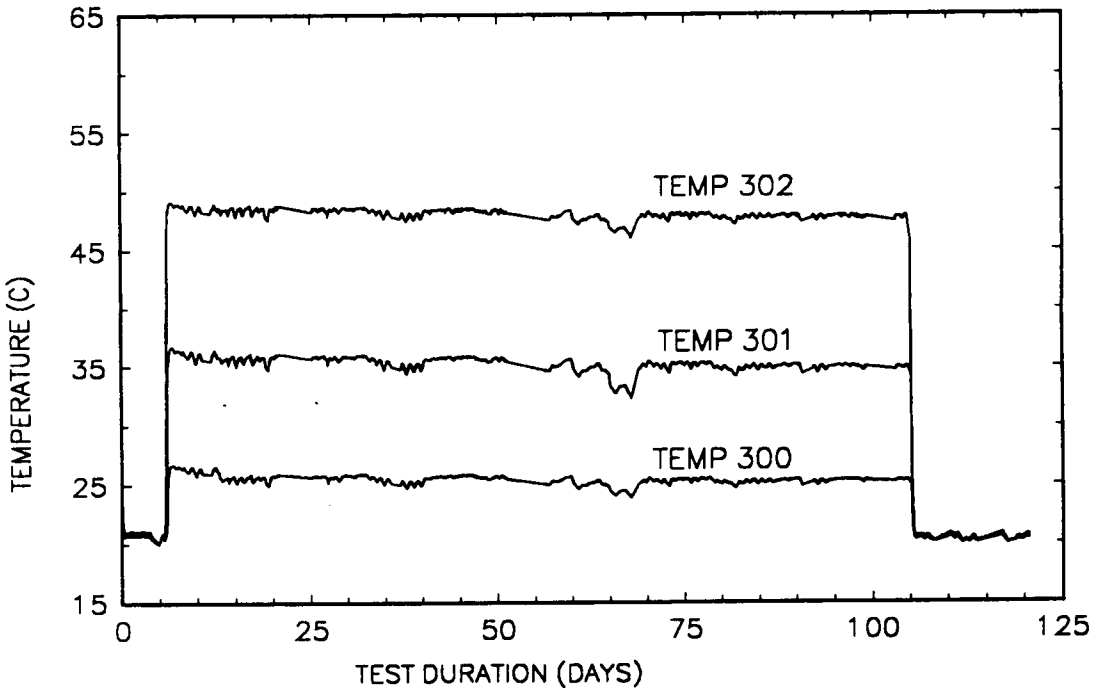

Figure 3-5. Temperatures measured on outside of plexiglass container

The graph of tensiometer measurements illustrates changes in the suction pressures versus time (Figure 3-3). Tensiometer 4, located near the cooler boundary, recorded essentially constant suction pressures until the time the right boundary heat exchanger was allowed to return to the ambient temperature. Tensiometer 4 dried out once late in the experiment and had to be refilled with water. Tensiometer 5 was located near to the higher temperature heat exchanger. Tensiometer 5 dried out three times during the course of the experiment and had to be refilled with water. These events are labeled on Figure 3-3.

Tensiometer 5, located near the heated boundary, measured an increase in suction (negative pressure) shortly after the test started. This observation concurred with the presumption that the saturation content of the heated portion of the container medium became drier as water vaporized and moved away toward the cooler portion of the medium where it recondensed. The suction at tensiometer 5 continued to increase (except for periods when the tensiometer dried out) through about day 80 of the test. A slight decrease in suction is detectable from about day 95 through day 105, indicating that (1) the test had not yet attained steady state even after over 100 days of activity and (2) the decrease in suction means an increase in saturation content. This increase in saturation was not expected, and an explanation is being sought through modeling.

The trends of measurements of both tensiometers behaved in similar fashion at the time the heater was turned off. At this time the suction at each of the two tensiometers rapidly increased (within several hours at tensiometer 5 and within about a day at tensiometer 4) by about 0.5 psi, then rapidly decreased. Tensiometer 5 decreased by about 0.75 psi and then asymptotically approached a suction of about 1.5 psi. Tensiometer 4, however, continued to increase suction (except for a period when the tensiometer dried out) until the time when the container medium was saturated at the end of the test. Tensiometer 4 eventually (near 115th day of the test) increased suction to a level (about 1.8 psi) that was greater than that recorded with tensiometer 5 (about 1.5 psi), and it appeared that the recorded suction at this point would increase slightly more before stabilizing. It is not obvious what could cause the suction on the cooler side to increase to a higher value than the heated side.

Densitometer measurements were normalized relative to the baseline aluminum block measurements taken prior to the densitometer measurements taken of the test container. Direct densitometer measurements and the resulting normalized measurements are given in Figures 3-6 and 3-7, respectively. Figure 3-6 illustrates the densitometer measurements taken through the 5.08-cm thick aluminum block. A digital interface counter was installed at day 88.9 in an effort to reduce fluctuations in the recorded measurements attributable to variations in temperature. As illustrated in Figure 3-6, there appears to be a slight reduction in gamma count fluctuations appeared to reduce slightly after the counter installation. Figure 3-7 illustrates the densitometer measurements taken through a 5.08 cm thick aluminum block after they were normalized by dividing each measurement by the measurement from the 3.8 cm thick aluminum standard.

Figures 3-8 and 3-9 illustrate normalized densitometer measurements for two positions in the container. The positions shown in these figures are 1.27 cm from the right (60°C) heat-

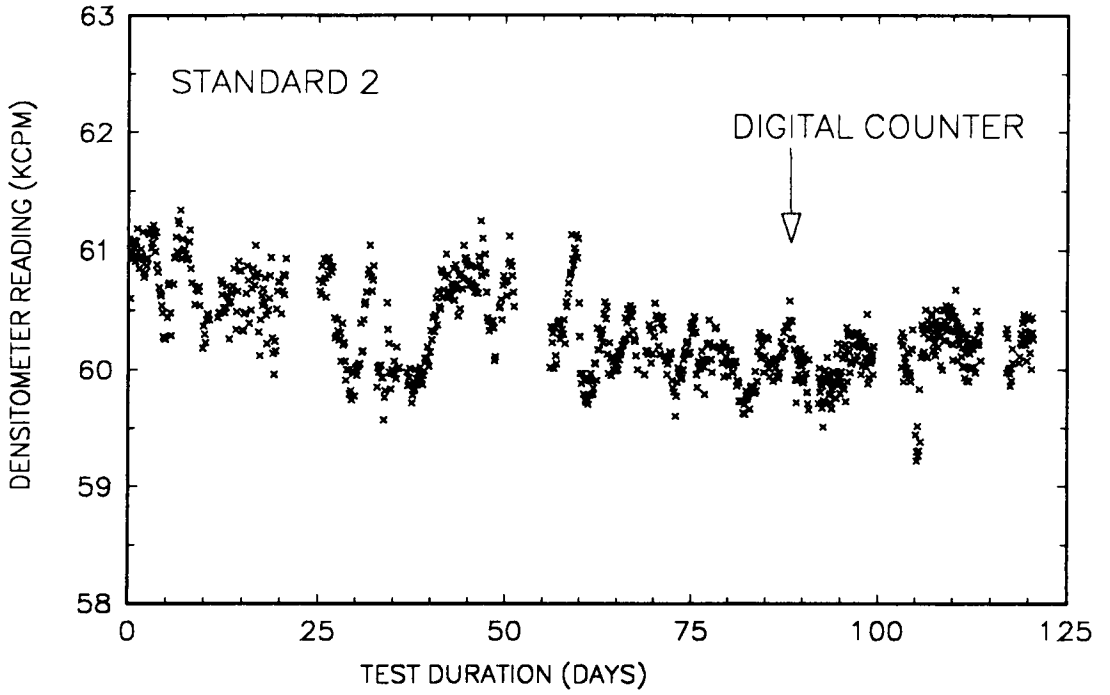

Figure 3-6. Densitometer measurements of 5.08 cm aluminum block

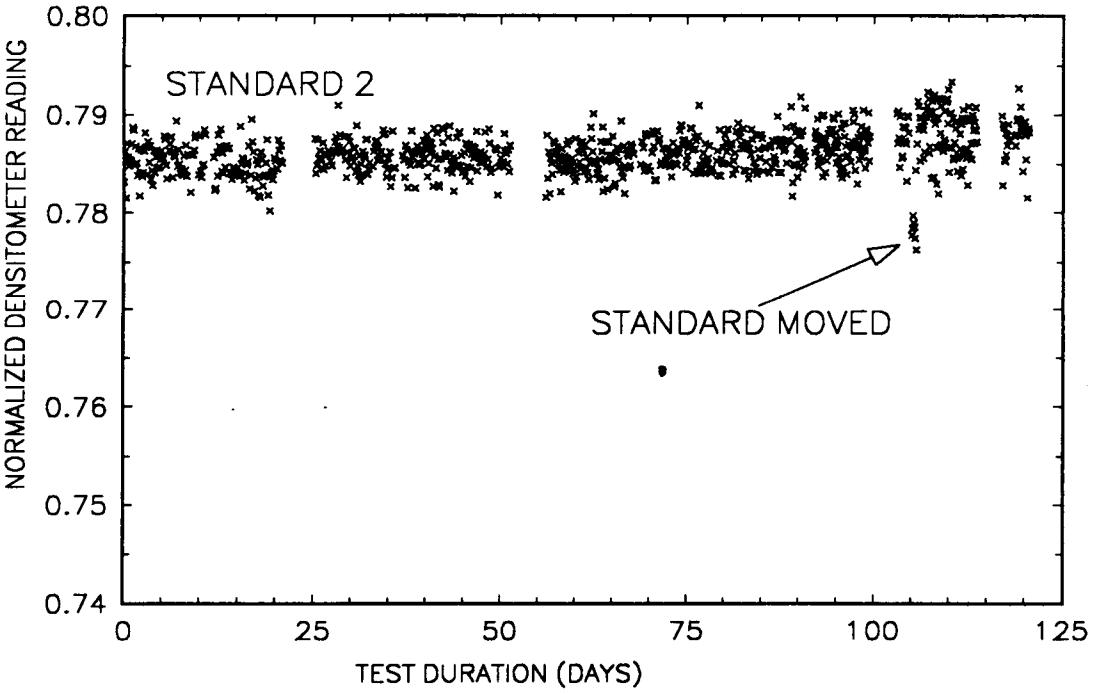

Figure 3-7. Normalized densitometer measurements of 5.08 cm aluminum block

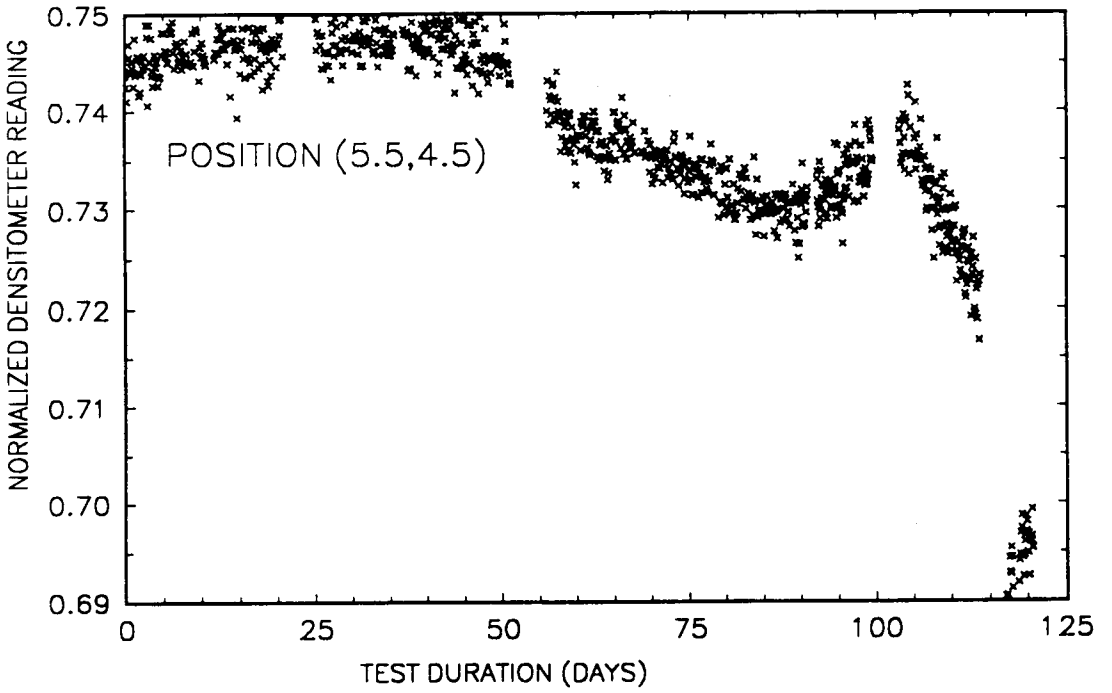

Figure 3-8. Normalized densitometer measurements at location (5.5,4,5)

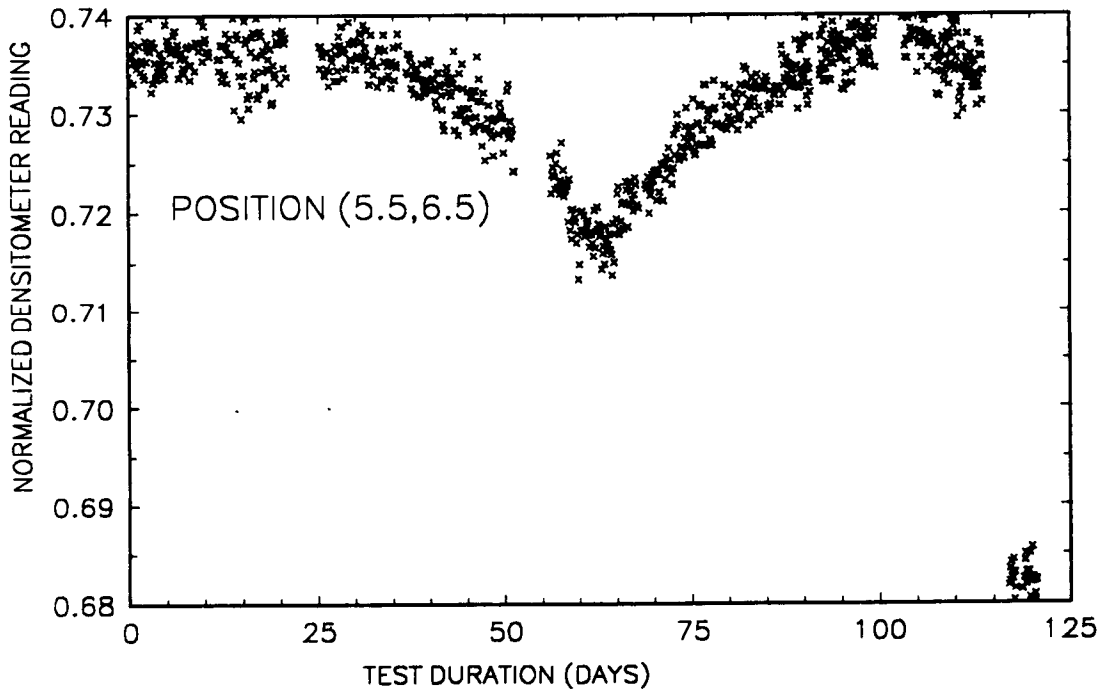

Figure 3-9. Normalized densitometer measurements at location (5.5,6,5)

exchanger plate. The normalized values can be considered as relative counts with a decrease in the normalized count indicating an increase in moisture content. Little change in the moisture content calculated at the point (5.5 <in. to the right of the left heat exchanger>,4.5<in. from the top of the container>) is detected in the first 50 days of the test, after which the local moisture content increases through day 90 and then starts to dry out. At day 105 the heater was turned off, and the local moisture level increased.

The densitometer measurement at (5.5,6.5) illustrated in Figure 3-9 exhibits the same trend as the measurements at point (5.5,4.5) except the maximum in moisture content occurs more quickly at day 65 as compared to day 90. Based on the data and visual evidence from the front of the container, the lower right corner of the test medium appeared to became noticeably drier. Associated with this drier area was an adjacent area of higher moisture content. The wetter area was located on the cool side of the demarcation line at the leading edge of the noticeably drier area. After the demarcation line or front progressed and the beads started to dry out, the measured water content would start to fall as indicated by the densitometer measurements. Water returned to the dried region only after the heater was turned off.

In an attempt to quantify the moisture distribution in the medium during the test, contour plots were made of water distribution at days 5, 25, 50, 75, 99, and 113. These plots were generated by averaging all the normalized densitometer measurements collected over a 1-day period (typically between 7 and 13 measurements per day). These averages were then converted into a saturation value by the following method:

(1) The initial normalized densitometer measurements were assigned a saturation value of 65 percent (day 1 measurements).

(2) The densitometer measurements at day 119, I_w, (after the medium was saturated) were assigned a saturation value of 100 percent.

(3) The dry (0 percent saturation) densitometer count, I_d, and the saturations of interest were calculated using the Beer-Lambert relation:

$$\text{Saturation} = \frac{\ln (I_d/I)}{\ln (I_d/I_w)} .$$

A second method was used to check the calculated saturation levels because the measured counts at some of the densitometer sampling locations did not indicate the expected change when saturated. These locations possibly may not have been fully resaturated when measured. The method was as follows:

(1) The initial normalized densitometer measurements were assigned a saturation value of 65 percent (day 1 measurements).

(2) The media thickness (w) was assumed to be 5.3 cm; and the bead void fraction (v) was assumed to be 0.35, resulting in an equivalent "thickness" of water in the medium of 65-percent saturation of 1.2 cm.

(3) Saturation was approximated using the flowing exponential attenuation formula:

$$\text{Saturation} = \frac{\frac{1}{(\frac{\mu_0}{\rho})\rho(2.54)}\ln(\frac{I}{I_{65}})+X_{65}}{w\phi} \qquad (3\text{-}1)$$

where μ_o is the mass attenuation coefficient of water, ϕ is the media void fraction (0.35), ρ is the density of water, w is the media thickness and X_{65} is the equivalent water thickness at 65-percent saturation. The results of the second method were in close agreement (within 0.5-percent saturation) to the first method over the range of interest (approximately 58 to 82 percent).

Contour plots of liquid saturation at three separate days during the test (days 25, 75, and 113) are presented in Figures 3-10 through 3-12. These saturation values are estimates based upon the above mentioned methodology, and the precision indicated in the contour intervals is beyond the precision of the gamma-ray densitometer. The plots were obtained by spline fitting the data and plotting equi-potential contours using the resulting spline fits. The spline fit procedure smoothed the data, so care must be taken when interpreting the plots. The orientation of the plots is such that the simulated fracture would be a line at "Horizontal-Position" equal to 3.00 inches. The boundary heated to 60°C (right side) corresponds to the line at "Horizontal-Position" value to 6.00 inches on the graph. The 20°C boundary (left side) would be at "Horizontal-Position" value to 0.00 inches. The top of the container corresponds to the "Vertical-Position" location at 0.00 inches and the bottom at 8.00 inches on the graph.

Localized minima in saturation measurements at day 25 are illustrated in Figure 3-10. Because of the fairly high uncertainty in the densitometer measurements, it is not clear if these minima are real or artifacts due to uncertainty in the measurements and the plotting methodology. Local minima are difficult to explain on a physical basis.

A significant saturation gradient appears to have formed between the heated wall and the location of the fracture. This saturation gradient is most severe close to the heated wall, but also relatively large in the area near the heated side of the fracture.

The moisture gradients are considerably more apparent by day 75, as seen in Figure 3-11. The range of saturation values seen on the contour plot is from approximately 55 to 72 percent. A distinct saturation gradient is detected along the fracture ("Horizontal-Position" equal to 3.00 inches). Because the data presented in these plots are from a sparse data set (24 points

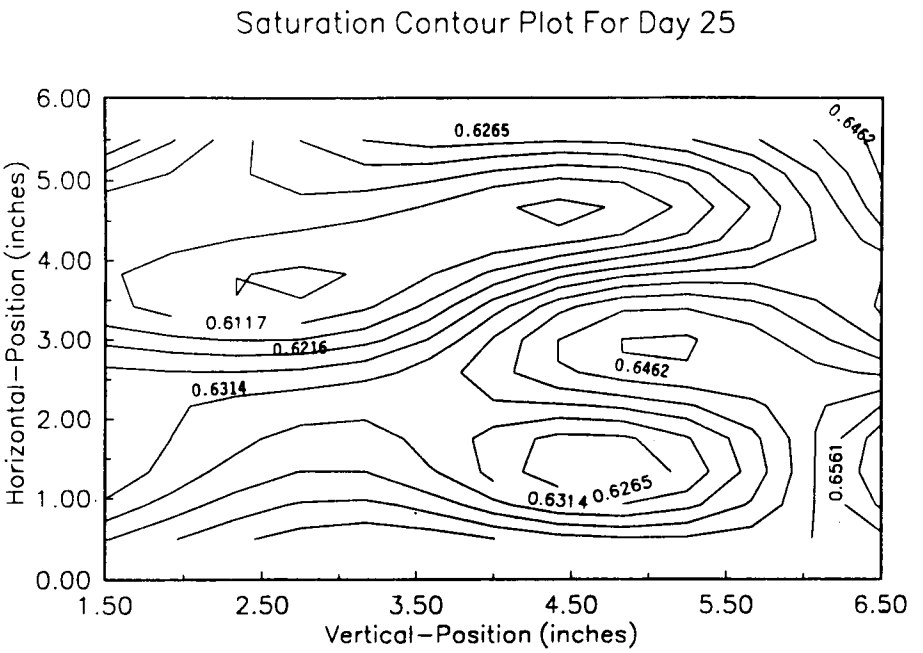

Figure 3-10. Saturation contour plot at day 25 in Test 6

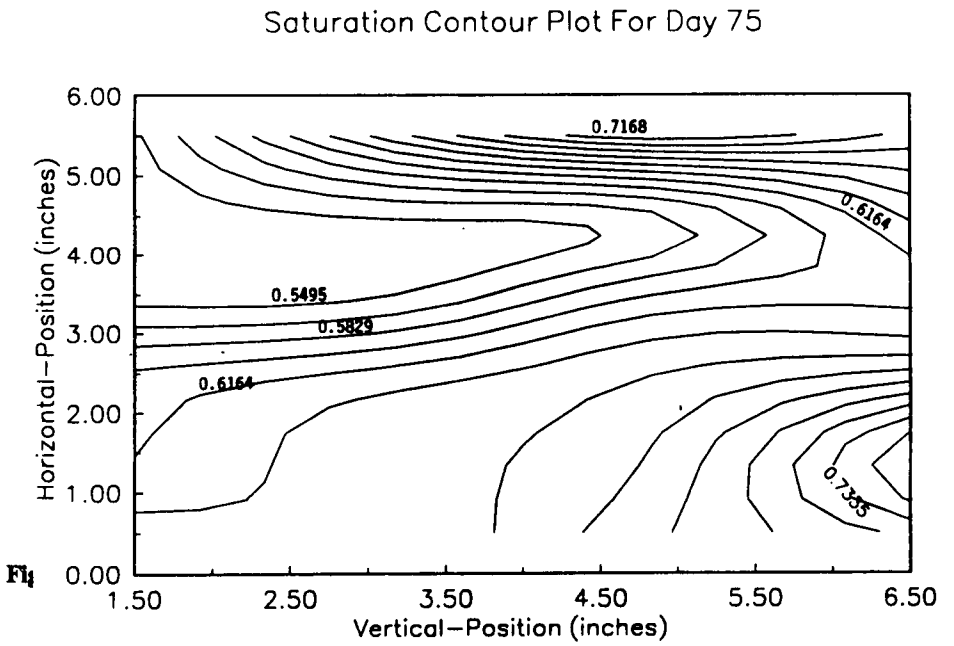

Figure 3-11. Saturation contour plot at day 75 of Test 6

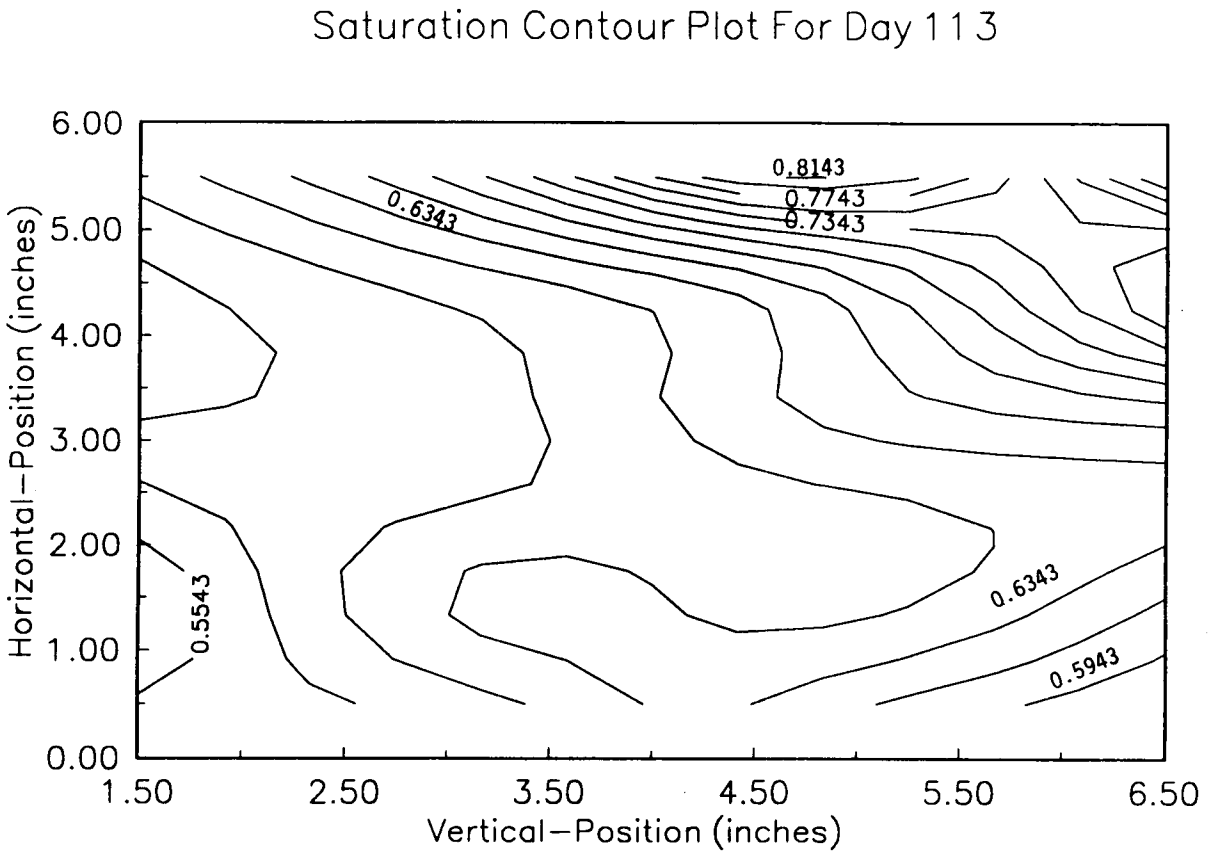

Figure 3-12. Saturation contour plot at day 113 of Test 6

per set) smoothed with a cubic-spline fit the gradual gradient between the sampling points on either side of the fracture ("Horizontal-Position" 2.5 and 3.5 inches), may actually be closer to a step function. The local minimum between the heated plate and the fracture has increased by day 75.

The drying front in the lower right-hand corner has become apparent in the saturation plots by 113 days. It appears that a surplus of water accumulated in front (to the left) of the drying front. Although this phenomenon is not entirely understood at this time, it appears the drying front seems to "push" water ahead of it because, as the front moves along, the moisture content in front of it increases. Furthermore, the majority of the saturation gradient is on the right side of the fracture. Another interesting feature is the decreased saturation level on the left side of the fracture by day 113 as compared to day 75. The saturation in the lower left corner had decreased from 74 percent on day 75 and to about 59 percent on day 113.

The initial trend after heating started appeared to be an accumulation of water on the left (cooler) side of the fracture. The trend reversed however, as the test progressed; and the left side of the fracture became depleted in moisture. The dye-tracer data confirmed this, as the dye injected on the left side of the fracture initially moved upward. By day 75 the upward movement stopped, and the dye began to move downward than toward the fracture along the bottom of the container.

4. SEISMIC ROCK MECHANICS

by Simon M. Hsiung and Asadul H. Chowdhury

Investigators: Mikkō P. Ahola (CNWRA), Asadul H. Chowdhury (CNWRA), Jaak J. Daemen (University of Nevada), Roger Hart (ITASCA), Simon M. Hsiung (CNWRA), and Daniel D. Kana (SwRI)

4.1. TECHNICAL OBJECTIVES

Six specific objectives have been identified for the Seismic Rock Mechanics Research Project. These are as follows:

- Develop a good understanding of the information currently available concerning seismic effects on underground structures.
- Assess, by conceptual models and experimental studies, the capabilities and limitations of rock-joint models and computer codes currently in use.
- Demonstrate by laboratory model studies and instrumented field studies the degree of accuracy (validation) for the rock-joint models and computer codes used for seismic analysis in a tuff medium.
- Assess by instrumented field studies the significance of seismic pumping and demonstrate the degree of validation for the rock-joint models and computer codes for simulation of seismic effects on groundwater hydrology.
- Identify and assess the key seismic-related parameters that are applicable to the Yucca Mountain site.
- Generate technical data for preparing licensing-related positions as they relate to the effect of seismic action on the underground repository in a tuff medium.

The objectives are to be addressed in the following eight tasks.

- Task 1 - Focused Literature Search
- Task 2 - Laboratory Characterization of Jointed Rock
- Task 3 - Assessment of Analytical Models/Computer Codes
- Task 4 - Rock Dynamics Laboratory and Field Studies and Code Validation
- Task 5 - Groundwater Hydrology Field Studies and Code Validation

- Task 6 - Yucca Mountain Scoping Analysis
- Task 7 - Technical Report
- Task 8 - Quarterly Research Report

The second and fourth objectives are currently in progress. Specific work conducted included qualification studies of 3DEC against benchmark analytical problem "Circular Excavation with an Adjacent Discontinuity in an Infinite Elastic Medium" and data collection of instrumented field studies at the Lucky Friday Mine, Mullan, Idaho. Results on the qualification study of 3DEC code are reported herein. The instrumented filed studies data from the Lucky Friday Mine will be analyzed and reported at a later date.

4.2. QUALIFICATION STUDIES ON THE DISTINCT ELEMENT CODE 3DEC

Two Types of qualification studies are being conducted. The first type is to confirm that a computer code can reproduce the response of four well-established conceptual models (benchmark analytical problems) of the performance of a jointed rock mass. Codes with acceptable performance will be candidates for the second type of study to analyze the dynamic response of a well-designed and well-executed laboratory experiment on a single rock-joint. The objective of the qualification studies is to determine whether existing rock-joint models and associated computer codes are capable of simulating the behavior of a jointed rock mass subjected to displacements, velocities, and accelerations imparted by earthquake or ground shock motions. Qualification studies on the HONDO II and UDEC codes against the four benchmark analytical problems, and on the 3DEC code against three of the four benchmark analytical problems have been reported in *Report on Research Activities for Calendar year 1990* (CNWRA, 1991).

In this quarterly research report, the results of the qualification study on the 3DEC code against the benchmark analytical problem "Circular Excavation with an Adjacent Discontinuity in an Infinite Elastic Medium" is presented. This benchmark problem concerns the influence of a plane of weakness transgressing a circular excavation or its zone of influence in an infinite elastic medium. Five specific plane of weakness cases (Figure 4-1) described originally by Brady and Brown (1985) were selected for the study of this problem. These planes of weakenss were those

(1) Intersecting an opening along the diameter perpendicular to the major principal stress,

(2) Intersecting an opening along the diameter parallel to the major principal stress,

(3) Intersecting an opening along a diameter with a 45-degree angle with respect to the major principal stress,

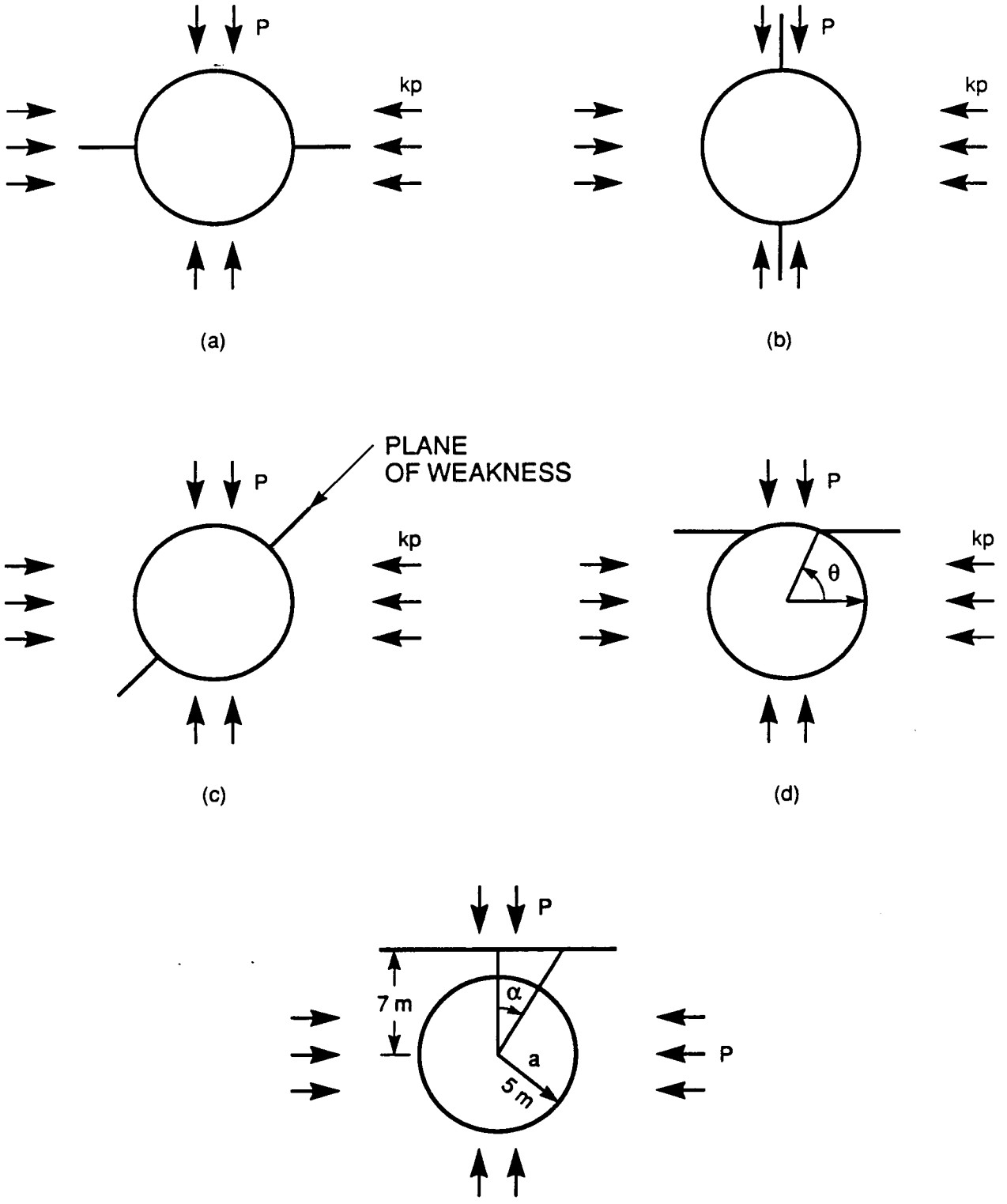

Figure 4-1. Five specific cases for a circular excavation with an adjacent discontinuity

(4) Lying perpendicular to the major principal stress and intersecting an opening non-diametrically, and

(5) Transgressing the zone of influence of an opening.

The plane stress closed-form solutions according to Kirsch (1898) for the stress distributions around a circular opening in an infinite elastic medium without a discontinuity are as follows:

$$\sigma_{rr} = \frac{p}{2}\left[(1 + K)\left(1 - \frac{a^2}{r^2}\right) - (1 - K)\left(1 - 4\frac{a^2}{r^2} + 3\frac{a^4}{r^4}\right)\cos 2\theta\right]$$

$$\sigma_{\theta\theta} = \frac{p}{2}\left[(1 + K)\left(1 + \frac{a^2}{r^2}\right) + (1 - K)\left(1 + 3\frac{a^4}{r^4}\right)\cos 2\theta\right] \qquad (4\text{-}1)$$

$$\sigma_{r\theta} = \frac{p}{2}\left[(1 - K)\left(1 + 2\frac{a^2}{r^2} - 3\frac{a^4}{r^4}\right)\sin 2\theta\right]$$

where a = radius of the circular opening,

r = distance from the center of the opening,

p = magnitude of a field principal stress,

K = ratio of the field principal stresses,

θ = counter clockwise angle between the x-axis and the line passing through the point where the stresses are calculated and the center of the opening,

σ_{rr} = radial stress,

$\sigma_{\theta\theta}$ = tangential stress, and

$\sigma_{r\theta}$ = shear stress.

No closed-form solutions are available to deal with the condition in which a discontinuity and a circular excavation are co-existent. For the purpose of this study, the simple treatment proposed by Brady and Brown (1985) was adopted to approximate the response of a discontinuity in the presence of a circular excavation. In this simple treatment,

a discontinuity was assumed to be nondilatant in shear; and its shear strength and tensile strength are defined by:

$$\tau = \sigma_n \tan \phi$$
$$T = 0 \qquad (4\text{-}2)$$

where τ = limiting shear stress along a discontinuity,

σ_n = normal stress perpendicular to the discontinuity,

ϕ = angle of friction of the discontinuity, and

T = tensile strength of the discontinuity.

If the state of stress in an area of a discontinuity calculated from the Kirsch solution Eqn. (4-1) exceeds the limiting criteria set by Eqn. (4-2), slip or separation is indicated in that area. This treatment is by no means a rigorous one and it is only capable of predicting the initiation of slip or separation. Any prediction made beyond that state through this treatment is an approximation. Nevertheless, the simple treatment provides adequate information for the purpose of the study.

The five typical cases noted above were modeled using the 3DEC code Version 1.0, and the results were compared to the predictions from the Kirsch solution subject to the limitations of Eqn. (4-2). The results and discussion are presented on a case-by-case basis. The following material properties of the continuous medium, and the plane of weakness were used throughout this study:

- Elastic properties and mass density

  - Mass density (ρ) = 10 kg/m^3
  - Shear modulus (G)= 35 GPa
  - Bulk modulus (K)= 60 GPa

Note that the Kirsch solution for stress distribution around a circular opening was derived under the assumption of zero mass density. However a mass density must be defined in 3DEC. For convenience, it is set to an arbitrarily small value.

- Joint properties

Coulomb friction model as used to simulate the plane of weakness. The specific 3DEC parameters for plane of weakness were listed as follows:

- Joint Normal Stiffness (JKN) = 200 GPa/m
- Joint Shear Stiffness (JKS) = 200 GPa/m
- Joint Cohesion (JCOH) = 0 MPa
- Joint Tensile Strength (JTENS) = 0 MPa

The continuous medium was modeled in the 3DEC analysis with elastic fully deformable blocks, which were further discretized into tetrahedral finite-difference zones. Joints simulated in the 3DEC model other than the plane of weakness were assigned high cohesion and tensile strength, to impose continuous response. The axes used in the 3DEC model followed a left-handed set (x, y, z), as x (east), y (vertically up), and Z (north). Cases 1, 2, 4, and 5 used only half of the geometrical models for simulation due to the existence of plane of symmetry for the respective cases. The dimensions for the four models were 60 x 120 x 1 m. Full model was used for Case 3 with a dimension of 120 x 120 x 1 m. The radius of the opening for all the cases was 5 m. The dimension is considered sufficient large such that boundary effects on the area of interest are minimum. Plane strain conditions were assumed during 3DEC run by restricting displacement in the z-direction. It is shown that calculated shear stresses along z-direction on planes of weakness for all five cases were at least six order of magnitude smaller than the shear stresses along x- or y- direction. It is therefore believed that the 3DEC results and the Kirsch solution are comparable.

4.2.1. Purpose

The purpose of this set of problems is to assess the capacity of 3DEC to simulate slip and separation on the planes of weakness under conditions of nonuniform local stress distribution. The intention is to determine if response of the planes of weakness predicted with 3DEC is consistent with the various modes of response indicated by the approximation to the response inferred from the Kirsch solution.

4.2.2. Case 1: Discontinuity Oriented Parallel to the Minor Principal Stress

4.2.2.1. Analytical Assessment

The problem illustrated in Figure 4-1 concerns a circular opening transected by a plane of weakness oriented along the diameter perpendicular to the major principal field stress; that is, the angle between the discontinuity and the minor principal field

stress is zero. Based on Eqn. (4-1), the state of stress along the discontinuity can be shown to be:

$$\sigma_n = \sigma_{\theta\theta} = \frac{p}{2}\left[(1 + K)\left(1 + \frac{a^2}{r^2}\right) + (1 - K)\left(1 + 3\frac{a^4}{r^4}\right)\right] \qquad (4\text{-}3)$$

$$\tau = 0 .$$

The zero shear stress along the plane of weakness indicates that no slip can occur. In other words, for a high-joint normal stiffness, the plane of weakness will have no effect on stress distribution around the circular opening.

4.2.2.2. Numerical Model

Figure 4-2 shows the 3DEC model for Case 1. Only fully deformable blocks in the model are shown. These blocks were further discretized into small tetrahedral finite-difference zones during 3DEC run. The yz-plane is the plane of symmetry. The plane of weakness was located on the xz-plane, where $y = 0$. The major principal stress, 24 MPa, was applied vertically to the top and bottom surfaces of the model. Minor principal stress, 12 MPa, was applied horizontally to the right surface of the model.

4.2.2.3. Results

Figure 4-3 shows the normal and shear stresses along the plane of weakness for Case 1. Both 3DEC result and Kirsch solution are shown. Although the normal stresses calculated by the 3DEC code are in general smaller than those from the Kirsch solution, 3DEC prediction and Kirsch solution are in a reasonable agreement.

The state of shear stresses on the plane of weakness calculated by the 3DEC code is not zero. The magnitude of the shear stress was found to be a function of edge length of tetrahedral finite-difference elements used in the 3DEC model. Shear stress decreases as the edge length becomes smaller. For an edge length equal to 1 m, the maximum shear stress on the plane of weakness is about 2 percent of the applied major principal stress. This level of error on the shear stress result is not expected to have significant consequences for similar engineering problems.

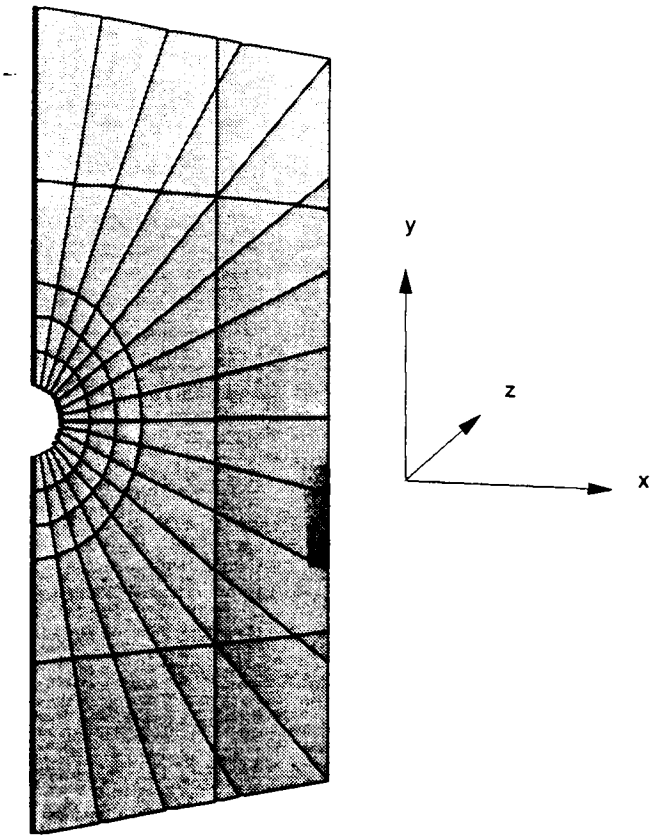

Figure 4-2. 3DEC model for case 1

4.2.3. Case 2: Discontinuity Oriented Parallel to the Major Principal Stress

4.2.3.1. Analytical Assessment

Case 2 concerns a circular opening transected by a plane of weakness oriented along the diameter parallel to the major principal stress, as illustrated in Figure

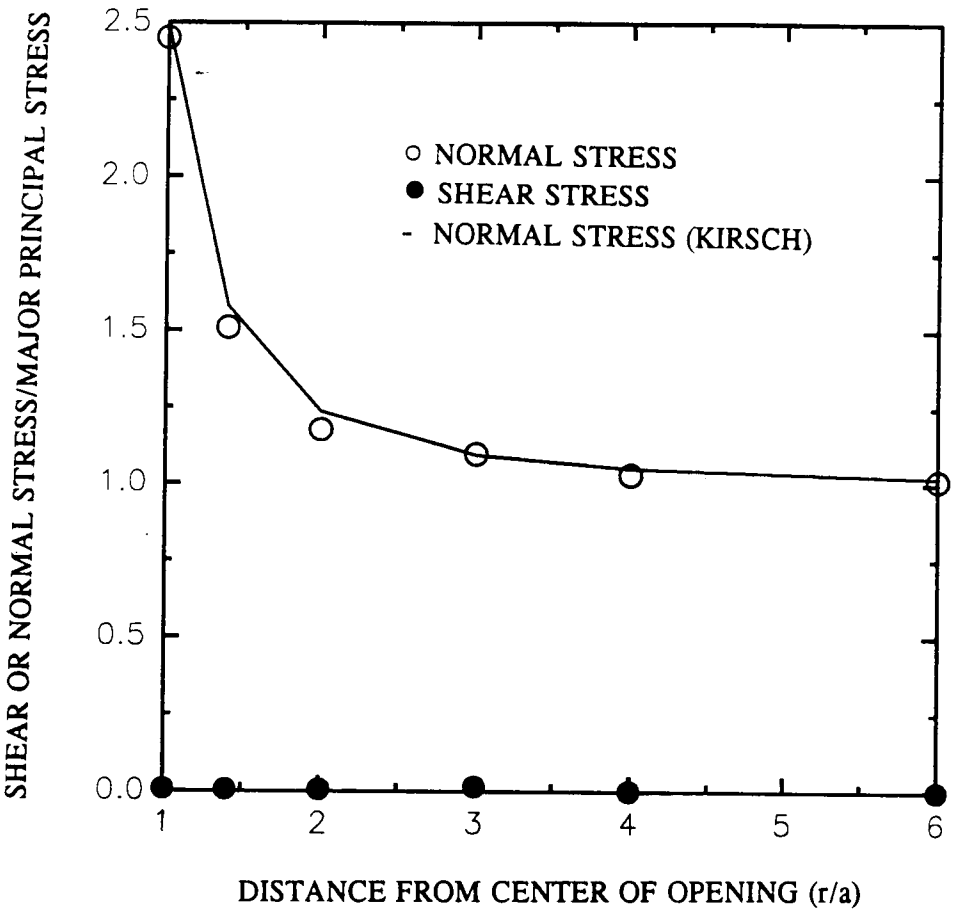

Figure 4-3. Normal and shear stress along the horizontal plane of weakness

4-1. The angle θ between the discontinuity and the minor principal stress in this case is 90 degrees, reducing Eqn. (4-1) to:

$$\sigma_{rr} = \frac{p}{2}\left[(1 + K)\left(1 - \frac{a^2}{r^2}\right) + (1 - K)\left(1 - 4\frac{a^2}{r^2} + 3\frac{a^4}{r^4}\right)\right]$$

$$\sigma_{\theta\theta} = \frac{p}{2}\left[(1 + K)\left(1 + \frac{a^2}{r^2}\right) - (1 - K)\left(1 + 3\frac{a^4}{r^4}\right)\right] \qquad (4\text{-}4)$$

$$\sigma_{r\theta} = 0 .$$

The state of stress along the plane of weakness can be expressed by:

$$\sigma_n = \sigma_{\theta\theta} = \frac{p}{2}\left[(1 + K)\left(1 + \frac{a^2}{r^2}\right) - (1 - K)\left(1 + 3\frac{a^4}{r^4}\right)\right] \qquad (4\text{-}5)$$

$$\tau = 0 .$$

As for Case 1, the state of zero shear stress along the plane indicates that no slip should occur and the elastic stress distribution will be sustained. The possibility of separation on the plane of weakness arises if tensile stress exceed tensile strength in the crown of the opening, that is, if $K < 1/3$. The height, h, of separation along the plane of weakness may be approximated by locating the zero joint normal stress (Brady and Brown, 1985).

$$h = a\left(\frac{1 - 3K}{2K}\right) . \qquad (4\text{-}6)$$

For $K \geq 1/3$, the elastic stress distribution will not be affected since neither slip nor separation is indicated along the plane of weakness.

4.2.3.2. Numerical Model

Figure 4-4 shows the 3DEC model for Case 2. The plane of weakness is located on the xz-plane where $x = 0$. The major principal field stress was 24 MPa and was applied along the model boundary surface located at $y = 12a$, where a was the radius of the opening.

4.2.3.3. Results

The 3DEC code did not predict zero shear stress on the plane of weakness as it did by the Kirsch solution. Figure 4-5 shows a plot of τ/σ_n on the plane of weakness versus distance from the center of the opening. The 3DEC model for this plot used 1-m edge length for the tetrahedral finite-difference elements near the opening; a value of 0.781 as the coefficient of joint friction, and a K value of 1/3. Although the error (nonzero shear stress on the plane of weakness) introduced by the 3DEC code does not have very significant consequence for Case 1, its impact on Case 2 is substantial. For example, the 3DEC code predicts slip at the intersection of the opening and the plane of weakness when K is equal to 1/3 while the Kirsch solution predicts the initiation of separation.

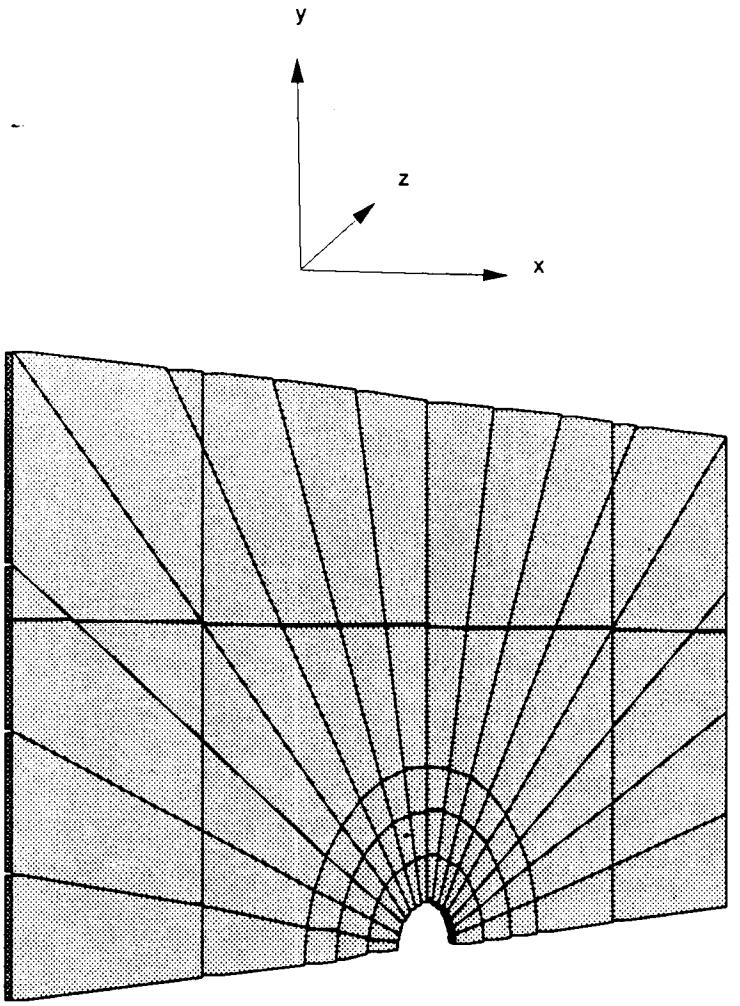

Figure 4-4. 3DEC model for case 2

For a case where K is equal to 1/6, the 3DEC code does predict separation along the plane of weakness with a height of 1 m. The Kirsch solution using Eqn. (4-6) predicts a height of separation at least 7.5 m. In a region where the stress and displacement gradients are high and discretization relatively coarse, the gross disparities are explicable. Further reducing element size may improve 3DEC prediction on separation. Immediately following the zone of separation, the 3DEC results also indicate an area of slip. This slip zone extends 4 m outward. This observation is not in accordance with the Kirsch solution. While it is possible to restrain the slip by further refinement on discretization, it may not be possible to eliminate the slip predicted by the 3DEC code due to the nonzero shear stresses on the plane of weakness.

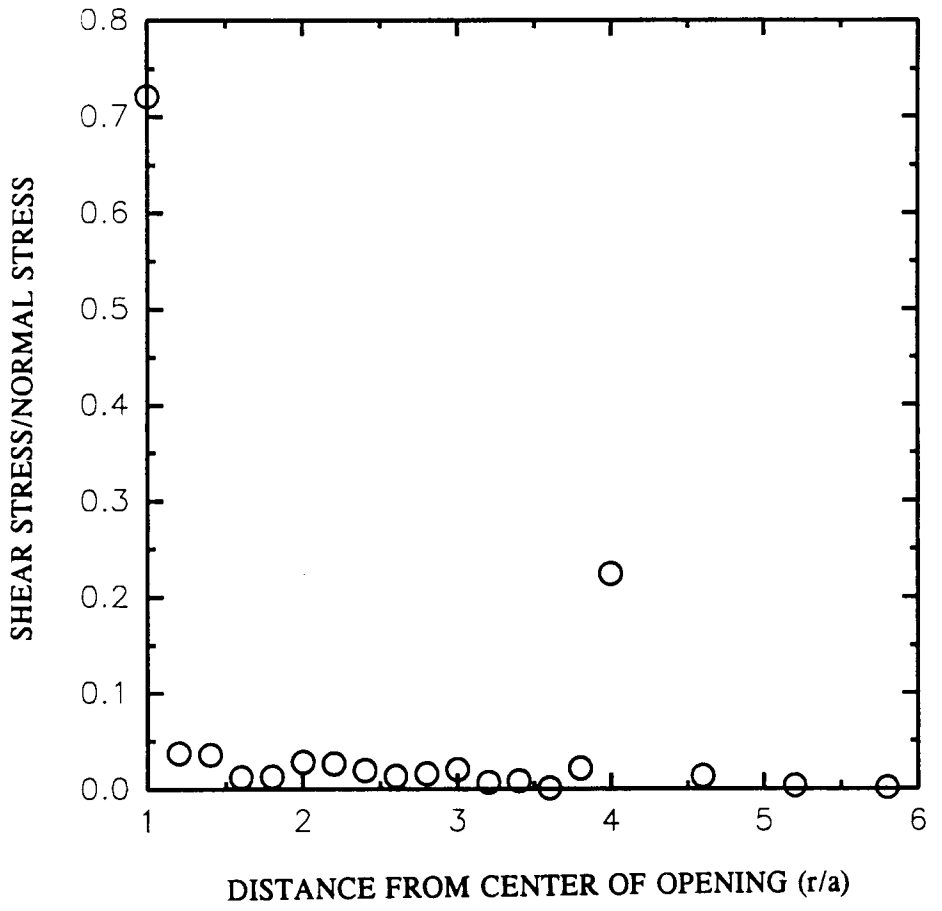

Figure 4-5. Plot of τ/σ_n on the plane of weakness versus distance from the center of

4.2.4. Case 3: Inclined Diametral Joint

4.2.4.1. Analytical Assessment

Case 3 considers a circular opening intersected by a plane of weakness along the diameter inclined at 45 degrees with respect to the applied major principal

stress [Figure 4-1(c)]. The elastic solution for the normal and shear stresses along this plane according to the Kirsch solution of Eqn. (4-1) is:

$$\sigma_n = \sigma_{\theta\theta} = \frac{p}{2}\left[(1 + K)\left(1 + \frac{a^2}{r^2}\right)\right]$$

$$\tau = \sigma_{r\theta} = \frac{p}{2}\left[(1 - K)\left(1 + 2\frac{a^2}{r^2} - 3\frac{a^4}{r^4}\right)\right]. \qquad (4\text{-}7)$$

For K = 0.5, the maximum value for the ratio of τ/σ_n, as calculated by Brady and Brown (1985) from Eqn. (4-7), is 0.3573 at a location 2.54a from the center of the opening. This ratio is equivalent to a mobilized angle of friction of 19.7 degrees; that is, for $\phi > 19.7$ degrees, no slip is possible on the plane of weakness. The mobilized angle of friction at infinity is 18.43 degrees. Interestingly the difference between these two angles is only about 1.3 degrees, and indicates the very restricted range within which joint slip can be investigated using the Kirsch equations.

4.2.4.2. Numerical Model

Figure 4-6 shows the 3DEC model for Case 3. The plane of weakness is inclined at 45 degrees. The major principal field stress was 24 MPa and applied to the model boundaries at y = 12a and y = -12a where a is the radius of the opening.

4.2.4.3. Results

The ratios of shear stress to normal stress (τ/σ_n) along the plane of weakness for Case 3 before the excavation of circular opening should be a constant of 0.3333, based on the Kirsch solution. This constant is equivalent to a mobilized friction angle of 18.43 degrees. For conditions where joint friction angle is greater than 18.43 degrees, no slip should be expected on the plane of weakness. The results from 3DEC analysis indicated that τ/σ_n ratios along the plane are not constant. Figure 4-7 shows the distribution of τ/σ_n ratios for a joint friction coefficient of 0.3839 (i.e., 21 degrees in terms of joint friction angle). Slip was observed in an area between 0.792a and 1.0a, and at a point 5.66a from the center of future opening. If joint friction coefficient is reduced from 0.3839 to 0.3522, additional slip will develop between 5.37a and 5.94a. These observations from the 3DEC analysis are not in good agreement with the Kirsch solution.

The existence of an opening in Case 3 will certainly modify the state of stresses on the plane of weakness. The consequence (in terms of slip) will not be realized according to the Kirsch solution if the joint friction angle is greater than 19.7 degrees. The 3DEC result, however, shows a zone of slip along the plane of weakness

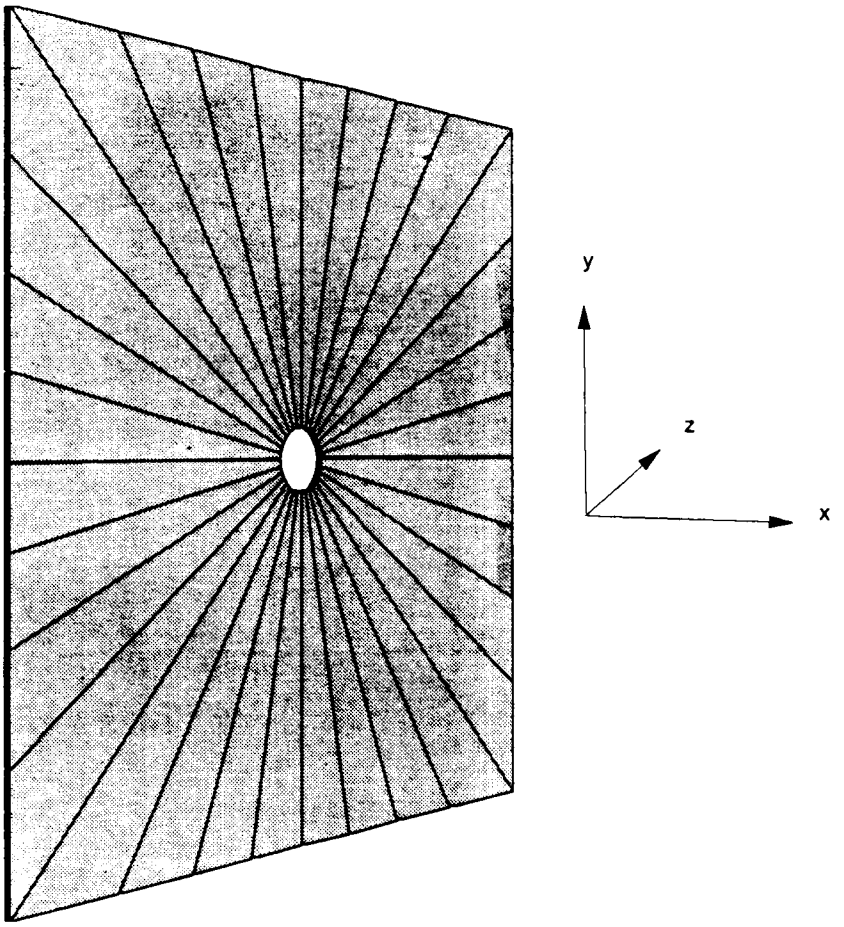

Figure 4-6. 3DEC model for case 3

between 1.41a and 4a from the center of the opening for a joint friction angle of 21 degrees. Give the sensitivity of the Case 3 problem to the angle of friction of the plane of weakness, the 3DEC prediction is apparently not in a good agreement with the Kirsch solution.

4.2.5. Case 4: Horizontal Joint Near Crown of Excavation

4.2.5.1. Analytical Assessment

The problem considered in this case is the response to construction of an excavation of a plane of weakness which is perpendicular to the direction of the major principal field stress and transects the excavation nondiametrically. The problem geometry is shown in Figure 4-1(d). Consideration of the state of stress on the plane of weakness shows that, at the intersection with the excavation, slip occurs when $\theta > \phi$ where θ defines the

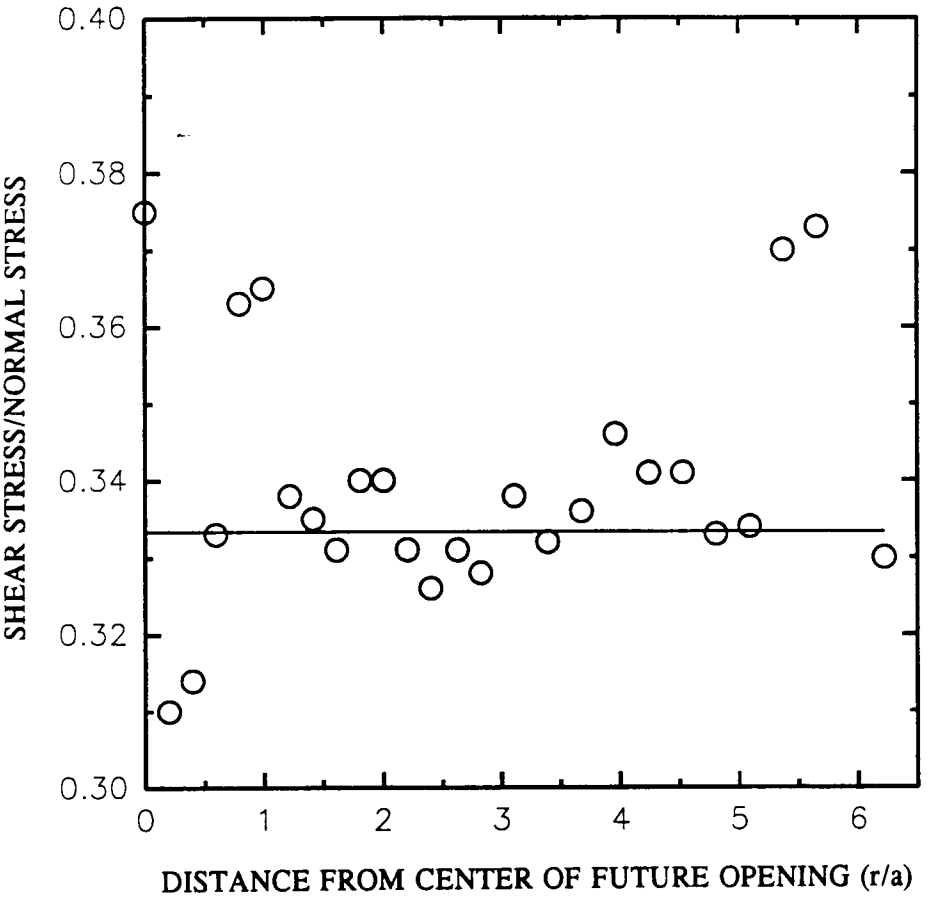

Figure 4-7. Distribution of τ/σ_n ratio along plane of weakness without excavation with coefficient of joint friction of 0.3839

angular coordinate of the joint intersection and ϕ is the angle of friction of the joint. Static equilibrium can be achieved only if, at the boundary-joint intersection;

$$\sigma_\theta \sin(\theta - \phi)/\cos\phi = 0 \; . \qquad (4\text{-}8)$$

Eqn. (4-8) can be satisfied only if $\sigma_{\theta\theta} = 0$ at the boundary. This implies that substantial redistribution of stress, accompanied by joint slip, may occur if $\theta > \phi$.

4.2.5.2. Numerical Model

Figure 4-8 shows the 3DEC model for Case 4. The model consisted of a section, symmetrical about the vertical center-surface through the circular opening, of radius a = 5 m. With the horizontal plane of weakness located at y = 4.33 m,

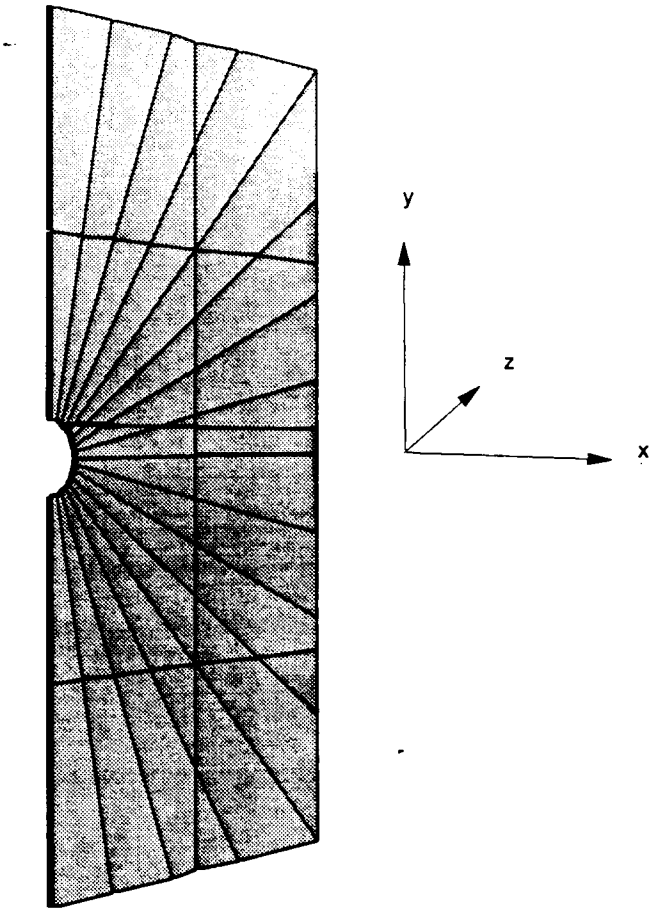

Figure 4-8. 3DEC model for case 4

its angular orientation is defined by $\theta = 60$ degrees. The virgin stress field was hydrostatic, of magnitude 24 MPa.

4.2.5.3. Results

Although the Kirsch solution predicts slip for Case 4 only if $\theta > \phi$, slip at the intersection between the circular opening and the plane of weakness was predicted by the 3DEC analysis even when ϕ is equal to 75 degrees. (Please note that the θ angle for 3DEC analysis is 60 degrees.) Substantial stress redistribution associated with the slip was observed. The slip predicted by the 3DEC analysis is limited at the intersection without spreading until ϕ becomes smaller than θ.

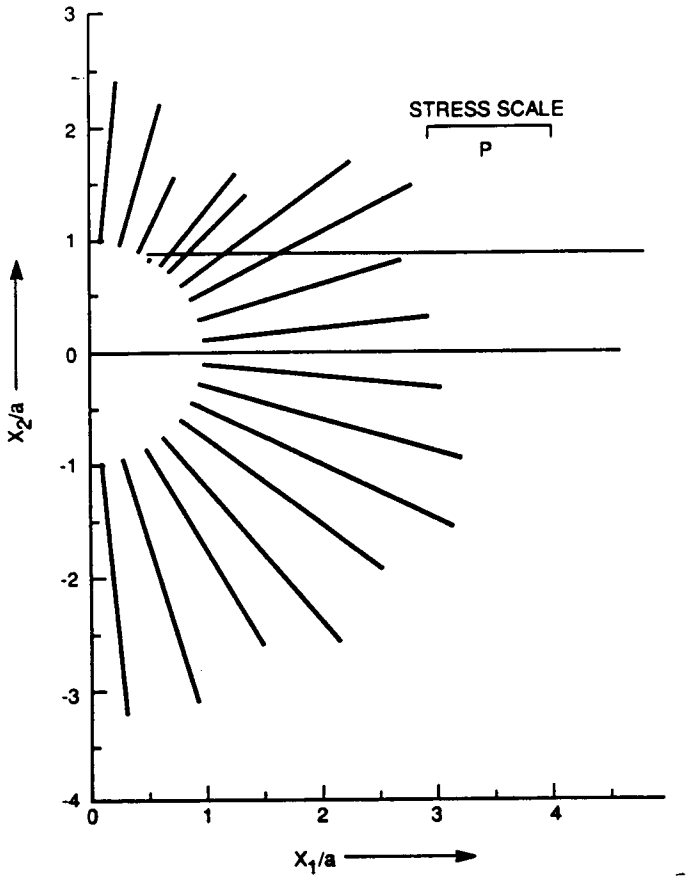

Figure 4-9. Polar plot of tangential component of boundary stress around a circular excavation intersected nondiametrically by a plane of weakness

Figures 4-9, 4-10, and 4-11show the 3DEC results with joint friction angle of 16.3 degrees. In Figure 4-9, the tangential component of boundary stress around opening, σ_θ, is presented as a polar plot, with stress magnitudes plotted perpendicular to the boundary location at which the σ_θ stress component is calculated. It is observed that a small tensile zone around the intersection exists. This tensile zone causes separation at the intersection. This finding substantially departs from the Kirsch solution. Despite this departure, it is notable that compared with the elastic solution, the boundary stress is reduced in the crown of the excavation and increased in the floor. This is consistent, in general, with slip outwards from the excavation on the upper side of the plane of weakness, and inwards on the lower side, as is indicated in the formal analysis.

A comparison between the results of the 3DEC analysis and an independent boundary element analysis (two-dimensional) of this problem, due to Crotty and

Brady (1990), is presented in Figure 4-10. The comparison is between normal and shear stresses along the plane of weakness. Given the relatively coarse discretization, both the normal and shear stresses distributions are in a reasonable agreement with the independent solution except in the area close to the boundary of the excavation.

Figure 4-11 shows the plot of τ/σ_n ratios along the plane of weakness. It is observed that the range of joint slip extends over a range (x/a) of about 1.5, fairly consistent with the value of 1.6 calculated from the independent solution. The τ/σ_n ratio on the plane of weakness is consistently equal to the coefficient of joint friction (i.e. 0.29) over the range of slip. This excludes the region close to the boundary of the excavation where separation takes place.

4.2.6. Case 5: Plane of Weakness Adjacent to Excavation

4.2.6.1. Analytical Assessment

The problem considered in Case 5 is the response of a plane of weakness located within the zone of influence of a circular excavation, but not intersecting it. The problem geometry is shown in Figure 4-1(e). For convenience in the study, the initial state of stress is taken to be hydrostatic. According to Brady and Brown (1985), the normal and shear stresses on the plane of weakness can be calculated from the expressions:

$$\sigma_n = p\left(1 - \frac{a^2}{r^2}\cos 2\alpha\right)$$

$$\tau = p\,\frac{a^2}{r^2}\sin 2\alpha \qquad (4\text{-}9)$$

where α is the angle measured from the radius perpendicular to the joint to the radius passing through the point of interest on the plane.

For the cohesionless joint, slip is possible on the plane of weakness when the ratio of τ/σ_n defined by Eqn. (4-9) exceeds the coefficient of friction for the surface.

4.2.6.2. Numerical Model

The 3DEC model for the problem is shown in Figure 4-12. The model is symmetrical about a plane located at y = 0. With the excavation of 5 m radius, the plane of weakness lying at y = 7 m is 2 m above the crown of the opening. The magnitude of the hydrostatic stress was 24 MPa.

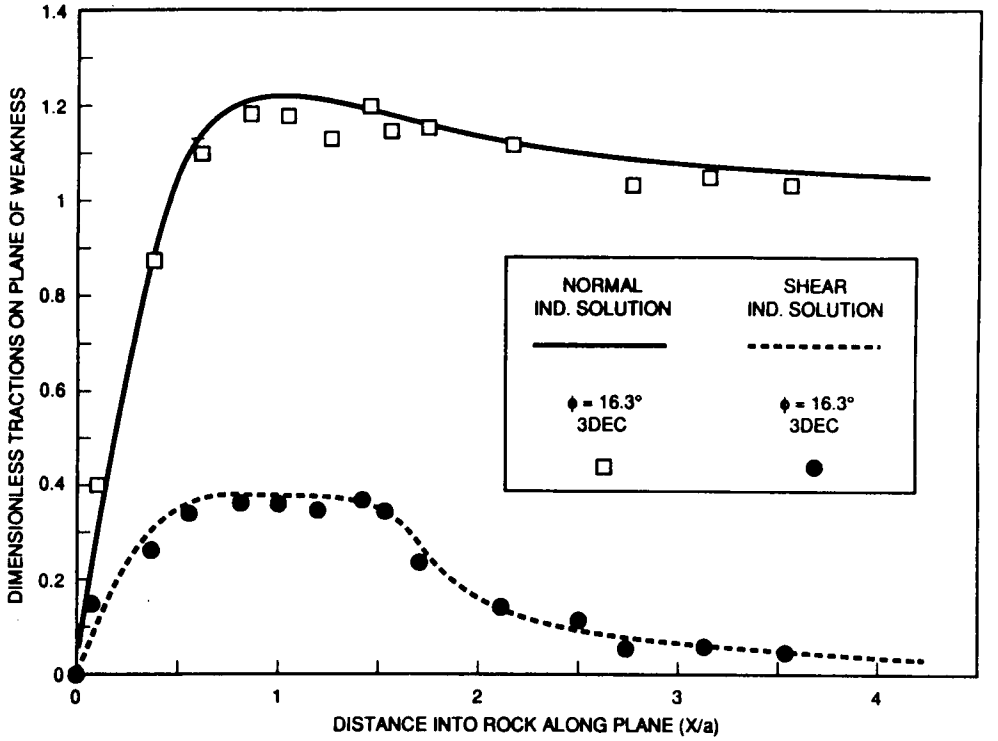

Figure 4-10. Normal and shear stress distributions onplane of weakness following joint slip

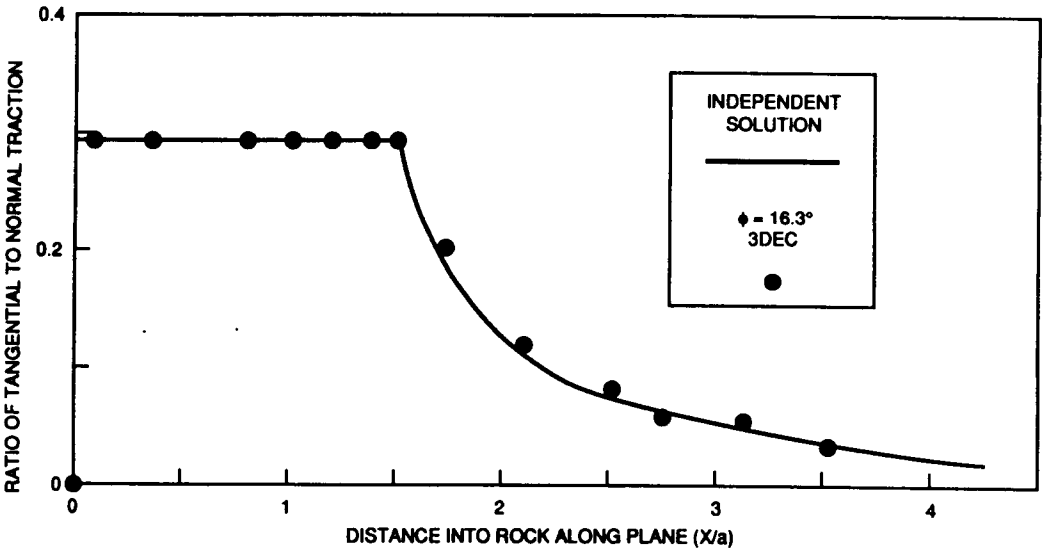

Figure 4-11. Shear normal stress ratio along a plane of weakness showing effect of joint slip

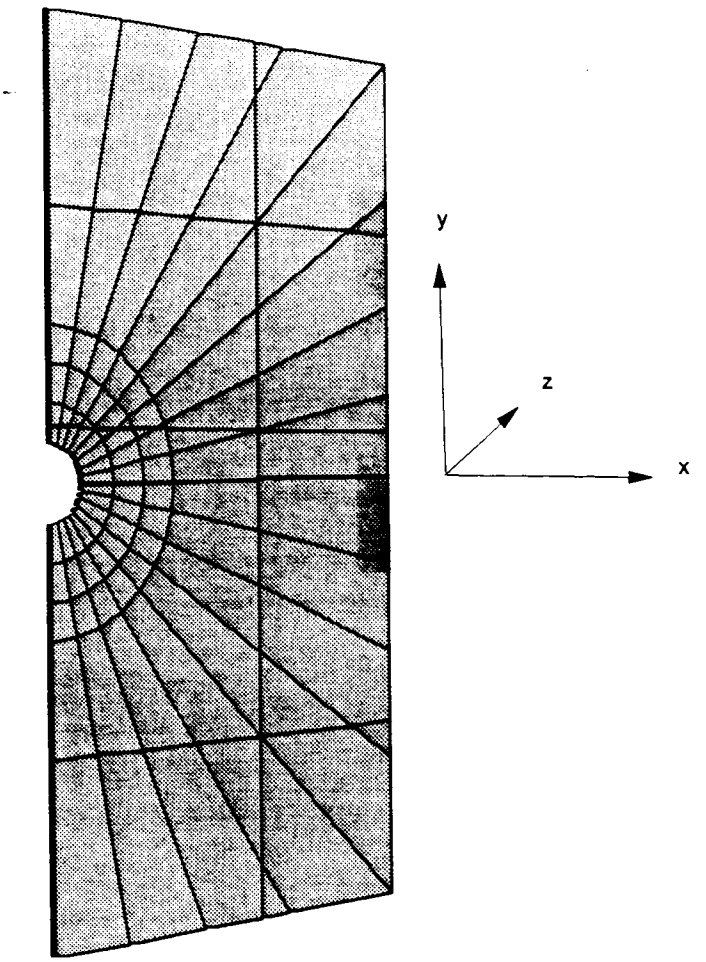

Figure 4-12. 3DEC model for case 5

4.2.6.3. Results

As stated previously, slip on the plane of weakness for Case 5 is controlled by the τ/σ_n ratio. Figure 4-13 shows the τ/σ_n curve calculated by Eqn. (4-9). The maximum value of the ratio is 0.445, which is located at about 3 m from the vertical diameter of the opening, corresponding to the mobilized angle of friction of 24 degrees. Thus, for an angle of friction for the plane of weakness exceeding 24 degrees, no slip will take place. Conversely, according to the elastic solution, an angle of friction less than 24 degrees will permit joint slip and stress redistribution. Slip on the plane of weakness at a location about 1.4 m from the vertical diameter of the opening was predicted by the 3DEC code with an angle of joint friction of 45 degrees. This prediction is not in a good agreement with the Kirsch solution. Reducing the angle of friction to 28.8 degrees, two slip zones will develop; one with a length of 2.4 m is located at 1.4 m from the vertical diameter of the opening, and

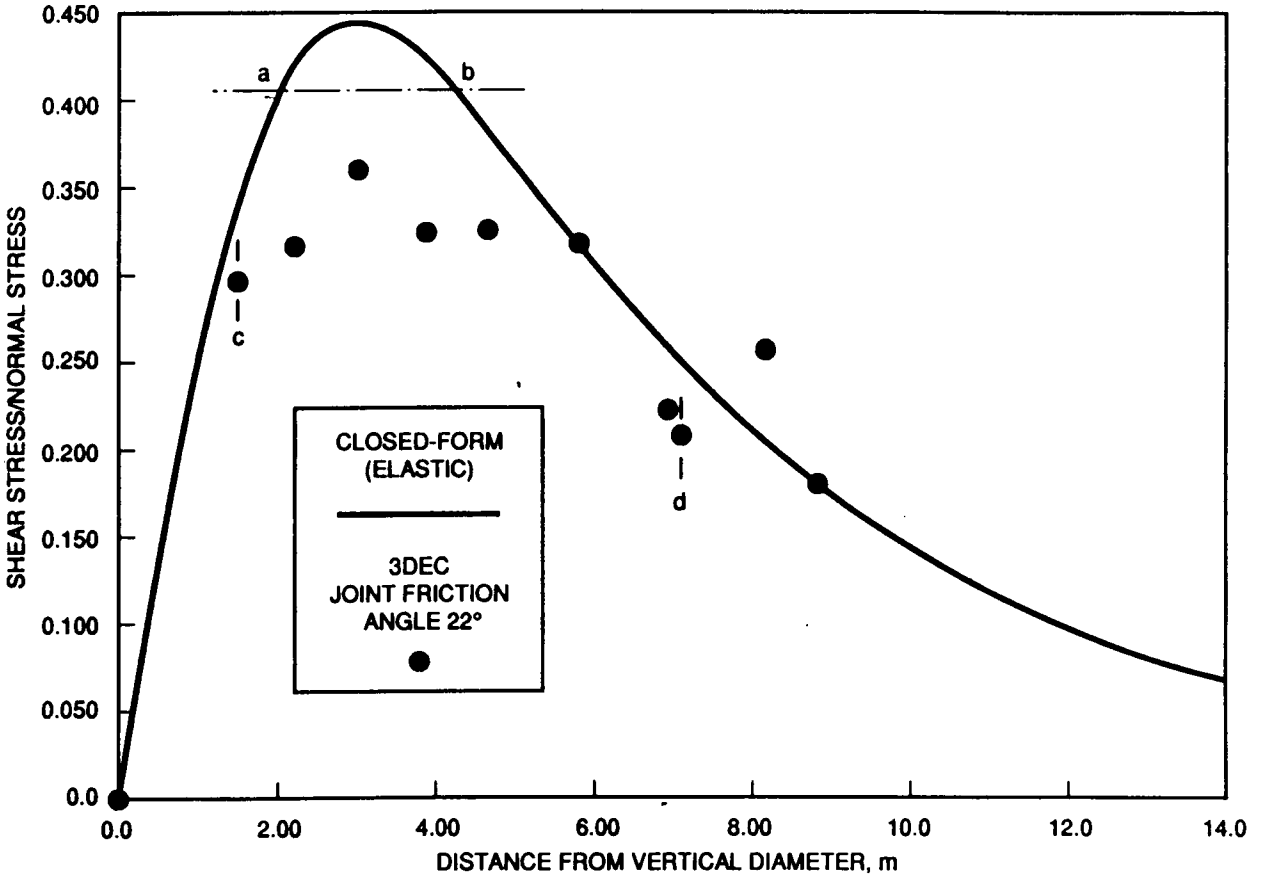

Figure 4-13. Stress ratio on plane of weakness, case 5

the other with a length of 0.1 m is located at 7 m from the vertical diameter. These two slip zones will join together if the angle of friction is reduced further to 22 degrees. Figure 4-13 also shows the τ/σ_n ratio on the plane of weakness calculated by the 3DEC code. The range of slip predicted from the Kirsch solution is denoted by the interval **ab** in the figure and is denoted by the interval **cd** as predicted by the 3DEC code.

4.2.7. Summary

The preceding sections examined the capability of the 3DEC code to simulate slip and separation on planes of weakness subject to heterogeneous states of stress developed around excavations in stressed rock. Because the benchmark problem assumes elastic-perfectly plastic joint deformation, only the Coulomb friction joint model could be properly exercised against the analytical (Kirsch) solution.

In general, the 3DEC code does not seem to be able to adequately simulate slip and separation on planes of weakness subject to the heterogeneous states of stress developed around excavations in stressed rock. Contrary to the prediction from the Kirsch solution, the 3DEC analyses give nonzero results for the shear stresses on the planes of weakness for both Cases 1 and 2. The magnitude of the nonzero shear stresses is very small compared with the associated normal stresses for Case 1; consequently, its impact is insignificant. The magnitude will become even smaller if the edge length of the tetrahedral finite-difference elements is smaller. For Case 2, the normal stresses to be dealt with on the plane of weakness near the excavation are normally small. As a result, the ratios of the nonzero shear stresses to the associated normal stresses may be greater than the assigned coefficient of joint friction and therefore may result in joint slip prior to joint separation. Two observations confirm the previous statement: (1) a slip instead of separation at the intersection of the plane of weakness and the excavation when K = 1/3 and (2) slip zone following the zone of separation when K = 1/6 from the 3DEC results. Similar error on shear-stress prediction introduced by the 3DEC code may be largely responsible for the observation of slip prior to the excavation of the opening for Case 3 and for the inadequacy of the 3DEC code to simulate Case 3 problem. For Cases 4 and 5 the 3DEC code predicts slip at angles of joint friction substantially greater than the angles suggested by the Kirsch solution. The reason for the departure of the 3DEC predictions from the predictions of the Kirsch solution for Case 4 and 5, is not clear. However, when the assigned angle of joint friction (16.3 degrees) is considerably smaller than the critical angle (60 degrees), the 3DEC results for the normal and shear-stress distribution on the plane of weakness for Case 4 are in a reasonable agreement with the independent solution from a boundary-element code except close to the excavation boundary. The 3DEC calculation showed that the state of stresses in this area is tensile instead of compressive and predicted that separation is at the intersection of the plane of weakness and the excavation.

In summary, further work seems to be needed to calibrate the 3DEC code so that it can adequately simulate the benchmark analytical problem "Circular Excavation with an Adjacent Discontinuity in an Infinite Elastic Medium."

4.3. REFERENCES

Brady, B.H.G., and E.T. Brown. 1985. *Rock Mechanics for Underground Mining.* London: George Allen and Urwin.

CNWRA. 1991. *Center for Nuclear Waste Regualtory Analyses Report (CNWRA) on Research Activities for Calendar Year 1990.* W. C. Patrick, ed. CNWRA 90-01A. San Antonio, Texas: CNWRA: 4-1 to 4-97.

Crotty, J.M. and B.H.G. Brady. 1990. Boundary element analysis of excavations in sparsely jointed rock. Submitted to *Int. J. Num. Meth. in Geomech.*

Kirsch, G. 1898. Die Theorie der elastizitat und die bedurfnisse der festigkeitslehre, *Viet. Ver. Deut. Ing.* 42: 797-807.

5. INTEGRATED WASTE PACKAGE EXPERIMENTS

by Gustavo Cragnolino and Narasi Sridhar

Investigators: Narasi Sridhar (CNWRA), Gustavo Cragnolino (CNWRA), Walter Machowski (SwRI), and Thomas C. Page (CNWRA)

5.1. TECHNICAL OBJECTIVES

The overall technical objectives of the Integrated Waste Package Experiments (IWPE) Project are to

- Develop a good understanding of the information currently available on metal corrosion and on other metal degradation processes.
- Assess the current status of Yucca Mountain Project (YMP) Waste-Package Programs.
- Conduct waste-package experiments to scope and study the key parameters affecting long-term material performance.
- Assess experimentally YMP selected waste-package materials and designs and provide independent evaluation for reasonable assurance of long-term performance.
- Facilitate a continuous technical integration support to NRC and the CNWRA in the area of waste package performance.

The objectives of the IWPE are planned to be accomplished under the following tasks, which are consistent with Revision 3 of the program plan:

- Task 1 - Corrosion, including Localized, Uniform, and Internal Corrosion
- Task 2 - Stress Corrosion Cracking
- Task 3 - Materials Stability
- Task 4 - Microbiologically Influenced Corrosion
- Task 5 - Other Degradation Modes
- Task 6 - Periodic Reporting

The current report focuses on work performed for Task 1. Literature reviews were performed in Tasks 2, 3, and 4. Test plans for Tasks 2 and 3 were approved, and experimental

programs will be initiated during the next reporting period. Studies on hydrogen absorption and embrittlement, conducted under Task 5, were completed at The Ohio State University and a Major Milestone report was issued. A brief summary of this report is provided here.

5.2. TASK 1 - CORROSION OF CONTAINER MATERIALS

Activities and salient results in two subtasks within Task 1 are described in this section. These subtasks are:

- Task 1.1.3a - Pitting Variability Studies
- Task 1.1.3b - Full Factorial Tests

5.2.1. Effect of Environmental Factors on Localized Corrosion of Type 316L Stainless Steel

The effects of anionic and cationic species on the localized corrosion resistance of alloy 825 have been examined. Screening-type electrochemical tests were performed using solutions simulating the natural water in the vicinity of the Yucca Mountain repository site (Cragnolino, 1990a; Cragnolino, 1991). This approach was extended to some of the other candidate container materials. The results of experiments on type 316L stainless steel are presented in this report.

Test Techniques. Cyclic potentiodynamic polarization tests were used as described before (Cragnolino, 1990a). At the end of the tests, the samples were examined visually using scanning electron microscopy (SEM). The visual observation was performed through a stereoscope at a magnification of 70X. The samples were rated on a 0-4 scale, using previously established criteria (Cragnolino, 1990a). The variation in pH during the tests has been reported for alloy 825 (Cragnolino, 1990a) and analyzed using EQ3/EQ6 codes (Pabalan, 1990). Similar pH levels and variations in pH were observed in the tests on type 316L stainless steel.

A two-level full factorial matrix was used for type 316L stainless steel to examine four factors: chloride, fluoride, nitrate, and sulfate. The initial bicarbonate concentration was maintained constant at 85 ppm, and all tests were conducted at 95°C. Subsequently, additional tests were conducted at various concentration levels of bicarbonate, chloride, nitrate, and sulfate. The effect of temperature was also examined separately. The results of the factorial experiments are shown in Table 5-1.

Visual Rating. In the case of alloy 825, there was a lack of correlation between visual observation and electrochemical parameters such as E_p and E_{rp}. This fact was pronounced at intermediate values of (E_p-E_{rp}). SEM observations indicated differences in the type of localized corrosion that led to the precipitation of a Fe-rich corrosion product in some cases and Cr-rich corrosion products in others. In the case of type 316L stainless steel, the correlation

Table 5-1. RESULTS OF TWO-LEVEL, FULL FACTORIAL EXPERIMENTS ON TYPE 316L STAINLESS STEEL.

TRIAL NUMBER	CHLORIDE (PPM)	NITRATE (PPM)	FLUORIDE (PPM)	SULFATE (PPM)	E_{corr} (mV SCE)	E_p (mV SCE)	E_{rp} (mV SCE)	VISUAL RATING	MOD LCI
1	6	10	2	20	-739	510	62	4	351.4
2	1000	10	2	20	-680	97	-171	4	1105.2
3	6	1000	2	20	-602	740	740	0	0.0
4	1000	1000	2	20	-721	204	-136	4	666.7
5	6	10	200	20	-513	749	680	0	0.0
6	1000	10	200	20	-666	179	-242	4	940.8
7	6	1000	200	20	-637	705	633	0	0.0
8	1000	1000	200	20	-454	283	-61	3	364.7
9	6	10	2	1000	-642	728	728	0	0.0
10	1000	10	2	1000	-701	176	-224	3	681.8
11	6	1000	2	1000	-682	700	700	0	0.0
12	1000	1000	2	1000	-596	333	-11	3	309.9
13	6	10	200	1000	-683	711	647	0	0.0
14	1000	10	200	1000	-502	187	-286	4	1011.8
15	6	1000	200	1000	-626	732	676	0	0.0
16	1000	1000	200	1000	-663	266	-83	3	393.6

Table 5-1. RESULTS OF TWO-LEVEL, FULL FACTORIAL EXPERIMENTS ON TYPE 316L STAINLESS STEEL. (cont'd.)

TRIAL NUMBER	CHLORIDE (PPM)	NITRATE (PPM)	FLUORIDE (PPM)	SULFATE (PPM)	E_{corr} (mV SCE)	E_p (mV SCE)	E_{rp} (mV SCE)	VISUAL RATING	MOD LCI
REPEAT RUNS									
17	6	10	2	20	-705	577	12	4	391.7
18	3.6	10	2	20	-454	787	755	0	0.0
19	3.6	10	2	20	-625	785	785	0	0.0
20	20	10	2	20	-647	771	771	0	0.0
21	20	10	2	20	-652	746	746	0	0.0
22	20	10	2	20	-622	764	—	2	—
23	100	10	2	20	-656	313	-63	4	480.5
24	100	10	2	20	-657	340	-68	4	480.0
25	100	10	2	20	-638	435	-49	4	445.1
26	300	10	2	20	-661	188	-68	4	544.7
27	300	10	2	20	-607	282	-46	4	465.2
28	300	10	2	20	-578	231	-85	4	547.2

HCO_3 = 85.5 ppm ($NaHCO_3$ = 122 ppm)
Temperature = 95°C

between electrochemical parameters and visual observation was very good; i.e. when pitting/crevice corrosion was indicated visually, there was a significant hysteresis in the polarization curve. Other differences also were observed in the behavior of type 316L stainless steel:

(1) The potential at which a rapid increase in current density was noted, E_p, was low whenever type 316L stainless steel had pitting, whereas E_p was high and relatively unaffected by pitting for alloy 825.

(2) Unlike the case of alloy 825, only one type of corrosion product was noted in type 316L stainless steel through the SEM.

As seen in Table 5-1, localized corrosion occurred even in the 6 ppm solution when all other ionic species were at their lowest concentrations. This test was repeated three times, and similar observations were made. The E_p values were high in this environment. Because of the good correlation between visual observation and electrochemical parameters for type 316L stainless steel, analysis of the effects of environmental parameters on localized corrosion can be made without recourse to a Localized Corrosion Index (LCI) (Cragnolino, 1990a) which was defined as:

$$LCI = (E_p - E_{rp})\ Visual\ Rating. \tag{5-1}$$

However, in order to compare the behavior of type 316L stainless steel and alloy 825, a modified version of a LCI is used here. Ongoing investigations into the behavior of Cu-base alloys also indicate that electrochemical parameters are insufficient to characterize the localized corrosion behavior; and hence, the Modified LCI concept may be extended to these alloys. The Modified LCI may be defined as:

$$Modified\ LCI = \frac{(E_p - E_{rp}).100}{E_p}\ .\ Visual\ Rating. \tag{5-2}$$

The Modified LCI is obtained by normalizing LCI with E_p. This enables a better comparison of alloys whose E_p values differ, although the hysteresis, E_p-E_{rp}, is about the same. The visual rating in the index permits consideration of only those cases where localized corrosion occurred.

Analysis of Factorial Experiments. The factorial experiments on type 316L stainless steel and alloy 825 were analyzed using the Modified LCI as the measured parameter. In this analysis, the effect of instrumentation was considered by performing two blocks of experiments using two potentiostats. The effect of instrument was found to be insignificant. The results of the analysis of variance (ANOVA) are shown in Tables 5-2 and 5-3.

Table 5-2. ANOVA TABLE FOR THE FACTORIAL EXPERIMENTS ON TYPE 316L STAINLESS STEELS FOR MODIFIED LCI. BLOCKING WAS NOT CONSIDERED.

Factor	Effect	Coefficient	Std. Error	95% C.I.	p-value
Average	364.12	364.119	15.17	-	-
Cl	640.39	320.195	30.34	385.6	0.0297
NO_3	-294.51	-147.255	30.34	385.6	0.0645
F	-50.51	-25.255	30.34	385.6	0.3392
SO_4	128.96	-64.48	30.34	385.6	0.1451
Cl*NO_3	-206.66	-103.33	30.34	385.6	0.0915
Cl*F	37.34	18.67	30.34	385.6	0.4275
Cl*SO_4	-41.11	-20.555	30.34	385.6	0.3984
NO_3*F	-4.06	-2.03	30.34	385.6	0.9164
NO_3*SO_4	46.99	23.495	30.34	385.6	0.3595
F*SO_4	153.94	76.97	30.34	385.6	0.1222
Cl*NO_3*F	-91.91	-45.955	30.34	385.6	0.2001
Cl*NO_3*SO_4	-40.86	-20.43	30.34	385.6	0.4002
Cl*F*SO_4	66.09	33.045	30.34	385.6	0.2701
NO_3*F*SO_4	-57.51	-28.755	30.34	385.6	0.3045

R^2 = 0.998
Adjusted R^2 = 0.977

Table 5-3. ANOVA TABLE FOR THE FACTORIAL EXPERIMENTS ON ALLOY 825 FOR MODIFIED LCI. BLOCKING WAS NOT CONSIDERED.

Factor	Effect	Coefficient	Std. Error	95% C.I.	p-value
Average	95.48	95.48	2.49	-	-
Cl	169.01	84.505	4.99	12.2	0.000
T	2.29	1.145	4.99	12.2	0.667
F	-20.38	-10.19	4.99	12.2	0.006
NO_3	-169.43	-84.715	4.99	12.2	0.000
SO_4	4.58	2.29	4.99	12.2	0.403
Cl*T	11.35	5.675	4.99	12.2	0.063
Cl*F	-3.77	-1.885	4.99	12.2	0.486
Cl*NO_3	-174.01	-87.005	4.99	12.2	0.000
Cl*SO_4	6.36	3.18	4.99	12.2	0.249
T*F	18.76	9.38	4.99	12.2	0.009
T*NO_3	-16.28	-8.14	4.99	12.2	0.017
T*SO_4	8.22	4.11	4.99	12.2	0.150
F*NO_3	-1.16	-0.58	4.99	12.2	0.827
F*SO_4	6.37	3.185	4.99	12.2	0.248
NO_3*SO_4	-10.98	-5.49	4.99	12.2	0.070
Cl*T*F	4.35	2.175	4.99	12.2	0.425
Cl*T*NO_3	-13.9	-6.95	4.99	12.2	0.032
Cl*T*SO_4	8.64	4.32	4.99	12.2	0.134
Cl*F*NO_3	8.76	4.38	4.99	12.2	0.129
Cl*F*SO_4	-0.75	-0.375	4.99	12.2	0.887
Cl*F*NO_3*SO_4	0.37	0.185	4.99	12.2	0.945

Table 5-3. ANOVA TABLE FOR THE FACTORIAL EXPERIMENTS ON ALLOY 825 FOR MODIFIED LCI. BLOCKING WAS NOT CONSIDERED. (cont'd.)

Factor	Effect	Coefficient	Std. Error	95% C.I.	p-value
$T*F*NO_3$	-4.77	-2.385	4.99	12.2	0.385
$T*F*SO_4$	0.45	0.225	4.99	12.2	0.932
$T*NO_3*SO_4$	-9.36	-4.68	4.99	12.2	0.109
$F*NO_3*SO_4$	0.025	0.0125	4.99	12.2	0.996

$R^2 = 0.998$
Adjusted $R^2 = 0.991$

The analysis considers the independent variables to be scaled on a -1 to +1 range. The factor effect is the contribution of any factor to Modified LCI at its highest level (+1). The coefficient is the factor effect divided by 2. The standard error and 95 percent confidence interval are calculated for each of the factor effects. The p-value is used to test for significance. Any p-value above 0.05 is considered to be insignificant (this corresponds to the 95 percent confidence criterion).

Table 5-2 indicates that, for type 316L stainless steel, the only factor of major importance is chloride, which promotes localized corrosion (positive coefficient). Nitrate and chloride-nitrate interaction are borderline cases, whereas all the other factors have no significant effect. For Alloy 825, Table 5-3 indicates that chloride, fluoride, and nitrate are all significant; and the interactions of $Cl*NO_3$, T*F, $T*NO_3$, and $Cl*T*NO_3$ are also significant. The interactions, Cl*T and NO_3*SO_4, are borderline cases. The average value of Modified LCI for type 316L stainless steel is higher than that of alloy 825, indicating that the latter is more resistant to localized corrosion.

It must be emphasized that the above analysis is valid only within the range of factors examined. For example, it was shown before (Cragnolino, 1991) that when the sulfate concentration was increased to 20,000 ppm, complete inhibition of localized corrosion occurred. The two-level factorial experiment also assumes a linear behavior, which is not observed (Cragnolino, 1990a). Hence, additional experiments were performed to explore the effect of various factors beyond and within the factorial test ranges.

Effect of Chloride. Tests at various levels of chloride indicated that the relationship of both E_p and E_{rp} was logarithmic with respect to chloride concentration. This is shown in Figure 5-1. Even 6 ppm chloride was sufficient to promote pitting, provided the

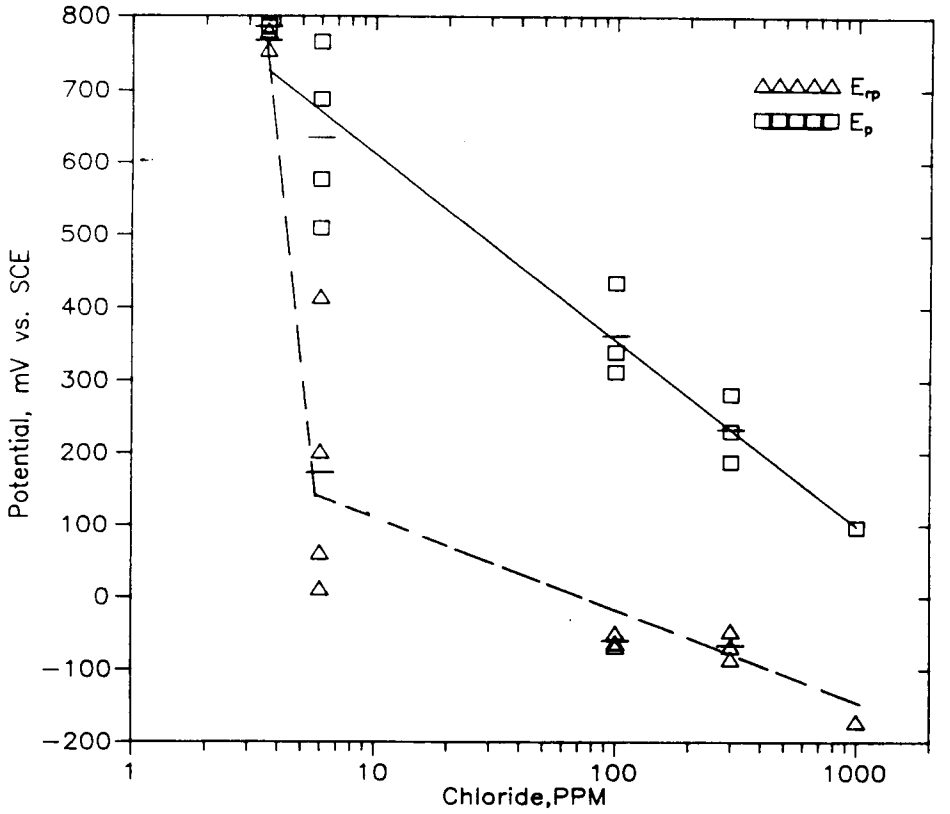

Figure 5-1. Effect of chloride on localized corrosion of type 316L stainless steel at 95°C.

applied potential was high. The repassivation potential, however, was quite low, indicating that crevice corrosion may be a potentially important form of corrosion for this alloy in the 6 ppm chloride solution.

Effect of Nitrate. The inhibiting effect of nitrate for alloy 825 and type 316L stainless steel is compared in Figure 5-2. A lower concentration of nitrate is required to inhibit localized corrosion of alloy 825 completely. This can be rationalized by the higher chromium content of the alloy in comparison to type 316L stainless steel.

Effect of Sulfate. While sulfate inhibits localized corrosion of alloy 825 more efficiently than of type 316L stainless steel (Figure 5-3), it is not as effective an inhibitor as nitrate.

Effect of Bicarbonate. Bicarbonate additions beyond 85 ppm decreased the localized corrosion tendency of type 316L stainless steel, as shown in Figure 5-4. In contrast, bicarbonate additions resulted in a slight increase in the localized corrosion tendency of alloy 825. The inhibiting effect of bicarbonate for type 316L stainless steel is in rough agreement with literature findings (Bogaerts, 1985; Jallerat, 1984). For example, Jallerat et al. (Jallerat,

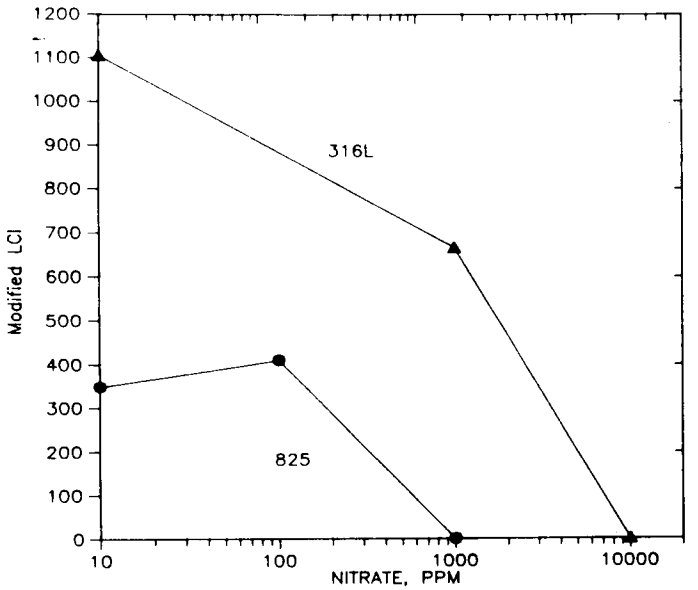

Figure 5-2. Effect of nitrate on localized corrosion in a 1000 ppm Cl solution at 95°C.

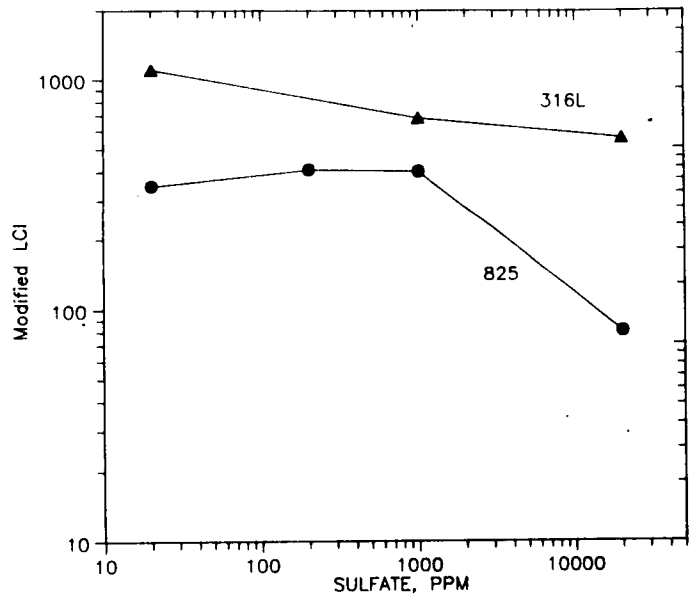

Figure 5-3. Effect of sulfate on localized corrosion in a 1000 ppm Cl solution at 95°C.

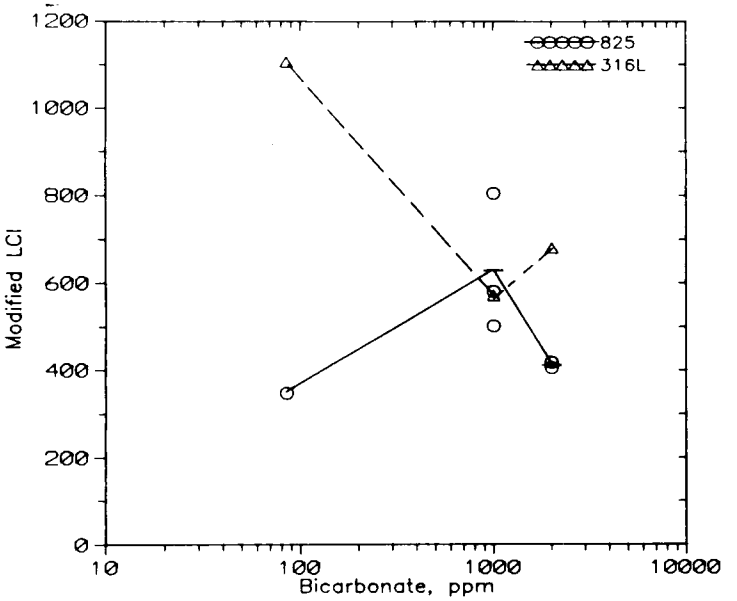

Figure 5-4. Effect of bicarbonate on localized corrosion in a 1000 ppm Cl solution at 95°C.

1984) showed that the concentration of bicarbonate required to inhibit localized corrosion in 316L stainless steel is related to chloride concentration by

$$Log(Cl^-) = 0.23 + 2.02\ Log\ (HCO_3^-). \qquad (5\text{-}3)$$

In this relationship, for a chloride concentration of 1000 ppm (0.028M), 8000 ppm bicarbonate is required for complete inhibition.

5.2.2. Measurement of Bicarbonate Concentration in Aqueous Solutions

Most of the studies on localized corrosion of the candidate container materials included in this task involved aqueous solutions containing bicarbonate ions. Thus, an appropriate method must be applied for the determination of the HCO_3^- concentration, particularly for long-term tests where this concentration may vary with time. A simple technique for this purpose is described in ASTM D 513-88: Standard for Total and Dissolved Carbon Dioxide in Water, Test Method A - Gas Sensing Electrode Test Method. The total concentration of dissolved carbonate species present as CO_2, H_2CO_3, HCO_3^-, and CO_3^{2-} in water are determined

potentiometrically by using a carbon dioxide electrode. Volatile weak acids, such as HNO_2, H_2SO_3, acetic acid, and formic acids, are known as potential interferences in this method. This is not a matter of concern because these anions are not included in the model solutions to be tested. By knowing the total concentration of dissolved carbonate species, the pH of the solution, and the partial pressure of CO_2 in equilibrium with the solution, the concentration of each species can be calculated by using the thermodynamic constants for the various equilibria involved. These equilibria were briefly discussed in a previous report (Cragnolino, 1991).

In addition to bicarbonate, the model solutions may eventually contain other anions, such as chloride, sulfate, nitrate, and fluoride, which are the predominant anionic species in the groundwaters in the proximity of the proposed Yucca Mountain repository site. For this reason, a test matrix including 10 solutions (Table 5-4) was designed to measure the HCO_3^- ion concentration in the presence of various concentrations of those anions to confirm whether interference by the various anions can be disregarded. Additionally, for each solution the pH and the chloride concentration were measured. The measurements were conducted using a Model 95-02 Orion carbon dioxide electrode, a Model 94-17B Orion chloride electrode, and a Model 81-02 Orion pH combination electrode in conjunction with a Model 728 Orion pH-ion selective electrode meter.

Table 5-4. NOMINAL COMPOSITION OF THE BICARBONATE-CONTAINING SOLUTIONS FOR HCO_3^-, Cl^-, AND pH MEASUREMENTS.

Solution	HCO_3^- (ppm)	Cl^- (ppm)	SO_4^{2-} (ppm)	NO_3^- (ppm)	F^- (ppm)
1	88	6	20	10	2
2	88	10000	20	10	2
3	88	6	10000	10	2
4	88	6	20	10000	2
5	88	6	20	10	200
6	8800	6	20	10	2
7	8800	10000	20	10	2
8	8800	6	10000	10	2
9	8800	6	20	10000	2
10	8800	6	20	10	200

Following the procedure described in ASTM D 513-88, the carbon dioxide electrode was calibrated within the specified range of 0 to 400 ppm CO_2. The CO_2 concentration was measured in all the solutions, but a dilution factor of 1:20 was used for solutions 5 to 10. For the measurement of the chloride concentration, a dilution factor of 1:100 was applied to solutions 2 and 7.

Results of the measurements of HCO_3^- and Cl^- concentrations for each solution as well as the corresponding pH values are summarized in Table 5-5. Triplicate measurements were conducted for each solution, and the values reported are the mean of those measurements. In addition, triplicate samples were prepared in the specific case of solutions 1 and 5, as denoted by the suffixes -a, -b, and -c.

Table 5-5. VALUES OF HCO_3^- CONCENTRATION, Cl^- CONCENTRATION, AND pH FOR SOLUTIONS INCLUDED IN TABLE 5-4.

Solution	HCO_3^- (ppm)	Cl^- (ppm)	pH
1-a	93.3	10.6	8.17
1-b	94.0	9.3	8.35
1-c	95.2	10.1	8.41
2	101.0	11000	8.16
3	102.3	8.6	8.09
4	100.2	8.5	8.51
5	108.1	7.6	8.13
6-a	8263	7.5	8.21
6-b	8928	8.6	8.29
6-c	9372	8.6	8.28
7	9261	12500	8.05
8	9067	7.8	8.13
9	9400	8.1	8.14
10	10120	8.3	8.25

The mean value of the HCO_3^- concentration for solutions 1-a to 1-c is 94.2 ppm with a standard deviation of 1.0 ppm. For solutions 2 to 4, the mean value is 101.2 ppm with a standard deviation of 1.1 ppm. Since the 95 percent confidence interval for solutions 1-a to 1-c is $\pm$ 2.4, it can be concluded that the addition of 10000 ppm chloride, sulfate, or nitrate affects the determination of the bicarbonate concentration at the low bicarbonate concentration level, probably through their effect on the ionic strength of the solutions. On the other hand, for solutions 6 to 9, the mean value is 9048 ppm with a standard deviation of 425 ppm. In this case the nominal bicarbonate composition of 8800 ppm lies within the 95 percent confidence interval for the measurements, which is 446 ppm. It can be concluded that the presence of chloride, sulfate, and nitrate at the high bicarbonate concentration level does not affect the determination of the bicarbonate concentration.

According to Table 5-5, the measured values of the HCO_3^- concentration in the presence of 200 ppm fluoride (solutions 5 and 10) lie outside the 95 percent confidence limits for solutions 2 to 4 and 6 to 9, which are $\pm$ 2.7 and $\pm$ 446 ppm, respectively. These results seem to indicate that fluoride interferes with the determination of bicarbonate, presumably through an effect similar to that mentioned above for weak volatile acids. It should be noted that the pK of HF is 3.45, whereas that of HNO_2 is 3.37, suggesting that both anions (F^- and NO_2^-) may have a very similar effect if their volatility is comparable. For example, a 10 percent positive error in the determination of 61 ppm HCO_3^- (10^{-3} M) is caused by 160 ppm NO_2^- (3.5 x 10^{-3} M) according to ASTM D-513. Additional work is needed to identify beyond doubts the nature of the interference and determine the possibility of using a correction term.

The mean pH values were found to be 8.26 $\pm$ 0.16 and 8.19 $\pm$ 0.09 for the nominal bicarbonate concentration of 88 and 8800 ppm, respectively. Obviously, under conditions of equilibrium of the solutions with the partial pressure of CO_2 in the atmosphere, the HCO_3^- anion constitutes more than 99 percent of the total concentration of dissolved carbonate species. No variation of pH should be expected in that concentration range. The reason is that the pH value should be practically equal to the arithmetic mean of the pK values for the two successive dissociation or acidity constants of dissolved carbon dioxide, which are 6.35 and 10.33 at 25°C (Stumm, 1981). Therefore, by assuming infinite dilution conditions, a pH of 8.34 should be expected, which is very close to that measured.

The mean value of the chloride concentration for all the solutions, with the exception of solutions 2 and 7, was 8.6 ppm with a standard deviation of 1 ppm. No statistical significance can be attributed to the difference in the mean values between both sets of solutions containing 88 and 8800 ppm bicarbonate. It is apparent that higher values than the nominal chloride concentration were measured in all solutions, including those containing 10000 ppm chloride.

5.3. HYDROGEN ABSORPTION AND EMBRITTLEMENT

The sources of hydrogen in the repository, kinetics of hydrogen absorption, and embrittlement were examined under Task 5. The experimental investigation was performed by Wilde et al. at Fontana Corrosion Center of The Ohio State University under a sub-contract from CNWRA. The results have been discussed in detail in a major milestone report (Sridhar, 1991). What follows is a synopsis of the report.

5.3.1. Sources of Hydrogen

Four sources of hydrogen can be identified in the proposed repository at Yucca Mountain:

(1) Galvanic contact with less noble borehole liner material

(2) Crevice corrosion generating acidic conditions conducive to hydrogen evolution

(3) Microbiologically generated hydrogen

(4) Radiolysis of aqueous or gaseous environments surrounding the container

Both galvanic coupling with less noble metals and crevice corrosion are viable sources of hydrogen, provided an aqueous environment contacts the container and borehole liner. Microbiologically influenced hydrogen generation has been observed on steels due to organisms such as *Clostridium Acetobutylicum*, but the survivability of these organisms under repository thermal and radiation conditions is not known. Radiolytic generation of hydrogen from aerated water at near neutral pH or air+steam mixture is unlikely because of the formation of oxidizing species such as nitrate and hydrogen peroxide. However, radiolytically generated hydrogen is a possibility in crevices where more acidic and reducing conditions prevail.

Hydrogen permeation was measured on some of the austenitic alloys and copper based alloys. The calculated hydrogen diffusivities from these measurements have been reported previously (Cragnolino, 1990b). These values agree with the reported values in the literature for similar alloys. It was found that among the Ni-base alloys, alloy 825 exhibited lower diffusivity for hydrogen than alloy C-22.

Preliminary tests were conducted to measure the hydrogen embrittlement susceptibility of the austenitic materials using the slow strain rate testing. For this purpose, the samples were machined from the same plates that are being used at CNWRA and sent to Fontana Corrosion Center. The chemical compositions and microstructures of these plates have been reported before (Cragnolino, 1990c). The samples were machined such that the tensile loading direction was perpendicular to the rolling direction (transverse orientation) because this direction has been shown to be the most susceptible to hydrogen embrittlement. The samples were

charged in 0.1N NaOH solution at various cathodic current densities for 24 hours prior to straining and continuously during straining. No hydrogen recombination poisons were used. The results are shown in Table 5-6.

Table 5-6. SUMMARY OF SLOW STRAIN RATE TESTS ON ALLOYS 825 AND C-22 UNDER CONDITIONS OF ELECTROLYTIC HYDROGEN CHARGING.

Alloy	Temp°C	i_c, mA/cm^2	TTF, Hrs	UTS, ksi	% R.A.
C-22	25	0	165	112.6	74.6
C-22	25	20	118	103.6	42.9
C-22	50	20	135	105.2	47.5
C-22	85	20	160	111.8	64.2
825	25	0	99	97.9	71.3
825	25	20	95	95.0	67.9
825	50	20	96	95.5	69.6
825	85	20	94	95.7	68.6

Charging solution: 0.1N NaOH
Nominal Strain Rate: 4×10^{-6} per sec.

In the case of alloy C-22, a low iron containing alloy, charging hydrogen at 25°C reduced the time-to-failure from 165 hours to 118 hours and the reduction in fracture area from 74.6 to 42.9 percent. There was a concomitant change in fracture mode observed through a SEM from ductile fracture to a partial intergranular fracture. Table 5-6 also indicates that the extent of embrittlement in alloy C-22 decreases with an increase in temperature, and at 85°C no significant embrittlement was observed. In contrast, alloy 825, a higher-iron containing alloy, did not exhibit any signs of embrittlement at any temperature.

The above results are typical of hydrogen embrittlement of a number of Ni-base alloys. Factors that can exacerbate embrittlement include acidic conditions; presence of cold-work; prolonged exposure to low temperatures ranging from 200 to 500°C; and presence of hydrogen recombination poisons such as S, P, Sn, Sb.

5.4. SUMMARY

The results of work performed during this reporting period can be summarized as follows:

(1) Factorial experiments on type 316L stainless steel indicated that chloride is the predominant factor enhancing localized corrosion. Within the range of other factors tested in this matrix, nitrate, sulfate, and fluoride did not have a dominant effect.

(2) Using a modified localized corrosion index, the response of alloy 825 and type 316L stainless steel to environmental changes can be compared. Generally, alloy 825 exhibited superior resistance to localized corrosion.

(3) Localized corrosion was observed in type 316L stainless steel even in the 6 ppm chloride solution. Increasing the concentration of nitrate to 10,000 ppm resulted in complete inhibition of localized corrosion in type 316L stainless steel in a 1000 ppm chloride solution.

(4) Bicarbonate and sulfate also inhibited localized corrosion but were less effective than nitrate.

(5) The bicarbonate and chloride concentrations were analyzed in some of the test solutions, and the measured values at room temperature were in reasonable agreement with the calculated additions. At low concentrations of bicarbonate and high ionic strengths, deviations were observed from the calculated concentrations of bicarbonate.

(6) Sources of hydrogen in the repository at Yucca Mountain were examined. Galvanic coupling with less noble borehole liner and crevice corrosion may generate the most hydrogen, but require an aqueous environment contacting the container and liner. However, even if copious amounts of hydrogen were generated, embrittlement of some of the candidate container materials was not observed at 85°C under accelerated laboratory testing.

5.5. REFERENCES

Bogaerts, W. F., and A. A. Van Haute. 1985. Chloride pitting and water chemistry control in cooling or boiler circuits. *Corrosion Science*, 25:1149-1161.

Cragnolino, G. A., and N. Sridhar. 1990a. *Report on Research Activities for the Quarter July 1 through September 30, 1990.* CNWRA 90-03Q, Chapter 5. San Antonio, Texas: CNWRA.

Cragnolino, G. A., and N. Sridhar. 1990b. *Report on Research Activities for the Quarter April 1 through June 30, 1990.* CNWRA 90-02Q, Chapter 5. San Antonio, Texas: CNWRA.

Cragnolino, G. A., and N. Sridhar. 1990c. *Report on Research Activities for the Quarter January 1 through March 30, 1990.* CNWRA 90-01Q, Chapter 5. San Antonio, Texas: CNWRA.

Cragnolino, G. A., and N. Sridhar. 1991. *Report on Research Activities for the Quarter January 1 through March 31, 1991.* CNWRA 91-01Q, Chapter 5. San Antonio, Texas: CNWRA.

Jallerat, N., F. L. Pari, F. Bourelier, and K. Vu Quang. 1984. Specific inhibition effect of carbonate and bicarbonate ions on pitting corrosion of stainless steels and Ni-base alloys. *Proc. 9th International Congress on Metallic Corrosion*, Vol. 4. Ottawa, Canada: National Research Council: 404-406.

Pabalan, R. T., and W. M. Murphy. 1990. *Report on Research Activities for the Quarter July 1 through September 30, 1990.* CNWRA 90-03Q, Chapter 2. San Antonio, Texas: CNWRA.

Sridhar, N., B. E. Wilde, C. Manfredi, S. Kesavan, and C. Miller. 1991. *Hydrogen Absorption and Embrittlement of Candidate Container Materials.* CNWRA 91-008. San Antonio, Texas: CNWRA.

Stumm, W., and J. J. Morgan. 1981. *Aquatic Chemistry.* 2nd. ed. New York, NY: John Wiley & Sons.

6. STOCHASTIC ANALYSIS OF UNSATURATED FLOW AND TRANSPORT

by Rachid Ababou

Investigator: Rachid Ababou (CNWRA)

6.1. TECHNICAL OBJECTIVES

A quantitative characterization of large-scale flow and radionuclide transport through the heterogeneous unsaturated fractured rock of Yucca Mountain will be necessary to evaluate compliance with the siting criteria and performance objectives associated with the proposed Yucca Mountain HLW repository (10 CFR 60.112 and 60.113). The pertinent technical issues concerning radionuclide migration at Yucca Mountain will need to be understood so as to demonstrate that the hydrogeologic conditions at the repository site strongly inhibit radionuclide transport to the accessible environment and meets performance criteria. Realistic modeling of the complex, heterogeneous flow and transport processes at Yucca Mountain will require incorporating the effects of relatively small-scale space-time variability in modeling large-scale unsaturated flow and radionuclide transport.

The specific objectives of the Project on "Stochastic Analysis of Large Scale Flow and Transport Through Unsaturated Fractured Rock" are as follows:

- To perform a review of the literature, assess available models and data relevant to the subject site, and select a global approach to model large-scale flow and transport in unsaturated fractured rock.
- To develop hydrodynamic submodels for incorporation into the global model.
- To perform large-scale simulations and participate in the validation of flow/transport models for Yucca Mountain.

The project is divided in three tasks to accomplish the objectives.

- Task 1 - Review, Analysis, and Initial Development of Modeling Approach
- Task 2 - Stochastic Submodel Development and Implementation
- Task 3 - Large-Scale Flow/Transport Simulation and Data Analysis

6.2. RESEARCH ACCOMPLISHMENTS

During the reporting period, progress has been made in the development of auxiliary submodels under Task 2 of the Project. As explained in earlier progress reports (see also Chapter 6 in Ababou, 1991), auxiliary hydrodynamic models are needed in order to achieve

realistic full-scale simulations of unsaturated flow and transport in complex three-dimensional environments like Yucca Mountain. In particular, there is a need for physically-based models of effective unsaturated conductivity in the following cases: (1) flow through a single rough-wall fracture imbedded in a porous medium (possibly with contact areas), (2) flow through a fracture network imbedded in a porous matrix (requires also realistic fracture network models), and (3) flow through a heterogeneous and stratified porous matrix (possibly with variable micro-fracturing density). Work on items (1) and (2) is ongoing and will be reported at later stages. Recent developments for case (3), based on a probabilistic formulation of unsaturated conductivity, are reported below in some detail.

6.3. PROBABILISTIC ANALYSIS OF UNSATURATED CONDUCTIVITY: ANISOTROPY, CROSSING POINT, AND UPPER ENVELOPE

6.3.1. Introduction

One of the problems encountered in field-scale modeling of unsaturated flow phenomena is how to integrate the combined effects of nonlinearity and spatial heterogeneity in the most efficient and parsimonious way. How should field heterogeneity be taken into account in nonlinear functional models of unsaturated hydrodynamic properties? What are the appropriate constitutive relations to be used for field-scale models of unsaturated flow in the presence of multiple heterogeneities, stratification, and fractures? And what is the effective macroscale hydrodynamic behavior of such heterogeneous geologic media? In relation to these questions, the goal of this study is to analyze how the spatial structure of small-scale hydrodynamic properties affects the overall hydrodynamic behavior of unsaturated geologic media.

The nonlinear hydraulic conductivity of unsaturated geologic media is a case in point. In what follows, focus is primarily on the conductive behavior of heterogeneous unsaturated media under quasi-steady flow conditions, thereby neglecting transient moisture storage phenomena. It will also be assumed that the geologic medium satisfies, locally, the quasilinear Darcy-Buckingham law with nonlinear pressure-dependent hydraulic conductivity, and that heterogeneity can be represented through spatially correlated, cross-correlated, and statistically anisotropic random field parameters. The premise is, at least initially, that geologic heterogeneity can be represented as a statistical continuum on sufficiently large measurement scales. For a sandy soil, for instance, the continuum scale may be just large enough to encompass a few of the largest pore sizes (cm). For a rock with well-connected fractures (e.g., microfractures), the appropriate continuum scale -- if it exists -- should be larger than the inverse linear density of fracturation.

The next subsection reviews the literature and examines the implications of anisotropy and cross-correlations on unsaturated flow processes from the point of view of field-scale modeling. Following this overview, a two-parameter model of spatially random and statistically anisotropic unsaturated conductivity-pressure curves is formulated, subject to the existence of cross-correlation between intercept and slope. The latter feature accounts for

variable fracturation of the material. Based on this microscale model of unsaturated conductivity, subsequent sections develop a series of closed-form statistical characterizations of power averages, crossing points, and upper envelope of the random set of local conductivity curves. The results of this study will provide a quantitative characterization of the effective behavior of unsaturated flow systems in terms of effective anisotropy, critical suction, and upper-bound envelope conductivity curve, in terms of simple statistical properties of the medium.

6.3.2. Field-Scale Modeling, Anisotropy, and Cross-Correlation

6.3.2.1. Field-Scale Flow Modeling

One possible modeling approach for a statistical continuum is to generate high-resolution numerical simulations of the spatially distributed flow field based on Darcy-type equations involving spatially random microscale parameters. This direct modeling approach requires statistical inputs, which must be inferred from in-situ measurements, observed structural features, analyses of other analogous sites, and so on. For instance, the direct approach has been used in the past for modeling steady groundwater flow under natural gradient conditions, using synthetically generated random fields for saturated conductivity. Multiple Monte-Carlo realizations of saturated flow systems were generated by Smith and Freeze (1979) in one- and two-dimensional space. Large single-realizations of three-dimensional flow systems on the order of one million grid points were numerically generated and statistically analyzed in Ababou (1988) and Ababou et al. (1989).

Unsaturated flow systems have been investigated similarly. Multiple Monte-Carlo simulations of one-dimensional unsaturated flow were generated by Andersson and Shapiro (1983), using random fields for saturated conductivity while other parameters were held constant. More recently, relatively large single realizations of unsaturated flow systems were generated in three-dimensional space by Ababou (1988) and Ababou and Gelhar (1988), and in one-dimensional space by Yeh (1989). For the microscale conductivity curves, these authors used a random two-parameter exponential function of pressure, each parameter being represented as a spatially random field (as will be discussed later).

An alternative to the direct modeling approach is to implement coarser-scale numerical simulations, using "effective" hydrodynamic equations or constitutive properties in order to account for unmodeled, finer-scale heterogeneity. Polman et al. (1991) compared the direct high-resolution approach to an effective "mean flow" model in the case of multidimensional infiltration and drainage, both models being implemented numerically. For effective conductivity, the mean flow model used a unique effective conductivity tensor that depends nonlinearly on pressure head, space-time pressure differentials, and various statistical parameters (Mantoglou and Gelhar, 1987a,b,c). The latter approach is essentially an "equivalent continuum model," which accounts indirectly for the underlying spatial variability of randomly heterogeneous and stratified soils, while avoiding explicit numerical representation of detailed spatial variability. A number of other approaches have been proposed in the literature to model

coarse-scale or subdomain heterogeneity as equivalent homogeneous media, e.g., using ad-hoc pseudo-functions to represent multiphase fluid conductivities in oil reservoir simulations.

Coarse-scale and equivalent continuum approaches require physically based auxiliary models for relating spatially variable microscale properties to effective, coarse-scale flow properties. Moreover, even fine-scale models must ultimately rely on some auxiliary models for subgrid flow processes. Darcy's law is a case in point. Indeed, the usual Darcy-Buckingham equation can be viewed as a submodel that expresses pore-scale flow processes in terms of continuum variables at the scale of the REV, or Representative Elementary Volume (Bear, 1972). The advantage of this approach is that the Darcy-Buckingham model has been extensively tested at the laboratory scale, particularly for granular media and soils. However, a fine-scale simulation approach may or may not be computationally feasible, depending on the assumed degree of heterogeneity, the presence or absence of fissures, and the space-time scales of interest. On the other hand, while coarse-scale effective models should be less demanding computationally, they require auxiliary models for expressing the relation between fine- and coarse-scale flow behavior in the presence of heterogeneity.

The development of reliable and physically meaningful subscale models requires careful analyses of heterogeneous flow phenomena based on realistic representations of diverse geologic heterogeneities, not necessarily arranged in simple periodic patterns. This is a particularly difficult task in the case of unsaturated flow processes, which are inherently nonlinear. A statistical continuum representation of three-dimensional heterogeneity can serve as a starting point, first, to identify those spatial-statistical features that are likely to play a significant role in unsaturated hydrodynamics and second, to investigate their effects on the overall behavior of unsaturated flow systems. It will be shown in particular that two factors are likely to play an important role: anisotropy, and cross-correlation among hydraulic conductivity parameters.

6.3.2.2. Statistical Anisotropy

Recent analytical and numerical studies of multidimensional unsaturated flow indicate that random stratification and layering of soils causes, overall, a pressure-dependent anisotropic behavior of unsaturated flow (Yeh et al., 1985a,b,c; Mantoglou and Gelhar, 1987a,b,c; Ababou, 1988, Chap. 7; and Polman et al. 1991). This phenomenon is manifested in the functional form of the resulting effective conductivity tensor obtained by approximate analytical solutions, and in observations on the spreading patterns of transient moisture plumes obtained by direct numerical experiments. In addition, this anisotropic behavior appears to be corroborated by various field observations reported in Gelhar et al. (1984) and Ababou (1991), as well as by in-situ infiltration experiments (Wierenga et al., 1988; McCord et al., 1991), and by multidimensional laboratory experiments (Stephens and Heerman, 1988). More generally, anisotropic spatial structures are known to occur not only in soils but also in other types of geologic formations. Thus, large-scale anisotropy can be due to the stratification of sedimentary deposits, as in the case of the Borden aquifer (Sudicky, 1986), or to oriented

patterns of fracturation, as observed at the Oracle granite site (Hsieh et al., 1983; Depner and Neuman, 1988).

6.3.2.3. Cross-Correlation

Parameters used to describe the relation between unsaturated conductivity and pressure, such as saturated conductivity and "slope" of relative conductivity curve, are likely to be significantly cross-correlated in the presence of fracture-like heterogeneities. In their numerical experiments, Ababou (1988, Chap. 7) and Yeh (1989) considered the case of a random two-parameter conductivity-pressure curve, with random field properties assigned to both K_s, the saturated conductivity, and α, the slope of log-conductivity versus pressure. Comparing the cases of perfect correlation and perfect independence between the two parameters, Ababou (1988, Chap. 7) found a significant sensitivity of simulated three-dimensional moisture plumes to the presence or absence of cross-correlation. It was also found that a moderate coefficient of variation in the α-parameter can produce highly heterogeneous moisture plumes. The uncorrelated case produced the most heterogeneous moisture patterns. Similar conclusions were reached by Yeh (1989), based on a more detailed one-dimensional analysis of the perfectly correlated and uncorrelated cases, through comparisons with analytical results by Yeh et al. (1985a,b,c).

However, no analysis is available for the more general case of imperfect cross-correlation. A two-parameter model of spatially random and statistically anisotropic unsaturated conductivity curves, which accounts in a simple way for cross-correlation between intercept and slope, is described in the next section.

6.3.3. Cross-Correlated, Two-Parameter Random Conductivity Model

The proposed random field model of unsaturated conductivity, described below, is an extension of the random exponential model previously introduced by Yeh et al. (1985a,b,c), Mantoglou and Gelhar (1987a,b,c), Ababou (1988), and Yeh (1989) in their analytical and numerical studies of stochastic unsaturated flow. In this section, the new conductivity curve model is defined and discussed in terms of its spatial-statistical properties.

Let h designate the water pressure head relative to atmospheric pressure, and $\Psi = -h$ the suction head (meters). As in the above-mentioned references, the spatially random, nonlinear unsaturated conductivity is assumed to be of the form:

$$\mathbf{K(\Psi(x),x) = K_S \exp(-\alpha(x)\Psi(x))} \qquad \textbf{(6-1a)}$$

where $K_s(\mathbf{x})$ is saturated conductivity, defined by

$$\mathbf{K_S(x) = K(0,x)} \quad , \qquad \textbf{(6-1b)}$$

and $\alpha(\mathbf{x})$ is the log-conductivity slope, defined by

$$\alpha(\mathbf{x}) = \left.\frac{\partial \ell n K(\Psi,\boldsymbol{x})}{\partial \Psi}\right|_{\boldsymbol{x}} \quad . \tag{6-1c}$$

Note that K, K_s, and α are all positive quantities. The logarithms of these quantities are well defined and range from $-\infty$ to $+\infty$, whereas the range of the untransformed quantities is 0 to $+\infty$. For this reason, the probability distributions of the logarithms are expected to be less skewed, and therefore more nearly symmetric, than the untransformed quantities. The log-conductivity curve can be expressed as:

$$\mathrm{Y}(\Psi,\mathbf{x}) = F(\boldsymbol{x}) - \exp(A(\boldsymbol{x}))\Psi \tag{6-2}$$

where $\mathrm{Y}(\psi,\mathbf{x}) = \ell n\{\mathrm{K}(\psi,\mathbf{x})\}$, $\mathrm{F}(\mathbf{x}) = \ell n\{\mathrm{K_s}(\mathbf{x})\}$, and $\mathrm{A}(\mathbf{x}) = \ell n\{\mathrm{a}(\mathbf{x})\}$. In Eqn. (6-2), both the saturated log-conductivity F and the log-slope A are assumed to be spatially correlated random functions of space. Conductivity curves can be represented as a family of intersecting straight lines in a semilog graph (see ensuing discussion of crossing points and envelopes).

The conductivity model, as described so far, possesses two notable features. First, the log-transform of unsaturated conductivity is a simple linear function of suction (Ψ), with random intercept (F) and random slope [$\exp(A)$] at each point in space. The linear dependence of log-conductivity versus pressure approximates experimental conductivity curves quite well for intermediate ranges of pressure, but breaks down near saturation and at large negative pressures (for a more complete discussion, see Ababou, 1991, Section 4.3). Nevertheless, the proposed exponential conductivity function can be generalized by allowing the log-conductivity slope to be mildly pressure dependent in order to better fit data within large ranges of pressures. Second, since the random log-conductivity slope is assumed to be of the form $\exp(A)$, it will never take negative values. This is in accordance with the intuitively reasonable requisite that conductivity always increases in a wetting porous medium.

In principle, to completely define the random conductivity curves requires specifiying all moments of the joint probability distribution of the random field parameters $F(\boldsymbol{x})$ and $A(\boldsymbol{x})$. Assuming however that (F,A) are jointly gaussian random fields, only their means and two-point cross-covariances, or covariance tensor, need to be specified. Field measurements of hydrodynamic soil properties indicate that K_s and α are separately log-normal, although some authors assumed normality in cases where coefficients of variations were to small too distinguish normal from log-normal (Ababou, 1991, Section 5.3). Based on this observation, the jointly gaussian hypothesis for the log-parameters $F = \ell n K_s$ and $A = \ell n \alpha$ is adopted here. Furthermore, a special class of jointly gaussian random fields is introduced in order to further reduce the number of statistical parameters while retaining crucial features such as spatial correlations and cross-correlations. A linear combination approach is chosen, as previously suggested by Ababou

[1988, Chap. 7, Eqn. (7.7)]. First, each of the gaussian random field parameters is decomposed as follows:

$$\mathrm{F}(\mathbf{x}) = \bar{F} + f(\boldsymbol{x}) \tag{6-3a}$$

$$\mathrm{A}(\mathbf{x}) = \bar{A} + a(\boldsymbol{x}) \tag{6-3b}$$

where $(\bar{A},\bar{F})$ are the ensemble means and $(a(\boldsymbol{x}),f(\boldsymbol{x}))$ are the zero-mean random field perturbations of $A(\boldsymbol{x})$ and $F(\boldsymbol{x})$. The desired model is obtained by choosing $a(\boldsymbol{x})$ to be a linear combination of two independent replicates of $f(\boldsymbol{x})$. Let for instance $g(\boldsymbol{x})$ be a normally distributed zero-mean unit-variance random field, having the same stationary correlation structure as $f(\boldsymbol{x})$. Then, construct $f(\boldsymbol{x})$ and $a(\boldsymbol{x})$ from two independent replicates $g_1(\boldsymbol{x})$ and $g_2(\boldsymbol{x})$ of $g(\boldsymbol{x})$, as shown below:

$$\mathrm{f}(\mathbf{x}) = \sigma_f \, g_1(\mathbf{x}) \tag{6-4a}$$

$$\mathrm{a}(\mathbf{x}) = \sigma_a(\rho g_1(\mathbf{x}) + \sqrt{1-\rho^2} g_2(\mathbf{x})) \quad . \tag{6-4b}$$

It follows that A and F are jointly gaussian. Furthermore, their joint covariances $<\mathrm{a}(\mathbf{x})\mathrm{a}(\mathbf{x}')>$, $<\mathrm{f}(\mathbf{x})\mathrm{f}(\mathbf{x}')>$, $<\mathrm{a}(\mathbf{x})\mathrm{f}(\mathbf{x}')>$, depend only on the two-point lag vector $\xi=\boldsymbol{x}'-\boldsymbol{x}$ by virtue of statistical homogeneity, and together they form a cross-covariance tensor which takes the special form:

$$\mathrm{R}_{af}(\xi) = \begin{bmatrix} \mathrm{R}_{aa}(\xi) & \mathrm{R}_{af}(\xi) \\ \mathrm{R}_{fa}(\xi) & \mathrm{R}_{ff}(\xi) \end{bmatrix} = \begin{bmatrix} \sigma_a^2/\sigma_{f_2} & \rho\,\sigma_a/\sigma_f \\ \rho\,\sigma_a/\sigma_f & 1 \end{bmatrix} \mathrm{R}_{ff}(\xi) \quad . \tag{6-5}$$

The proposed statistical model of unsaturated conductivity, as described by Eqns. (6-2, -4 and -5), is relatively parsimonious and tractable, while accommodating several complex features of natural heterogeneity. Note that only one spatial covariance function, $R_{ff}(\xi)$, is needed to describe the joint spatial structure of suction-dependent conductivity curves. An anisotropic covariance function can be selected in order to reflect preferred orientations in texture or structure. On the other hand, the constant correlation coefficient, ρ, uniquely characterizes the cross-correlation between random field parameters $A(\boldsymbol{x})$ and $F(\boldsymbol{x})$.

The existence of positive cross-correlation is supported by the intuitive notion that the conductivity of coarser granular and fractured materials tends to decrease faster as they desaturate. The positive correlation hypothesis seems particularly well suited to the case of densely fractured media. Where larger apertures occur, there will be an increase of saturated conductivity and a simultaneous decrease of the value of capillary suction head below which

fissures desaturate and become nonconductive. Averaging over many fractures and applying scale analysis indicate that the latter phenomenon has indeed the effect of steepening the slope of log-conductivity versus suction (Ababou, 1991).

6.3.4. Power Averages and Effective Conductivities

In this section, various types of averages taken over the ensemble of random conductivity curves are analyzed and interpreted as effective conductivities. An entire class of average conductivity curves, including arithmetic, geometric, and harmonic means, can be computed using log-normal power-averaging formulas similar to those given by Ababou and Wood (1990) and Ababou (1990) for stochastic groundwater flow. These power averages will be used to infer, in particular, the approximate effective anisotropic behavior of unsaturated flow in highly stratified media.

The parametrized family of power-averaged conductivity curves is defined by:

$$K_p(\Psi) = \langle K(\Psi,\mathbf{x})^p \rangle^{1/p} \qquad (6\text{-}6)$$

where the parameter p is the exponent or averaging power, satisfying $-1 \leq p \leq +1$. The ensemble average operator $\langle . \rangle$ can be interpreted in two ways. One possible interpretation is that the average is taken over random variations of conductivity curves due solely to the randomness of its cross-correlated parameters K_s and α, while holding suction Ψ fixed. The resulting average is universal in that it does not involve solution of a specific flow problem. The second interpretation is that the average is taken over random variations of suction as well as parameters. The latter interpretation requires more complex calculations based on solution of stochastic unsaturated flow equations under specific mean flow conditions. As shown below, the power averages, obtained by holding suction fixed inside the averaging operator, yield approximate effective conductivities for steady-state unsaturated flow systems.

In highly stratified geologic formations, the arithmetic and harmonic means, $p = +1$ and $p = -1$, yield approximate effective conductivity components along directions parallel and orthogonal to bedding, respectively. This idea has been previously advocated by Zaslavsky and Sinai (1981) and Mualem (1984), based on simplified nonlinear models of unsaturated flow anisotropy. Briefly, consider the case of a perfectly stratified soil with very thin horizontal layers such that the conductive properties of each layer are statistically independent from other layers (Figure 6-1). By the Darcy-Buckingham equation, water flux in the horizontal (X) and vertical (Z) directions is given by:

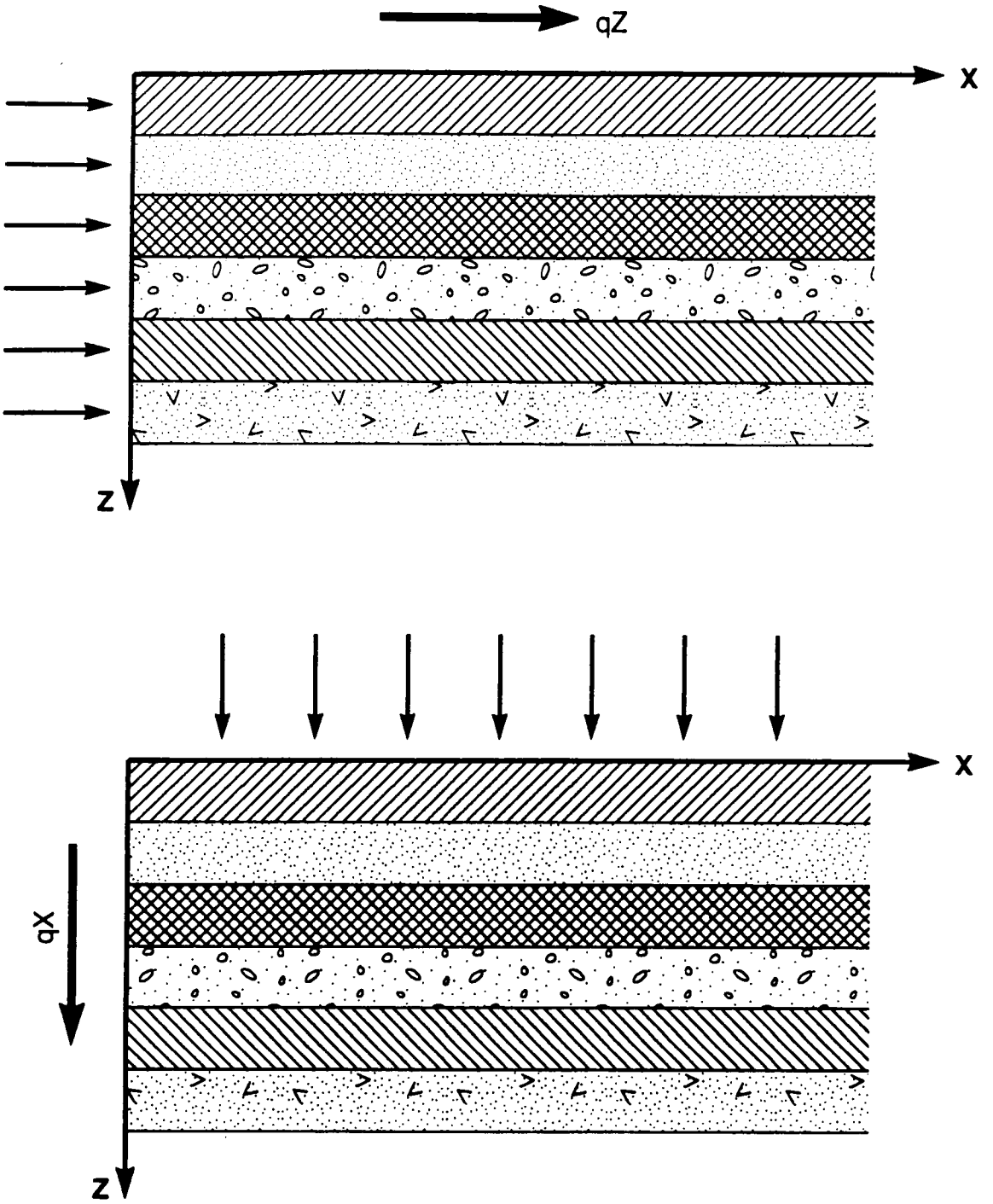

Figure 6-1. Sketch of horizontal flow (above) and vertical flow (below) in perfectly layered soil. Conductivity parameters are spatially independent across layers, but are cross-correlated; i.e., not independent of each other.

$$q_X = K(\Psi,Z)\ J_X$$
$$q_Z = K(\Psi,Z)\ J_Z \qquad \textbf{(6-7)}$$

where **J** represents the hydraulic gradient vector:

$$J_X = \frac{\partial \Psi}{\partial X}$$
$$J_Z = \frac{\partial \Psi}{\partial Z} + 1 \quad . \qquad \textbf{(6-8)}$$

To ensure mass conservation, the steady-state flux vector must also satisfy:

$$\frac{\partial q_X}{\partial X} + \frac{\partial q_Z}{\partial Z} = 0 \quad . \qquad \textbf{(6-9)}$$

For horizontal flow, $q_Z=0$, which implies that $q_X=q_X(Z)$. Averaging q_X vertically over all layers and neglecting the average of the product of perturbations of conductivity and hydraulic gradient around their means yield $<q_X> \approx <K><J_X>$ where the symbol $<.>$ designates vertical averaging. This approximation is accurate if the conductivity and horizontal gradient are not well correlated vertically. The horizontal effective conductivity resulting from this approximation is an arithmetic average.

For vertical flow, $q_X=0$, which implies that $q_Z=q_Z(X)$. Since the product $K(\psi,Z)J_Z=q_Z$ is constant over depth, there must be some statistical dependence of conductivity and vertical gradient among the different layers. Therefore, instead of averaging flux, the gradient $J_Z=q_Z/K$ is now averaged vertically over all layers at each fixed location X. Note that $<q_Z>=q_Z$. This gives $<q_Z> = <K^{-1}>^{-1}<J_Z>$ where the symbol $<.>$ represents again depth-averaging. In conclusion, the resulting effective conductivity is a harmonic average.

More generally, the power-average model proposed above allows the exponent p to take values in the whole interval $[-1,+1]$, in addition to the two extreme values $\{-1,+1\}$. This observation leads to a useful generalization of the above-mentioned perfectly stratified approximations of Mualem (1984). A first step towards such generalization is, for instance, to recognize that the geometric mean ($p = 0$) can provide an approximate estimate of effective conductivity for a nonstratified, structurally isotropic formation. In the case of groundwater flow, the geometric mean of random saturated conductivity is actually known to be the exact effective conductivity for statistically isotropic and symmetric log-conductivity distributions. Furthermore, Ababou (1990) indicates that a good approximation to the ith-component of effective saturated conductivity in random anisotropic media is given by the power-average Kp_i,

where p_i depends uniquely on space dimension D, fluctuation length or correlation length ℓ_i, and harmonic mean length scale ℓ_h, according to the equation: $p_i = 1 - 2D^{-1}\ell_H/\ell_i$. In the case of isotropic bedding in the x-y plane, this yields: $p_x = p_y = 1/(2\ell_z/\ell_x + 1)$ and $p_z = (2\ell_z/\ell_x - 1)/(2\ell_z/\ell_x + 1)$. And, in the limit $\ell_z/\ell_x \to 0$, this yields as before an arithmetic average for conductivity parallel to the x-y plane, and a harmonic average along the orthogonal direction z.

These considerations suggest that similar expressions among averaging power, correlation scales, and space dimension, may exist for *unsaturated* effective conductivities as well. However, such relations are not derived here. Instead, the focus is on the special cases of isotropy and perfect stratification, assuming that the geometric, arithmetic, and harmonic means provide sufficient approximations to unsaturated effective conductivity in these situations. It should be cautioned that the proposed power averages are approximate "zero-order" estimates of effective conductivities. More accurate calculations of effective conductivity curves would require taking into account the full three-dimensional interactions between random fluctuations of conductivity and hydraulic gradient occuring in the nonlinear Darcy equation, $q = K(\Psi,x)\{\nabla\Psi + 1\}$. These calculations have been achieved by Yeh et al. (1985) and Mantoglou and Gelhar (1987), based on first order perturbation and linearization approximations. Closed form expressions of effective conductivities are confined to the case of perfect stratification and complete independence of K_s and α, whereas the alternative approach proposed here treats the more general case of imperfect cross-correlation ($-1 \le \rho \le +1$). The alternative expressions developed will be compared to the stochastic closed form solutions of Yeh, Mantoglou, and Gelhar in cases where these are available (see below).

6.3.5. Suction-Dependent Effective Conductivities and Anisotropy Ratios

The suction-dependent effective conductivity components for the two special cases of (1) structurally isotropic and (2) perfectly stratified geologic formations are now being evaluated explicitly. As explained earlier, averages are computed by holding suction fixed inside the averaging operator. In all cases, the existence of cross-correlation (ρ) between the intercept and slope of the local log-conductivity curves is taken into account.

6.3.5.1. Isotropic Case ($p=0$)

As explained earlier, the isotropic effective conductivity is approximated by the geometric mean conductivity curve, $K_G(\Psi)$. The geometric mean can be obtained in closed form by calculating the arithmetic mean of the log-conductivity curve [Eqn. (6-2)] and taking the exponential transform. The result is:

$$K_G(\Psi) = \exp\{\langle Y(\Psi,x)\rangle\} = K_G \exp\left\{-\alpha_G \exp(\sigma_A^2/2)\Psi\right\} \qquad \textbf{(6-10a)}$$

where the second equality follows from Eqns. (6-2a), (6-4b), and from the identities $\langle a\rangle = \langle g_1\rangle = \langle g_2\rangle = \langle g_1 g_2\rangle = 0$ and $\langle \exp(a)\rangle = \exp(\sigma_A^2/2)$. Subscript "$G$" in K_G

designates a geometric mean. Note that Eqn. (6-10a) is exact for fixed suction, regardless of how accurately it approximates the true effective conductivity curve of isotropic media. However, since a linearization approximation will be ultimately required for obtaining closed form results in the case $p \neq 0$, the corresponding linearized approximation for $K_G(\Psi)$ is:

$$K_G(\Psi) \approx K_G \exp\{-\alpha_G \Psi\} + O(\sigma_A^2) \quad . \tag{6-10b}$$

The previous results can also be expressed in terms of effective saturated conductivity and effective slope, as follows:

$$\begin{aligned} \hat{K}(\Psi) &\approx \hat{K}(0)\exp\{\hat{\alpha}\Psi\} \\ \hat{K}(0) &= K_G \\ \hat{\alpha} &= \alpha_G \exp(\sigma_A^2/2) \approx \alpha_G(1+O(\sigma_A^2)) \quad . \end{aligned} \tag{6-10c}$$

In view of this result, it is concluded that the (approximate) effective conductivity curve is independent of the cross-correlation coefficient ρ in the case of structurally isotropic media. As will be seen, this is no longer true in the anisotropic case.

6.3.5.2. Nonisotropic Case ($p \neq 0$)

For exponents other than $p=0$, the power-averaged conductivity curve can be calculated by inserting the log-conductivity of Eqn. (6-2) into Eqn. (6-6). Keeping Eqns. (6-4) in mind, this yields ($p \neq 0$):

$$K_p(\Psi) = \left\langle \exp\left\{p\left[\ln K_G + f(\mathbf{x}) - \alpha_G \exp(a(\boldsymbol{x}))\Psi\right]\right\}\right\rangle^{1/p} \quad . \tag{6-11a}$$

However, note that this equation involves the average of a double-exponential function of a gaussian variable. For ease of calculation, the right-hand side expression is now approximated by a simple exponential, based on the linearization:

$$\exp(a(\mathbf{x})) \approx 1 + a(\boldsymbol{x}) + O(a(\boldsymbol{x})^2) \quad . \tag{6-11b}$$

This approximation is quite accurate if $\sigma_A \ll 1$ (say $\sigma_A \leq 0.1$), and is still acceptable even if σ_A is a sizeable fraction of unity (say $\sigma_A \leq 0.5$). A review of available field data (Ababou, 1991, Section 5.3) indicates that σ_A is indeed quite moderate for unsaturated soils: the coefficient of variation of α is generally less than 0.5, which is roughly equivalent to $\sigma_A \leq 0.5$. Inserting the linearized exponential (6-11b) in Eqn. (6-11a) yields:

$$K_p(\Psi) \approx \left\langle \exp\left\{p\left[\ln K_G + f(\mathbf{x}) - \alpha_G (1 + a(\boldsymbol{x}))\Psi\right]\right\}\right\rangle^{1/p} \quad . \tag{6-11c}$$

The random quantity that directly affects the power-averaged conductivity, according to Eqn. (6-11c), is the slope multiplied by suction. The coefficient of variation of the latter quantity can

be much higher than 100 percent in the case of large suction Ψ, even when σ_A is moderate or small. We conclude that the linearization approximation remains valid in the case of large conductivity variability due to large suction Ψ. The resulting power-averaged conductivity should be a good approximation of the exact power average (with fixed suction).

The average in Eqn. (6-11c) is now evaluated in closed form based on the following statistical identities. Rewriting the approximate Eqn. (6-11c) in the form:

$$K_p(\Psi) \approx \langle \exp(pZ(x)) \rangle^{1/p} \tag{6-11d}$$

and observing that

$$Z(x) = \ell_n K_G + f(x) - d_G(1 + a(x))\Psi \tag{6-11e}$$

is a gaussian random field (Ababou and Wood 1990):

$$K_p(\Psi) \approx \exp\left\{ \langle Z \rangle + \frac{1}{2} p \, \mathrm{Var}(Z) \right\} \tag{6-11f}$$

$$\langle Z \rangle = \ell n K_G - \alpha_G \Psi \tag{6-11g}$$

$$\begin{aligned} \mathrm{Var}(Z) &= \langle (f(x) - \alpha_G \psi a(x))^2 \rangle \\ &= \langle f(x)^2 \rangle - 2\alpha_G \psi \langle f(x) a(x) \rangle + \alpha_G^2 \psi^2 \langle a(x)^2 \rangle \\ &= \sigma_F^2 - 2\rho \alpha_G \sigma_A \sigma_F \Psi + \alpha_G^2 \sigma_A^2 \Psi^2 \end{aligned} \tag{6-11h}$$

The final result for the power-averaged conductivity curve is therefore:

$$K_p(\Psi) \approx K_G \exp\left\{ \frac{1}{2} \left[p\sigma_F^2 - 2\alpha_G \Psi (1 + \rho p \sigma_A \sigma_F) + p\sigma_A^2 \alpha_G^2 \Psi^2 \right] \right\} \tag{6-11i}$$

where the approximate character of the relation is entirely due to the linearization of Eqn. (6-11b). With this proviso, Eqn. (6-11i) holds for all values of the exponent p in the $[-1, +1]$ interval. Moreover, comparing Eqns. (6-11i) and (6-10b), the first-order geometric mean conductivity is recovered in the limit $p \to 0$.

6.3.5.3. Perfectly Stratified Case ($p=\pm 1$)

In the special case of structurally anisotropic, perfectly stratified formations, the parallel (X) and orthogonal (Z) components of effective conductivity can be expressed as follows. For the parallel component (arithmetic mean $p=+1$):

$$\begin{aligned} \hat{K}_X(\Psi) &\approx \hat{K}_X(0)\exp\left\{-\hat{\alpha}_X(\Psi)\Psi\right\} \\ \hat{K}_X(0) &= K_G\exp\left(+\frac{1}{2}\sigma_F^2\right) = \langle K_s(x)\rangle \\ \hat{\alpha}_X(\Psi) &= \alpha_G\left[1-\frac{1}{2}\sigma_A^2(\alpha_G\Psi-2\rho\sigma_F/\sigma_A)\right] \quad . \end{aligned} \tag{6-12a}$$

And, for the orthogonal component (harmonic mean $p=-1$):

$$\begin{aligned} \hat{K}_Z(\Psi) &\approx \hat{K}_Z(0)\exp\left\{-\hat{\alpha}_Z(\Psi)\Psi\right\} \\ \hat{K}_Z(0) &= K_G\exp\left(-\frac{1}{2}\sigma_F^2\right) = \langle K_s(x)^{-1}\rangle^{-1} \\ \hat{\alpha}_Z(\Psi) &= \alpha_G\left[1+\frac{1}{2}\sigma_A^2(\alpha_G\Psi-2\rho\sigma_F/\sigma_A)\right] \quad . \end{aligned} \tag{6-12b}$$

Unlike the isotropic case, the correlation coefficient ρ affects each component of effective conductivity. Recall that ρ characterizes the degree of correlation between saturated conductivity and slope. Its influence is analyzed below, particularly with regard to anisotropy.

The effective anisotropy ratio is defined here as the ratio of parallel to orthogonal components of effective conductivities, that is:

$$A_{XZ}(\Psi) = \hat{K}_X(\Psi)/\hat{K}_Z(\Psi) \quad . \tag{6-13a}$$

Substituting Eqns. (6-12) in (6-13a) yields:

$$A_{XZ}(\Psi) \approx \exp\left\{\sigma_F^2+\alpha_G\sigma_A^2\left[\alpha_G\Psi-2\rho\sigma_F/\sigma_A\right]\Psi\right\} \quad . \tag{6-13b}$$

Equivalently, in terms of dimensionless suction:

$$\psi = \alpha_G\Psi \quad . \tag{6-13c}$$

The anisotropy ratio can also be expressed as:

$$A_{XZ}(\psi) \approx \exp\left\{\sigma_F^2+\sigma_A^2\left[\psi-2\rho\,\sigma_F/\sigma_A\right]\psi\right\} \quad . \tag{6-13d}$$

Note that the anisotropy ratio is a nonlinear function of suction. Moreover, the logarithm of the anisotropy ratio is a quadratic function of suction, as are the individual components of effective log conductivities. In contrast, the local log-conductivity model is a linear function of suction [Eqn. (6-2)].

Focus on the case of positively cross-correlated parameters, which has more physical relevance than the anti-correlated case. Assuming $\rho \geq 0$ in Eqn. (6-13d) leads to the existence of a minimum anisotropy ratio. Indeed, the *critical suction* where this minimum occurs, ψ_0, can be evaluated by differentiating the log transform of Eqn. (6-13d). For $\rho \geq 0$, this yields in dimensionless terms:

$$\psi_0 = \frac{\sigma_F}{\sigma_A}\rho \quad ; \tag{6-14}$$

and the corresponding minimum value of the anisotropy ratio is

$$A_0 \approx \exp\left\{\sigma_F^2\left[1-\rho^2\right]\right\} \quad . \tag{6-15}$$

The individual components of effective conductivity follow a similar pattern. It can be seen from Eqns. (6-12a)-(6-12b) that each log-conductivity component is quadratic in ψ. The parallel component $\hat{K}_X$ goes to infinity, as $\psi \to \infty$ can artifact due to approximations [also present in the results developed by Yeh et al. (1985) and Mantoglou and Gelhar (1987)], and has a local minimum at a value of suction that is always larger than critical function, namely,

$$\psi_x = \frac{\rho\,\sigma_F\sigma_A+1}{\sigma_A^2} \quad . \tag{6-16a}$$

On the other hand, the orthogonal component $\hat{K}_Z$ goes to zero as $\psi \to \infty$. If $\rho\sigma_A\sigma_F \leq 1$, it is a monotonically decreasing function of suction. Otherwise, if $\rho\sigma_A\sigma_F \geq 1$, it has a local maximum at

$$\psi_z = \frac{\rho \sigma_F \sigma_A - 1}{\sigma_A^2} \quad . \tag{6-16b}$$

Finally, note that the minimum anisotropy ratio, A_0, decreases with ρ, while the corresponding critical suction, ψ_0, increases linearly with ρ. For the case of perfect correlation, $\rho = 1$, we obtain $A_0 \approx 1$ and $\psi_0 \approx (\sigma_F/\sigma_A)$. On the other hand, the minimum anisotropy ratio increases with σ_F, occurs at smaller suctions as σ_A increases, becomes flatter as σ_A decreases, and remains greater than unity in all cases.

6.3.5.4. Comparisons with Higher-Order Effective Conductivities

The previous calculations of effective conductivities ignored the effects of random suction fluctuations, since suction was held fixed in the power-averaging operator. In fact, the previous results can be interpreted in terms of mean suction, $<\psi>$. This can be seen by inserting $\psi = <\psi> + \delta\psi$, and carrying on the averaging operations with $<\psi>$ fixed and $\delta\psi$ an unknown zero-mean random field perturbation of suction. The resulting power averages would now contain an additional second-order perturbation term of the form $<\delta\alpha(\mathbf{x})\delta\psi(\mathbf{x})>$. This single-point covariance is small if (1) the variability of α is small or (2) the suction field is poorly correlated to α. To evaluate this term requires solving a stochastic flow equation for suction perturbations for prescribed mean hydraulic gradient, based on Darcy-Buckingham and mass conservation laws. In fact, the latter approach can lead directly to effective conductivities without assuming a particular form of power averaging (Yeh at al., 1985, and Mantoglou and Gelhar, 1987). It is therefore instructive to compare the present results with theirs, since they take into account the interaction term $<\delta\alpha(\mathbf{x})\delta\psi(\mathbf{x})>$ whereas this analysis does not.

The above-mentioned authors give closed-form solutions for unsaturated effective conductivity in the case of perfectly uncorrelated parameters ($\rho=0$) and perfect stratification corresponding to vanishing vertical correlation scale ($\lambda_Z=0$). In their calculations, they treated α as a normal rather than log-normal random field. Nevertheless, equivalent statistics can be obtained by replacing their mean $<\alpha>$ by the geometric mean α_G, and their standard deviation σ_α by $\alpha_G\,\sigma_s$, at least for moderate coefficient of variation of α. Comparing their effective conductivities to Eqns. (6-12a)-(6-12b)-(6-13b) with $\rho=0$, both results can be expressed in the form:

$$K_{XX}(\psi) = K_G \exp\{\frac{1}{2}\sigma_F^2 - \psi + \frac{(1+\epsilon)}{2} \sigma_A^2 \psi^2\} \quad (6\text{-}17)$$

$$K_{ZZ}(\psi) = K_G \exp\{-\frac{1}{2}\sigma_F^2 - \psi - \frac{(1+\epsilon)}{2} \sigma_A^2 \psi^2\} \quad (6\text{-}18)$$

$$A_{XZ}(\psi) = \frac{K_{XX}(\psi)}{K_{ZZ}(\psi)} = \exp\{\sigma_F^2 + \sigma_A^2 \psi^2\} \quad (6\text{-}19)$$

where $\epsilon=0$ for the stochastic perturbation solution expressed in terms of mean suction and $\epsilon=1$ for the power-average result expressed in terms of fixed suction (dimensionless suction is denoted by ψ in both cases). At large dimensionless suctions, where the quadratic term becomes large, the power-average result tends to overestimate horizontal conductivity and to underestimate vertical conductivity. Nevertheless, the basic functional forms are the same in both cases; and most importantly, the suction-dependent anisotropy ratio predicted by the power-averaging method is identical to that predicted by the stochastic perturbation approach.

The foregoing comparisons with other stochastic solutions indicate that the power-averaging results, which yield simple closed-form expressions for all values of the cross-correlation coefficient, are representative of the functional behavior of anisotropic effective conductivities in highly stratified media.

6.3.5.5. Summary and Discussion on Effective Conductivity

To recap, this section analyzed the effective conductivity of perfectly isotropic and perfectly stratified unsaturated formations in the presence of cross-correlation between intercept and slope of local log-conductivity functions. The power-averaging approach used here ignores fluctuations of suction in computing effective conductivities. Based on comparisons with perturbation solutions of the full stochastic flow equations in the case of perfect stratification and uncorrelated parameters, the results obtained by using power averages with fixed suction appear similar, albeit not identical, to the more complete perturbation approach. In the general case of nonzero correlation, the results obtained by the power-averaging approach can be summarized as follows.

For perfectly isotropic media, the effective conductivity does not depend on the correlation coefficient. For perfectly stratified media, the effective conductivity is anisotropic, and each component depends on the correlation coefficient. The log components of effective conductivity parallel and othogonal to stratification are quadratic functions of suction, unlike the local log-conductivity curves, which vary linearly with suction [Eqn. (6-2)]. The slope of the parallel component of effective log conductivity is a decreasing function of

suction. This has the effect of enhancing parallel flow at large suctions, compared to what a simple average of the microscale conductivity would predict. On the other hand, the slope of the orthogonal component of effective log conductivity increases with suction, which has the effect of impeding orthogonal flow at large suctions. Finally, the parallel-to-orthogonal anisotropy ratio is a function of suction and has a local minimum at $\Psi = \Psi_o$ for any positive value of the correlation coefficient, ρ. As will be seen in the next section, the critical suction Ψ_o that minimizes effective anisotropy ratio is also related to the cluster of crossing points of local conductivity curves.

6.3.6. Critical Suction and Crossing Point Cluster

In this section, the conductive behavior of the unsaturated medium is characterized in terms of crossing points, or intersections between individual realizations of the local conductivity-suction curves. For significantly positive cross-correlation coefficients, we will show in particular that there exists a relatively dense crossing-point cluster at a certain suction, ψ_1, that minimizes the statistical dispersion of conductivity values, $K(\psi,x)$. It turns out that ψ_1 is closely related to the suction ψ_0 that minimizes the effective conductivity anisotropy ratio.

In order to identify a dense cluster of crossing points, it is convenient to seek the value of suction, ψ_1, that minimizes the variance of the log-conductivity perturbation around its mean. As before, suction is fixed when computing conductivity curve statistics; the results obtained in this fashion will characterize the conductive behavior of the medium in a generic way, without reference to any particular flow system. If a minimum variance exists and is exactly zero, the cluster is reduced to a single crossing point where all conductivity curves intersect. As will be seen, there is no case that produces such a perfect crossing point. If minimal variance exists and is strictly positive, a cluster of crossing points results, centered at suction ψ_1 and such that the dispersion of conductivity values is mimimal at that suction. This cluster is the statistical equivalent of a crossing point; however, for a meaningful interpretation of results, the dispersion of the cluster must be evaluated as well (is it crisp or fuzzy?). Finally, in the case where no local minimum exists for any positive suction, it would have to be concluded that there is no distinguishable crossing-point cluster.

Let Y be the unsaturated log conductivity as in Eqn. (6-2), and let y be its perturbation around the mean:

$$y(\psi,\mathbf{x}) = Y(\psi,\boldsymbol{x}) - \bar{Y}(\psi) \tag{6-20}$$

where $\bar{Y}(\psi) = \ell n K_G(\psi)$. The geometric mean conductivity was computed previously, and the exact expression is given by Eqn. (6-10a). Inserting Eqns. (6-2), (6-3), and (6-10a) in Eqn. (6-20) yields, in terms of dimensionless suction:

$$y(\psi,\mathbf{x}) = f(\boldsymbol{x}) - \left[\exp\{a(\boldsymbol{x})\} - \exp\{\sigma_A^2/2\}\right]\psi \tag{6-21}$$

where (a,f) are the jointly gaussian zero-mean random fields defined by Eqns. (6-4) and (6-5).

The variance $\sigma_y^2(\psi) = \mathrm{Var}\{y(\psi,\boldsymbol{x})\}$ can now be computed as follows. Squaring Eqn. (6-21) and taking the ensemble mean yield the intermediate result:

$$\sigma_y^2(\psi) = \mathrm{Var}\{e^a\}\psi^2 - 2\langle f e^a\rangle\psi + \mathrm{Var}\{f\} \tag{6-22}$$

where we used $\langle f\rangle = \langle a\rangle = 0$ and the following identities (Vanmarcke, 1983):

$$\langle \exp(a)\rangle = \exp(\sigma_A^2/2) \tag{6-23a}$$

$$\mathrm{Var}\{\exp(a)\} = \exp(2\sigma_A^2) \quad . \tag{6-23b}$$

In addition, the mixed covariance $\langle f\, e^a\rangle$ must be evaluated. Skipping some tedious calculations, the final result is given by

$$\langle f(\mathbf{x})\exp(a(\boldsymbol{x}))\rangle = \langle \exp(a(\boldsymbol{x}))\rangle \langle f(\boldsymbol{x})a(\boldsymbol{x})\rangle \quad . \tag{6-24}$$

Furthermore, using the cross-correlation structure defined by Eqn. (6-4) yields $\langle f(\boldsymbol{x})a(\boldsymbol{x})\rangle = \rho\sigma_A\sigma_F$. Therefore, the desired expression of log-conductivity variance is, finally

$$\sigma_y^2(\psi) = \exp(\sigma_A^2)\{\exp(\sigma_A^2) - 1\}\psi^2 - 2\rho\sigma_A\sigma_F\exp(\sigma_A^2/2)\psi + \sigma_F^2 \quad . \tag{6-25}$$

Note that the log-conductivity variance [Eqn. (6-25)] is a quadratic function of suction. Thus, using as before the notation $\psi = \alpha_G \Psi$ for dimensionless suction, Eqn. (6-25) can be expressed in the compact form

$$\sigma_y^2 = A\psi^2 + B\psi + C \quad . \tag{6-26}$$

The goal is now to find the local minima of the nonnegative variance function $\sigma_y^2(\psi)$. First evaluate whether this variance vanishes for some value(s) of suction. The right-hand side of Eqn. (6-26) can be factored as

$$\sigma_y^2(\psi) = A(\psi - \psi')(\psi - \psi'') \tag{6-27}$$

where ψ' and ψ'' are the roots, $\psi = (-B \pm \sqrt{\Delta})/A$, of the quadratic equation $\sigma_y^2(\psi) = 0$. The discriminant $\Delta = B^2 - 4AC$ is positive, and the roots are real if and only if $B \geq \sqrt{4AC}$. Inserting the actual expressions of A, B, C from Eqn. (6-25) yields the necessary and sufficient condition for a vanishing variance, namely $1 + \rho^2 \sigma_A^2 - \exp(\sigma_A) \geq 0$. Using the fact that $\rho^2 \leq 1$, it is easily shown that the previous inequality can never be satisfied as long as σ_A^2 remains strictly positive. It is concluded that there does not exist a perfect crossing point where all the conductivity curves would intersect.

On the other hand, the existence of a more or less dense cluster of crossing points is not precluded (Figure 6-2). This may be investigated by studying the local minima of $\sigma_y^2(\psi)$. The first- and second- order conditions for the existence of a local minimum (with zero slope and positive curvature) can be expressed as follows:

$$\frac{d\sigma_y^2}{d\psi} = 0 \Leftrightarrow \psi_1 = -\frac{B}{2A} \tag{6-28a}$$

$$\frac{d^2\sigma_y^2}{d^2\psi} > 0 \Leftrightarrow A > 0 \quad . \tag{6-28b}$$

By inspection of Eqns. (6-25)-(6-26), it can be seen that $A > 0$ is always satisfied, and that $B < 0$ if and only if $\rho > 0$. As a consequence, in the case of strictly positive correlation, the minimizing suction ψ_1 exists and is strictly positive. Substituting A and B by their actual expressions from Eqn. (6-25) yields, in terms of dimensionless suction,

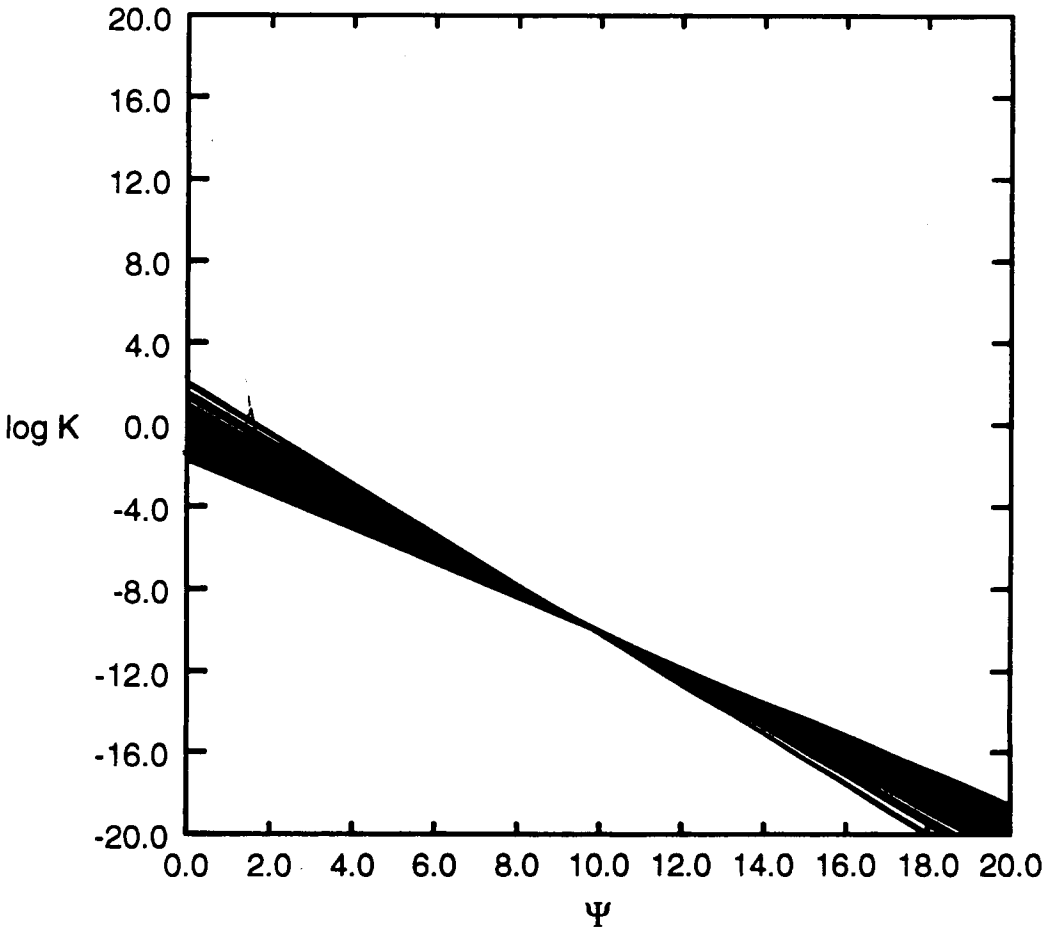

Figure 6-2. Random set of conductivity curves $K(\Psi, \vec{x})$ for $\sigma_A=0.1$, $\sigma_F=1.0$, and $\rho=+1$. Case of relatively low variability and perfect correlation. Notice the crossing-point cluster at $\Psi_0 \approx 10$ (very crisp).

$$\psi_1 = \rho \frac{\sigma_F}{\sigma_A} \frac{\sigma_A^2 \exp\{-\sigma_A^2/2\}}{\exp\{\sigma_A^2\} - 1} \quad . \tag{6-29}$$

And, for small to moderate values of σ_A, say $\sigma_A \leq 0.1$ to $\sigma_A \leq 0.5$, we obtain approximately:

$$\psi_1 \approx \rho \frac{\sigma_F}{\sigma_A} \quad . \tag{6-30}$$

Note in particular that the approximate expression of ψ_1 is identical to that given for ψ_0 in Eqn. (6-14).

It is concluded that the critical value $\psi \approx \rho\sigma_F/\sigma_A$ minimizes both the effective anisotropy ratio of perfectly stratified media (ψ_0) and the spread of the crossing points of microscale conductivity curves (ψ_1). To put it differently, the crossing-point cluster of the random $K(\psi,x)$ curves minimizes the anisotropy ratio of effective conductivities ($A(\psi) \geq 1$). This means that unsaturated flow tends to be more nearly isotropic for the particular value of suction where many conductivity curves intersect. This phenomenon can be explained intuitively as follows: although the medium is structurally stratified, its hydraulic conductivity becomes more homogeneous, and therefore less stratified, for values of suctions that minimize the range of spatial variations of unsaturated conductivity.

The crossing-point cluster may be characterized more precisely in terms of its spread, or dispersion. A measure of the spread of the crossing-point cluster is given by the standard deviation of log conductivity, $\sigma_{y1}=\sigma_y(\psi_1)$, at the crossing-point suction ψ_1. Inserting ψ_1 of Eqns. (6-28a)-(6-29) into Eqns. (6-25)-(6-26) yields:

$$\sigma_y^2(\psi_1) = -\frac{1}{4}\frac{B^2}{A} + C \quad . \tag{6-31}$$

Upon substituting the actual expressions for (A, B, C), this leads to

$$\sigma_y^2(\psi_1) = \sigma_F^2 \left(1 - \rho^2 \frac{\sigma_A^2}{\exp\{\sigma_A^2\} - 1} \right) = \sigma_F^2 - \rho\,\sigma_F \sigma_A \exp\{\sigma_A^2/2\}\psi_1 \quad . \tag{6-32}$$

For $\sigma_A \leq$ 0.1-0.5, this yields approximately

$$\sigma_y^2(\psi_1) \approx \sigma_F^2(1-\rho^2) \approx \sigma_F^2 - \rho\sigma_F\sigma_A\psi_1 \quad . \tag{6-33}$$

An appropriate measure of relative spread is given by the ratio $s_1 = \sigma_y(\psi_1)/\sigma_F$. This ratio characterizes the dispersion of unsaturated log conductivities at the crossing point $\psi=\psi_1$, relative to the dispersion of saturated log conductivities at $\psi=0$. From previous results, the spread ratio is given by

$$s_1 = \sqrt{1-\rho^2\frac{\sigma_A^2}{\exp\{\sigma_A^2\}-1}} \quad . \tag{6-34a}$$

It is instructive to analyze the behavior of the crossing-point cluster in terms of the spread ratio [Eqn. (6-34)]. First, note that the spread ratio never reaches zero, except as $\rho \to +1$ and $\sigma_A \to 0$ jointly. Second, for a fixed positive correlation $0 \leq \rho \leq 1$, the spread ratio increases monotonically with σ_A, starting with the lower bound $s_1 = \sqrt{1-\rho^2}$ at $\sigma_A=0$, and eventually reaching the upper bound $s_1=100$ percent as $\sigma_A \to \infty$. Third, when σ_A is fixed, $\rho = 1$ yields the smallest value of s_1 while $\rho = 0$ yields the largest possible value $s_1=100$ percent. In other words, the case of perfect cross correlation maximizes the density of the crossing-point cluster, while the case of perfect independence yields no distinguishable cluster. Although it is found that the cluster never collapses to a single crossing point, the relatively dense cluster obtained for positive cross-correlation can be viewed as a fuzzy or statistical crossing point. See Figures 6-2 through 6-12 for direct illustration of these properties.

6.3.7. Upper-Bound Conductivity and Upper Envelope Curve

We show in this section that the family of cross-correlated conductivity curves possesses, in addition to the previously studied cluster of crossing points, a more or less crisp upper envelope, $K_{sup}(\psi)$. The existence of this envelope is due to the skewed distribution of random log-conductivity slopes, which reflects the fact that ascending slopes are not permitted. It turns out that the envelope curve $K_{sup}(\psi)$ behaves like a power law rather than an exponential function. The upper envelope of conductivities is a scalar quantity which does not distinguish vertical and horizontal flow. It could be used however as an alternative to directional effective conductivities for large-scale predictions of vadose contaminant transport. Indeed, for certain applications such as high-level nuclear waste contamination, bounding calculations based on worst case scenarios may be required.

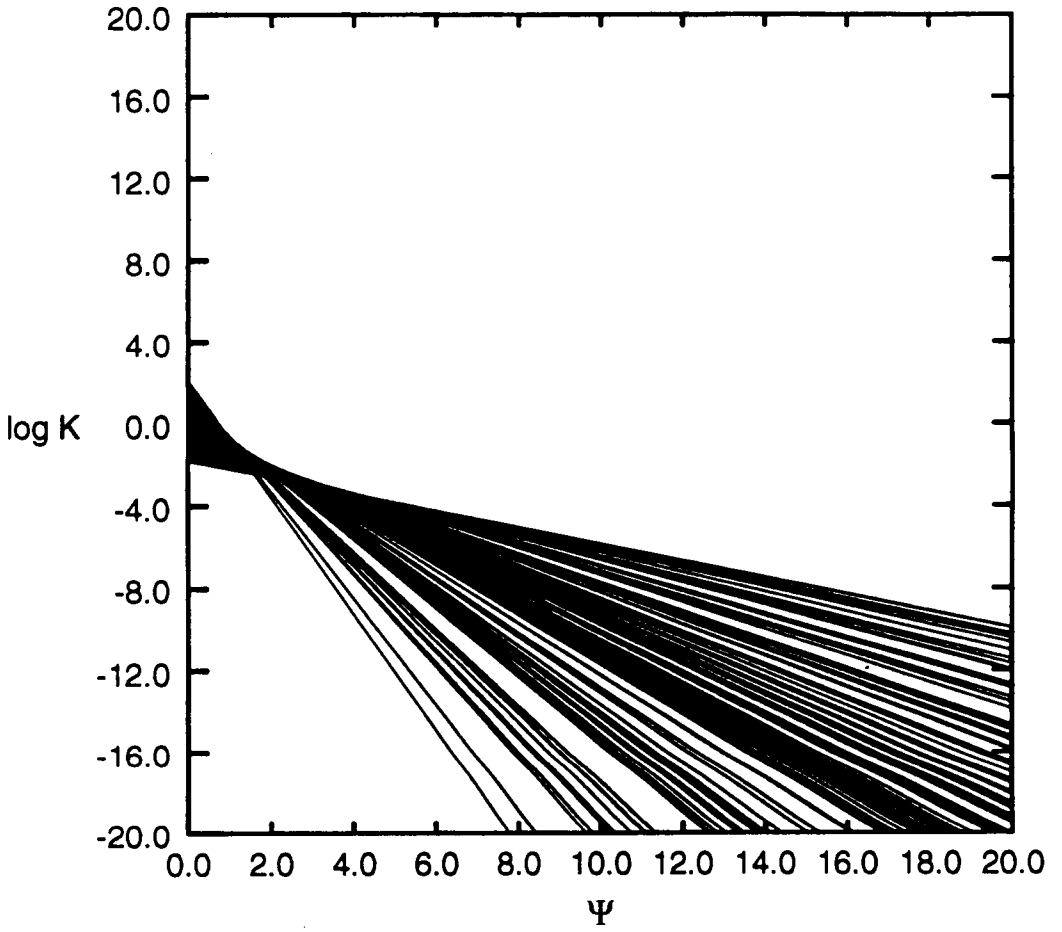

Figure 6-3. Random set of conductivity curves $K(\Psi, \vec{x})$ for $\sigma_A=0.5$, $\sigma_F=1.0$, and $\rho=+1$. Case of significant variability and perfect correlation. Notice the crossing-point cluster at $\Psi_0 \approx 2$ (relatively fuzzy), and the upper envelope (crisp).

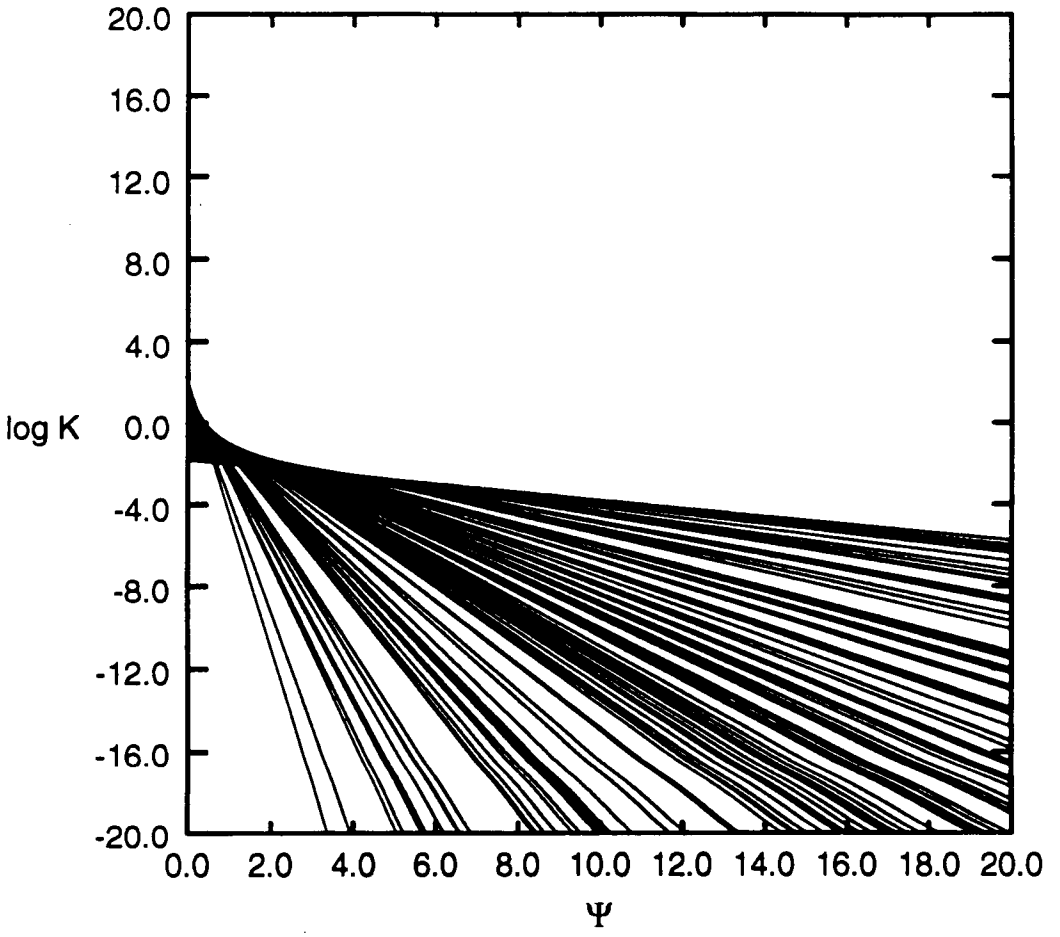

Figure 6-4. Random set of conductivity curves $K(\Psi, \vec{x})$ for $\sigma_A=0.9$, $\sigma_F=1.0$, and $\rho=+1$. Case of high variability and perfect correlation. Notice the crossing-point cluster at $\Psi_o \approx 2$ (relatively fuzzy), and the upper envelope (crisp).

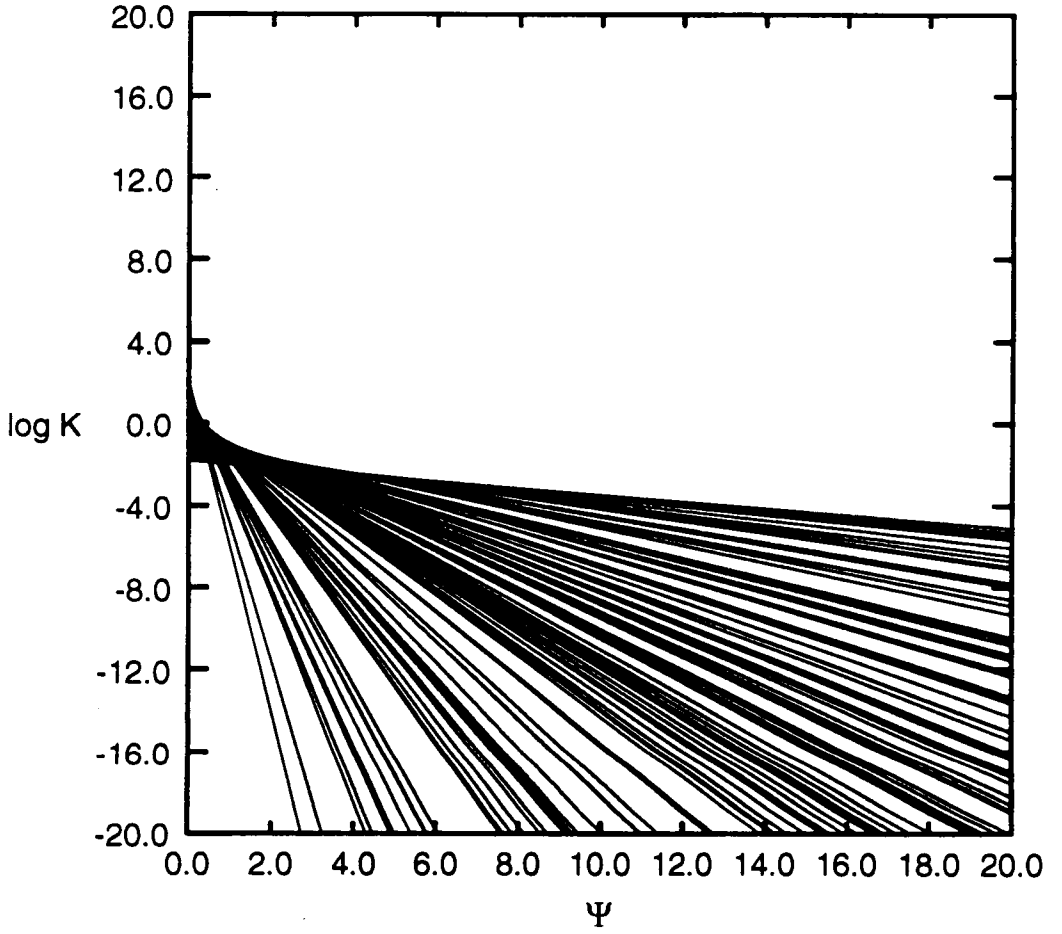

Figure 6-5. Random set of conductivity curves $K(\Psi, \vec{x})$ for $\sigma_A=1.0$, $\sigma_F=1.0$, and $\rho=+1$. Case of high variability and perfect correlation. Notice the crossing-point cluster at $\Psi_o \approx 2$ (relatively fuzzy), and the upper envelope (crisp).

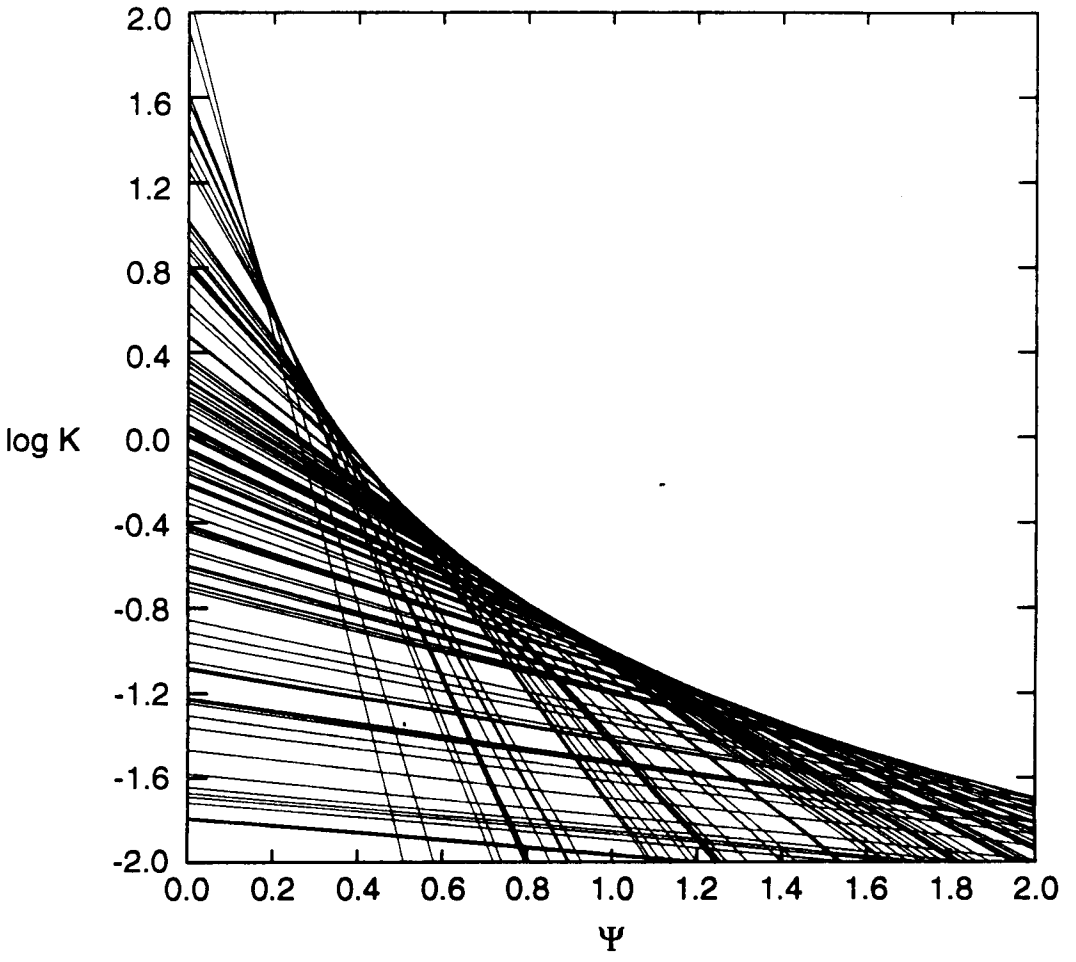

Figure 6-6. Random set of conductivity curves $K(\Psi, \bar{x})$: close-up on Figure 6-5 in the low suction range for high variability ($\sigma_A = \sigma_F = 1.0$) and perfect correlation ($\rho = 1.0$). Notice the crisp upper envelope due to perfect correlation.

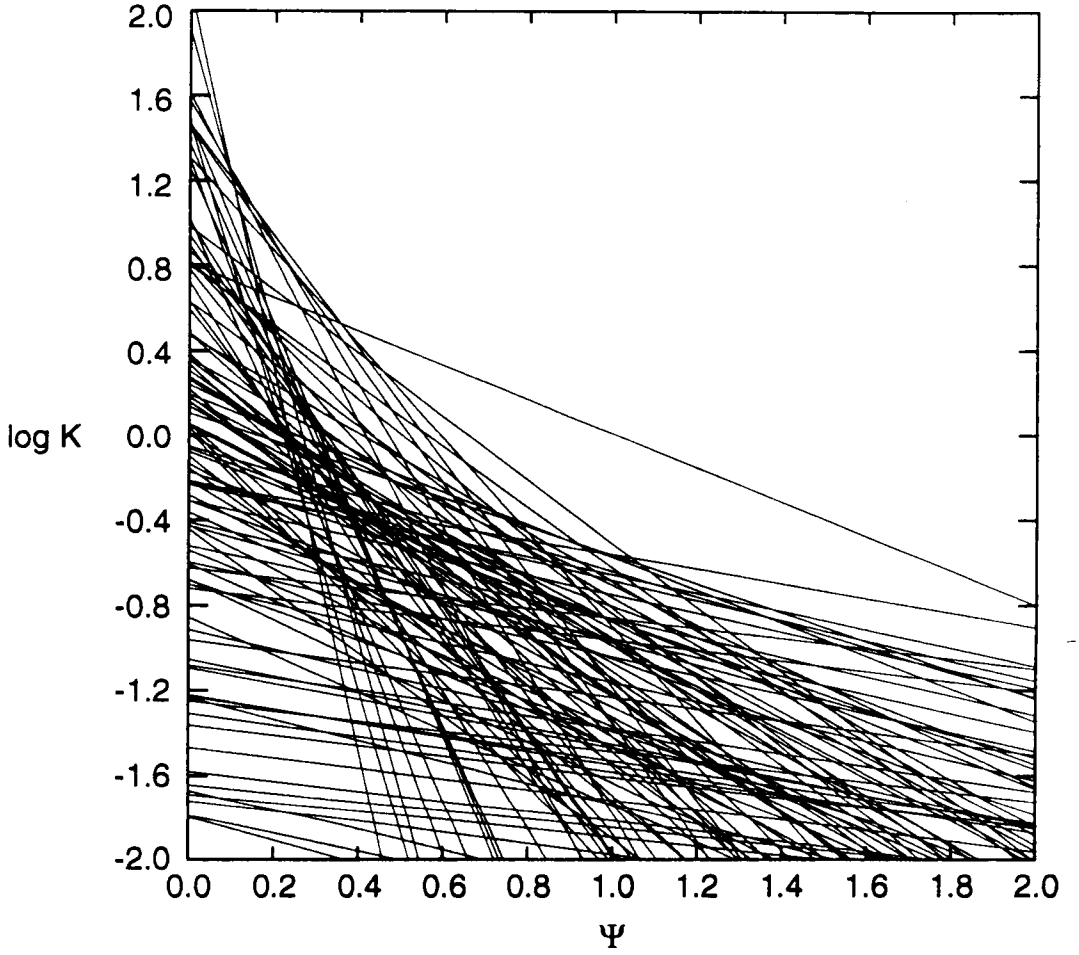

Figure 6-7. Random set of conductivity curves $K(\Psi, \bar{x})$: close-up on the low suction range for the case of high variability ($\sigma_A=\sigma_F=1.0$) and nearly perfect correlation ($\rho=+0.9$). Notice the relatively fuzzy, but perceivable upper envelope.

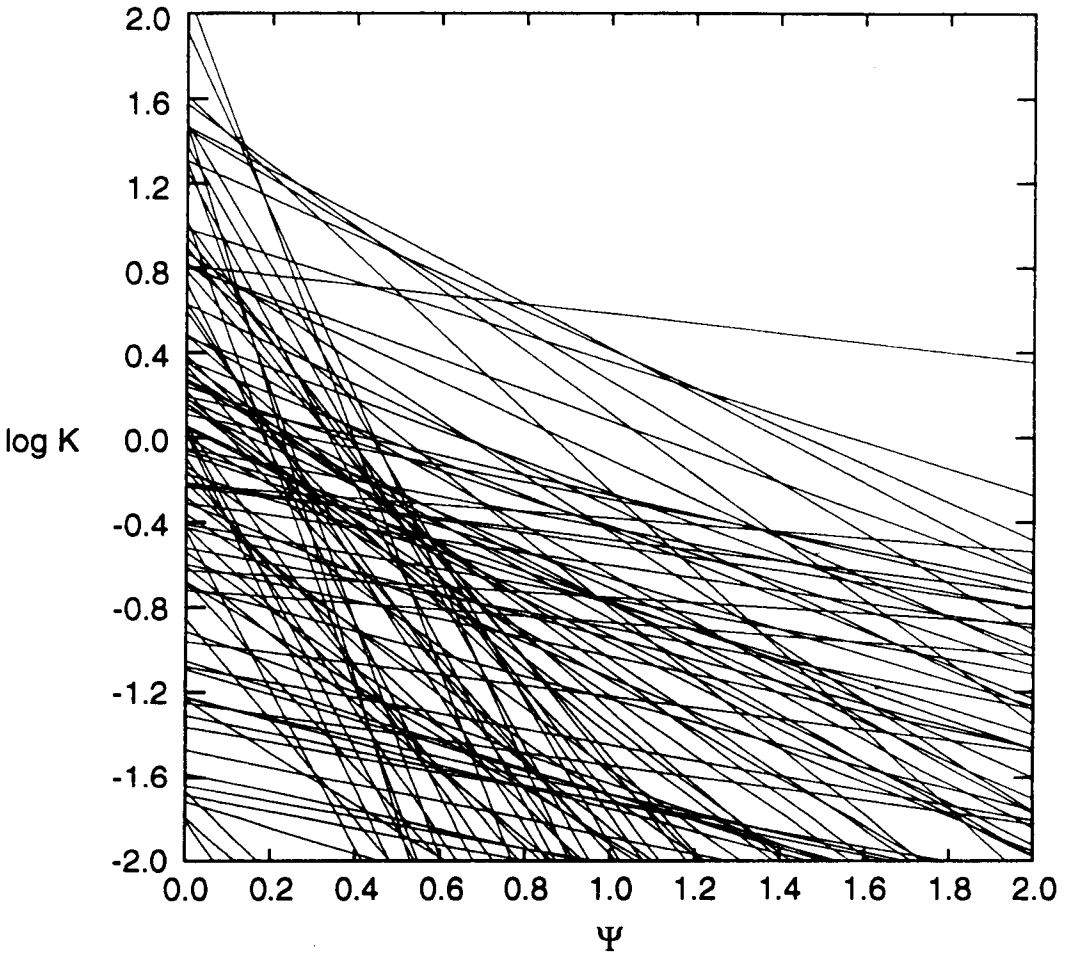

Figure 6-8. Random set of conductivity curves $K(\Psi, \bar{x})$: close-up on the low suction range for the case of high variability ($\sigma_A = \sigma_F = 1.0$) and partial correlation ($\rho = +0.5$). Notice the fuzzy, but still perceivable, upper envelope.

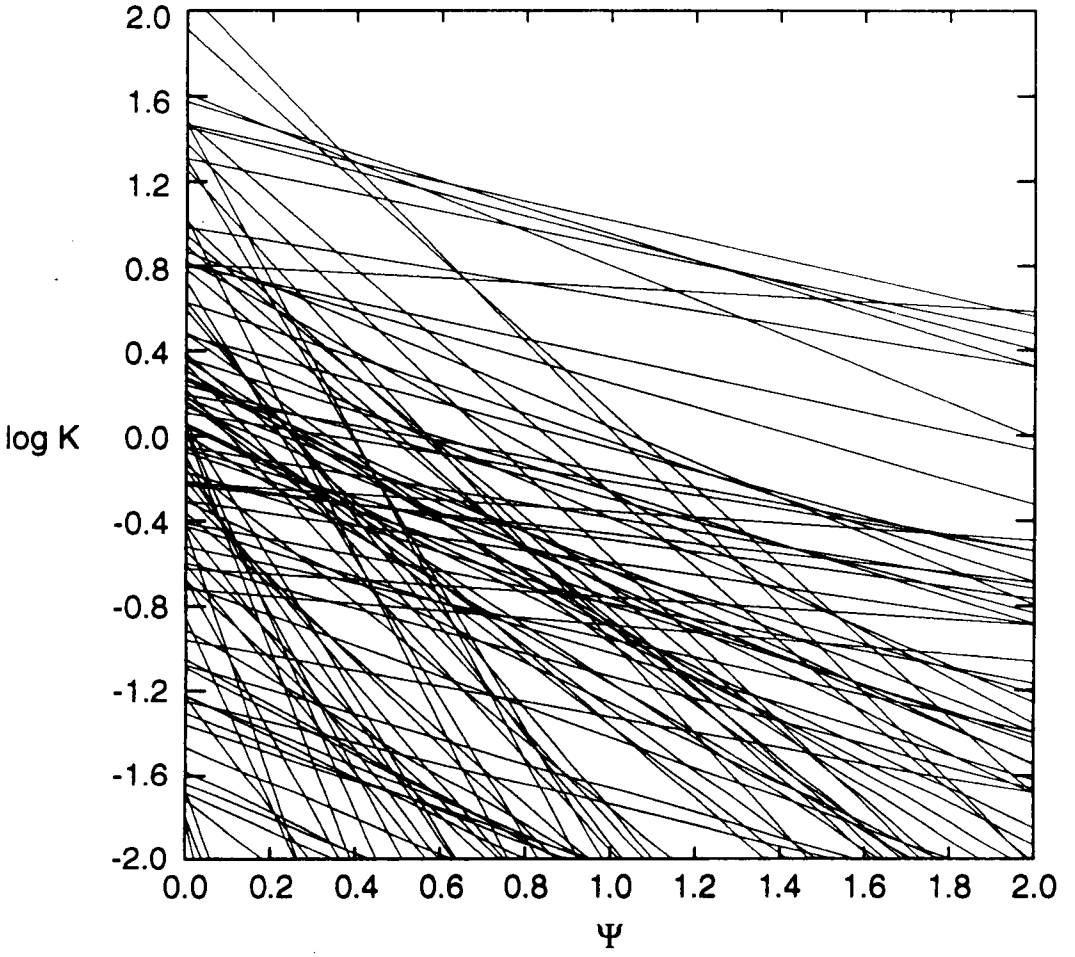

Figure 6-9. Random set of conductivity curves $K(\Psi, \bar{x})$: close-up on the low suction range for the case of high variability ($\sigma_A=\sigma_F=1.0$) and perfect independence ($\rho=0$). No upper envelope can be seen in this case.

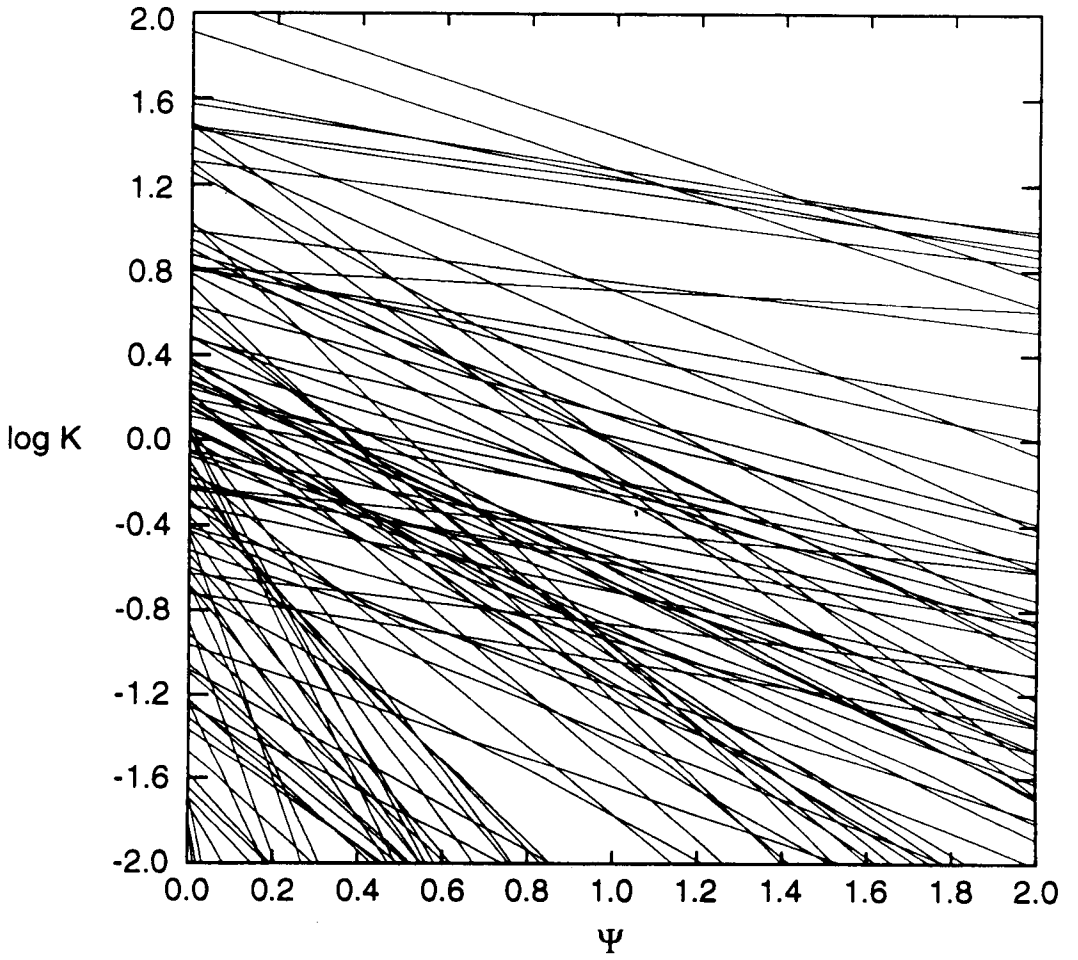

Figure 6-10. Random set of conductivity curves $K(\Psi, \bar{x})$: close-up on the low suction range for the case of high variability ($\sigma_A=\sigma_F=1.0$) and negative correlation ($\rho=$ -0.5). Probably not realistic physically.

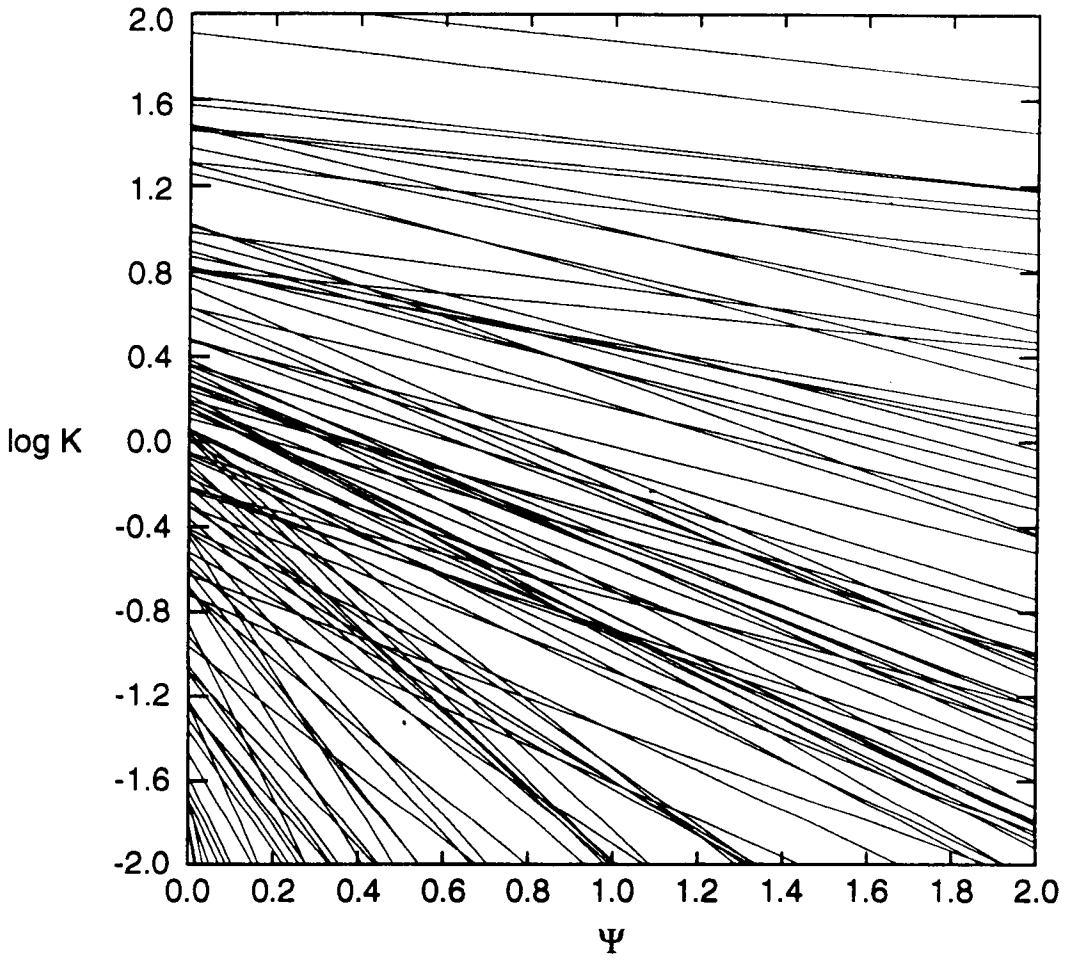

Figure 6-11. Random set of conductivity curves $K(\Psi, \bar{x})$: close-up on the low suction range for the case of high variability ($\sigma_A=\sigma_F=1.0$) and negative correlation ($\rho=$ -0.9). Probably not realistic physically.

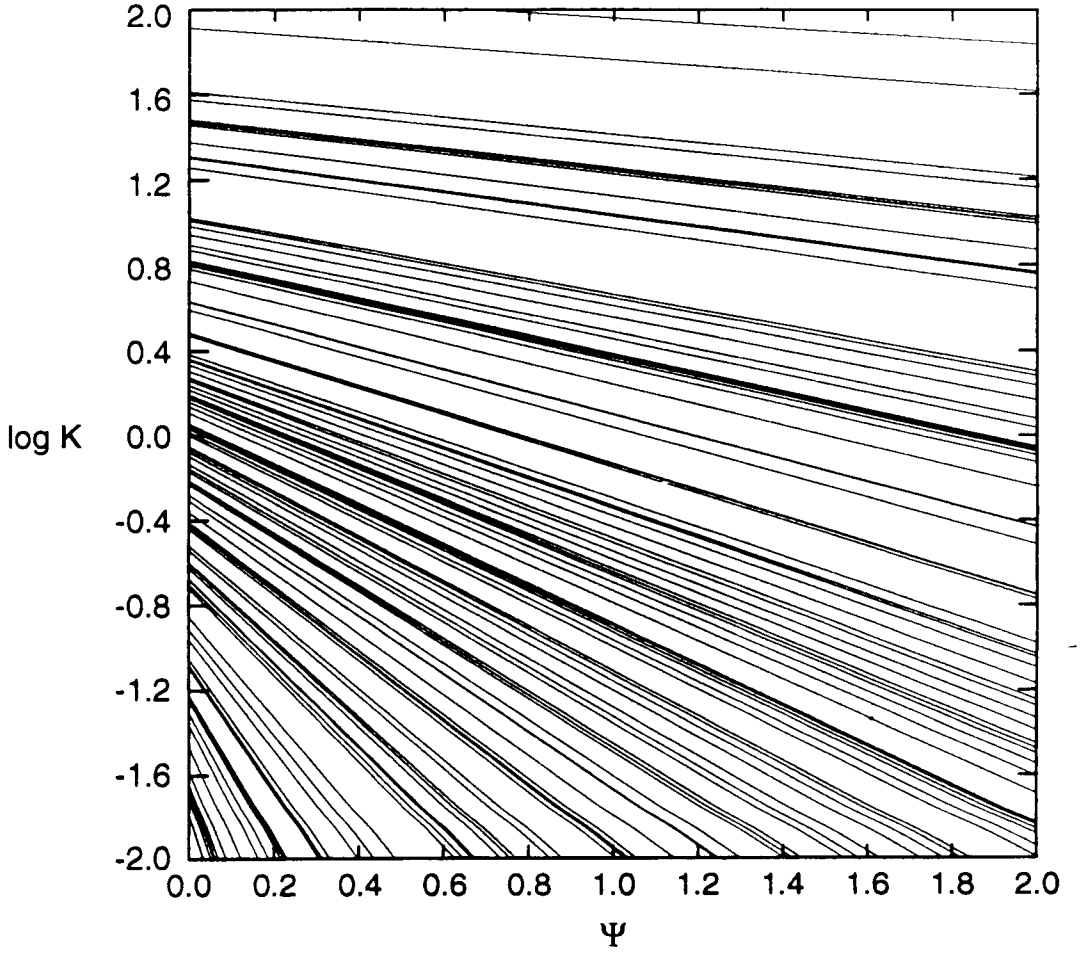

Figure 6-12. Random set of conductivity curves $K(\Psi, \vec{x})$: close-up on the low suction range for the case of high variability ($\sigma_A = \sigma_F = 1.0$) and perfect anti-correlation ($\rho = -1$). Probably not realistic physically.

Consider again the log-conductivity perturbation of Eqn. (6-21), which we reproduce below in terms of the dimensionless suction $\psi = \alpha_G \Psi$:

$$y(\psi,x) = f(x) - \left[\exp\{a(x)\} - \exp\{\sigma_A^2/2\}\right]\psi \quad . \tag{6-34b}$$

Substituting the cross-correlated random fields (a,f) of Eqns. (6-4) by their expressions in terms of the independent normalized gaussian random fields (g_1,g_2):

$$y(\psi,x) = \sigma_F g_1(x) - \left[\exp\{\sigma_A[\rho g_1(x) + \sqrt{1-\rho^2} g_2(x)]\} - \exp\{\sigma_A^2/2\}\right]\psi \quad . \tag{6-34c}$$

In view of these expressions, the random log-conductivity field appears to be negatively skewed in distribution for all values of suction, being equal to the difference between a gaussian random field $(f=\sigma_F g_1)$ and a suction-dependent, log-normal random field (exponential terms). Given the negative skewness, it is suspected that the probability of occurrence of conductivity values drops sharply above a certain threshold value, which depends on suction.

In the general case of imperfect correlation $(0 < \rho < 1)$, the exact probability distribution of $y(\psi,x)$ is difficult to evaluate in closed form. However, the special case of perfect correlation produces simplifications which allow for a complete analysis of suction-dependent upper-bound conductivity. For this reason, the case $\rho = 1$ is examined first, below. The more general case $0 \le \rho \le 1$ will be treated subsequently. Finally, evaluation of third-order moment and skewness of unsaturated conductivity will provide additional information along these lines.

6.3.7.1. Exact Upper Envelope for Perfect Cross-Correlation

In the special case $\rho = 1$, to be denoted hereafter with subscript (*), there exists an exact deterministic upper bound to the random set of conductivity curves. The log-conductivity perturbation given by Eqn. (6-34b) depends only on $g_1(\mathbf{x})$, not $g_2(\mathbf{x})$. For any fixed value of suction, the log-conductivity perturbation can be expressed formally as a one-to-one function of g_1, that is $(\rho=1)$:

$$y_*(g_1) = \sigma_F g_1 - \psi \exp\{\sigma_A g_1\} + \psi \exp\{\sigma_A^2/2\} \quad . \tag{6-35}$$

Recall that g_1 is normally distributed with zero-mean and unit variance, so that $g_1 \in [-\infty, +\infty]$. It turns out that the function $y_*(g_1)$ has a global maximum at:

$$g_1 = -\frac{1}{\sigma_A} \ell n \{\psi \sigma_A / \sigma_F\} \quad . \tag{6-36}$$

Inserting Eqn. (6-36) in Eqn. (6-35) yields the corresponding maximum value, $y_{sup}*(\psi)$. Adding to this the mean log-conductivity $<Y(\psi,x)> = \ell n K_G(\psi)$ given by Eqn. (6-10a) yields, after some manipulations, a closed-form expression for the upper-bound log-conductivity curve:

$$Y_{sup*}(\psi) = \ell n K_G + \frac{\sigma_F}{\sigma_A}\left[\ell n\left\{\frac{\sigma_F}{\sigma_A}\right\} - 1\right] - \frac{\sigma_F}{\sigma_A} \ell n \{\psi\} \quad . \tag{6-37}$$

Equivalently, taking the exponential transform of Eqn. (6-37), and using as before the dimensionless suction ψ as dependent variable, the upper-bound conductivity curve is obtained:

$$K_{sup*}(\psi) = K_G \exp\left\{-\frac{\sigma_F}{\sigma_A}\right\} \left\{\frac{\sigma_F}{\sigma_A}\right\}^{\frac{\sigma_F}{\sigma_A}} \{\psi\}^{-\frac{\sigma_F}{\sigma_A}} \quad . \tag{6-38}$$

Interestingly, the upper-bound or upper-envelope conductivity curve is a power law rather than an exponential function of suction. It should be emphasized that this upper envelope is exact (crisp): see for instance Figure 6-6. Moreover, it coexists with the fuzzy crossing-point cluster defined earlier (see Figures 6-2 through 6-5). The location of the crossing-point cluster coincides, in fact, with a particularly dense point of the envelope. This can be seen by using the fact that g_1 of Eqn. (6-35) follows a normalized gaussian distribution. The maximizing value of g_1, which yields the upper-bound conductivity, occurs therefore with probability density

$$p = \frac{dP}{dg_1} = \frac{1}{\sqrt{2\pi}} \exp\left\{-\frac{1}{2\sigma_A^2}\left[\ell n \{\psi \sigma_A / \sigma_F\}\right]^2\right\} \quad . \tag{6-39}$$

This density is maximal for suction $\psi = \sigma_F/\sigma_A$, which coincides with the critical suction ψ_1 of Eqn. (6-30) in the case $\rho = 1$. In other words, the highest density point on the upper-bound conductivity curve occurs at the same critical suction that maximizes the density of crossing

points. This is particularly obvious in the case of Figure 6-2 and is further illustrated by Figure 6-13, which summarizes the properties just discussed. The focus is on the upper envelope rather than the crossing points. The more general case of imperfect cross-correlation is examined next.

6.3.7.2. Fuzzy Upper Envelope for Imperfect Cross-Correlation

In the more general case of imperfect correlation, $0 \leq \rho \leq 1$, there is no longer an exact upper-bound conductivity curve, except asymptotically as $\rho \rightarrow 1$. Nonetheless, in the case of significant correlation, an approximate or fuzzy upper bound exists in some statistical sense. This fuzzy upper bound can be characterized, as before, by examining the properties of the function $y(g_1,g_2)$:

$$y_*(g_1,g_2) = \sigma_F g_1 - \psi \exp\{\sigma_A(\rho g_1 + \sqrt{1-\rho^2} g_2)\} + \psi \exp\{\sigma_A^2/2\} \quad \text{(6-40)}$$

The slopes of this function with respect to g_1 and g_2 are, respectively;

$$\frac{\partial y}{\partial g_1} = \sigma_F - \psi \rho \sigma_A \exp\{\sigma_A(\rho g_1 + \sqrt{1-\rho^2} g_2)\} \quad \text{(6-41)}$$

$$\frac{\partial y}{\partial g_2} = - \psi \sqrt{1-\rho^2} \sigma_A \exp\{\sigma_A(\rho g_1 + \sqrt{1-\rho^2} g_2)\} \quad . \quad \text{(6-42)}$$

Note that $\partial y/\partial g_2$ does not vanish except in the trivial case where either $g_1 \rightarrow -\infty$ or $g_2 \rightarrow -\infty$. As a consequence, a local maximum of y in the (g_1,g_2) plane does not exist. However, since $\partial y/\partial g_1$ does vanish for finite values of the arguments, it can be shown that a *directional* maximum does exist with respect to g_1, along the straight line defined by

$$\rho g_1 + \sqrt{1-\rho^2} g_2 = \frac{1}{\sigma_A} \ln\{\frac{\sigma_F}{\rho \sigma_A \psi}\} \quad . \quad \text{(6-43)}$$

Expressing g_1 in terms of g_2, substituting into $y(g_1,g_2)$, and adding the mean log conductivity $<Y>$ to its perturbation y, yield log conductivity on the locus of the directional maxima of y. More precisely, the result is a family of suction-dependent curves of the form

$$Y_{sup}(\psi,g_2) = \ln K_G + \frac{\sigma_F}{\rho \sigma_A}(\ln\{\frac{\sigma_F}{\rho \sigma_A \psi}\} - 1) - \sigma_F \frac{\sqrt{1-\rho^2}}{\rho} g_2 \quad \text{(6-44)}$$

where g_2 is a gaussian random variable with zero mean and unit variance. The above equation defines a fuzzy upper-bound log-conductivity curve. The degree of fuzziness can be

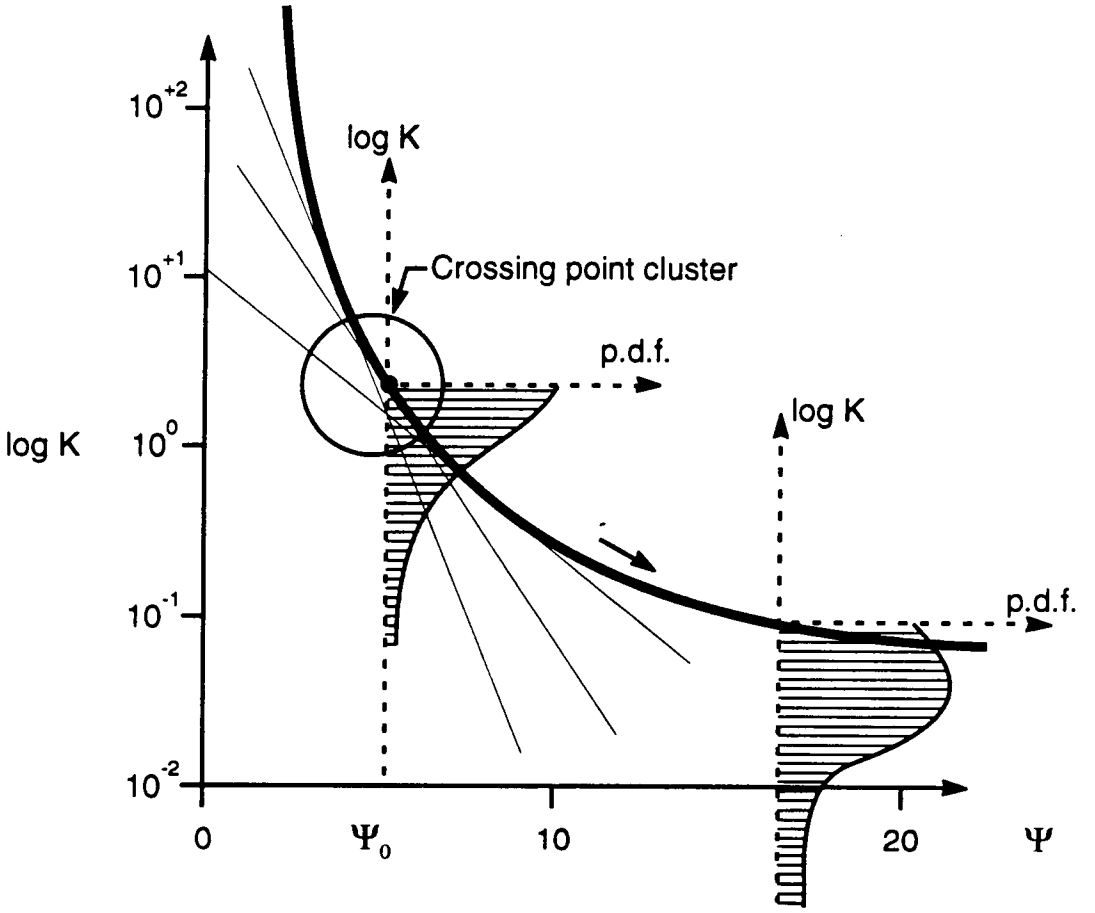

Figure 6-13. Properties of Upper-Envelope Conductivity Curve $K \sim 1/\Psi^{\sigma_f/\sigma_k}$ (Case $\rho = +1$).

characterized by the relative spread

$$s = \sqrt{\frac{\mathrm{Var}(Y_{sup})}{\mathrm{Var}(F)}} = \frac{\sqrt{1-\rho^2}}{\rho} \quad . \tag{6-45}$$

Note in particular that the spread of the curve becomes infinite for $\rho \to 0$, and becomes null for $\rho \to 1$. In other words, the upper-bound curve becomes so fuzzy as to be indistinguishable as ρ tends to zero. On the other hand, the upper-bound curve becomes crisper and eventually exact as ρ tends to one. Taking the ensemble mean of $Y_{sup}(\psi, g_2)$ with respect to g_2 and exponentiating yield finally the general expression of the fuzzy upper-bound conductivity curve, or upper envelope curve

$$K_{sup}(\psi) \approx K_G \exp\left\{-\frac{\sigma_F}{\rho\sigma_A}\right\} \left\{\frac{\sigma_F}{\rho\sigma_A}\right\}^{\frac{\sigma_F}{\rho\sigma_A}} \{\psi\}^{-\frac{\sigma_F}{\rho\sigma_A}} \quad , \tag{6-46}$$

which reduces to Eqn. (6-38) and Figure 6-13 in the case of perfect cross-correlation, as it should. Note again that the upper-envelope conductivity curve is a power law with respect to suction, in contrast with the postulated exponential form of local conductivity curves. Comparing Figures 6-6 through 6-9 indicates visually how the crispness of the upper envelope degrades as the coefficient of correlation decreases from $\rho = +1$ to $\rho = 0$. (For completeness, the anticorrelated case is covered by Figures 6-10 through 6-12.)

6.3.7.3. Suction-Dependent Skewness

The suction-dependent skewness of unsaturated log conductivity is now evaluated. Only final results are given here; the details of calculations are somewhat tedious, although results appear in relatively simple form. Briefly, the skewness coefficient is defined by

$$S = \frac{\langle y^3 \rangle}{\langle y^2 \rangle^{3/2}} \quad . \tag{6-47}$$

The second-order moment $\langle y^2 \rangle$ was calculated previously [Eqn. (6-25)]. The third-order moment $\langle y^3 \rangle$ can also be evaluated in closed form (not shown here). Some simplifications occur in the case of moderate variability of $A = \ell n\alpha$; that is, for $\sigma_A^2 << 1$, or $\sigma_A \leq 0.3$ approximately. With this provision, log-conductivity skewness is given by

$$S \simeq \frac{-3\sigma_A^2\psi(\sigma_A\psi-\rho\sigma_F)^2}{\{(\sigma_A\psi-\rho\sigma_F)^2+(1-\rho^2)\sigma_F^2\}^{3/2}} \quad . \tag{6-48}$$

The skewness curve given above has a few notable properties. Firstly, note that skewness is negative for all values of suction, ψ, and all values of the correlation coefficient, ρ. Secondly, for all values of the correlation coefficient, skewness tends to a constant negative value $S \approx -3\sigma_A$ as suction becomes significantly larger than σ_F/σ_A. For instance, the case $\sigma_A \approx 0.3$ yields a skewness coefficient of -1, which is quite significant. Finally, in the special case $\rho=1$ (i.e., perfect cross-correlation), it can be shown that $S \to -\infty$ as $\psi \to \sigma_F/\sigma_A$. The latter value corresponds to the critical suction that minimizes effective anisotropy ratio, and maximizes the occurence of crossing points. As can be seen, this critical value of suction also produces maximal negative skewness in the case of perfect cross-correlation (see p.d.f. curves shown on Figure 6-13).

6.3.8. Summary and Discussion

The effects of statistical anisotropy and of cross-correlation on the conductive properties of heterogeneous unsaturated media have been investigated. The main results were obtained by interpreting statistical properties of random sets of unsaturated conductivity curves in terms of effective conductivity and effective anisotropy on the one hand, and in terms of fuzzy crossing point and upper envelope on the other hand.

The foregoing analysis relies on a few simple postulates. At the local scale, the conductivity curve is assumed to be an exponential function of suction with spatially random parameters, namely intercept and slope of log conductivity. The random-field parameters were assumed to have two essential features, thought to be representative of the spatial structure of geologic formations: (1) statistical anisotropy or stratification and (2) positive cross-correlation of intercept and slope parameters. The latter assumption has its origin in capillary theories of flow through porous media, and may be applicable in particular to fissured media where positive cross-correlation can account for the distinct conductive properties of large/small aperture fissures. However, the statistical continuum hypothesis was retained; and gaussian or log-normal distributions were assumed for the parameters.

The methodology developed with these postulates could form the basis for a more explicit and more realistic treatment of the bulk conductive properties of densely fractured unsaturated media. The results obtained with the gaussian-continuum hypotheses are however instructive in themselves, particularly in terms of the sensitivity of bulk conductive properties of unsaturated media with respect to parameter variances and degree of cross-correlation.

First, effective conductivity was examined in the case of a highly stratified cross-correlated medium. The *critical suction* was defined, initially, as the value of suction that

minimizes the effective anisotropy ratio. Subsequent analysis of conductivity curve crossings showed that this critical suction that minimizes the anisotropy ratio is close to the suction that maximizes the density of crossing points of local conductivity curves when plotted as functions of suction. Thus, Figure 6-14 illustrates schematically the connection between minimal anisotropy and crossing points for the ideal case where only two distinct conductivity curves coexist. This would be the case, ideally, in (1) regularly layered soils of rocks composed of only two type of layers or (2) fractured rocks whose fractures are identical and regularly distributed and whose porous matrix is otherwise homogeneous.

A more direct indication of the peculiar conductive behavior of unsaturated media is exemplified by Figure 6-15, which depicts a two-dimensional numerical simulation of unsaturated flow in a bilayered medium that exhibits, albeit crudely, the spatial features analyzed in this work (anisotropy is represented by vertical layers, and cross-correlation by the alternation of only two types of conductivity curves). According to the foregoing analyses, it is expected that, as suction changes away from the critical suction, parallel conductivity should become larger than orthogonal conductivity (subsection 6.3.4), and the flow field should become increasingly variable due to increasing variance of ℓnK (subsection 6.3.5). The shapes of the suction contour lines shown in Figure 6-15 seem to support this predicted behavior. Note that the iso-suction contour line corresponding to the crossing point of the sand/silt conductivity curves appears to be the least heterogeneous and the more nearly isotropic notwithstanding the effect of the gravitational driving force.

In summary, the cross-correlated effective conductivity model developed in subsection 6.3.3, although approximate, appears tractable and could be considered as a candidate model for effective subscale conductivities in large-scale unsaturated flow simulations, possibly in a more general form than the one presented here. Two types of numerical applications are of interest: (1) flow in a spatially uniform equivalent medium having effective anisotropic effective conductivities and (2) coarse-scale simulation of flow in a heterogeneous medium using effective anisotropic conductivities for subgrid or subdomains conductivities. The above findings may be applicable to fractured media, under restricted conditions; that is the above study is limited to the case of a locally isotropic *continuum*. This assumption may be valid in the case of dense fracturation, but will break down in the case of a sparse fracture network with few preferred orientations. In the former case, our model can account for variable fracture density through correlation between a saturated-conductivity and unsaturated-conductivity slope. (Also, macro-scale anisotropy is taken into account.) In the latter case, however, it should be recognized that further progress will require a more explicit formulation of unsaturated flow through fracture networks, which requires realistic models of fracture-network geometry, single-fracture models, and so on. This research, currently ongoing, is beyond the scope of the work reported here.

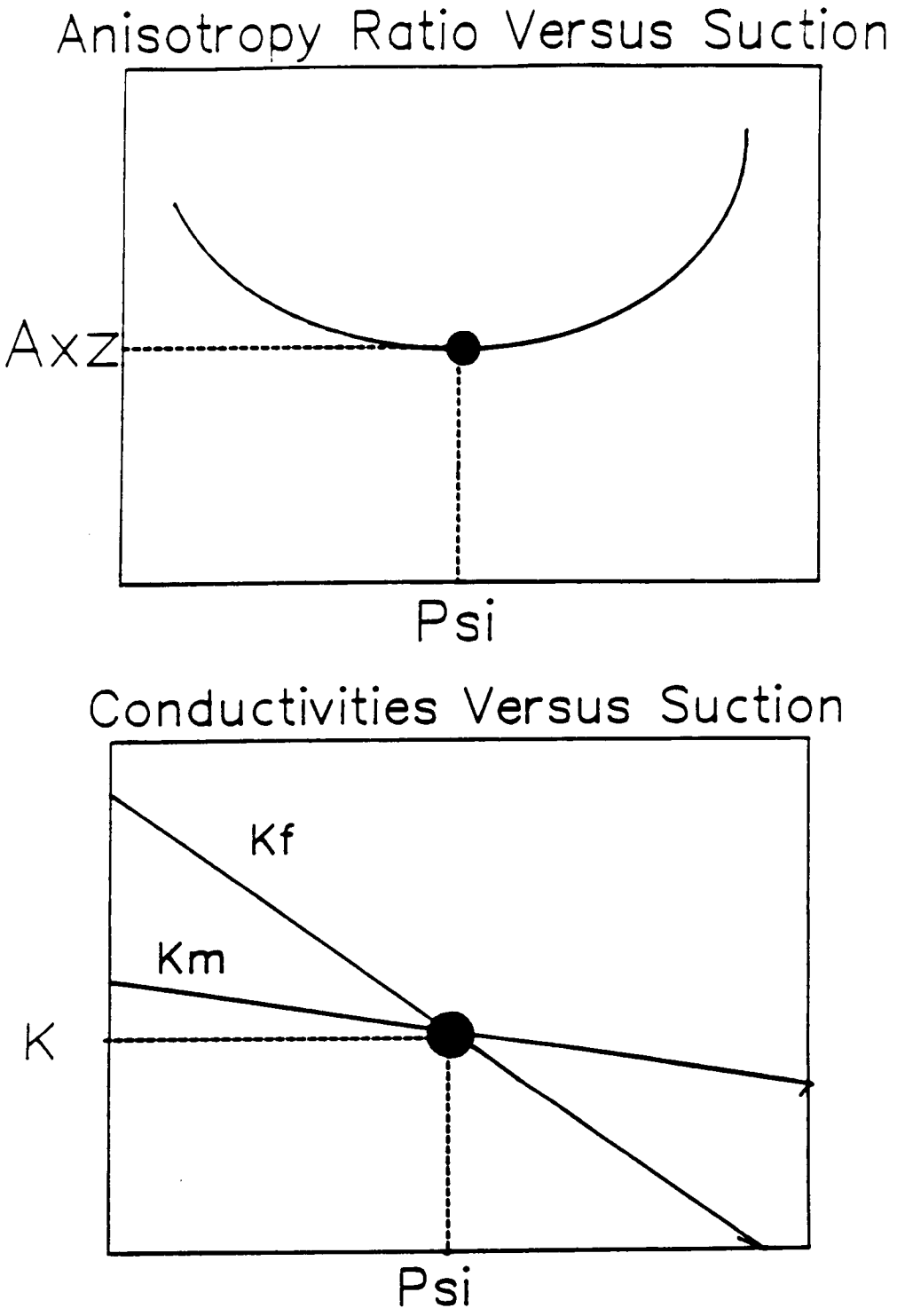

Figure 6-14. Schematic representation of the critical suction in a heterogeneous or fractured unsaturated geologic medium: local minimum of effective anisotropy ratio (top), and intersection of conductivity curves (bottom).

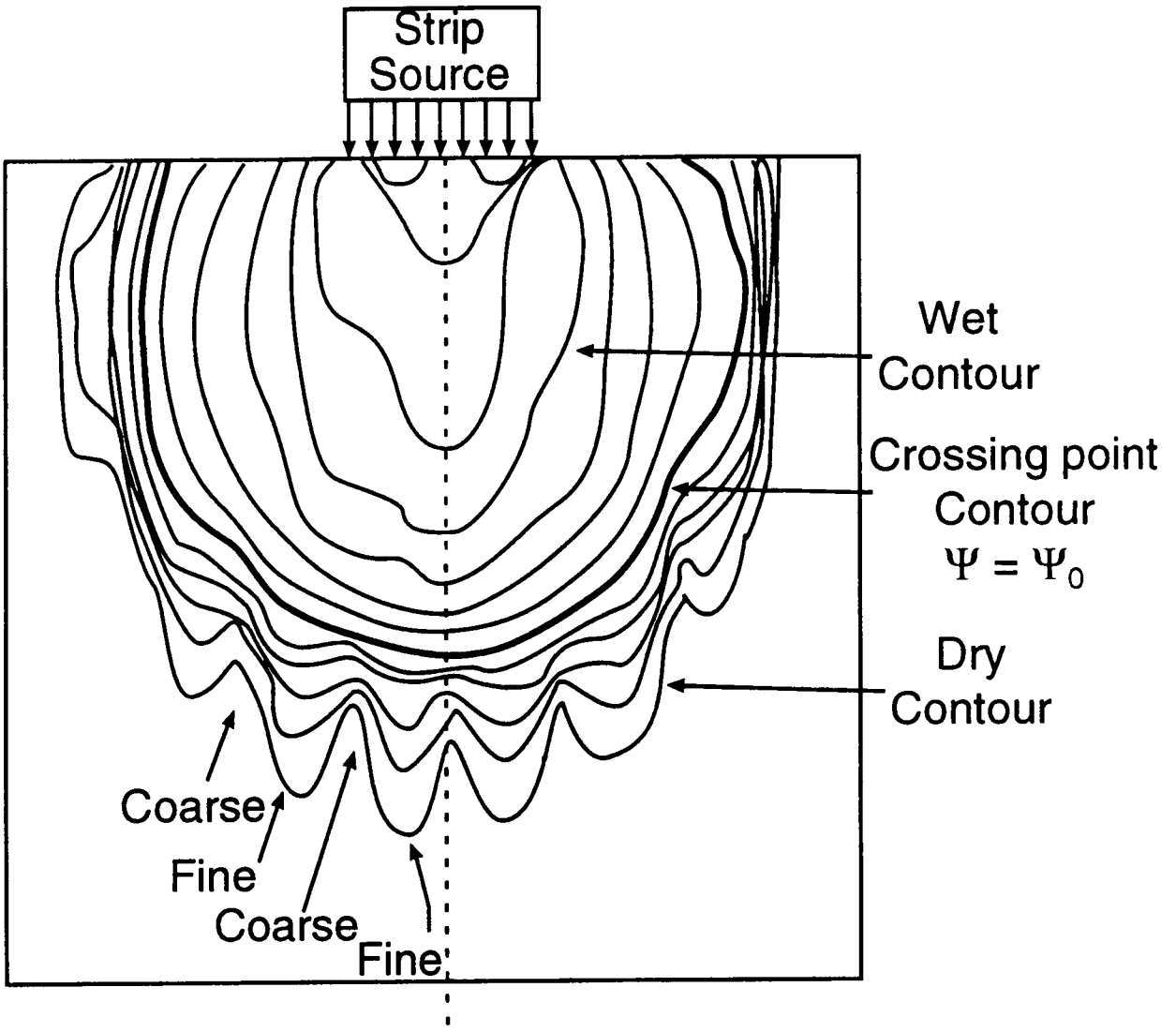

Figure 6-15. Two-dimensional strip-source moisture plume after 1 day of infiltration in a perfectly layered unsaturated soil with alternating vertical sand/silt layers (modified from Ababou, 1988). The thicker contour line $\Psi = \Psi_0$ corresponds to the crossing point between sand and silt conductivity curves.

6.4. REFERENCES

Ababou, R. 1988. *Three-Dimensional Flow in Random Porous Media.* Ph.D. Thesis, 2 vols. Massachusetts Institute of Technology, Cambridge, Massachusetts: Department of Civil Engineering.

Ababou, R., and L. W. Gelhar. 1988. A high-resolution finite difference simulator for 3D unsaturated flow in heterogeneous media. *Computational Methods in Water Resources.* New York: Elsevier: 173-178.

Ababou, R., D. McLaughlin, L. W. Gelhar, and A. F. Tompson. 1989. Numerical simulation of three dimensional saturated flow in randomly heterogeneous porous media. *Transport in Porous Media* 4: 549-565.

Ababou, R., and E. F. Wood. 1990. Comment on "Effective groundwater model parameter values: influence of spatial variability of hydraulic conductivity, leakance, and recharge" by Gomez-Hernandez and Gorelick. *Water Resour. Res.* 26(8): 1843-1846.

Ababou, R. 1990. Identification of effective conductivity tensor in randomly heterogeneous and stratified aquifers. *Proceedings Fifth Canadian-American Conference on Hydrogeology: Parameter Identification and Estimation for Aquifer and Reservoir Characterization.* September 18-20, Calgary, Alberta, Canada [to be published by National Water Well Association].

Ababou R. 1991. *Approaches to Field-Scale Unsaturated Flow in Heterogeneous, Stratified, and Fractured Geologic Media.* NUREG/CR 5743. Washington D. C.: Nuclear Regulatory Commission [in press].

Andersson, J., and A. M. Shapiro. 1983. Stochastic analysis of one-dimensional steady state unsaturated flow: a comparison of Monte-Carlo and perturbation methods. *Water Resourc. Res.* 19(1): 121-133.

Bear, J. 1972. *Dynamic of Fluids in Porous Media.* New York: Elsevier.

Gelhar, L. W., A. Mantoglou, C. Welty, and K. Rehfeldt. 1984. *A Review of Field Scale Subsurface Solute Transport Processes under Saturated and Unsaturated Conditions.* Report RP-22485-05. Palo Alto, California: Electrical Power Research Institute.

Hsieh, P. A., S. P. Neuman, and E. S. Simpson, 1983. *Pressure Testing of Fractured Rocks - A Methodology Employing Three-Dimensional Cross-Hole Tests.* NUREG/CR-3213 RW. Washington D.C.: U. S. Nuclear Regulatory Commission.

Isserlis, L. 1918. On a formula for the product-moment coefficient in any number of variables. *Biometrika* 12(1-2): 134-139.

Mantoglou, A., and L. W. Gelhar. 1987a. Stochastic modeling of large-scale transient unsaturated flow systems. *Water Resour. Res.* 23(1): 37-46.

Mantoglou, A., and L. W. Gelhar. 1987b. Capillary tension head variance, mean soil moisture content, and effective specific soil moisture capacity of transient unsaturated flow in stratified soils. *Water Resour. Res.* 23(1): 47-56.

Mantoglou, A., and L. W. Gelhar. 1987c. Effective hydraulic conductivities of transient unsaturated flow in stratified soils. *Water Resour. Res.* 23(1): 57-67.

Mualem, Y. 1984. Anisotropy of unsaturated soils. *Soil Sci. Soc. Am. J.* 48: 505-509.

Neuman, S. P., and J. S. Depner. 1988. Use of variable-scale pressure test data to estimate the log hydraulic conductivity covariance and dispersivity of fractured granites near Oracle, Arizona. *J. of Hydrology* 102: 475-501.

Polmann, D. J., D. McLaughlin, L. W. Gelhar, and R. Ababou. 1991. Stochastic modeling of large-scale flow in heterogeneous unsaturated soils. *Water Resourc. Res.* 27: 1447-1458.

Smith, L., and R. A. Freeze. 1979a. Stochastic analysis of steady state groundwater flow in a bounded domain, 1: One-dimensional simulations. *Water Resour. Res.* 15(3): 521-528.

Smith, L., and R. A. Freeze. 1979b. Stochastic analysis of steady state groundwater flow in a bounded domain, 2: Two-dimensional simulations. *Water Resour. Res.* 15(6): 1543-1559.

Stephens, D. B., and S. H. Heerman, 1988. Dependence of anisotropy on saturation in a stratified sand. *Water Resour. Res.* 24(5): 770-778.

Sudicky, E. A. 1986. A natural gradient experiment on solute transport in a sand aquifer: spatial variability of hydraulic conductivity and its role in the dispersion process. *Water Resour. Res.* 22(13), 2069-2082.

Vanmarcke, E. 1983. *Random Fields: Analysis and Synthesis.* Cambridge, Massachusetts: Massachusetts Institute of Technology Press.

Wierenga, P. J. 1988. Validation of flow and transport mdoels at the Jornada test facility. *Validation of Flow and Transport Models for the Unsaturated Zone.*

P. J. Wierenga and D. Bachelet, eds. Report 88-SS-04. Las Cruces, New Mexico: New Mexico State University: 525-530.

Yeh, T.-C. J. 1989. One-dimensional steady state infiltration in heterogeneous soils. *Water Resour. Res.* 25(10): 2149-2121.

Yeh, T.-C., L. W. Gelhar, and A. L. Gutjhar. 1985a. Stochastic analysis of unsaturated flow in heterogeneous soils: (1) Statistically anisotropic media. *Water Resour. Res.* 21(4): 447-456.

Yeh, T.-C., L. W. Gelhar, and A. L. Gutjhar. 1985b. Stochastic analysis of unsaturated flow in heterogeneous soils: (2) Statistically anisotropic media with variable α. *Water Resour. Res.* 21(4): 457-464.

Yeh, T.-C., L. W. Gelhar, and A. L. Gutjhar. 1985c. Stochastic analysis of unsaturated flow in heterogeneous soils: (3) Observations and applications. *Water Resour. Res.* 21(4): 465-471.

Zaslavasky, D., and G. Sinai. 1981. Surface hydrology: III. causes of lateral flow. *J. Hydraul. Div. ASCE* 107 (HY1): 37-52.

7. GEOCHEMICAL NATURAL ANALOGS

by English C.Pearcy, William M. Murphy, and James D. Prikryl

Investigators: English C. Pearcy (CNWRA), William M. Murphy (CNWRA), Ronald T. Green (CNWRA), and James D. Prikryl (CNWRA)

7.1. Technical Objectives

The Geochemical Natural Analog Research Project is designed to provide knowledge of the state of the art in natural analog studies applied to contaminant transport, to conduct investigations of a specific site or sites, and to permit evaluation of the use of analog data to support modeling appropriate for performance assessment of a Yucca Mountain repository. Task 1 of the project, "Literature Review," was completed with the submission of the report entitled "Geochemical Natural Analog Literature Review" (Pearcy and Murphy, 1991a). The first activity within Task 2, "Identification of Site and Development of Workplan," has been completed with the submission of a workplan report for the Peña Blanca natural analog. The remainder of Task 2 will consist of field evaluation of the Akrotiri natural analog; this work is planned for 1992 when the Akrotiri site will next be available for direct observation.

Objectives of Task 2 included selection of a site at which to conduct analog research likely to yield information relevant to processes and events controlling contaminant transport in the proposed high-level nuclear waste (HLW) repository at Yucca Mountain, Nevada, and development of a workplan to obtain that information. These objectives were partially met through literature review (Pearcy and Murphy, 1991a) and the conduct of field research (Pearcy and Murphy, 1991b). Further evaluation of the Peña Blanca analog site and development of a workplan (Pearcy and Murphy, 1991c) required an initial assessment of the mineralogy of the ore and host rocks and determination of the gross chemistry of the host rocks.

7.2. Research Results During the Second Quarter of 1991

During this quarter, laboratory work (optical microscopy, electron microscopy, X-ray diffractometry, and inductively-coupled plasma emission spectrometry) was conducted on samples from the Peña Blanca analog site to characterize the ore and host rock petrography, mineralogy, and chemical composition. Based on these laboratory studies, on field research conducted at the site, and on information available in the literature, a workplan for natural analog research at the Peña Blanca site was developed (Pearcy and Murphy, 1991c). In this report, the results of the laboratory analyses and preliminary interpretations of the data are presented. Additionally, empirical source-term constraints for radioelement migration derived from the Peña Blanca work to date are discussed.

7.2.1. Peña Blanca Host Rock Mineralogy

Among the several uranium deposits present in the Peña Blanca district, the Nopal I deposit has been chosen for analog investigation (Pearcy and Murphy, 1991c). The

deposit occurs in tertiary-age tuffaceous host rocks of the Nopal and Coloradas Formations. Initial petrographic studies indicate that the Nopal Formation is a rhyolitic tuff, densely welded and hematitic in unaltered zones, with a lithic vitrophyre at its base. Unaltered tuff consists of phenocrysts of quartz, feldspar, and biotite, and of minor volcanic fragments in a devitrified groundmass of cryptocrystalline quartz and feldspar. X-ray diffraction analyses indicate that sanidine is the predominant feldspar phase in the groundmass. Vitroclastic textures and eutaxitic (flattening and welding of glass shards parallel to the depositional plane) structures are often preserved in the groundmass, suggesting deposition by pyroclastic air fall. Phenocryst content ranges from 10 to 20 percent, and partial alteration of phenocrysts, generally to kaolinite, is common. Removal of hematite and total alteration of phenocrysts to clays and calcite characterize tuff altered by hydrothermal solutions associated with the ore body.

Where preserved, the basal Nopal vitrophyre consists of lithic volcanic fragments along with phenocrysts of quartz and feldspar in a partially devitrified groundmass of perlitic glass and cryptocrystalline quartz and feldspar. Calcite-infilled microfractures are pervasive in the groundmass and volcanic fragments.

The Coloradas Formation underlies the Nopal Formation and also hosts uranium mineralization at the Nopal I deposit. The Coloradas is a reddish, lithic-crystal rhyolitic tuff with well-developed eutaxitic textures. The tuff is densely welded and consists of volcanic fragments and phenocrysts in a devitrified groundmass of cryptocrystalline quartz and sanadine. Volcanic fragment content ranges from 15 to 20 percent. Phenocryst content ranges from 2 to 5 percent and includes quartz, alkali feldspar, plagioclase, and rare biotite. Most phenocrysts and lithoclasts have undergone partial or complete replacement by clays (kaolinite), calcite, and/or alkali feldspar. Unaltered Coloradas tuff is hematitic and red whereas weathered tuff is tan or light brown in color.

7.2.2. Peña Blanca Uranium Ore Mineralogy

Preliminary petrographic analyses indicate formation of the Nopal I deposit by emplacement of uranium minerals in fractures, cavities, and intergranular spaces within brecciated host rocks. The uranium mineralization is compositionally and texturally complex ranging from primary uraninite to uranyl silicate minerals. Initial X-ray diffraction analyses have identified uranophane [$Ca(UO_2)_2Si_2O_7 \bullet 6H_2O$)], soddyite [$(UO_2)_2SiO_4 \bullet 6H_2O$], and weeksite [$K_2(UO_2)_2Si_6O_{15} \bullet 4H_2O$)] as major uranyl silicate phases present in the deposit. Textural evidence suggests that the primary uraninite has been partially replaced by secondary oxidized corrosion products. Remnant pods of uraninite are irregularly shaped and have maximum dimensions on the order of 1 to 2 centimeters; most are on the order of millimeters. Oxidation of the uraninite appears to have occurred both by pervasive replacement of the microcrystalline aggregate, as indicated by deep embayments in the remnant uraninite bodies, and by dissolution and reprecipitation along microfractures within the uraninite masses.

7.2.3. Chemical Composition of the Nopal and Coloradas Formations

Samples of the Nopal and Coloradas Formations were analyzed by inductively coupled plasma emission spectrometry (ICP) to determine major oxide abundances. The results are shown in Table 7-1 and Figures 7-1 and 7-2. These analyses show that the Nopal Formation is a peraluminous, high-silica rhyolitic tuff. The Coloradas Formation is also a rhyolitic tuff, but the silica content is significantly lower. Other differences between the Nopal and the Coloradas include lower K_2O and Na_2O contents in the Coloradas as well as higher CaO abundance and a greater proportion of volatile species [reflected in the loss on ignition (LOI) percentage]. Comparison of the Nopal Formation composition with that of the Topopah Spring Member of the Paintbrush Tuff Formation (the proposed repository horizon at Yucca Mountain) illustrates a high degree of chemical similarity between the two units (Figure 7-1). The differences noted above between the Nopal Formation and the Coloradas also distinguish the Coloradas and the Topopah Spring Member, but these differences are relatively small (Figure 7-2).

7.3. Preliminary Source Term Constraints Based on the Peña Blanca Analog

The source term for nuclear waste repository performance assessments can be constrained by the solubilities of radioelement-bearing solids and/or the rates of release of radioelements from nuclear waste forms (Murphy and Pearcy, 1991). Both solubility and rate limits for the proposed repository at Yucca Mountain, Nevada, can be assessed using information from the natural analog at Peña Blanca, Mexico. Both the proposed repository horizon at Yucca Mountain and the uranium deposits at Peña Blanca are in the oxidizing, hydrologically unsaturated zone hundreds of meters above the water table (Pearcy and Murphy, 1991a; Pearcy and Murphy, 1991b). As discussed above, primary uraninite in the Nopal I deposit at Peña Blanca has been largely altered to a suite of uranyl silicate minerals. On both a structural and compositional basis, uraninite constitutes an excellent analog of the spent nuclear fuel waste form proposed for Yucca Mountain. Alteration of uraninite and formation of a secondary uranium phase assemblage at Nopal I is analogous to spent-fuel degradation processes expected to occur in the Yucca Mountain environment.

7.3.1. Solubility and Rate Limits

Thermodynamic calculations show that uraninite is unstable in an oxidizing silicic environment. Partial equilibrium reaction-path simulations of uraninite and/or spent fuel dissolution in model groundwaters for the unsaturated zone at Yucca Mountain indicate that uranyl silicate minerals would control the equilibrium aqueous concentration of uranium. However, a review of experimental and estimated thermodynamic and kinetic data for uranyl silicate mineral dissolution reveals that large uncertainties preclude accurate predictions of uranium solubilities or the solubility-controlling phases. The presence of soddyite, uranophane, and weeksite determined by petrographic and x-ray diffration studies suggests that these minerals control the groundwater uranium concentrations. If the conditions under which these minerals formed were similar to those anticipated for the Yucca Mountain repository,

Table 7-1. COMPARISON OF THE CHEMICAL COMPOSITION OF THE NOPAL FORMATION, THE COLORADAS FORMATION AND THE TOPOPAH SPRING MEMBER OF THE PAINTBRUSH TUFF FORMATION (VALUES IN WEIGHT PERCENT)

Oxide	Nopal Formation	Coloradas Formation	Topopah Spring Member *
SiO_2	75.24	67.49	74.00
Al_2O_3	12.75	12.00	12.40
K_2O	6.48	4.13	4.00
Fe_2O_3	1.54	1.99	1.07
Na_2O	1.07	0.47	3.40
CaO	0.41	4.41	0.66
TiO_2	0.26	0.24	0.10
MgO	0.15	0.16	0.31
P_2O_5	0.07	0.04	0.01
MnO	0.06	0.11	0.08
LOI	2.60	8.17	3.79
Total	100.63	99.21	99.82

*Data from Broxton et. al. (1986)

then they could be expected to control aqueous uranium concentrations in the repository near-field environment and affect the source term for radioelement release.

Petrographic, thermodynamic, and kinetic data indicate that oxidation of uraninite to pitchblende, oxidative dissolution of pitchblende, incongruent precipitation of uranyl silicates, and transport of uranium into the geologic surroundings at Nopal I occur in kinetic series. Therefore, the occurrence of a large quantity of uranyl silicates surrounding remnant pods of the antecedent reduced uranium oxide in this deposit implies that the rate of uraninite oxidation and formation of the uranyl silicate assemblage has exceeded the rate of uranium transport out of the mineralized zone. Pitchblende dissolution appears not to control the rate of removal of uranium from the Nopal I system. Relatively rapid pitchblende oxidation is also supported by the common occurrence of ore deposits in the Peña Blanca district in which relict textures indicate primary reduced mineralization, but in which only

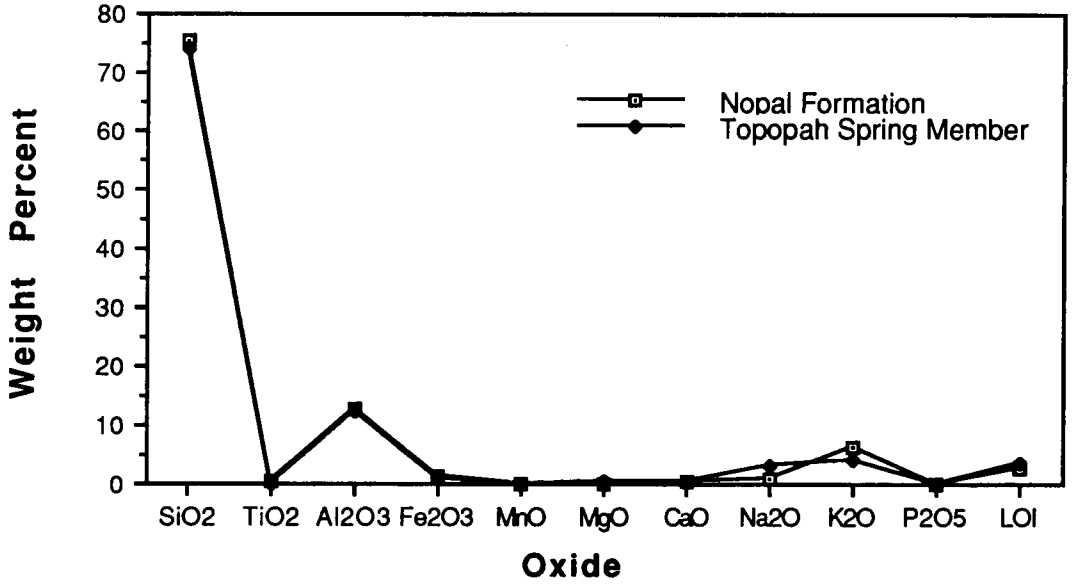

Figure 7-1. Compositions of the Nopal Formation and Topopah Spring Member of the Paintbrush Tuff Formation

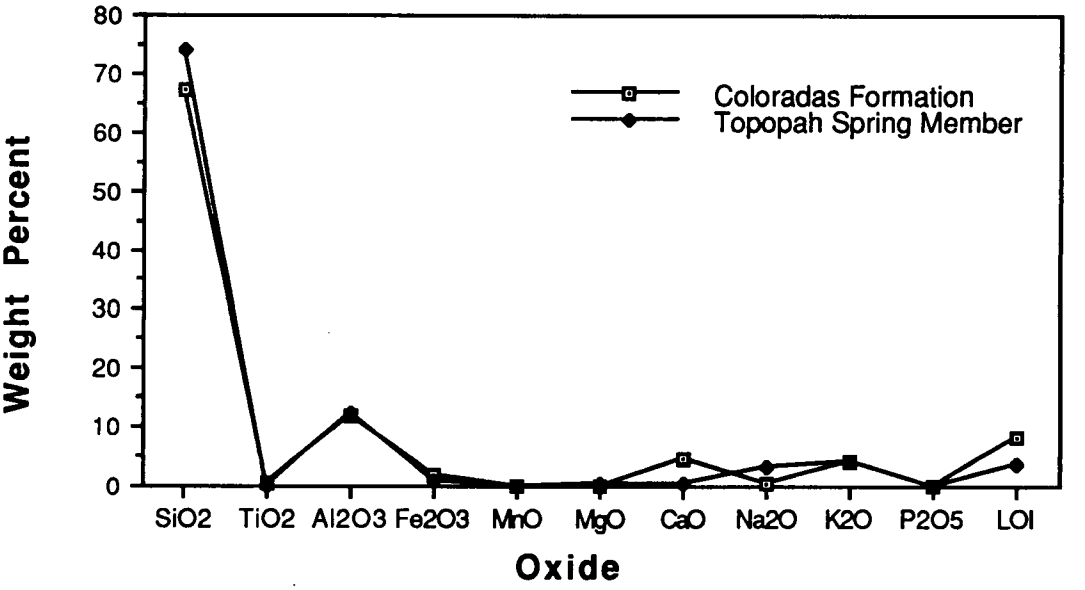

Figure 7-2. Compositions of the Coloradas Formation and Topopah Spring Member of the Paintbrush Tuff Formation

oxidized uranium silicate minerals (and gangue) remain. Although pitchblende dissolution does not appear to control the rate of uranium removal, it may control release of trace elements that are not incorporated in secondary solids.

An upper limit on the rate of uranium oxidation at Nopal I is given by the ratio of the maximum possible amount of primary uraninite to the minimum time available for oxidation. Geometric and geologic interpretations of the ore deposit at Nopal I can provide estimates for these limiting values. For example, the maximum amount of uraninite oxidation can be estimated assuming the uranium ore was entirely reduced initially and the current size of the orebody (322 equivalent metric tons of UO_2; George-Aniel et al., 1991) reflects its original size. Uplift rates in the Basin and Range are on the order of millimeters/year; the most rapid rate of unroofing (i.e., motion of a point relative to an erosion surface) calculated for the Basin and Range is about 1 centimeter/year (B. Wernicke, personal communication). At present, the orebody at Nopal I is at least 200 m above the local water table, based on field measurements. Assuming that 1 centimeter/year is the maximum limit on the uplift rate relative to the water table and 200 meters is the minimum limit on distance, and supposing conservatively that no oxidation occurred before the ore emerged above the water table, then the minimum period for oxidation is 20,000 years. Pods of unoxidized uraninite remaining in the ore at Nopal I demonstrate that complete oxidation has not occurred in a shorter time period. With these parameters, oxidation of the entire 322 tons of UO_2 over a period of 20,000 years defines an oxidation rate of 0.016 tons of UO_2 per year (or 10^{-7} fraction of the original inventory per day) as the fastest geologically reasonable rate. Remarkably, this estimate is similar to oxidative dissolution rates for spent fuel estimated from laboratory experiments (10^{-7} to 10^{-8} per day; Grambow et al., 1990).

7.4. Conclusions

Applications of source-term constraints derived from the Peña Blanca analog to performance assessment of the Yucca Mountain repository must be judicious. Additional work is required to establish the physical conditions of uranium oxidation at Peña Blanca (e.g., temperature, hydrologic saturation, fluid compositions, timing) and the consequent implications for relevance of the natural data to the Yucca Mountain system. Also, assumptions in the limiting rate analysis require further testing (e.g., the oxidation state of primary uranium, and the geologic history of oxidizing conditions). Nevertheless, this work demonstrates that corroborative information with respect to solubility-controlled radionuclide concentrations and the rate of spent-fuel oxidation at the proposed Yucca Mountain repository may be obtained through geochemical and geologic analyses of the Peña Blanca system. UO_2 oxidation and transformation to secondary uranyl silicate minerals appear to be rapid relative to mass transport of uranium out of the Peña Blanca system. The rate-limiting process is likely to be transport in fluids with uranium contents controlled by interactions with uranyl silicate minerals such as uranophane, soddyite, and weeksite.

7.5. References

Broxton, D. E., R. G. Warren, R. C. Hagan, and G. Luedemann. 1986. Chemistry of diagenetically altered tuffs at a potential nuclear waste repository, Yucca Mountain, Nye County, Nevada. LANL. LA-10802-MS. Los Alamos, New Mexico: Los Alamos National Laboratory (LAML).

George-Aniel, B., J. L. Leroy, and B. Poty. 1991. Volcanogenic uranium mineralization in the Sierra Peña Blanca District, Chihuahua, Mexico: three genetic models. *Economic Geology* 86:233-248.

Grambow, B., L. O. Werme, R. S. Forsyth, and J. Bruno. 1990. Constraints by experimental data for modeling of radionuclide release from spent fuel. *Materials Research Society Symposium Proceedings* Vol. 176. Pittsburg: Materials Research Society (MRS) 465-474.

Murphy, W. M., and E. C. Pearcy. 1991. Source-term constraints for the proposed repository at Yucca Mountain, Nevada, derived from the natural analog at Peña Blanca, Mexico. *Scientific Basis for Nuclear Waste Management.* Pittsburg: MRS. Abstract submitted for NRC review.

Pearcy, E. C., and W. M. Murphy. 1991a. *Geochemical Natural Analogs Literature Review.* CNWRA 90-008 (draft). San Antonio, Texas: Center for Nuclear Waste Regulatory Analyses (CNWRA).

Pearcy, E. C., and W. M. Murphy. 1991b. Geochemical natural analogs. W. C. Patrick, ed. *Center for Nuclear Waste Regulatory Analyses Report (CNWRA) on Research Activities for the Quarter January 1 through March 31, 1991.* CNWRA 91-01Q. San Antonio, Texas: CNWRA.

Pearcy, E. C. and W. M. Murphy. June, 1991c. *Site Selection and Workplan Report for the Geochemical Natural Analog Research Project.* Center for Nuclear Waste Regulatory Analyses (CNWRA), San Antonio, Texas: CNWRA.

8. PERFORMANCE ASSESSMENT RESEARCH

by Budhi Sagar and Gordon Wittmeyer

PHASE 2 INTRAVAL PROJECT: LAS CRUCES TRENCH SOLUTE TRANSPORT MODELING STUDY, PLOT 2, EXPERIMENT A

Investigators: Budhi Sagar (CNWRA) and Gordon Wittmeyer (CNWRA)

8.1. TASK OBJECTIVES

The objective of this task is to use the PORFLO-3, Version 1.2 (single-phase version) computer code to simulate the flow of water and transport of tracers (bromide and tritium) at the Las Cruces Trench site in New Mexico. Based on the work reported in the previous quarterly research report, the objectives of this task have been expanded to include a study of the relation of various performance measures (e.g., ground water travel time and contaminant flux) to strategy for model validation. This work is performed under task 7 (Methodology for Validation of Models) of the Performance Assessment (PA) Research project plan. The Las Cruces Trench experiment data used in this study are identified as Test Case 10 for Phase 2 of the INTRAVAL project. This experiment has been specially designed for model validation purposes and extensive data have been accumulated.

8.2. TECHNICAL OBJECTIVES

Specific technical objectives of this task are as follows:

- Develop conceptual and mathematical models of the unsaturated flow and transport processes observed during the Plot 2a Experiment performed at the Las Cruces Trench. Development of the conceptual model includes determining the relevant physical processes and the appropriate set of partial differential equations which describe these processes, locating model boundaries and describing the physical conditions at the boundaries, and determining the initial values of pressure and solute concentration in the area to be modeled.

- Develop a suite of auxiliary computer codes to assist in the construction of input data sets for PORFLO-3. In particular, these codes are required to facilitate mapping the location of neutron probes, tensiometer and suction lysimeter measurement points, and the location of zones in which soil hydraulic properties were measured to the block-centered finite difference mesh assembled for PORFLO-3.

- Calibrate the model both for flow of water and transport of tracers by adjusting boundary and initial conditions, soil hydraulic property zones and associated property values, and sorptive and dispersive properties assigned to the model.

- Use the model calibrated on the Plot 2a experiment data to predict the movement of tritium, bromide, boron, chromium, pentafluorobenzoic acid, and 2,6-difluorobenzoic acid applied with the water during the Plot 2b experiment.

- Study the effects of smoothing the observed soil hydraulic properties data on model predictability. Start from no smoothing to assuming a single homogeneous layer will allow determination of the degree of resolution in the model's structure needed to adequately model the movement of the solute.

- Develop model validation strategies which are based on specific site performance measures such as groundwater travel time (GWTT) and integrated mass flux at a compliance boundary. This work will aid in developing methods that can be used to define the precision with which the shape and movement of a contaminant plume need to be described in order to accurately assess integrated performance measures at a compliance boundary.

- Establish guidelines that prescribe the requisite degree of site characterization for computing integrated performance measures with a specified level of certainty, based on the existing description of the heterogeneity of the site.

8.3. DESCRIPTION OF EXPERIMENT AND OBSERVED DATA

8.3.1. Experimental Setting

The experimental trench is located northeast of Las Cruces, New Mexico, on the New Mexico State University College Ranch near the north end of the Doña Ana Mountains. The climate at the experiment site is semi-arid. Class A pan evaporation is 239 cm per year, while average annual precipitation is only 23 cm, over half of which falls during the summer monsoon season. As shown in Figure 8-1, the trench is 26.4 meters long, 4.8 meters wide, and 6 meters deep. Plot 2, located adjacent to the north face of the trench, is irrigated by an array of 80 drip lines aligned parallel to the trench face and covering a surface strip 12 meters long and 1.2 meters wide. During the Plot 2a experiment, water was applied to the strip at a rate of 0.43 cm/day for 75.5 days. Tritium and bromide were applied to the strip during the first 11.5 days at concentrations of 0.1mCi/l and 0.8g/l, respectively. Water content was monitored by neutron probes through the network of access tubes shown in Figure 8-1; matric potential was monitored by tensiometers installed in the face of the trench, and solute samples were obtained using suction lysimeters installed in the trench face. Locations of soil samples for which the hydraulic properties were measured are shown in Figure 8-2.

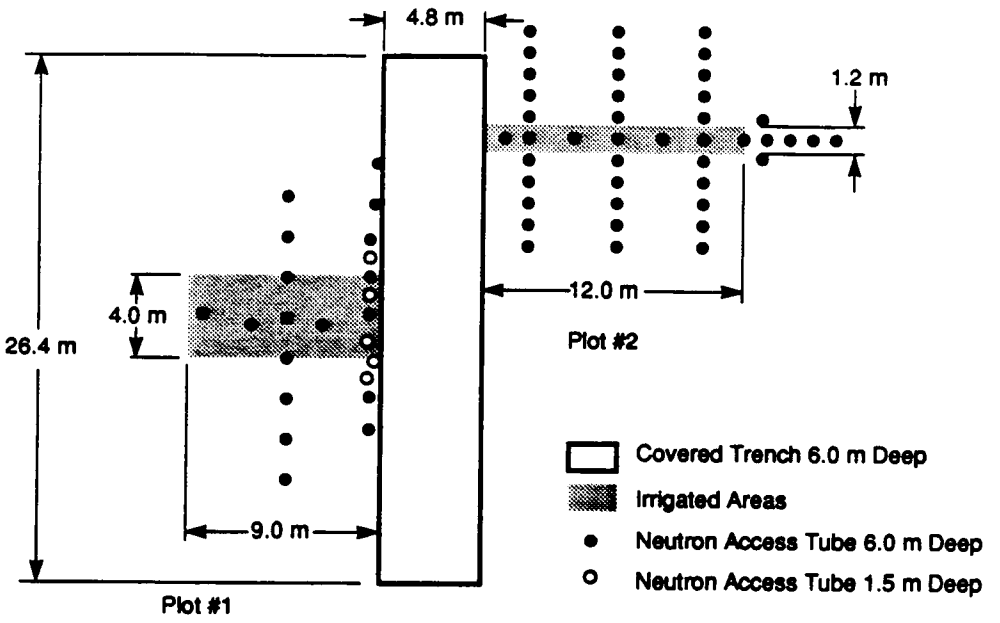

Figure 8-1. Plan view of Las Cruces Trench Site

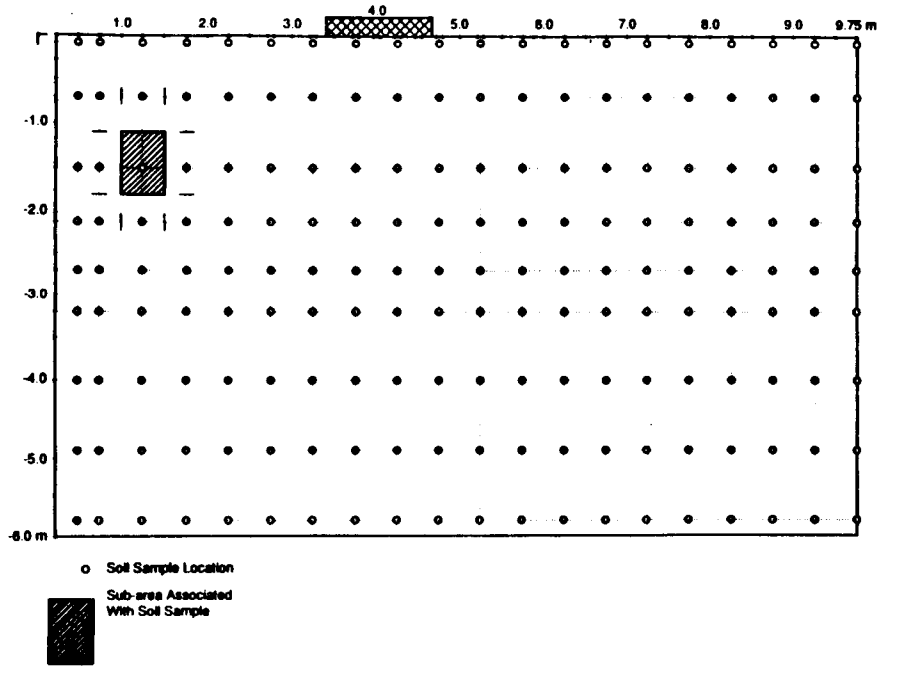

Figure 8-2. Soil-sample locations and model material zones

8.3.2. Observed Data

Extensive data, many more than are normally expected to be available at any waste disposal site, have been collected in the Las Cruces trench experiment. The Las Cruces Data Base is accessible by FTP at HELEN.NMSU.EDU (128.123.3.7) with username SOILS and password LASCRUCES. A description of each file in the database is given in the files 1_README.TXT and 2_README.TXT. Soil-hydraulic properties consist of measured and estimated parameters for the van Genuchten model. These data are listed by soil sample in the file VGPARM.DAT. The x, y, and z coordinates of each soil sample are contained in the file SAMPLOC.DAT. The measured water-content data from the Plot 2a experiment are listed by day, neutron-probe access-tube number, and the z coordinate of the neutron probe in the file THETA2.DAT. The x and y coordinates of each neutron access tube are listed in the file TUBELOC2.DAT. Measured relative concentrations for bromide and tritium are listed by day and solution sampler number in the files BR2.DAT and TRIT2.DAT, respectively. The x, y, and z coordinates of each suction lysimeter are listed in the file SOLLOC2.DAT.

8.4. CONCEPTUAL MODEL DESCRIPTION

Since the completion of the previous quarterly report, three new model simulations were performed in order to rectify noted inconsistencies in the initial suction and to more directly address the performance measure based validation strategy. The three models differ only in the degree to which measured soil hydraulic property data, and measured initial water contents are incorporated into the model. For ease of discussion, the simulations are referred to by their NQS batch queue numbers, as outlined in Table 8-1. The first simulation, designated by RUN 6024, employs all of the measured soil hydraulic-properties data and initial water content data from neutron probes with minimum smoothing. The second simulation, designated as RUN 6527, uses the same high resolution soil hydraulic property description as RUN 6024; but its initial conditions are based on measurements of matric potential made with tensiometers and thermocouple psychrometers. The third simulation, designated as RUN 6602, has initial conditions identical to those of RUN 6527; however, the soil hydraulic properties are represented by a single homogenous unit. The exact description of the soil hydraulic property zonation and definition of the initial conditions used for each simulation are described in more detail below.

In Experiment 2a, water and solute are applied in a thin surface strip. From the perspective of modeling, the thin strip can be thought of as a line source from which both the water and the solute migrate. Assume that in a cartesian coordinate system, the y-coordinate direction coincides with the line source. Considering the layout of the experiment, it is then a fair assumption that the migration of the fluid and tracer will be mostly in the x-z plane. Furthermore, soil-property variations in the y-direction are not measured. Therefore, as a first approximation, it was decided that a 2-D model of flow and transport in the x-z plane was adequate. A three-dimensional simulation may be undertaken later to study the effect of this assumption. In the x- and z-directions, the model domain extends from the northwest corner of the trench 975 cm to the east and from the ground surface down 579 centimeters. In order to

Table 8-1. TRENCH SIMULATION COMPUTER RUNS

Simulation	Material Zones	Initial Conditions
RUN 6024	180 Zones	Based on measured water contents
RUN 6527	180 Zones	Thermocouple psychrometers and tensiometers
RUN 6602	1 Zone	Thermocouple psychrometers and tensiometers

be able to assign measured properties to measurement locations, the finite difference mesh was designed so that computational nodes were coincident with both tensiometer and suction lysimeter locations.

The van Genuchten parameters were estimated or measured on 594 collected soil samples. Of these 594 samples, 180 lie within the modeled domain and have complete records of the van Genuchten parameters-- α, n, θ_s, and θ_r --and the saturated hydraulic conductivity, K_s. To use these property data without any smoothing, a high-resolution model was constructed in which the model domain was made up of 180 material zones. The boundaries of each one of these material zones in the finite difference mesh were determined by drawing right bisectors through the lines joining the measurement points. In this manner, rectangular zones are obtained, one of which is shown in Figure 8-2. This 'blocky' soil hydraulic property structure was used for both RUN 6024 and RUN 6527. The van Genuchten parameters as well as mass transport properties were assumed to be uniform at all nodes within each material zone. For RUN 6602, a second model was constructed in which the soil hydraulic properties were defined to be spatially homogeneous and equal to the mean values of the measured soil hydraulic property data. Other deterministic and stochastic interpolation techniques for the interpretation of the hydraulic data should also be investigated.

Initial pressure heads for RUN 6024 were determined from the neutron-probe measurements of water content made in the neutron-probe access tubes which lie in a vertical plane 2 meters north of the trench face. The pressure levels were calculated from the van Genuchtn model, which relates water content to matric potential. The same procedure described above for defining material zones for RUN 6024 and RUN 6527 was used to define quadrilateral zones centered on each water-content measurement location within which the initial water content was defined to be constant. Both the soil-hydraulic-property material zone and initial water-content material zone in which each node in the computational grid resides were determined, and the appropriate initial water content and van Genuchten parameters were then assigned to that node.

The initial matric potential, ψ_m, was computed from the van Genuchten model relating water content, θ, and ψ_m. In many cases the water content measured with the neutron probe was less than the estimated residual water content, θ_r. Inasmuch as the residual water-content values from the soil samples were defined to be the water content of the soil after reaching equilibrium in a pressure chamber fitted with a 15-bar porous pressure-plate (15,300 cm H_2O), if $\theta < \theta_r$, then ψ_m=-15300 cm H_2O. Moreover, it was decided that if the computed initial matric potential at any node was less than -15300 cm H_2O, the initial matric potential at that node would be set to -15300 cm H_2O.

Thermocouple psychrometer measurements of matric potential of soil samples retrieved during installation of neutron probe-access holes at depths greater than 210 cm exceeded 65,000 cm. of water. To assess the effect of these higher matric potentials, a second set of initial conditions based on these thermocouple psychrometer and additional tensiometer measurements was constructed for RUN 6527 and RUN 6602. For both of these simulations, the initial pressure heads were assumed to be constant along any horizontal transect. The variation of the initial matric potential along any vertical transect was determined by linear interpolation between adjacent measurement points. The initial pressure heads were determined simply by adding the position head, z, of the node to the computed initial matric potential, $\psi = \psi_m + z$.

Boundary conditions for the pressure-head variable, ψ, is defined to be no-flow type, $K(\psi_m)\nabla(\psi_m+z)\cdot\mathbf{n} = 0$, except at the bottom of the model and at the portion of the surface where the strip was located. On the bottom boundary of the model, the negative of the pressure head gradient is directed downwards and has magnitude 1 to simulate gravity drainage. At the strip source, the boundary condition is a Neuman type, $K(\psi_m)\nabla(\psi_m+z)\cdot\mathbf{n} = q$. During the first 75.5 days of the simulation, q=0.43 cm/day; then the flux changed to q=0.

Boundary conditions for the concentration variable, c, are defined to be no-flux type at all nodes except where the strip source was located. The no-flux at the boundary means only that the diffusive and dispersive fluxes are zero. Tracer mass crossing the boundary along with convecting water is never put to zero even when a no-flux boundary condition is applied. During the first 11.5 days of simulation, a Dirichlet, or prescribed concentration boundary condition, was used to simulate the presence of dissolved bromide ion in the infiltrating water. To simulate the abrupt cut-off of dissolved bromide in the infiltrating water after 11.5 days, two alternative boundary conditions were tried initially. In the first case, the boundary condition at the strip after 11.5 days was changed to no-flux. In the second case, keeping all other boundary conditions the same, the boundary condition at the strip was changed to a Dirichlet zero concentration condition. The results from the first case failed to duplicate the observed detachment of the measured bromide plume from the strip source. The second case, on the other hand, was able to effect the observed detachment of the plume and was used for all three simulations described herein.

No data on mass transport properties such as dispersivities were available. As discussed later in the section on model results, an attempt was made to characterize the time-dependent longitudinal and transverse dispersion by plotting the second moments of the observed bromide

plume versus time. At present, however, no theory is well established for stochastic unsaturated zone macro-dispersivity for use to extract the associated unsaturated zone dispersivities. Consistent with the grid dimensions, longitudinal dispersivity of 1 cm and transverse dispersivity of 0.1 cm were assumed. The coefficient of molecular diffusion was assumed to be 10^{-3} cm^2/sec.

For all three simulations, the finite-difference mesh used for the PORFLO-3 runs consisted of 87 nodes in the x-direction, 3 nodes in the y-direction, and 99 nodes in the z-direction. The 3 nodes in the y-direction are the minimum required to run the three-dimensional code. All nodes in the x-z planes located at the first and third y-nodes were assigned as no-flow boundary nodes to effect 2-D flow in the middle plane. In all three simulations, the grid spacing in both the x and z directions is nonuniform. In general, the grid is finer close to the strip source and gradually becomes coarser towards the boundaries. The grid spacing is also nonuniform in several regions to accommodate the spacing of the points at which material properties, initial conditions, and solution sample measurements were made.

8.5. MATHEMATICAL MODEL DESCRIPTION

As mentioned previously, the mathematical model used in this study is the PORFLO-3, Version 1.2. The theory of PORFLO-3, Version 1.0, is described by Sagar and Runchal (1990). Three main differences exist between Version 1.0 and Version 1.2. These are, first, modifications were made to Version 1.0 so that data on medium properties can be read from files external to the main input file. This modification was made to accommodate data generated to represent medium properties when these are assumed to be represented as stochastic random fields [e.g., Ababou (1990)]. This feature was not used in the study reported here. Second, Version 1.0 does implement the flux (or Neuman) boundary condition but not a gradient boundary condition. Since for partially saturated porous media, hydraulic conductivity is a function of saturation, implementation of flux boundaries and gradient boundaries is not the same. In Version 1.2, the implementation of gradient boundary condition was added. This feature was used in setting the lower boundary condition in this study. Finally, third, in Version 1.0, the finite difference formulation is based upon a pressure-based partial-differential equation. This has been found to provide unsatisfactory local mass balance, especially when large time steps were taken in the presence of sharp fronts. To remedy this situation, the discretization was changed to consider a mixed, saturation-pressure based equation. In the mixed equation, the time derivative is kept as a function of moisture content while all the remaining terms are functions of pressure (Celia, 1990). As reported by Rockhold and Wurstner (1991), this formulation of PORFLO-3 provides almost perfect local mass balance.

Because of the rather large amount of input data to be processed, preprocessors were written for this specific problem. These preprocessors were used to read the data directly from the data bases described in Section 8.3.2 and write to a PORFLO-3 input file.

8.6. SIMULATION RESULTS

8.6.1. Comparison of Bromide Plume

All simulations of Experiment 2a were performed using the CRAY X-MP/216 at the Idaho National Engineering Laboratory (INEL) operated for the U.S. Department of Energy (DOE) by the Computer Operations and Data Processing Group (CO&DP) of EG&G Idaho, Inc., in Idaho Falls, Idaho. Output from the simulation runs were analyzed graphically by constructing color contour plots of pressure head, water content, and bromide concentration at various times. These contour plots were constructed using the TECPLOT plotting package on a Silicon Graphics IRIS 4D/210 VGX work station. The measured water content and bromide concentration data were also contoured using the TECPLOT package. For the measured data, the data had to be interpolated to a regular grid using the IMSL routine SURF prior to contouring with TECPLOT.

Contour plots of the measured bromide plumes at 30, 50, 71, and 481 days of the experiment are shown in Figure 8-3. Contour plots of the computed bromide plumes are shown for RUN 6024, RUN 6527, and RUN 6602 in Figures 8-4 through 8-6. As seen by visual comparison of the measured and computed plumes, the results from RUN 6602, which is the least complex (in terms of detail of heterogeneity) of the three models, best matches the overall shape and position of the observed plumes.

8.6.2. Moment Analysis

In general, the moment M of order l in x-direction and k in z-direction is defined as follows:

$$M_{lk} = \int_z \int_x \theta(x,z) C(x,z) x^l z^k dx dz \quad . \tag{8-1}$$

In Eqn. (8-1), θ and C are respectively the moisture content and concentration at a point (x,z). Using Eqn. (8-1), the x- and z-coordinates of the plume centroid can be defined:

$$X_c = M_{10} / M_{00} \tag{8-2}$$

$$Z_c = M_{01} / M_{00} \quad . \tag{8-3}$$

In general, the locus of the movement of plume centroid indicates the movement of the center of the plume. On the other hand, the second moment about the centroid represents the extent of the spread of the plume around the center. Equations for the three second moments can be written as follows.

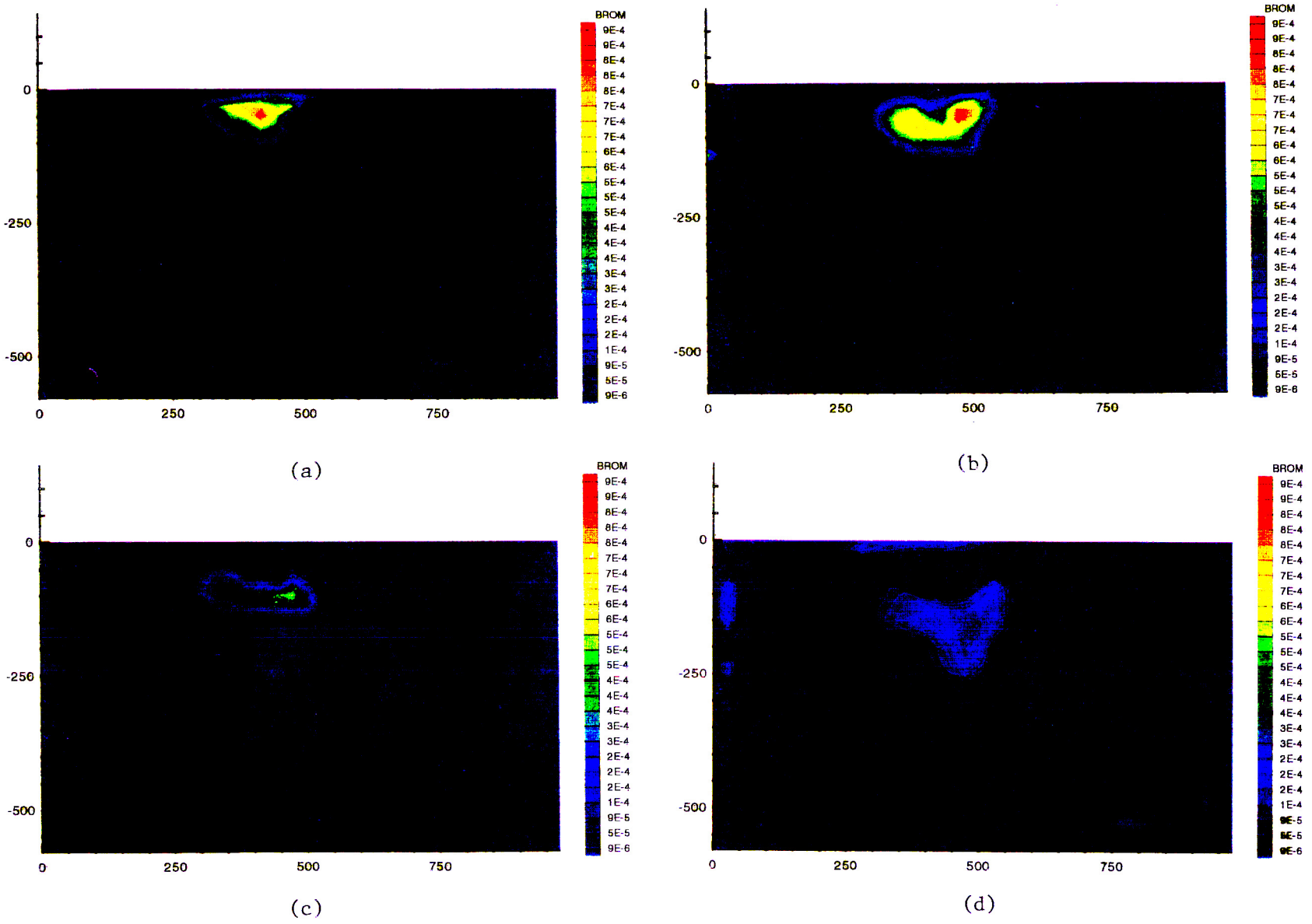

Figure 8-3. Measured bromide plume at (a) 30 days, (b) 50 days, (c) 71 days, and (d) 481 days

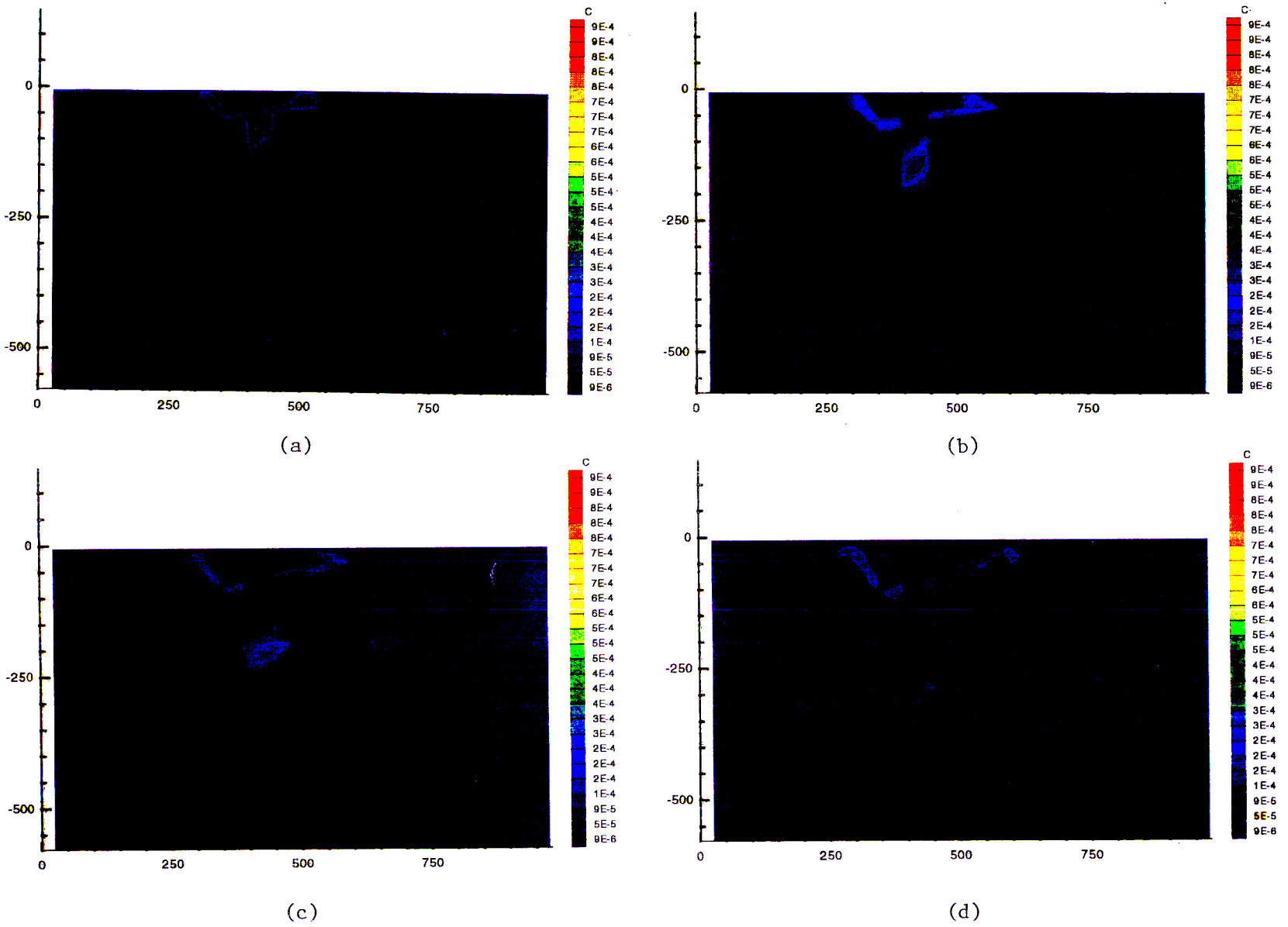

Figure 8-4. Computed bromide plume Run 6024, (a) 30 days, (b) 50 days, (c) 71 days, and (d) 481 days

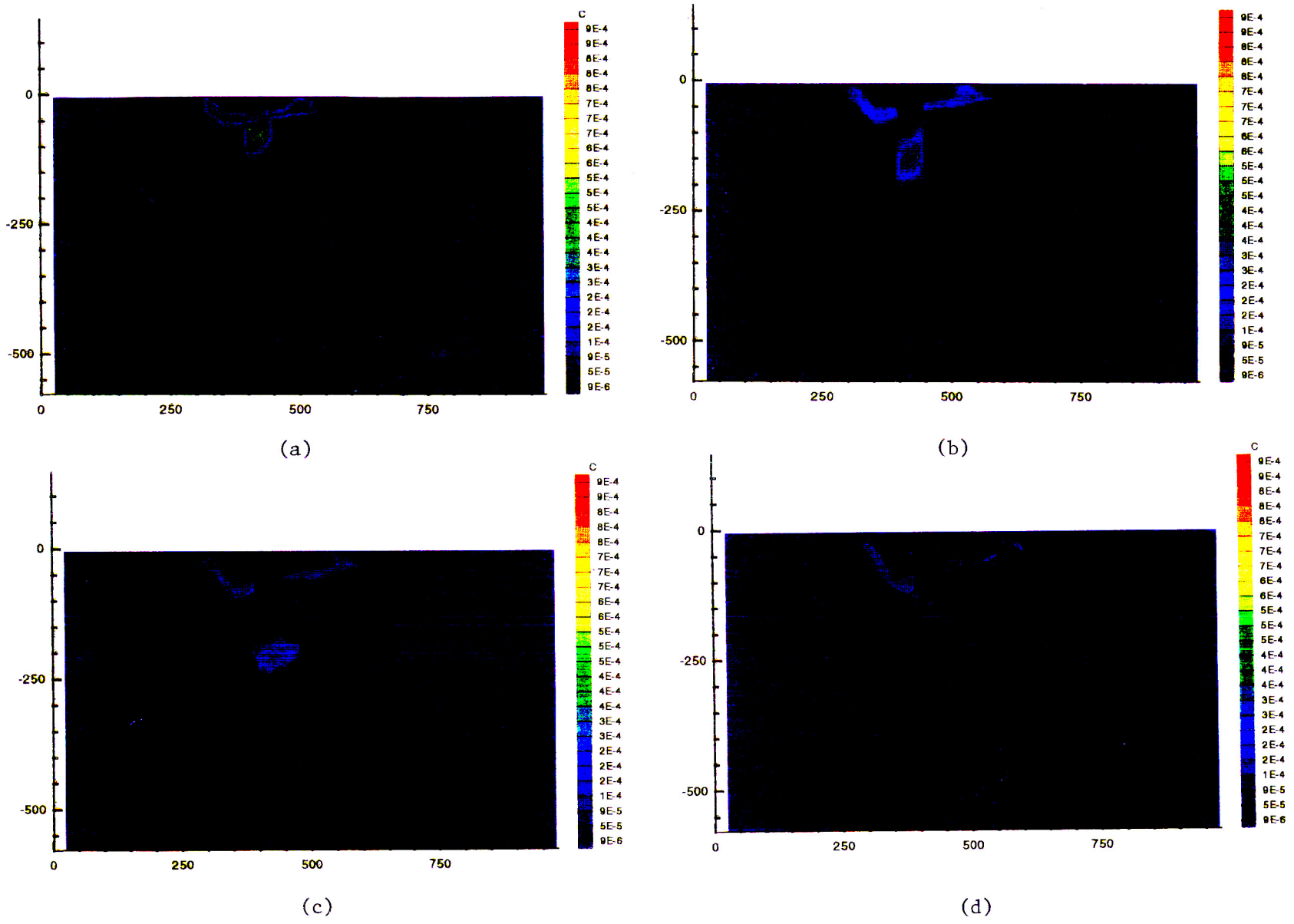

Figure 8-5. Computed bromide plume Run 6527, (a) 30 days, (b) 50 days, (c) 71 days, and (d) 481 days

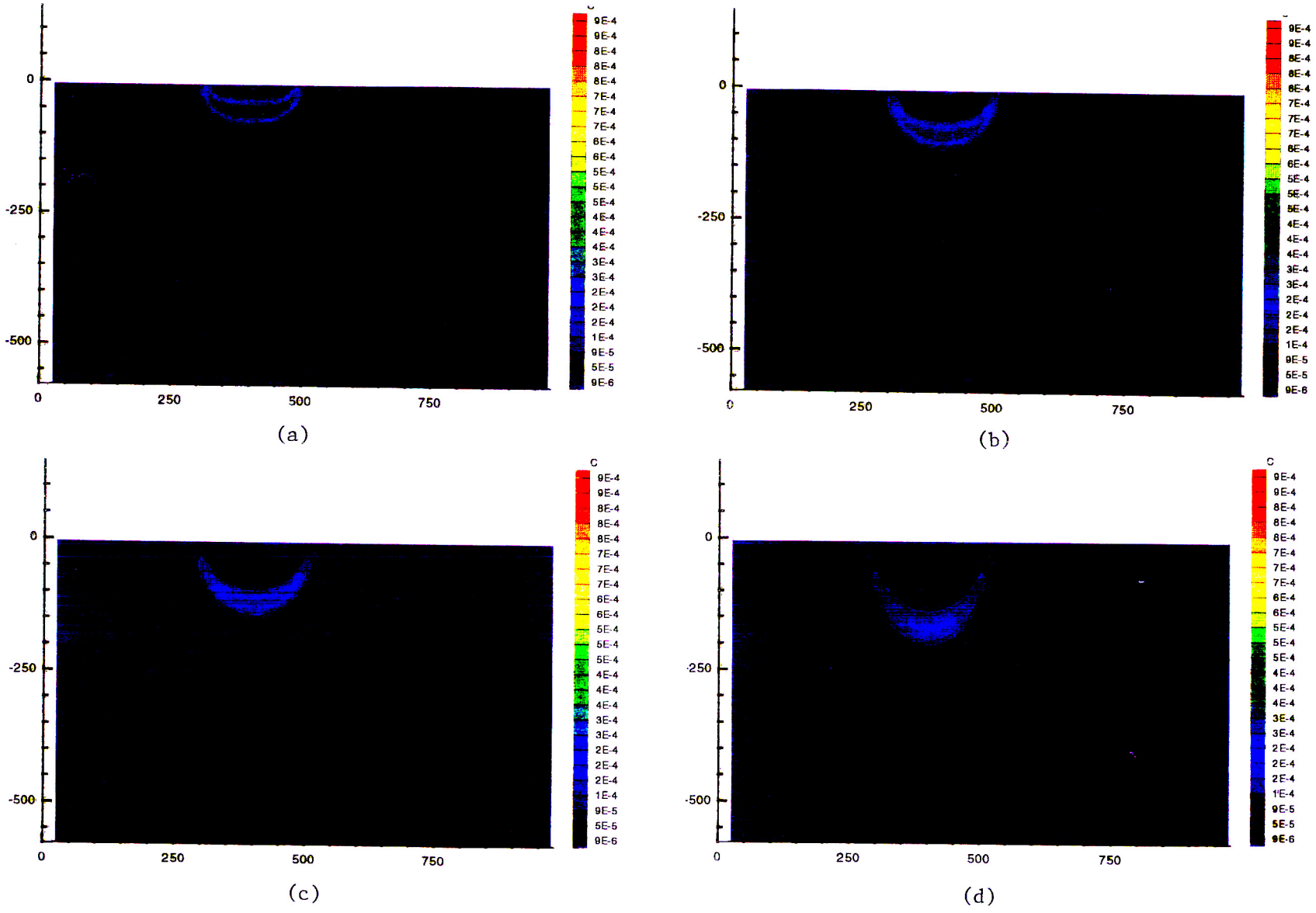

Figure 8-6. Computed bromide plume Run 6602, (a) 30 days, (b) 50 days, (c) 71 days, and (d) 481 days

$$S_{xx} = M_{20} / M_{00} - X_c^2 \tag{8-4}$$

$$S_{zz} = M_{02} / M_{00} - Z_c^2 \tag{8-5}$$

$$S_{xz} = M_{11} / M_{00} - X_c Z_c \, . \tag{8-6}$$

The square root of the second moment has units of length and are used as measures of plume spread in the following. The mixed second moment of Eqn. (8-6), although calculated, is difficult to interpret physically and is omitted from further discussion.

The somewhat surprising result described in Section 8.6.1 is further confirmed by comparing the second moments about the mean of the measured and computed bromide plumes shown in Tables 8-2 through 8-4. At days 30, 71, and 481, the transverse and longitudinal spread of the plume as measured by the standard deviations $\sqrt{S_{xx}}$ and $\sqrt{S_{zz}}$, respectively, clearly show that the plume simulated by RUN 6602 best matches the observed data plots. From this, one might conclude that, based on second moments as a comparative measure of model calibration, the model with least resolution in property description performs the best. However, such a conclusion will be wholly based on the premise that the measured bromide concentrations depict the "ground truth." In fact, because of the finite distances between solute sampling points, the plume continuum can only be sampled imperfectly. This result points to the difficulty inherent in conducting even the most carefully designed model validation experiment. A more prudent conclusion drawn from these simulations is that if the relative shape of the measured and computed bromide plumes is used as the calibration measure, the level of structural detail (i.e., variation in hydraulic properties) in the model must not, in some sense, exceed the resolution expected in plume measurement.

8.6.3. Plume Spreading and Dispersivities

A plot of the second moments of the measured plumes versus time is shown in Figure 8-7. The upper curve represents the least squares fit of a second order polynomial to the square root of the second moment about the plume centroid in the x or horizontal direction, S_{xx}, and the lower curve represents the square root of the second moment about the plume centroid in the z or vertical position, S_{zz}. For saturated flow, the apparent dispersion coefficient can be estimated by taking one half the time rate of change of the observed moments (Freyberg, 1986). The dispersivity is, in turn, estimated by dividing the apparent dispersion coefficient by the magnitude of the mean pore-water velocity. As can be inferred from Figure 8-7, the rate at which the plume spreads decreases with time; in fact some evidence indicates that at later times a slight decrease is seen in the spread of the plume. Data from the Borden experiment and theoretical curves from both the linear theory of dispersion of Dagan (1984) and the quasi-linear theory of dispersion of Neuman and Zhang (1990), --all of which are developed for saturated flow regimes--, show that the rate at which the plume spreads increases with time in the

Table 8-2. MOVEMENTS OF BROMIDE PLUME AT DAY 30

	X_c(cm)	Z_c (cm)	$\sqrt{S_{xx}}$ (cm)	$\sqrt{S_{zz}}$ (cm)
Measured	400.3	-74.1	39.9	18.3
RUN 6024	420.6	-57.4	57.7	30.6
RUN 6527	420.6	-60.9	53.5	31.3
RUN 6602	402.2	-49.9	52.8	18.3

Table 8-3. MOVEMENTS OF BROMIDE PLUME AT DAY 71

	X_c (cm)	Z_c (cm)	$\sqrt{S_{xx}}$ (cm)	$\sqrt{S_{zz}}$ (cm)
Measured *	391.4	-107.1	63.5	28.6
RUN 6024	437.3	-119.3	86.1	83.04
RUN 6527	429.4	-103.9	82.5	80.1
RUN 6602	402.4	-94.2	65.2	38.1

* Day 75

Table 8-4. MOVEMENTS OF BROMIDE PLUME AT DAY 481

	X_c (cm)	Z_c (cm)	$\sqrt{S_{xx}}$ (cm)	$\sqrt{S_{zz}}$ (cm)
Measured **	419.6	-189.7	68.1	45.2
RUN 6024	424.8	-133.1	110.6	107
RUN 6527	434.6	-93.7	111.8	65.6
RUN 6602	402.6	-134.4	70.7	49.7

** Day 479

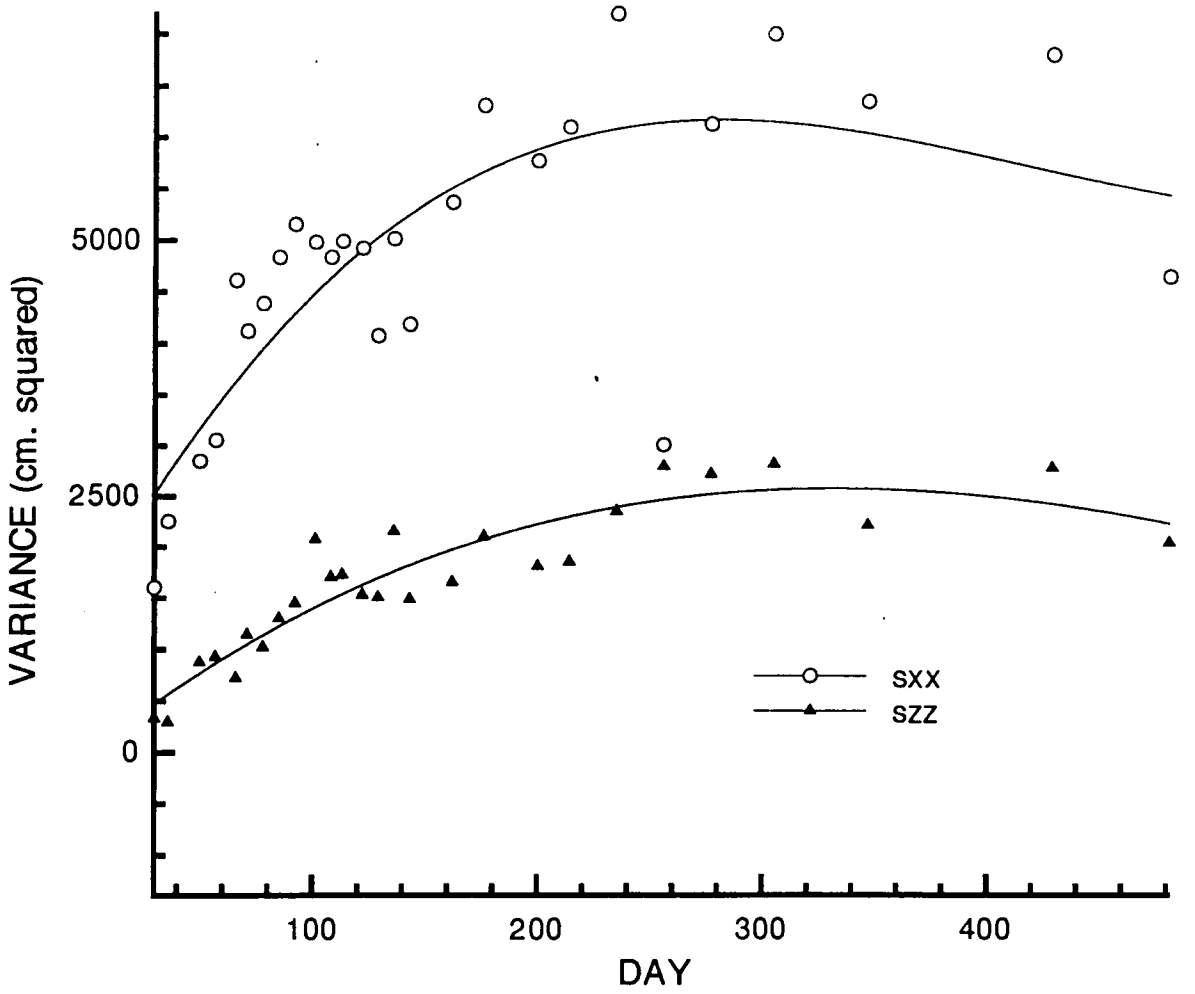

Figure 8-7. Measured plumes vs. time

longitudinal direction while the rate at which the plume spreads decreases with time in the transverse direction. Moreover, data from the Borden experiment (Zhang and Neuman, 1990) clearly show that, at any given time, the longitudinal spread exceeds the transverse spread of the plume this clearly is not the case for the Las Cruces trench experiment. To the best of the authors' knowledge, no published theory characterizes dispersion in unsaturated flow regimes. The authors believe that the larger transverse spreading at the Las Cruces trench experiment may be due to moisture-dependent anisotropy caused by the layered soil at the Las Cruces Trench site. The simulated plumes also appear to exhibit the same phenomena evidenced by the data of Tables 8-2 through 8-4.

8.6.4. Calculation of Ground-Water Travel Time

One hundred particles of infinitesimal mass were tracked from the source to specified compliance boundaries in all three simulations. Figures 8-8 through 8-10 show the

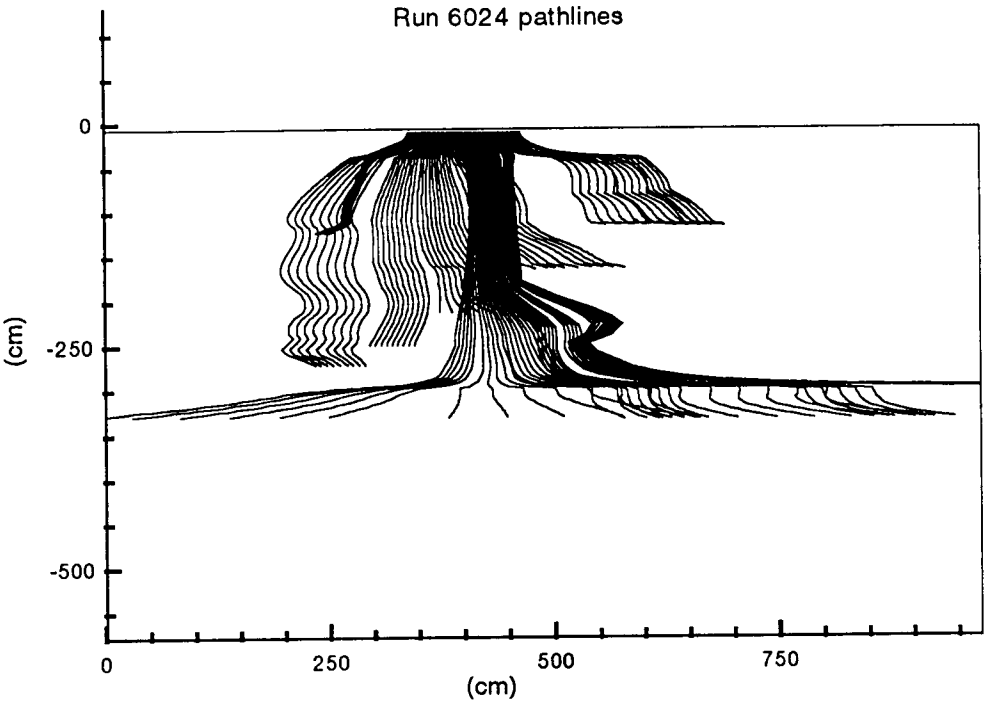

Figure 8-8. RUN 6024 pathlines

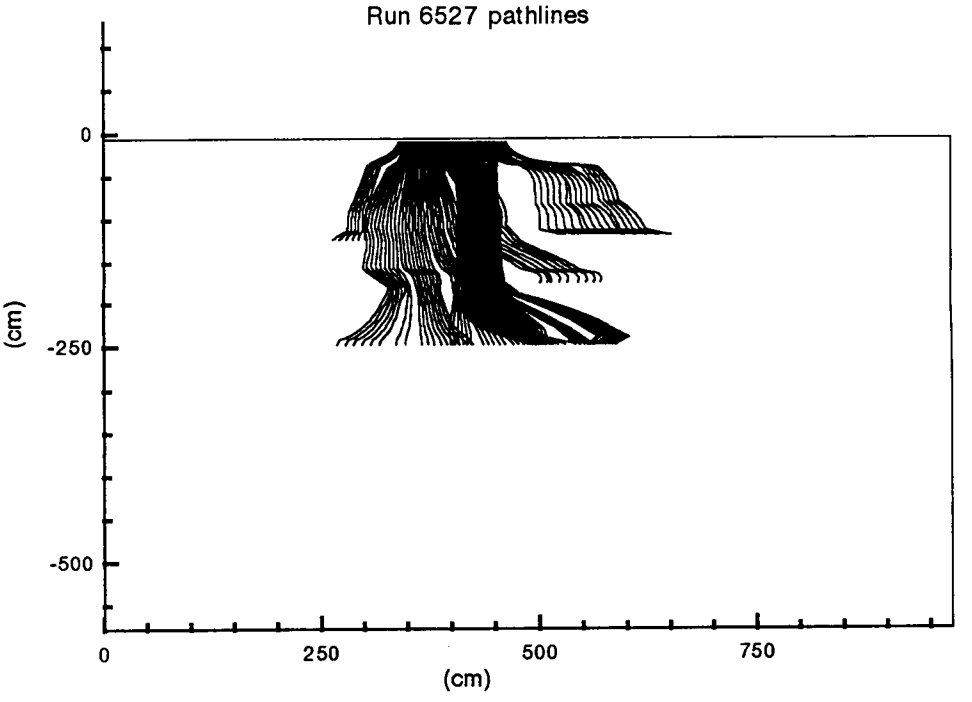

Figure 8-9. RUN 6527 pathlines

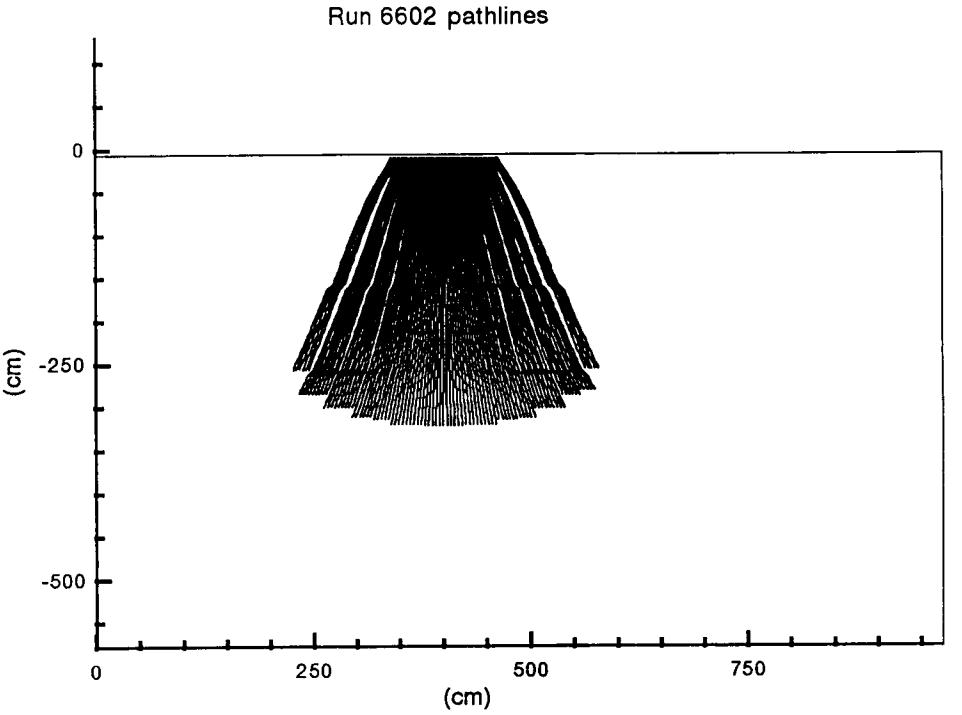

Figure 8-10. RUN 6602 pathlines

pathlines of these particles for RUN 6024, RUN 6527, and RUN 6602, respectively. From the pathlines, a number of statistics of particle travel were calculated. These included the first arrival time, mean travel time, and standard deviation of travel time. These results are presented in Tables 8-5 through 8-7. Also calculated were the mean and standard deviation of the time it took for the centroid of the instantaneous mass flux curves to travel to the same compliance planes. These results are presented in Tables 8-8 and 8-9.

Results in Table 8-5 indicate that greater heterogeneity can create faster paths at least for short distances. First arrival time at plane 2, located at 20.2 cm from the source for RUN 6024 with the blocky property structure, is only 1.1 days compared to 4.3 days for the homogeneous property RUN 6602. However, for the same two runs for 200 cm plane, the first arrival times are 73.5 and 71.7, days respectively. These date indicate that in the long run, a particle path may consist of slower and faster paths. From this result, it is not possible to infer whether the assumption of homogeneity is a conservative assumption in the context of travel time.

The mean travel times shown in Table 8-6 show that the smallest mean travel time results for the homogeneous case, indicating that, if mean travel time were the performance measure, assumption of homogeneity is conservative. This conclusion needs to be tempered by

the results on standard deviations shown in Table 8-7. The greatest travel time of 118.6 days for plane 6 in RUN 6024 is also associated with the largest standard deviation of 118.0 days. Assuming approximately a Gaussian distribution for the travel time, one may summarize that the travel time for RUN 6024 may vary from close to 0 days to as much as 500 days. By the same reasoning, the travel time for RUN 6602 may vary only from 40 to 125 days. Thus, the greater the heterogeneity in the definition of the material properties in the model, the greater is the uncertainty in the prediction of ground-water travel times. Note that in contrast to the Yucca Mountain repository site, the Las Cruces soils have no fractures and also that in these simulations, stochastic representation of uncertainties has been neglected.

From the numbers in Tables 8-8 and 8-9, no definitive correlation between either the first arrival times or the mean travel time and rate of movement of centroid of the instantaneous mass flux curve can be deduced. This may be because the instantaneous mass flux curve is obtained by integrating the flux across the spatial extent of the plume and is thus somewhat of an integrated measure compared to the travel time.

8.7. SUMMARY AND CONCLUSIONS

A two-dimensional simulation of experiment 2a at the Las Cruces experiment was performed with the PORFLO-3, Version 1.2. For two of the three simulations, to the extent possible, measured property data were used directly without any smoothing. For these two simulations, for each measurement, a representative volume was defined by drawing right bisectors between measurement points. From a stochastic view point, this is equivalent to assuming 180 statistically independent material zones. This interpretation of measured data resulted in assigning a heterogeneous but 'blocky' structure to the modeled domain. The third simulation assumed the entire domain to be homogeneous with mean properties. Other methods of interpolation including stochastic interpolation were not investigated.

The three simulation results were compared to the measured plume. In addition to visual comparison, plumes were compared by calculating the first and second moments. Comparison of first moments indicated how well the center of the measured plume compared to the center of the predicted plume. The second moments, on the other hand, compared the extent of plume spread around the center. Surprisingly, both through observation and through the comparison of moments, the third simulation with no heterogeneity in the model properties seemed to mimic the measured plume the best. The authors believe that this may partially be due to the location of suction cups for sampling of the plume. Due to a finite number of these sampling locations, the entire continuum of the plume could not be sampled. In fact, there are measurement locations where the plume was not observed at all because it passed around these locations. Thus serious mistakes can be made in model calibration if a single (or a few) measurement locations are used as calibration measures. A far stronger conclusion reached from this exercise is that introduction of heterogeneities at scales finer than the scale of plume measurement can be source of trouble during model calibration.

Table 8-5. FIRST PARTICLE ARRIVAL TIME (DAYS)

PLANE	RUN 6024	RUN 6527	RUN 6602
2 - 20.2 cm	1.1	1.4	4.3
3 - 50 cm	8.5	8.7	11.1
4 - 100 cm	18.2	16.0	29.0
5 - 150 cm	21.3	24.7	50.0
6 - 200 cm	73.5	32.9	71.7

Table 8-6. MEAN PARTICLE TRAVEL TIME (DAYS)

PLANE	RUN 6024	RUN 6527	RUN 6602
2 - 20.2 cm	2.8	3.1	4.8
3 - 50 cm	17.7	17.0	13.4
4 - 100 cm	71.0	62.9	32.8
5 - 150 cm	75.6	68.5	55.8
6 - 200 cm	118.6	102.7	83.3

Table 8-7. STANDARD DEVIATION OF PARTICLE TRAVEL TIME (DAYS)

PLANE	RUN 6024	RUN 6527	RUN 6602
2 - 20.2 cm	1.3	1.7	.16
3 - 50 cm	10.4	9.3	3.2
4 - 100 cm	69.1	60.0	4.4
5 - 150 cm	63.0	50.6	6.1
6 - 200 cm	118.0	86.6	12.9

Table 8-8. MEAN TRAVEL TIME OF INSTANTANEOUS MASS FLUX CENTROID (DAYS)

PLANE	RUN 6024	RUN 6527	RUN 6602
2 - 20.2 cm	48.1	15.1	14.9
3 - 50 cm	74.9	41.5	36.0
4 - 100 cm	90.0	57.3	76.8
5 - 150 cm	107.2	63.8	147.7
6 - 200 cm	158.3	85.2	245.1

Table 8-9. STANDARD DEVIATION OF INSTANTANEOUS MASS FLUX TRAVEL TIME (DAYS)

PLANE	RUN 6024	RUN 6527	RUN 6602
2 - 20.2 cm	42.0	19.9	14.3
3 - 50 cm	71.1	48.8	29.5
4 - 100 cm	78.7	60.2	56.1
5 - 150 cm	86.7	55.2	98.2
6 - 200 cm	111.0	55.7	113.1

Another conclusion arrived from the study of the second moments of both the measured and simulated plume is that at the Las Cruces experiment, the transverse spreading of the plume exceeds the longitudinal spreading. This is counter to most of the known observations and theoretical constructs on dispersion in saturated media. It appears that the lateral plume spreading in the case of unsaturated media is caused by anisotropy that may be manifestation of variations in moisture content.

Pathlines for 100 particles were calculated for all of the three simulations. First arrival times and the mean arrival times were calculated. It appeared that the first arrival times depend upon the degree of heterogeneity and the location of the compliance boundary. The results tentatively indicate that in heterogeneous media, first arrival times (or fastest travel times) may in fact be longer than in homogeneous media. Similarly, the mean travel times are far more uncertain for the heterogeneous case than for the homogeneous case. More investigation is needed before firm conclusions of this nature can be made.

8.8. REFERENCES

Celia, M. A., E. T. Boulatas, and R. L. Zarba. 1990. A general mass-conservative numerical solution for the unsaturated flow equation. *Water Resour. Res.* 26(7):1483-1496.

Dagan, G. 1984. Solute transport in heterogeneous porous formations. *J. Fluid Mech.* 145:151-177.

Freyberg, D. L. 1986. A natural gradient experiment on solute transport in a sand aquifer; 2. Spatial moments and the advection and dispersion of nonreactive tracers. *Water Resour. Res.* 22(13):2031-2046.

Hills, R. G., P. J. Wierenga, and M. R. Kirkland. 1990. *Two-Dimensional Flow Predictions for the Las Cruces Trench Experiment 2.* Unpublished Manuscript. Las Cruces, New Mexico: New Mexico State University.

Neuman, S. P., and Zhang, Y. K. 1990. A quasi-linear theory of non-fickian and fickian subsurface dispersion, 1. Theoretical analysis with application to isotropic media. *Water Resour. Res.* 26(5):887-902.

Zhang, Y. K., and Neuman, S. P. 1990. A quasi-linear theory of non-fickian and fickian subsurface dispersion, 2. Application to anisotropic media and the borden site. *Water Resour. Res.* 26(5):903-913.

Rockhold M. L., and S. K. Wurstner. 1991. *Simulation of Unsaturated Flow and Solute Transport at the Las Cruces Trench Site Using the PORFLO-3 Computer Code.* PNL-7562. Richland, Washington: Pacific Northwest Laboratory.

Runchal, A. K., and B. Sagar. 1989. *PORFLO-3: A Mathematical Model for Fluid Flow, Heat and Mass Transport in Variably Saturated Geologic Media - Users Manual, Version 1.0.* WHC-EP-0041. Richland, Washington: Westinghouse Hanford Company.

Sagar, B., and A. K. Runchal. 1990. *PORFLO-3: A Mathematical Model for Fluid Flow, Heat and Mass Transport in Variably Saturated Geologic Media - Theory and Numerical Methods, Version 1.0.* WHC-EP-0042. Richland, Washington: Westinghouse Hanford Company.

Wierenga, P. J., A. F. Toorman, D. B. Hudson, J. Vinson, M. Nash, and R. G. Hills. 1989. *Soil Physical Properties of the Las Cruces Trench Site.* NUREG/CR-5441. Washington, D.C. U.S. NRC.

ACKNOWLEDGMENTS: Support from Alfred Johnson and Alok Kushwaha in producing the graphics presented in this chapter is thankfully acknowledged. The authors also wish to thank the technical reviewers at the CNWRA.

9. SORPTION MODELING FOR HLW PERFORMANCE ASSESSMENT

by Roberto Pabalan and David Turner

Investigators: Roberto Pabalan (CNWRA), David Turner (CNWRA), James Prikryl (CNWRA), and Paula Muller (CNWRA)

9.1. INTRODUCTION

An evaluation of the effectiveness of geologic systems as barriers to radionuclide migration requires an understanding of the chemical and physical processes by which aqueous species are sorbed on geologic materials. These processes, which may include adsorption, ion exchange, or precipitation, are commonly represented collectively by empirical parameters, such as sorption coefficient (K_d) or retardation factor (R_f), in transport calculations supporting performance assessments (PA) of geologic repositories. The usefulness, however, of these empirical parameters in quantitatively describing aqueous-solute/rock interactions for calculations of radionuclide transport often used in PA is actively debated. Transport models using these parameters, particularly those that assume constant K_d's or R_f's, do not explicitly account for many potentially important geochemical phenomena occuring during transport in natural systems (e.g., Kent et al., 1988; Siegel, 1989; Siegel et al., 1990). These include aqueous complexation, precipitation/dissolution reactions, competitive sorption, changes in groundwater chemistry, and variability in substrate composition, as well as changes in temperature and pressure. Therefore, questions have been raised regarding the adequacy of transport calculations using K_d or R_f in PA (e.g., Kelmers et al., 1987).

9.2. TECHNICAL OBJECTIVES

To support the NRC HLW program, the CNWRA is conducting research activities under the Sorption Modeling for HLW Performance Assessment Research Project. The general objectives of this project are as follows:

- Obtain a mechanistic understanding of the important radionuclide sorption processes and the physical and chemical parameters that affect sorption behavior in the Yucca Mountain, Nevada, environment.

- Investigate the applicability of coupled-hydrogeochemical models which use simple representations of sorption phenomena to Yucca Mountain PA.

- Develop practical but scientifically defensible approaches to modeling sorption at Yucca Mountain, and the requisite databases to support such models.

The research project has been divided into three tasks, namely: Task 1 - Literature Review and Development of Approach; Task 2 - Coupled Hydrogeochemical Modeling: Application of Simplified Models to NRC Regulatory Needs; and Task 3 - Sorption Experiments. Only Tasks 1 and 3 were active during this report period. Task 1 consists of

literature review of experimental, theoretical, and modeling studies on sorption processes and evaluation of available coupled reaction-transport models. Results of the literature review conducted during this quarter are discussed in Section 9.3. Task 3 was initiated during this period, and initial work focused on experimental material preparation and on evaluation of analytical procedures. Results of Task 3 are discussed in Section 9.4.

9.3. TASK 1 - LITERATURE REVIEW: SORPTION MODELS

Much of the literature dealing with sorption processes has been developed in the fields of soil science and chemical engineering to study the interplay between water, organic and inorganic solutes, and soil particles. A number of approaches have been used to develop an experimental database and to construct models that reproduce the observed results. These range from simple empirical equations fit to a particular data set, to mechanistic theoretical treatments that address the microscale processes operating during solute uptake and removal from solution. A few of the more common approaches in use are described below.

9.3.1. Equilibrium Sorption Models

Equations relating solute concentrations in the liquid phase to the concentration of sorbed species are generated through fitting curves and empirical coefficients to data for equilibrated solid-liquid systems. Because experimental sorption data are generally obtained at a single, constant temperature, these empirical equations are known as sorption "isotherms." The simplest empirical model is a linear equilibrium adsorption isotherm of the general form:

$$S = K_d C \qquad (9\text{-}1)$$

where S (g/g) is the sorbed concentration, C (g/ml) is the concentration of the solute in solution, and K_d (ml/g) is an empirically determined "sorption coefficient." A linear isotherm (or K_d) approach to sorption modeling generally assumes that K_d is a constant, discrete value for a given system and species. Attractive in its simplicity, this strategy has been used to describe reactive transport in a number of systems through the construction of a retardation factor (R_f) for insertion into the convection-dispersion equation (Selim and Mansell, 1976; Krishnaswami et al., 1982; Ebinger et al., 1990).

Assuming local equilibrium, Valocchi (1984) has proposed an "effective K_d" approach to sorption modeling based on mass balance considerations for a finite step across a sharp migration front (i.e., negligible dispersion). Changes in aqueous and sorbed phase concentrations across the reaction front (ΔC and ΔS) are related to an "effective K_d" (i.e., $K_d = \Delta S/\Delta C$), which in turn can be related to an effective retardation factor. The advantage of this approach relative to the constant K_d approach is that the "effective K_d" considers S and C upstream and downstream of the reaction front, and K_d is no longer treated simply as a unique physical property of the medium.

Developed to model nonlinear sorption, the Freundlich isotherm (Freundlich, 1926) is defined by the relationship:

$$S = K_{Fr}C^{n} \tag{9-2}$$

where S and C are as in Eqn. (9-1), and $\mathbf{K_{Fr}}$ and **n** are empirical coefficients. For the special case where n = 1, Eqns. (9-1) and (9-2) are identical. If sorption/concentration data can be represented by a Freundlich isotherm, a plot of log S vs. log C results in a straight line with a slope equal to n and an intercept of log K_{Fr}. Freundlich isotherms have been used to model heavy metal and radionuclide sorption (Ames et al., 1983a,b; Alemi et al., 1991). Murali and Aylmore (1983a,b) have considered competitive sorption where all species follow Freundlich isotherms

$$S_i = \frac{K_{Fr,i}C_i^{n_i+1}}{[\Sigma_j \alpha_{ji}C_j]} \tag{9-3}$$

K_{Fr}, S, C, and n are the same as in Eqn. (9-2) and $\alpha_{ji}=K_{Fr,j}/K_{Fr,i}$ is an empirical parameter representing the competition for sorption sites between species i and j. A number of studies (Murali and Aylmore, 1983c, and references therein) have shown sorption characteristics that can be represented by the isotherm presented in Eqn. (9-3).

A particularly limiting characteristic of the linear and Freundlich isotherms is the lack of a maximum sorption limit. In actuality, because there is a finite number of sorption sites, sorption will reach a practical upper limit (Travis and Etnier, 1981). Adapted to solution chemistry, the Langmuir isotherm (Langmuir, 1918) introduces the idea of an upper limit to surface adsorption, avoiding this drawback of the simpler isotherms. Its general form is

$$S = \frac{K_{La}bC}{(1+K_{La}C)} \tag{9-4}$$

where b is the maximum adsorption capacity of the substrate (g/g) and K_{La} is an empirical measure of the strength with which the solute is bound to the sorbent phase. From Eqn. (9-4), the fraction of occupied sites is related to the product of K_{La} and C. For example, if $K_{La}C=1$, half (b/2) of the sites are occupied. Values for b can be determined for a given data set by plotting C/S versus C. From Eqn. (9-4), this should yield a straight line with a slope of 1/b and an intercept of $1/K_{La}b$.

Because the Langmuir isotherm assumes that all sorption sites are the same, it is most successful for those applications where variations in solution chemistry and sorbed ion concentration are limited (Ames et al., 1982; Serne et al., 1990). Polzer and Fuentes (1988, 1991) modified the Langmuir isotherm to incorporate sorption on different sites sorption in order to fit radionuclide sorption/concentration data for tuffs from Yucca Mountain. By introducing

an additional adjustable parameter β to represent site heterogeneities, K_{L_a} and C in Eqn. (9-4) are modified to $K_{L_a}^{\beta}$ and C^{β}, respectively.

The Dubinin-Radushkevich (D-R) isotherm (Dubinin and Radushkevich, 1947) has also been used to address heterogeneous sorption

$$S = b[\exp(K_{DR}[RT\ln(1+\frac{1}{C})]^2)] \quad . \tag{9-5}$$

S, C, K_{DR}, and b are similar in form to Eqn. (9-4), but are more general in nature, allowing for representation of heterogeneous types of sorption sites. R and T are the gas constant and absolute temperature, respectively. Because of the exponential form of the equation, a plot of ln S vs. $[RT(\ln(1+1/C)]^2$ results in a straight line with a slope of K_{DR} and an intercept of ln b.

9.3.2. Kinetic Sorption Models

Kinetic sorption models have been used to simulate conditions where sorption processes are believed to operate relatively slowly in relationship to solute residence time (Selim, 1978; Comans and Middleburg, 1987; Middleburg and Comans, 1991). Because of this slow process, the degree of sorption continues to change with time, and frequently does not reach a steady state, at least within the time constraints of the experiment.

First-order kinetics have found the most application in modeling nonequilibrium sorption (Selim, 1978; Murali and Aylmore, 1983a,b; Valocchi, 1989), using either a linear

$$\frac{dS}{dt} = k_1C - k_2S \tag{9-6}$$

or nonlinear

$$\frac{dS}{dt} = k_1C^n - k_2S \tag{9-7}$$

approach where S and C are as defined previously, n is an empirical coefficient, and k_1 and k_2 are rate constants for adsorption and desorption, respectively. While k_1 and k_2 can be determined experimentally, data are frequently unavailable; and an empirical approach is used to fit kinetic models to sorption data (Selim, 1978). At equilibrium (i.e., dS/dt = 0), Eqns. (9-6) and (9-7) reduce to the linear and Freundlich sorption isotherms, respectively with $K = k_1/k_2$.

Several studies (Murali and Aylmore, 1983a; Jennings and Kirkner, 1984) describe a modification of the Langmuir isotherm [Eqn. (9-4)] to address kinetic sorption, such that

$$\frac{dS}{dt} = k_1 C(b-S) - k_2 S \qquad (9\text{-}8)$$

where k_1 and k_2 are adsorption and desorption rate constants, respectively. At equilibrium, Eqn. (9-8) reduces to the Langmuir isotherm in a manner similar to linear and nonlinear rate equations, with $K_L = k_1/k_2$. Murali and Aylmore (1983a,b) have proposed a general kinetic Langmuir equation to model competitive sorption by substituting a summation of total sorbed concentrations (i.e., $b-\Sigma S_j$) for all species (j) of interest in the first term on the right side of Eqn. (9-8).

9.3.3. Electrostatic Sorption Models

During sorption, a variably charged particle surface will interact with an electrolyte solution in a complex manner. Electrical work done in moving ions across the zone of charge influence adjacent to the interface will affect the activity of aqueous species near the charged surface relative to the bulk solution. The electrostatic part of the change in activity is governed by the exponential Boltzmann relation

$$a_{i,s} = a_i[e^{\frac{-\Psi F}{RT}}]^z \qquad (9\text{-}9)$$

where $a_{i,s}$ is the activity of a given ion i in the aqueous phase near the charged surface, a_i is the activity in the bulk solution, $e^{-\Psi F/RT}$ is the Boltzmann factor, Ψ is electrostatic potential, z is the valence of the ion, F and R are the Faraday (J/volt equiv) and ideal gas (J/K·mole) constants, respectively, and T is absolute temperature (K).

Developed largely for iron oxide minerals, surface complexation models (Davis and Leckie, 1978; Hayes et al., 1989) are an attempt to address the effect of electrostatic potential on surface sorption processes. For oxides, these models assume a surface comprising of amphoteric hydroxyl groups (OH^{2+}, OH^{o}, O^{-}, etc.), and treat surface adsorption as a combination of equilibrium protonation/deprotonation and complexation reactions of the form

$$SOH + H^+ = SOH_2^+ \qquad \text{(Protonation, } K_+\text{)} \qquad \text{(9-10a)}$$

$$SOH = SO^- + H^+ \qquad \text{(Deprotonation, } K_-\text{)} \qquad \text{(9-10b)}$$

$$SOH + M^{2+} = SO{\cdot}M^+ + H^+ \qquad \text{(Complexation, } K_M2+\text{)} \qquad \text{(9-10c)}$$

where SOH represents a neutral surface site. Intrinsic surface acidity constants (K_+, K_-) and equilibrium constants (K_M2+), can be defined for these reactions using mass action considerations. In turn, activities modified by electrostatic effects (Eqn. 9-9) are inserted into these expressions, resulting in the mass action expression

$$K_{M^{2+}} = \left(\frac{[SO{\cdot}M^+][H^+]e^{-\Psi F/RT}}{[SOH][M^{2+}](e^{-\Psi F/RT})^2} \right). \qquad \text{(9-11)}$$

Adsorption reactions are modeled through solving simultaneously equations for mass balance of the surface sites, charge balance, and mass action. Mass balance for the surface sites is based on the total number of available sorption sites (T_{SOH}) such that

$$T_{SOH} = (N_S) \times (SA) \times (C_S) \qquad \text{(9-12)}$$

where N_s represents surface site density (sites/cm^2), SA (cm^2/g) is specific surface area, and C_s is the solid mass (g). Eqn. (9-12) is then combined with (1) charge-potential relationships specific to a given model (see below) and (2) activity and mass action relationships analogous to Eqn. (9-11) that describe concentration distributions of surface species and aqueous speciation as a function of solution chemistry and surface charge. The ability to account for variable physical-chemical conditions gives complexation models a flexibility of application based on theoretical considerations. This flexibility is an advantage compared to the restricted applicability of empirically-derived isotherms. The various complexation models differ in how the electrostatic potential (Ψ) is extended from the charged surface into the bulk solution, and how changes in solution electrolyte concentration affect reactions at the particle surface.

In all surface complexation models, the particle surface with specific charge σ_s, is separated from the solution by a diffuse layer of nonspecifically bound counterions. At the boundary between the two layers, the surface charge is balanced by the charge on the diffuse layer (σ_d) such that $\sigma_s + \sigma_d = 0$. The diffuse layer model (DLM) and constant capacitance model (CCM) propose that protonation/deprotonation and adsorption only occur in one plane at the surface/solution interface, and that only those ions specifically adsorbed in this inner "o-plane" contribute to the total surface charge (i.e., $\sigma_s = \sigma_o$). In the DLM, the Stern-Grahame extension of the Gouy-Chapman relationship for symmetrical electrolytes is used to describe the interdependence among electrolyte concentration (ionic strength), charge ($\sigma_d = -\sigma_o = -\sigma_s$ at the boundary with the o-plane), and electrostatic potential ($\Psi_d = \Psi_o$) such that

$$-\sigma_o = \sigma_d = -(\sqrt{\varepsilon \varepsilon_o IRT})\left[\sinh \frac{(z\psi_d F)}{2RT}\right] \qquad (9\text{-}13)$$

where F, R, z, and T are as defined in Eqn. (9-9), ϵ is the dielectric constant, ϵ_o is the permittivity in free space (8.85×10^{-12} coulombs^2/J m), and I is solution ionic strength.

In contrast to the DLM, the CCM assumes that the charged surface is separated from the bulk solution by a plane of constant capacitance. Based on this assumption, surface charge ($\sigma_d = -\sigma_o = -\sigma_s$) is related to surface potential ($\Psi_o = \Psi_d$) through the simple linear equation

$$-\sigma_o = \sigma_d \sim C_1 \psi_o \qquad (9\text{-}14)$$

where C_1 (Farads/m^2) is a constant capacitance term. This relationship results in a linear potential gradient from the charged substrate to the bulk solution. The constant capacitance approach is limited to a specific ionic strength, however; and changes in ionic strength require recalculation of C_1. Allison et al. (1990) indicate that the constant capacitance term is frequently not provided as a characteristic property of a given system, but applied instead as an empirical parameter fit to the data. This has the advantage of providing a better fit to a given data set, but at the expense of the theoretical basis of the model.

Like the DLM and CCM approaches, the triple layer surface complexation (TLM) model of Davis and Leckie (1978) assumes that the charged surface is comprised of amphoteric hydroxyl groups. Mass balance and mass action expressions for protonation/deprotonation reactions and surface complexation reactions are also treated in the same fashion. In contrast to the two previously discussed models, however, charge/potential relationships are described by a conceptual model that divides the zone influenced by surface charge into three layers. In the TLM, the outer, diffuse layer of counterions (d-plane) is separated from the charged surface by two inner layers of constant capacitance, designated (from the surface outwards) the o- and β-planes. Protonation/deprotonation reactions at surface sites are restricted to the inner, o-plane, while the specifically adsorbed ions are assigned to the β-plane. As a direct result of its construction, the TLM allows surface complexation reactions of ion-pairs of the general form

$$SOH + C^+ = SO^- \cdot C^+ + H^+ \qquad \text{(for cations)} \qquad (9\text{-}15a)$$

$$SOH + A^- + H^+ = SOH_2^+ \cdot A^- \qquad \text{(for anions)} \qquad (9\text{-}15b)$$

with K_{Cat} and K_{An} similar in form to Eqn. (9-11) (Kent et al., 1988; Serne et al., 1990).

Surface charges in the TLM are designated σ_o and σ_β for the o- and β-layers, respectively. At the boundary between the β-layer and the diffuse layer, the diffuse layer charge (σ_d) is defined such that $\sigma_o + \sigma_\beta + \sigma_d = 0$. Charge/potential for the outer, diffuse layer is defined by Eqn. (9-13), while the inner two layers are described such that

$$\sigma_o = (\psi_o + \psi_\beta)C_1 \qquad (9\text{-}16a)$$

$$\sigma_o + \sigma_\beta = (\psi_\beta + \psi_d)C_2 = -\sigma_d \qquad (9\text{-}16b)$$

where C_1, and C_2 (Farads/m^2) are capacitances associated with the areas between the o- and β-planes and β- and d-planes, respectively. In practice, the outer layer capacitance C_2 is usually fixed at 0.2 Farads/m^2, and the inner layer capacitance C_1 is used as a fitting factor (Kent et al., 1988).

The triple layer model has largely been restricted to modeling sorption in hydrous oxide systems (Tripathi, 1984; Hsi and Langmuir, 1985; Sanchez et al., 1985; Hayes and Leckie, 1986; LaFlamme and Murray, 1987; Payne and White, 1991). Kent et al. (1988) describe the approaches that will be necessary to characterize silicates, carbonates, aluminosilicates, and whole rocks in order to apply electrostatic models to these substrates. Benjamin and Leckie (1981) and Hiemstra et al. (1989) have proposed further elaboration of the model to incorporate several chemical distinct types of surface sorption sites, each interacting with the sorbing ions in a distinct fashion.

9.3.4. Model Comparison

Many of the advantages and disadvantages of the various models have been presented above. Empirical models are generally simpler in mathematical construction. Due to the relatively straightforward application of these models, abundant experimental data have been generated to determine the appropriate empirical coefficients for a variety of elements and substrates (Thomas, 1987; Beckman et al., 1988; Meijer, 1990). This simplicity comes at the expense of flexibility, however. Because the empirical nature of these models tends to lump retardation processes together (Siegel et al., 1990), it is difficult, if not impossible, to discriminate between the various factors influencing solute uptake. Without this mechanistic understanding of sorption processes, extrapolation of an empirical model beyond the experimental conditions used to generate the data fitted by the model is unjustified in many instances. For example, assumptions of constant K_d may not be appropriate, as solute concentration (Ames et al., 1983a,b,c) and water/rock ratio (Balistrieri and Murray, 1986) may affect sorption coefficients. In addition, the importance of various physical-chemical conditions cannot be determined using empirical models without running a large number of carefully controlled experiments (e.g., controlling all other variables, while varying pH through a range of values). Further complicating the application of empirical models is the frequent lack of good experimental control on the existing data (Siegel et al., 1989) such as temperature, grain size, pH, and sample preparation.

As the theoretical basis for the model increases, model flexibility and applicability generally increase as well. By explicitly defining the relationships among a number of system parameters, mass action and surface complexation models are more robust, and can be extended

beyond experimental conditions to a wide range of environments. As sophistication increases, however, the data requirements and the number of adjustable parameters increases as well. The incorporation of a mechanistic sorption approach such as surface complexation in a reactive solute transport model requires a more complex geochemical equilibrium code to monitor changes in solution/solid properties influencing the input parameters. Coupling complex geochemistry with transport codes may lead to excessive computational time and memory requirements (Yeh and Tripathi, 1989). Additionally, the data necessary for rigorous application of these models are frequently either unavailable or poorly constrained at present (Siegel et al., 1989; Hayes et al., 1989; Serne et al., 1990; Meijer, 1990). Much of the data are only available for pure or synthetic minerals, and extrapolation to natural solid solutions and composite materials is problematic (Kent et al., 1988; Meijer, 1990).

Several studies (Serne and Muller, 1987; Serne et al., 1990; Meijer, 1990) suggest using a K_d approach to place conservative limits on radionuclide sorption and transport. This is desirable in part due to computational simplicity, and in part due to the straightforward approach to data generation. If experiments are designed to approach the conditions in the environment of interest, and the natural conditions remain relatively constant, an empirical model may be suitable (Pietrzak et al., 1981). If the environment is anticipated to vary between known (or estimated) conditions, the extremes can be used to establish bounding limits on sorption. System parameters may also be approximated by incremental changes in experimental conditions to achieve an approximation of changing conditions in the geological environment. One problem with this approach is what constitutes the "extremes" will vary depending on the element under consideration. What is considered extreme for the sorption of one radionuclide may not be appropriate for a different element.

Meijer (1990) suggests that a conservative limit on overall sorption may be obtained by choosing the K_d value representative of the least sorptive unit for the radionuclide of interest. If solute transport modeled using this value significantly exceeds the performance objectives established in 10 CFR Part 60 and 40 CFR Part 191, then this can be taken to provide some level of assurance as a lower limit on radionuclide migration. This approach can also be used to identify those radionuclides that may be of concern and require a more mechanistic approach (Kerrisk, 1985). Serne and Muller (1987) support this use of the K_d approach as a bounding method, suggesting that if performance objectives can be met with a low K_d value and if experiments indicate that expected K_d values are much larger, then the need for more sophisticated modeling is reduced.

9.4. TASK 3 - SORPTION EXPERIMENTS

To develop a mechanistic understanding of important radionuclide sorption processes and the physical and chemical parameters that affect sorption behavior in the Yucca Mountain environment, a literature review of experimental and modeling studies of uranium sorption on geologic media was conducted during the first calendar quarter. Results of that review were discussed in the research report for that period (Pabalan and Turner, 1991). On the basis of the literature review, a work plan for conducting experimental studies on uranium sorption on

geologic media was developed. The experiments described in the work plan are designed to facilitate understanding the fundamental controls on uranium sorption; i.e., how and why sorption values change as a function of the properties of the sorbing solid and the aqueous phase. Experimental and analytical techniques and methods for data interpretation and modeling, developed in the uranium sorption experiments, will be useful in extending the studies to other actinides and radioelements. The experiments to be conducted will also provide useful data for validating hydrogeochemical transport codes (Task 2 of the Sorption Research Project), in interpreting and modeling results derived in the CNWRA's Geochemical Analog Research Project, and in evaluating data and modeling needs for the CNWRA's Performance Assessment Project.

The initial focus of the experiments is uranium sorption on zeolite minerals, particularly clinoptilolite. Because the presence of laterally extensive zones of clinoptilolite-rich tuff at Yucca Mountain might provide a significant contribution to the geologic barrier for radionuclide transport, the factors that control radionuclide sorption on clinoptilolite must be understood. The lack of uranium sorption data, however, on well-characterized clinoptilolite specimens under well-constrained experimental conditions presently makes the role of sorption on clinoptilolite in retarding uranium migration difficult to assess.

Activities on Task 3 were initiated during the middle part of the report period. These consisted of preparation of Na-form of clinoptilolite that will be used in the experiments, evaluation of methods for quantitative analysis of uranium in aqueous solutions, and acquisition of laboratory equipment and supplies required to support the experiments.

9.4.1. Preparation of Na-clinoptilolite

Powdered clinoptilolite material (100-200 mesh size) to be used in the sorption experiments was prepared from clinoptilolite-rich zeolitized tuff samples from Death Valley Junction, California, in a manner similar to that described previously (Pabalan, 1991). However, prior to removing mineral impurities by density separation using heavy liquid as described previously, the powdered material was treated with 1 N sodium acetate buffer (pH adjusted to 5) to dissolve any carbonate minerals present. In addition, subsequent to heavy liquid separation using mixtures of tetrabromoethane and dimethyl-formamide, iron oxide minerals were dissolved using a sodium dithionite-citrate-bicarbonate mixture (Jackson, 1956). Removal of iron oxides is especially important because they exhibit very high sorption coefficients for uranium (Tripathi, 1984; Hsi and Langmuir, 1985), and may lead to erroneously high sorption ratios on the clinoptilolite material if not eliminated.

Near homoionic Na-clinoptilolite was generated by treating twelve batches of 40 g of clinoptilolite powder with 400 ml of 3 m NaCl solution in 500 ml polypropylene bottles. The bottles were continuously agitated in a constant-temperature shaker water bath maintained at 90°C for about two weeks. The 3 m NaCl solution in each bottle was replaced every two days. The clinoptilolite powders thus treated were washed thoroughly with deionized water several times at 90°C to eliminate excess NaCl until no chloride was detected in the washings

using a $AgNO_3$ test. The clinoptilolite powders were next transferred into ten beakers, dried overnight in an oven at about 65°C, and then equilibrated with water vapor over saturated sodium chloride solution in dessicators. This last step was necessary to provide a constant moisture content prior to chemical analysis and to initiation of sorption experiments. To help accelerate the diffusion of water vapor into the zeolite structure, the dessicators were placed on New Brunswick Model G2 gyratory shakers. The uptake of water by clinoptilolite was monitored by weighing each beaker periodically. The approach to equilibrium is illustrated in Figure 9-1, which is a plot of the change in weight of clinoptilolite vs. time. Note that the total change in weight is not the same for the various samples because of the different amounts of material present in each beaker. Figure 9-1 shows that it took about ten days before equilibrium was achieved.

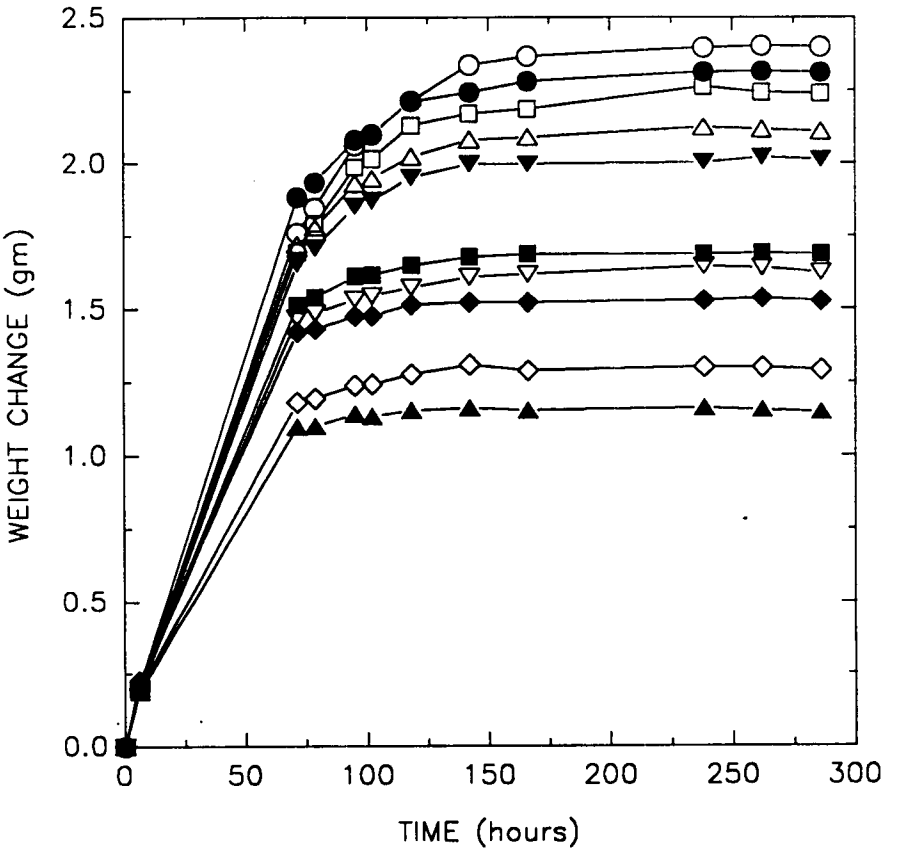

Figure 9-1. Plot of time (hr) vs. change in weight (gm) of clinoptilolite powders equilibrating with water vapor over saturated sodium chloride solutions

Reacting clinoptilolite with 3 m NaCl solutions at 90°C for two weeks may potentially cause precipitation of secondary phases and affect the results of the sorption experiments. Scanning electron photomicrographs were taken of the Na-exchanged clinoptilolite to check for the presence of secondary phases. The photomicrographs, an example of which is shown in Figure 9-2, do not indicate that secondary phases have precipitated.

9.4.2. Evaluation of Polarographic Techniques for Uranium Analysis

In the experiments, the sorption of uranium on the solid phase will be determined mainly by analyzing the concentration of uranium in the aqueous solution, although analysis of uranium on the solid may also be conducted. Numerous methods have been used in scientific studies to analyze uranium, including alpha spectrometry, fluorimetry, laser kinetic phosphorence method, UV-Visible spectrophotometry, plasma emission spectrometry, and polarography. The last was determined by CNWRA as the preferred method, and it will be used in this research project for measuring *total* uranium concentration in aqueous solution, based on speed of analysis, detection limits that can be achieved, and the wide range of concentrations that can be analyzed. The polarographic instrument used is an EG&G Princeton Applied Research Model 384B polarographic analyzer with a Model 303A static mercury drop electrode.

The term "polarography" is used here to describe the group of related electrochemical techniques in which one of the two electrodes of an electrochemical cell consists of mercury, which may be static or flowing. The mercury is in a capillary, the tip of which is immersed in the solution to be analyzed (Hunt and Wilson, 1986). A large amount of published literature on polarography is available, and the interested readers are referred to the books by Kolthoff and Lingane (1952), Meites (1965), and Bond (1980).

Polarography encompasses a wide variety of specific analytical techniques. The Model 384B polarographic analyzer provides eight different modes, namely, square-wave voltammetry, cyclic staircase voltammetry, staircase sweep voltammetry, differential pulse polarography, normal pulse polarography, sampled DC polarography, DC stripping, and differential pulse stripping. We have chosen to use square-wave voltammetry for the analysis of uranium because of its high sensitivity, fast scan rates, and its use of smaller amounts of triply-distilled mercury compared to other methods.

A variety of background electrolytes can be used in the polarographic analysis of uranium, some of which are reviewed by Kolthoff and Lingane (1952) and tabulated by Meites (1965, Appendix B). In our initial evaluation of the polarographic analysis of uranium, 0.1 M HCl solutions were chosen as the background electrolyte. Published information (Meites, 1965) indicate that the reduction of uranium in this medium produces two well-defined cathodic waves, whose half-wave potentials are -0.18 and -0.94 volts vs. a saturated calomel electrode (S.C.E.). The first wave results from the reversible reduction of +6 uranium to the +5 state, and has been interpreted by Kolthoff and Lingane (1952) to correspond to the reaction:

Figure 9-2. Scanning electron photomicrographs of clinoptilolite powders that have been exchanged with 3 M NaCl solutions at 90°C for about two weeks. Magnifications are indicated by the scale bars.

$$UO_2^{++} + e^- \rightleftharpoons UO_2^+ \,. \qquad (9\text{-}17)$$

The second wave, which is twice as large as the first, corresponds to a further 2-electron reduction to the +3 state. The second reduction wave, however, does not proceed reversibly (Harris and Kolthoff, 1945) due to instability in acidic solutions of +5 uranium to disproportionation into UO^{++} and UO_2^{++}, although the total height of the doublet wave remains constant (Kolthoff and Harris, 1946).

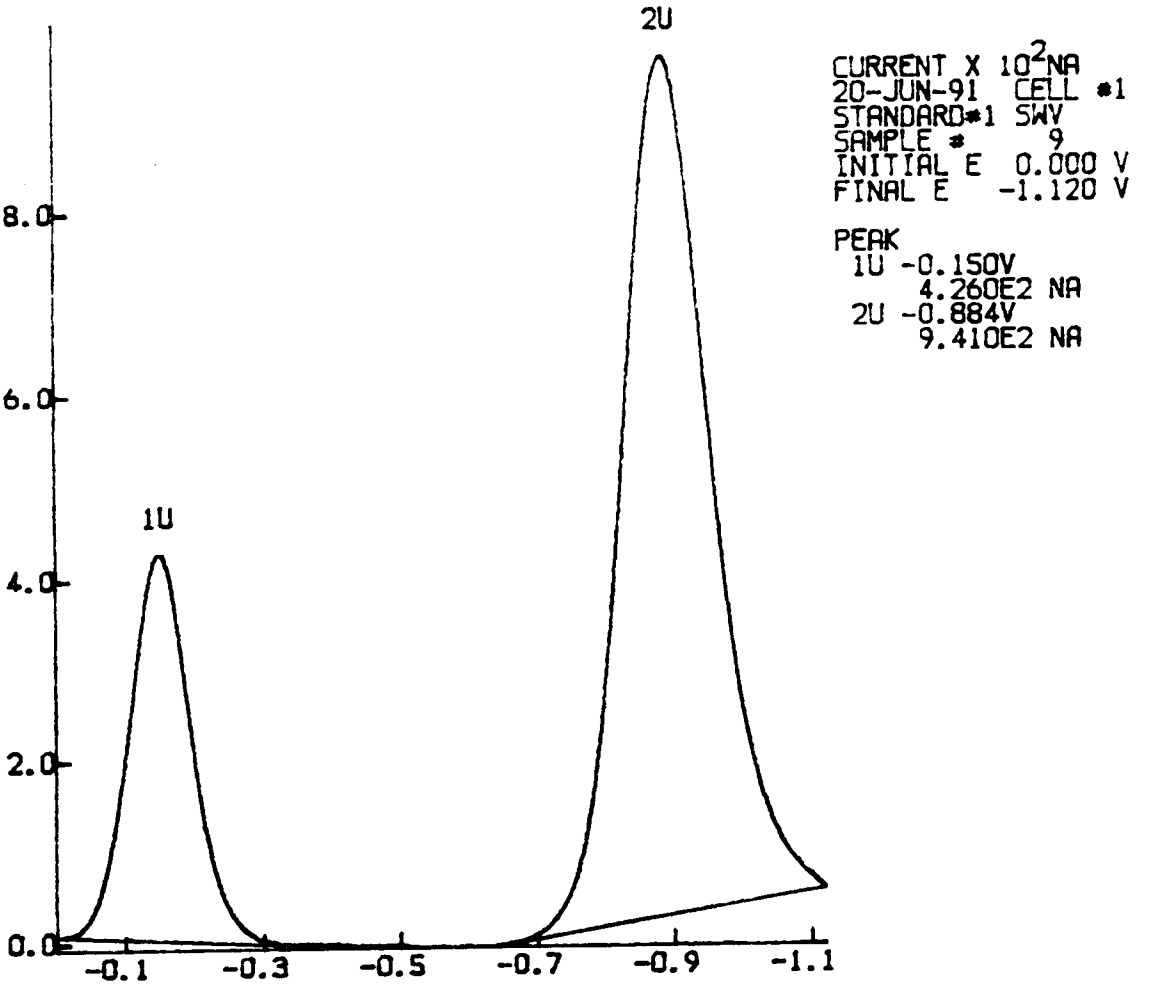

Figure 9-3. Square-wave voltammogram of 10 ppm uranium in 0.1 M HCl matrix. The two peaks at half-wave potentials of -0.15 and -0.88 volts vs. a KCl-saturated Ag/AgCl reference electrode correspond respectively to the reduction of uranium from +6 to +5 and from +5 to +3 states.

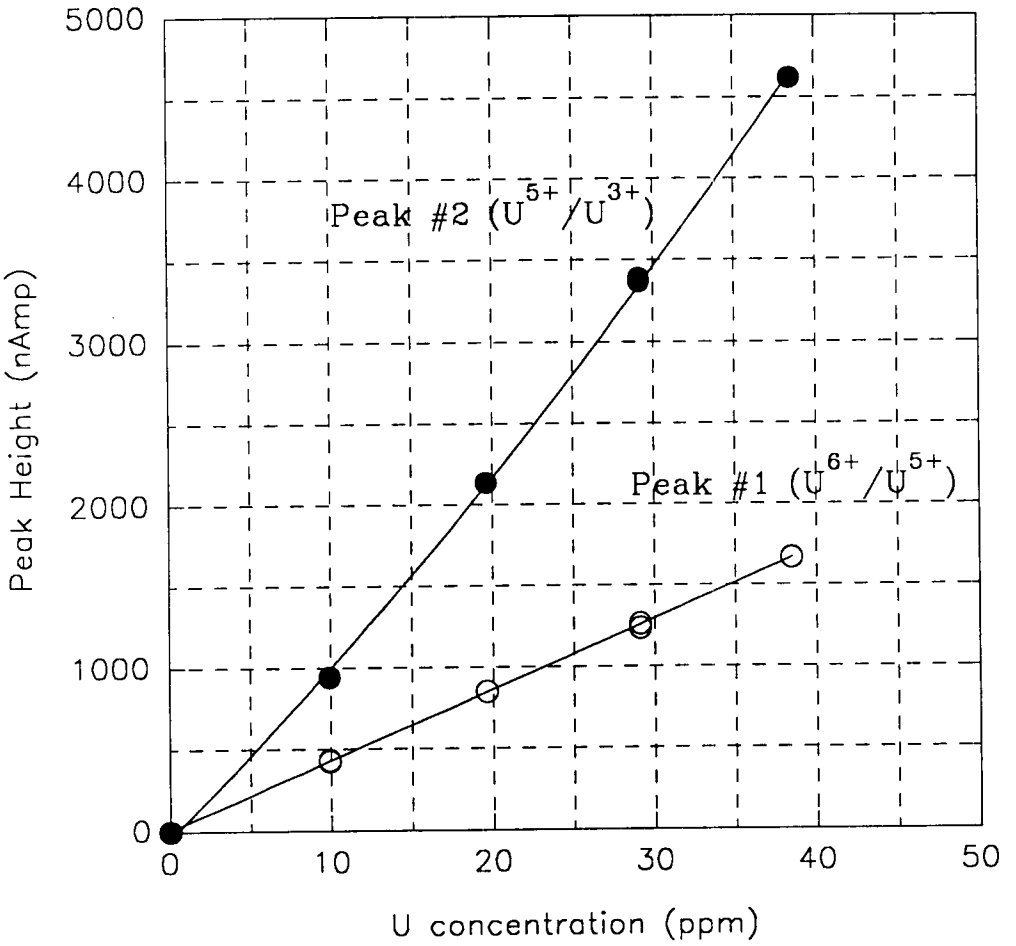

Figure 9-4. Peak height vs. uranium concentration for the two cathodic reactions of uranium.

In evaluating specific polarographic techniques and background electrolytes for uranium analysis, the parameters requiring consideration include sensitivity (detection limit), linear range of concentration vs. peak height, reproducibility, and possible interferences. Our initial tests of square-wave voltammetry using 0.1 M HCl matrix focused on uranium concentrations between 1 and 500 ppm. A typical square-wave voltammogram is given in Figure 9-3, for the analysis of an aqueous solution with 10 ppm U. The figure shows two peaks at half-wave potentials of -0.15 and -0.88 volts vs. a KCl-saturated Ag/AgCl electrode. These two peaks correspond to the two cathodic reactions of uranium. The linearity of concentration vs. peak height was tested by analyzing 10 ml of 0.1 M HCl solution and adding 100 μl spikes of 1000 ppm U standard (Ricca Chemical; $UO_2(NO_3)_2 \bullet 6H_2O$ dissolved in water). The results are plotted in Figure 9-4. The figure indicates that peak height vs. concentration is linear up to about 40 ppm for the peak corresponding to the first cathodic reaction. On the other hand, peak height vs. concentration for the second cathodic peak is nonlinear. This behavior is due to disproportionation of +5 uranium to the +6 and +4 states (Kolthoff and Lingane, 1952).

Linearity of concentration vs. peak height over a concentration range of 1-500 ppm U was tested by analyzing solutions prepared by diluting a 1000 ppm U standard with 0.1 M HCl solutions. Over this range of concentration, nonlinearity is observed at the high concentration end for both cathodic peaks as shown in Figure 9-5. Reproducibility of the results was tested by repeating the analyses on a different day. A comparison of the two analyses is shown in Figure 9-6, which indicates that reproducibility is relatively good, considering that no attempt was made to maintain the solutions at the same temperature for both analyses.

To some extent, the nonlinearity in peak height vs. concentration was caused by differences in HCl concentration of the solutions. The solutions with higher U concentrations effectively have lower HCl concentrations because a larger amount of U standard (dissolved in pure water) was mixed with the 0.1 M HCl solution. To confirm this, a 500 ppm U solution with an actual concentration of 0.1 M HCl was prepared and analyzed. The results for this sample are plotted as square symbols in Figure 9-5, and demonstrate that there is some dependence of peak height on the HCl concentration. Although not shown in the figures, HCl concentration was also observed to affect the half-wave potentials for the uranium cathodic reactions.

It is important to study quantitatively the dependence of peak height and half-wave potentials on HCl concentration to determine potential errors in polarographic analysis of uranium. Such a study is underway at present. In addition, evaluation of polarographic analysis of uranium will look at applications to lower concentrations (down to sub-parts-per-billion level) using stripping techniques, and potential interferences from other solutes.

9.5. REFERENCES

Alemi, M. H., D. A. Goldhamer, and D. R. Nielsen. 1991. Modeling selenium transport in steady-state, unsaturated soil columns. *Jour. Environ. Qual. 20:* 89-95.

Allison, J. D., D. S. Brown, and K. J. Novo-Gradac. 1990. *MINTEQA2/PRODEFA2, A geochemical assessment model for environmental systems: Version 3.0 user's manual.* Athens, GA: Environmental Research Laboratory, Office of Research and Development, Environmental Protection Agency.

Ames, L. L., J. E. McGarrah, B. A. Walker, and P. F. Salter. 1982. Sorption of Uranium and Cesium by Hanford Basalts and Associated Secondary Smectite. *Chemical Geology 35:* 205 - 225.

Ames, L. L., J. E. McGarrah, and B. A. Walker. 1983a. Sorption of trace constituents from aqueous solutions onto secondary minerals. I. Uranium. *Clays Clay Minerals 31:* 321-334.

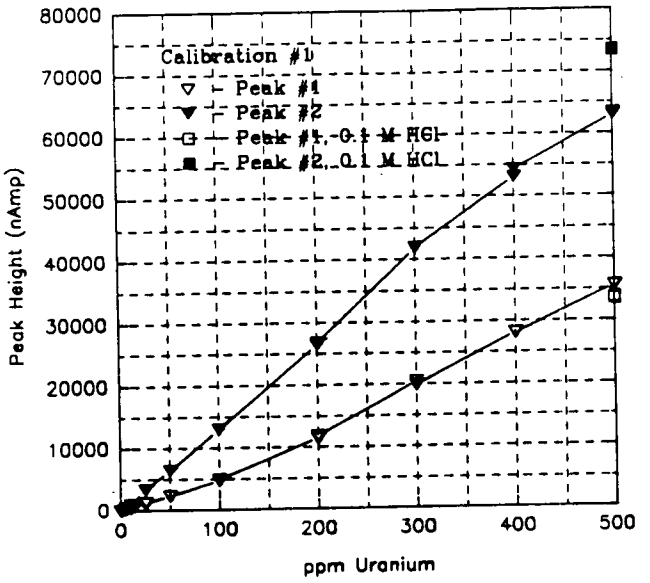

Figure 9-5. Peak height vs. concentration for uranium concentrations up to 500 ppm in HCl matrix. Square symbols correspond to 500 ppm solution with 0.1 M HCl concentration.

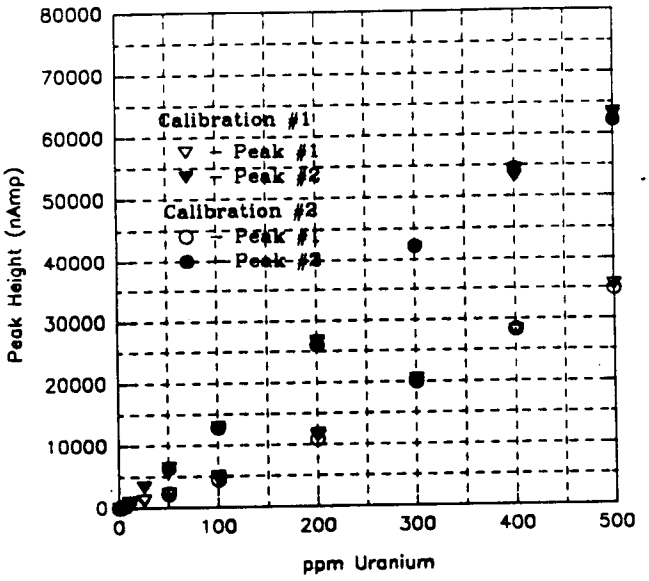

Figure 9-6. Comparison of results for duplicate polarographic analyses of uranium solutions. The second set of analyses were conducted on a different day.

Ames, L. L., J. E. McGarrah, and B. A. Walker. 1983b. Sorption of trace constituents from aqueous solutions onto secondary minerals. II. Radium. *Clays Clay Minerals 31:* 335-342.

Ames, L. L., J. E. McGarrah, and B. A. Walker. 1983c. Sorption of uranium and radium by biotite, muscovite, and phlogopite. *Clays Clay Minerals 31:* 343-351.

Balistieri, L. S., and J. W. Murray. 1986. The surface chemistry of sediments from the Panama Basin: The influence of Mn oxides on metal adsorption. *Geochim. Cosmochim. Acta 50:* 2235-2243.

Beckman, R., K. Thomas, and B. Crowe. 1988. *Preliminary Report on the Statistical Evaluation of Sorption Data: Sorption as a Function of Mineralogy, Temperature, Time, and Particle Size.* LA-11246-MS. Los Alamos, NM: Los Alamos National Laboratory (LANL).

Benjamin, M. M., and J. O. Leckie. 1981. Multiple-site adsorption of Cd, Cu, Zn, and Pb on amorphous iron oxyhydroxide. *Jour. Colloid Interface Sci. 79:* 209-221.

Bond, A. M. 1980. *Modern Polarographic Methods in Analytical Chemistry*. New York: Marcel Dekker.

Comans, R. N. J., and J. J. Middleburg. 1987. Sorption of trace metals on calcite: Applicability of the surface precipitation model. *Geochim. Cosmochim. Acta 51:* 2587-2591.

Davis, J. A., and J. O. Leckie. 1978. Surface ionization and complexation at the oxide/water interface II. Surface properties of amorphous iron oxyhydroxide and adsorption of metal ions. *Journal of Colloid and Interface Science 67:* 90-107.

Dubinin, M. M., and L. V. Radushkevich. 1947. Equation of the characteristic curve of activated charcoal. *Proc. Acad. Sci. U.S.S.R., Phys. Chem. Sect. 55:* 331-333.

Ebinger, M. H., E. H. Essington, E. S. Gladney, B. D. Newman, and C. L. Reynolds. June 1990. *Long-Term Fate of Depleted Uranium at Aberdeen and Yuma Proving Grounds Final Report, Phase I: Geochemical Transport and Modeling.* LA-11790-MS. Los Alamos, NM: LANL.

Freundlich, H. 1926. *Colloid and Capillary Chemistry.* London: Methuen.

Harris, W. E., and I. M. Kolthoff. 1945. *J. Amer. Chem. Soc.* 67: 1484.

Hayes, K. F., and J. O. Leckie. 1986. Mechanism of lead ion adsorption at the goethite-water interface. *Geochemical Processes at Mineral Surfaces.* ACS Symposium Series, v. 323. J. A. Davis and K. F. Hayes, eds. Washington, D.C.: American Chemical Society (ACS): 114-141.

Hayes, K. F., G. Redden, W. Ela, and J. O. Leckie. 1989. *Application of Surface Complexation Models for Radionuclide Adsorption: Sensitivity Analysis of Model Input Parameters.* NUREG/CR-5547. Washington, D.C.: NRC.

Hiemstra, T., W. H. van Riemsdijk, and G. H. Bolt. 1989. Multisite proton adsorption modeling at the solid/solution interface of (hydr)oxides: A new approach. I. Model description and evaluation of intrinsic reaction constants. *Journal of Colloid and Interface Science 133:* 91-104.

Hsi, C.- K. D., and D. Langmuir. 1985. Adsorption of uranyl onto ferric oxyhydroxides: Application of the surface complexation site-binding model, *Geochim. Cosmochim. Acta.* 49: 1931-1941.

Hunt, D. T. and A. L. Wilson. 1986. *The Chemical Analysis of Water - General Principles and Techniques.* Cambridge, UK: Royal Society of Chemistry.

Jackson, M. L. 1956. *Soil Chemical Analysis - Advanced Course.* Madison, WI: Dept. of Soil Science, Univ. of Wisconsin.

Jennings, A. A., and D. J. Kirkner. 1984. Instantaneous equilibrium approximation analysis. *Jour. Hydraul. Div. Am. Soc. Civ. Eng. 110:* 1700-1717.

Kelmers, A. D., R. E. Meyer, J. G. Blencoe, and G. K. Jacobs. 1987. Radionuclide sorption methodologies for performance assessment of high-level nuclear waste repositories: A perspective gained from an NRC workshop. *Nuclear Safety.* 28: 515-522.

Kent, D. B., V. S. Tripathi, N. B. Ball, J. O. Leckie, and M. D. Siegel. 1988. *Surface-Complexation Modeling of Radionuclide Adsorption in Subsurface Environments.* NUREG/CR-4807. Washington, D.C.: NRC.

Kerrisk, J. F. 1985. *An Assessment of the Important Radionuclides in Nuclear Waste.* LA-10414-MS: Los Alamos, NM. LANL.

Kolthoff, I. M., and W. E. Harris. 1946. *J. Amer. Chem. Soc.*, 68: 1175.

Kolthoff, I. M., and J. J. Lingane. 1952. *Polarography.* 2nd ed. New York: Interscience.

Krishnaswami, S., W. C. Graustein, K. K. Turekian, and J. F. Dowd. 1982. Radium, thorium and radioactive lead isotopes in groundwaters: Application to the in-situ determination of adsorption-desorption rate constants and retardation factors. *Water Resourc. Res. 18:* 1633-1675.

LaFlamme, B. D., and J. W. Murray. 1987. Solid/solution interaction: The effect of carbonate alkalinity on adsorbed thorium. *Geochim. Cosmochim. Acta 51:* 243-250.

Langmuir, D. 1918. The adsorption of gases on plane surfaces of glass, mica, and platinum. *Jour. Amer. Chem. Soc. 40:* 1361-1403.

Meijer, A. 1990. *Yucca Mountain Project Far-Field Sorption Studies and Data Needs.* LA-11671. Los Alamos, NM. LANL.

Meites, L. 1965. *Polarographic Techniques*. 2nd ed. New York: Interscience.

Middleburg, J. J., and R. N. J. Comans. 1991. Sorption of cadmium on hydroxyapatite. *Chemical Geology 90:* 45-53.

Murali, V., and L. A. G. Aylmore. 1983b. Competitive adsorption during solute transport in soils: 2. Simulations of competitive adsorption. *Soil Science 135:* 203-213.

Murali, V., and L. A. G. Aylmore. 1983a. Competitive adsorption during solute transport in soils: 1. Mathematical models. *Soil Science 135:* 143-150.

Murali, V., and L. A. G. Aylmore. 1983c. Competitive adsorption during solute transport in soils: 3. A review of experimental evidence of competitive adsorption and an evaluation of simple competition models. *Soil Science 136:* 279-290.

Pabalan, R. T. 1991. Unsaturated mass transport (geochemistry): Experimental studies. W. C. Patrick, ed. *Report on Research Activities for Calendar Year 1990.* CNWRA 90-01A. San Antonio, TX: CNWRA.

Pabalan, R. T., and D. Turner. 1991. Sorption modeling for HLW performance assessment. W. C. Patrick, ed. *Report on Research Activities for the Quarter January 1 Through March 31, 1991.* CNWRA 91-01Q. San Antonio, TX: CNWRA.

Payne, T. E., and T. D. Waite. 1991. Surface complexation modelling of uranium sorption data obtained by isotope exchange techniques. *Radiochimica Acta 52/53:* 487-493.

Pietrzak, R. F., K. S. Czyscinski, and A. J. Weiss. 1981. Sorption measurements performed under site-specific conditions: Maxey Flats, Kentucky, and West Valley, New York, Disposal Sites. *Nuclear and Chemical Waste Management 2:* 279-285.

Polzer, W. L., and H. R. Fuentes. 1988. The use of a heterogeneity-based isotherm to interpret the transport of radionuclides in volcanic tuff media. *Radiochim. Acta 44/45:* 361-365.

Polzer, W. L., and H. R. Fuentes. 1991. Fitting a modified Langmuir isotherm to data from batch sorption experiments for radionuclides on tuffs. *Radiochim. Acta 52/53:* 177-179.

Sanchez, A. L., J. W. Murray, and T. H. Sibley. 1985. The adsorption of plutonium IV and V on goethite. *Geochim. Cosmochim. Acta 49:* 2297-2307.

Selim, H. M. 1978. Transport of reactive solutes during transient, unsaturated water flow in multilayered soils. *Soil Science 126:* 127-135.

Selim, H. M., and R. S. Mansell. 1976. Analytical solution of the equation for transport of reactive solutes through soils. *Water Resourc. Res. 12:* 528-532.

Serne, R. J., and A. B. Muller. 1987. A perspective on adsorption of radionuclides onto geologic media. *The Geological Disposal of High Level Radioactive Wastes.* Athens, Greece: Theophrastus Publications: 407-433.

Serne, R. J., R. C. Arthur, and K. M. Krupka. 1990. *Review of Geochemical Processes and Codes for Assessment of Radionuclide Migration Potential at Commercial LLW Sites.* PNL-7285. Richland, Washington. Pacific National Laboratory (PNL).

Siegel, M. D. 1989. *Progress in Development of a Methodology for Geochemical Sensitivity Analysis for Performance Assessment: Speciation, Sorption, and Transport in Fractured Media.* Vol 2. NUREG/CR5085 V.2. Washington, D.C.: NRC.

Siegel, M. D., J. O. Leckie, S. W. Park, S. L. Phillips, and T. Sewards. 1990. *Studies of Radionuclide Sorption by Clays in the Culebra Dolomite at the Waste Isolation Pilot Plant Site, Southeastern New Mexico.* SAND89-2387. Albuquerque, NM: Sandia National Laboratories (SAND).

Thomas, K. 1987. *Summary of Sorption Measurements Performed with Yucca Mountain, Nevada, Tuff Samples and Water from Well J-13.* LA-10960-MS. Los Alamos, NM: LANL.

Travis, C. C., and E. L. Etnier. 1981. A Survey of Sorption Relationships for Reactive Solutes in Soil. *Jour. Environ. Qual. 10:* 8-17.

Tripathi, V. S. 1984. *Uranium transport modeling: geochemical data and submodels,* Ph.D. Dissertation. Stanford, CA: Applied Earth Sciences Department, Stanford University: 297.

Valocchi, A. J. 1984. Describing the Transport of Ion-Exchanging Contaminants Using an Effective K_d Approach. *Water Resourc. Res. 20:* 499-503.

Valocchi, A. J. 1989. Spatial moment analysis of the transport of kinetically adsorbing solutes through stratified aquifers. *Water Resourc. Res. 25:* 273-279.

Yeh, G.T., and V. S. Tripathi. 1989. A critical evaluation of recent developments in hydrogeochemical transport models of reactive multichemical components. *Water Resourc. Res. 25:* 93-108.